



Provided by the author(s) and University of Galway in accordance with publisher policies. Please cite the published version when available.

Title	Synthetic, Structural, Spectroscopic and Theoretical Studies on Homo- and Heterometallic Paramagnetic Complexes
Author(s)	Berg, Nelly
Publication Date	2013-01-08
Item record	<a href="http://hdl.handle.net/10379/3554">http://hdl.handle.net/10379/3554</a>

Downloaded 2024-04-25T11:50:43Z

Some rights reserved. For more information, please see the item record link above.





**Synthetic, Structural, Spectroscopic and  
Theoretical Studies on Homo- and  
Heterometallic Paramagnetic Complexes**

**Nelly Berg**

Supervisor: Dr. Leigh F. Jones  
Head of School: Prof. Paul V. Murphy

Thesis for the degree of PhD

2013  
School of Chemistry  
NUI Galway

## Table of Contents

<b>Abstract</b>	10
<b>Chapter 1: Introduction</b>	14
1.1. History and background of magnetism	15
1.2. Types of magnetic behaviour	17
1.2.1. Paramagnetism	17
1.2.2. Ferromagnetism	18
1.2.3. Antiferromagnetism	18
1.2.4. Ferrimagnetism	18
1.2.5. Superparamagnetism	18
1.3. Quantifying magnetic properties	19
1.4. Measuring magnetic properties	23
1.4.1. SQUID magnetometry	23
1.4.2. Electron Paramagnetic Resonance	23
1.5. Magnetic exchange	25
1.5.1. Introduction to magnetic exchange	25
1.5.2. Superexchange	26
1.5.3. Superexchange: Developments upon Kramer's proposed mechanism	28
1.5.4. Current methods used to rationalize superexchange	30
1.6. Magnetic anisotropy, spin-orbit coupling and zero-field splitting	31
1.7. Molecular magnetism	33
1.8. Applications of molecular magnetism	35
1.8.1. Single-Molecule Magnets	35
1.8.2. Single-Chain Magnets	38
1.8.3. Molecular coolants	38
1.8.4. Molecular spintronic devices	39
1.8.5. Spin-crossover complexes	40
1.9. Synthesis of magnetic clusters and coordination polymers	40
1.9.1. Choice of ligand	40
1.9.2. 2,2'-Biphenol	41
1.9.3. The role of co-ligands	41
1.9.4. Reactant Ratios	42
1.10 Bibliography	43
<b>Chapter 2: What Controls the Magnetic Interaction in bis-<math>\mu</math>-Alkoxo Mn(III) Dimers? A Combined Experimental and Theoretical Exploration</b>	47
2.1. Introduction	48
2.2. Results and discussion	50
2.2.1. Structural descriptions	50
2.2.2. Magnetic susceptibility measurements	56
2.3. Magneto-structural correlation study	57
2.3.1. Types I-III	57
2.3.2. Theoretical studies	62
2.3.2.1. DFT calculations	62
2.3.2.2. Orbital analysis	65
2.3.3. Other structural factors	67

2.3.3.1. Bond angle	67
2.3.3.2. Bond distance	68
2.3.3.3. Dihedral angle	69
2.3.3.4. Out of plane displacemene of alkyl groups ( $\tau$ )	69
2.4. Conclusion	69
2.5. Experimental section	71
2.5.1. Physical measurements	71
2.5.2. X-ray crystallography	71
2.5.3. Computational details	71
2.5.4. Syntheses	72
2.6. Bibliography	75
<b>Chapter 3: Synthetic, Structural, Spectroscopic and Theoretical Study of a Mn(III)-Cu(II) Dimer Containing a Jahn-Teller Compressed Mn(III) ion</b>	<b>82</b>
3.1. Introducion	83
3.1.1. Jahn-Teller effects	83
3.1.2. Relationships between magnetic coupling and Jahn-Teller effects	84
3.2. Results and discussion	87
3.2.1. Structural descriptions	87
3.2.2. SEM images	92
3.2.3. Squid magnetometry	93
3.2.4. EPR spectroscopy	96
3.3. Magneto-structural correlation	101
3.3.1. DFT analysis	101
3.4. Conclusion	106
3.5. Experimental section	107
3.5.1. Physical measurements	107
3.5.2. X-ray crystallography	107
3.5.3. Computational details	108
3.5.4. Syntheses	108
3.6. Bibliography	111
<b>Chapter 4: A Series of Alternating Na(I)/M(III) (M = Mn, Fe) Covalent and Ionic Chains</b>	<b>116</b>
4.1. Introduction	117
4.2. Results and discussion	118
4.2.1. Results	118
4.2.2. Discussion	132
4.3. Conclusion	135
4.4. Experimental section	136
4.4.1. Physical measurements	136
4.4.2. Syntheses	136
4.5. Bibliography	140
<b>Chapter 5: An Investigation into the Coordination Chemistry of 2,2'-biphenol with Co(II/III); a Structural and Magnetic Study</b>	<b>143</b>
5.1. Introduction	144

5.1.1. Cobalt	144
5.1.2. Co(II) in SMMs	144
5.1.3. Coordination polymers comprising Co(II) ions	146
5.2. Results and discussion	147
5.2.1. Discrete complexes of Co(II)	147
5.2.2. Magnetic susceptibility measurements	154
5.2.3. Coordination polymers comprising Co(II) nodes	157
5.3. Conclusion	161
5.4. Experimental section	162
5.4.1. Physical measurements	162
5.4.2. Crystallography	162
5.4.3. Syntheses	162
5.5. Bibliography	165
<b>Chapter 6: The Role of Cu(I)X (X = Cl<sup>-</sup>, Br<sup>-</sup>) in the Synthesis of Discrete {Ln(III)<sub>x</sub>Cu(I/II)<sub>y</sub>} Cage and Infinite Lattice Formations</b>	167
6.1. Introduction	168
6.1.1. Magnetic properties of the lanthanoids	168
6.1.2. Compounds containing both rare earth and transition metal ions	168
6.1.3. 2-hydroxypyridine as a bridging ligand in Cu(II)-Ln(III) clusters	171
6.2. Results and discussion	172
6.2.1. A family of discrete [Ln(III) <sub>4</sub> Cu(II) <sub>4</sub> ] clusters	172
6.2.1.1. Structural descriptions	173
6.2.1.2. Magnetic susceptibility measurements on complex <b>22</b>	178
6.2.2. Coordination polymers comprising {Ln(III) <sub>2</sub> Cu(III) <sub>8</sub> } cluster nodes	179
6.2.2.1. Structural descriptions	180
6.3. Conclusion	182
6.4. Experimental section	183
6.4.1. Physical measurements	183
6.4.2. X-ray crystallography	183
6.4.3. Syntheses	184
6.5. Bibliography	189
<b>Chapter 7: Conclusion</b>	192
<b>Appendix A</b>	196
<b>Appendix B</b>	201
<b>Appendix C</b>	202

## List of Figures

- Figure 1.** Schematic diagram depicting Zeeman Splitting.
- Figure 2.** Schematic diagram depicting the alignment of individual magnetic moments in (A) paramagnetic, (B) ferromagnetic, (C) antiferromagnetic and (D) ferrimagnetic systems.
- Figure 3.** Graph depicting the variation of  $\chi_M T$  with temperature.
- Figure 5.** Schematic representation depicting the splitting of the  $m_s$  states in the presence of an applied magnetic field.
- Figure 6.** Schematic diagram depicting the kinetic exchange interaction.
- Figure 7.** Schematic diagram depicting the ferromagnetic superexchange interaction in a hypothetical Mn(II)-O<sup>2-</sup>-Mn(II) 90° bonding scenario.
- Figure 8.** MO diagrams depicting the superexchange interaction between two Cu(II) ions.
- Figure 9.** Schematic representations of zero-field splitting.
- Figure 10.** Examples of a discrete cluster and a 1-D coordination polymer.
- Figure 11.** Crystal structure of the archetypal SMM – Mn<sub>12</sub>OAc.
- Figure 12.** Microstates of Mn<sub>12</sub>OAc, split due to ZFS.
- Figure 13.** Popular ligands employed in the field of molecular magnetism.
- Figure 14.** Diagram of 2,2'-biphenol.
- Figure 15.** Diagrams of three pyridyl ligands successfully utilized in this work.
- Figure 16.** Crystal structures of the complexes **1–5**.
- Figure 17.** Polyhedral representation of the packing observed in the unit cell of **1**.
- Figure 18.** Packing diagram of **2**.
- Figure 19.** Packing diagrams for complexes **3–5**.
- Figure 20.** Plots of magnetic susceptibility ( $\chi_M T$ ) vs T for complexes **1** and **2**.
- Figure 21.** Plots of magnetic susceptibility ( $\chi_M T$ ) vs T for complexes **3–5**.
- Figure 22.** Schematic illustrating the three types of magnetic orbital spatial orientations observed within recognised  $\mu$ -OR bridged [Mn(III)<sub>2</sub>] complexes.
- Figure 23.** Plot of  $J$  (cm<sup>-1</sup>) versus the angle forged between the two Jahn-Teller axes in [Mn(III)<sub>2</sub>] dimers of types I–III.
- Figure 24.** Crystal structures of complex **1** (a), complex II-**2** (b) and complex III-**2**.
- Figure 25.** B3LYP computed spin density plot for **1**, II-**2** and III-**2**.
- Figure 26.** Alpha magnetic orbitals of complexes **1**, II-**2** and III-**2** in order of decreasing energy.
- Figure 27.** Dominant interactions between the magnetic orbitals in type I – III structures.
- Figure 28.** Magneto-structural correlations developed by varying the structural parameters Mn-O-Mn and Mn-O-Mn-O angles, Mn-O distance and  $\tau$  using DFT calculations.
- Figure 29.** Schematic diagram showing the relative energies of the 3d orbitals in a Jahn-Teller elongated octahedral Mn(III) ion, and a Jahn-Teller compressed octahedral Mn(III) ion (right).
- Figure 30.** Schematic of the ( $\mu$ -oxo)bis( $\mu$ -carboxylato)dimanganese(III) core.
- Figure 31.** Molecular structure of the cationic heterobimetallic unit in **6**.
- Figure 32.** Packing diagram of **6** as viewed along the  $a$  direction of the unit cell.
- Figure 33.** Molecular structure of the cationic heterobimetallic unit in **7**.
- Figure 34.** Packing diagram of **6** as viewed along the  $b$  direction of the unit cell.
- Figure 35.** Molecular structure of the cationic unit in **8**.
- Figure 36.** Crystal packing diagram of complex **8** as viewed along the  $a$  axis of the unit cell.
- Figure 37.** SEM images showing the crystals of **6**, **7** and **8**.
- Figure 38.** Plot of the  $\chi_M T$  product of **6** vs.  $T$  in the 250 - 5 K temperature range in an applied field of 0.1 T.

**Figure 39.** Plot of reduced magnetisation of **6** in the 2.0 to 7.0 K temperature range.

**Figure 40.** Representative frequency dependent powder EPR spectra collected at 5 K.

**Figure 41.** Plot of the frequency dependent EPR peak positions as a function of the applied magnetic field strength.

**Figure 42.** ORTEP diagram of **9** showing Jahn-Teller elongation of Mn(III) ion.

**Figure 43.** DFT calculated magnetic orbitals of Mn(III) and Cu(II) in complex **6** with computed  $S_{ab}$  (overlap integral) values.

**Figure 44.** DFT computed spin density plot of **6** for the  $S = 2$  state.

**Figure 45.** Diagram illustrating the different contributions to the anisotropy in complex **6**.

**Figure 46.** DFT calculated orientation of  $D$ -tensor in **6**.

**Figure 47.** Crystal structure of the chain in **10**.

**Figure 48.**  $\eta^2:\eta^2:\mu_3$ -bonding motif observed in many complexes described in this chapter.

**Figure 49.** Crystal packing observed in the structure of **10**.

**Figure 50.** Crystal packing observed in **10** as viewed along the [011] cell face.

**Figure 51.** The H-bonded chain in **11**.

**Figure 52.** The chelating mode adopted by  $LH_2$  in the structure of the ionic chains.

**Figure 53.** The H-bonded chain in **12**.

**Figure 54.** Crystal packing observed in **12**.

**Figure 55.** The H-bonded chain in **13**.

**Figure 56.** The H-bonded chains in **13** (a) and covalent chains in **14** (b).

**Figure 57.** Asymmetric unit in the covalent polymer **14**.

**Figure 58.** (top) Part of a 1-D row in chain **15**. (bottom) View of the chains in **15**.

**Figure 59.** Crystal structure of the monomeric complex **16**. (bottom) View of **16** down the  $c$  axis of the unit cell.

**Figure 60.** Crystal packing observed in complex **16** as viewed along the  $b$  axis.

**Figure 61.** Crystal structure of the Na(I)/Fe(III) covalent chain of **17**.

**Figure 62.** Crystal structure of **17** showing various intra- and inter-chain interactions.

**Figure 63.** Schematic highlighting the different types of chains observed in this work.

**Figure 64.** Schematics illustrating the twisting of the 2,2'-biphenolate aromatic rings when ligated to Mn(III) and Na(I) ions in this study.

**Figure 65.** Crystal field splitting diagram of octahedral Co(II) in the high spin configuration.

**Figure 66.** Structure of the ligand 2,2'-biphenol ( $LH_2$ : top left) and the bonding modes it exhibits in this chapter under the various levels of deprotonation.

**Figure 67.** Crystal structures of **18** (top) and **19** (bottom) respectively.

**Figure 68.** Views perpendicular to the superimposable rows within the cells of **18** (top) and **19** (bottom).

**Figure 69.** Packing of **18** as viewed along the  $a$  axis of the unit cell.

**Figure 70.** Crystal structure of **20**.

**Figure 71.** Inorganic core in **20** highlighting the six face-sharing  $\{Co(II)_3O\}$  triangular units.

**Figure 72.** Crystal images of complexes **18** to **22** (left to right).

**Figure 73.** Plots of  $\chi_M T$  vs.  $T$  obtained from polycrystalline samples of **18** and **19** in the 300 - 5 K Temperature range in the applied field of 0.1 T.

**Figure 74.** Plots of  $\chi_M T$  vs.  $T$  obtained from polycrystalline samples of **20** in the 300 - 5 K Temperature range in the applied field of 0.1 T.

**Figure 75.** Plot of  $1/\chi$  vs.  $T$  obtained from a polycrystalline sample of **20** measured in an external field of 0.1 T in the 300-5 K temperature range.

**Figure 76.** Plot of  $M N^{-1} \mu_B$  vs.  $H/T$  ( $kG K^{-1}$ ) obtained on a polycrystalline sample of **20**.

**Figure 77.** The asymmetric unit of complex **21**.

**Figure 78.** Packing in **21**.

**Figure 79.** Space-fill representations of the separate 1-D Chains in **21**.

- Figure 80.** Asymmetric unit in **22**.  
**Figure 81.** Colour coded space-fill represented brickwork sheets in **22**.  
**Figure 82.** Crystal structures of **23**.  
**Figure 83.** The magnetic core of **23** highlighting all bridging pathways.  
**Figure 84.** Unit cell in **23** as viewed along the *a* axis accommodating one [Gd(III)<sub>4</sub>Cu(II)<sub>4</sub>] cluster.  
**Figure 85.** The unit cell of complex **24** comprising four quarter [Dy(III)<sub>4</sub>Cu(II)<sub>4</sub>] cluster units.  
**Figure 86.** The unit cell of complex **25** comprising two half {Tb(III)<sub>4</sub>Cu(II)<sub>4</sub>} cluster units.  
**Figure 87.** Temperature dependence of  $\chi_M T$  for **22** collected in an applied field of 0.1 T.  
**Figure 88.** Plot of reduced magnetization ( $N\mu_B$ ) vs  $H/T$  (kG K<sup>-1</sup>) obtained from **22** in the 2-7 K temperature range.  
**Figure 89.** Molecular structure of the 1-D polymer of **26**.  
**Figure 90.** The infinite linear structure of **26** showing the {Cu(I)Cl<sub>3</sub>}<sup>2-</sup> linker moieties.

## List of Tables

- Table 1.** Selected bond lengths (Å) and angles (°) for complexes **1-3**.  
**Table 2.** Selected bond lengths (Å) and angles (°) for complexes **4** and **5**.  
**Table 3.** Crystallographic data obtained from complexes **1-5**.  
**Table 4.** Selected magneto-structural parameters for type I dinuclear complexes discussed in this chapter and in the literature.  
**Table 5.** Selected magneto-structural parameters for type II dinuclear complexes discussed in this chapter and in the literature.  
**Table 6.** Selected magneto-structural parameters for type III dinuclear complexes discussed this chapter and in the literature.  
**Table 7.** DFT computed spin densities of selected atoms of complex **1**, II-2 and III-2.  
**Table 8.** Crystal data for complexes **6-8**.  
**Table 9.** DFT computed spin-flip/spin-conserved excitations for the Cu(II)-Mn(III) (**6**) and Zn(II)-Mn(III) complexes.  
**Table 10.** Experimental versus DFT computed single-ion and cluster anisotropies with SOC and SS contributions.  
**Table 11.** Crystallographic data for complexes **10-13**.  
**Table 12.** Crystallographic data for complexes **14-17**.  
**Table 13.** Crystallographic data table for complexes **18-22**.  
**Table 14.** Crystal data obtained from X-ray diffraction studies on **23-25**.

## Glossary of Abbreviations, Acronyms and Symbols

**SMM:** Single-Molecule Magnet  
**MOF:** Metal-Organic Framework  
**SCM:** Single-Chain Magnet  
**SQUID:** Superconducting Quantum Interference Device  
**FT-IR:** Fourier transform infra-red  
**UV-vis:** Ultraviolet-visible  
**ZFS:** Zero-Field Splitting  
**DFT:** Density Functional Theory  
**EPR:** Electron Paramagnetic Resonance  
**MO:** Molecular orbital  
**SOMO:** Singly occupied molecular orbital  
**VMO:** Virtual molecular orbital  
**DOMO:** Doubly occupied molecular orbital  
**LH<sub>2</sub>:** 2,2'-biphenol  
**2-hpH:** 2-hydroxypyridine  
**tmdp:** 4,4'-trimethylenedipyridine  
**trans-bpe:** trans-1,2-bis(4-dipyridyl)ethylene  
**M<sub>S</sub>:** Magnetic microstate  
**J:** Magnetic coupling constant  
**J<sub>F</sub>:** Ferromagnetic contribution to J  
**J<sub>AF</sub>:** Antiferromagnetic contribution to J  
**D:** Zero-Field Splitting parameter  
**S:** Spin quantum number  
**H:** External magnetic field  
**M:** Molar magnetization  
**χ<sub>M</sub>:** Molar magnetic susceptibility  
**g<sub>e</sub>:** electron g-factor  
**μ<sub>B</sub>:** Bohr Magnetron  
**N:** Avogadro's number  
**k<sub>B</sub>:** Boltzmann constant  
**α:** Spin-up  
**β:** Spin-down

## **Declaration**

No portion of the work referred to in this thesis has been submitted in support of an application for another degree or qualification, at this, or any other university or institute of higher learning.

## **Acknowledgements**

First of all, my gratitude goes to Dr. Leigh Jones for all his help and support throughout the three years of my PhD project. I could not have asked for a more helpful, creative and enthusiastic supervisor. Dr. Euan Brechin and his research team at the University of Edinburgh also deserve a very special thanks for performing all of the magnetic measurements reported in this thesis, and for giving me the opportunity to spend some time living and working in beautiful Edinburgh. The EPR and DFT studies of chapters 2 and 3 would not have been possible without the generosity of Prof. Steve Hill and co-workers of Florida State University, and Dr. Gopalan Rajaraman and his students at the Indian Institute of Technology in Mumbai. Of course, none of this work would have been possible without the financial support of the IRCSET EMBARK initiative. A big thanks goes to Sean Meally, Cecelia McDonald and Edel Houton for all the good times we've had inside and outside the lab, and to Fiona, Michelle, Brenda, Nikki, Jola and Oliver for all the tea breaks over the last three years. My mother Marie-Clare, sisters Louise and Róisín, and partner Conn were all a massive support during my write-up months and helped me to keep my sanity intact, so my final acknowledgements go to them.

## Abstract

This thesis covers many areas within the field of molecular magnetism. With the exception of chapter 6, all novel complexes in this thesis have been synthesized using the bidentate ligand 2,2'-biphenol (LH<sub>2</sub>), usually in conjunction with various pyridyl co-ligands. Investigation of this ligand in the context of molecular magnetism has been immensely successful and has led to a plethora of beautiful novel complexes.

In chapter 2 we report a new family of five  $\mu$ -alkoxide bridged [Mn(III)<sub>2</sub>] dimers. These complexes (**1-5**) have been used towards a full magnetic and DFT analysis of all [Mn(III)-(OR)<sub>2</sub>-Mn(III)] dimers in the literature. We have categorized this type of dimeric Mn(III) complex into three distinct groups, based on the relative orientations of the Mn(III) ions' Jahn-Teller axes. This study is an extremely useful contribution to the field of molecular magnetism as we have concluded that the main structural feature that determines the magnetic exchange coupling in these systems is in fact the Jahn-Teller axes relative orientation. Since the magnetic skeletons of large polynuclear Mn(III) clusters are often made up of dimeric building blocks linked via alkoxide bridges, this study aids in the rationalization of magnetic interactions in these larger clusters. These findings have been published in the Wiley journal: Chemistry - A European Journal [1].

From here we proceeded to investigate the ability of 2,2'-biphenol to complex both manganese and copper ions, which led to the production of two novel Cu(II)-Mn(III) dimers (**6** and **7**), each possessing a rare Jahn-Teller compressed Mn(III) ion, as detailed in chapter 3. To our knowledge, these are the first Cu(II)-Mn(III) dimers to possess a Mn(III) ion in a compressed octahedral environment. This chapter details another comparative study, in which we contrast the ferrimagnetic interaction between the Cu(II) and Mn(III) ions in one of our novel dimers (complex **6**), with that of a ferromagnetic Cu(II)-Mn(III) Single-Molecule Magnet from the literature (complex **9**). DFT calculations offer insight into the mechanism of magnetic coupling where the origin of the antiferromagnetic interaction is related to the nature of the Jahn-Teller distortion. The electronic structure and zero-field splitting of our Cu(II)-Mn(III) dimer (complex **6**) was analysed using single crystal high-frequency high-field EPR. This interesting study has been submitted for publication to the RSC journal: Dalton Transactions [2].

Continuing on the topic of heterometallic chemistry, in chapter 4 we report a family of 1-D coordination polymers (complexes **10-15** and **17**), whose nodes are comprised of alternating M(III) and Na(I) units (M = Mn / Fe). This M(III)–Na(I)–M(III)–Na(I) motif is extremely rare, and these complexes represent the first coordination polymers built using 2,2'-biphenol. These infinite chains have been obtained through the modification of the synthetic procedures used in the preparation of the [Mn(III)<sub>2</sub>] dimers described in chapter 2. By adding an excess of both 2,2'-biphenol and NaOH, 1-D Mn(III)/Na(I) coordination polymers are produced, rather than discrete [Mn(III)<sub>2</sub>] complexes. Additionally, in this study we show how modifying the functionality of the pyridyl co-ligand (from -CH<sub>3</sub> to -CH<sub>2</sub>CH<sub>3</sub>) or changing the position of the ligand functional group (from the 3- to the 4-position), changes the nature of the polymer formed; from a M(III)/Na(I) chain whereby the metal ions are bridged via the coordinate bonds of intermediate L<sup>2-</sup> oxygen atoms, to an ionic 1-D array comprising [Na]<sup>+</sup> and [M]<sup>-</sup> monomeric units linked via hydrogen bonding. Our initial findings have been published in the RSC journal CrystEngComm in 2010 [3], which was followed by a full paper in 2011 in the same journal [4].

In chapter 5 we move on to investigate the chemistry of 2,2'-biphenol with the highly magnetically anisotropic Co(II) ion. Here we report the Co(II) analogues (complexes **18** and **19**) to the homo- and heterometallic dimers of chapter 3, a ferromagnetic [Co(II)<sub>8</sub>] cluster (**20**), and 1- and 2-dimensional coordination polymers comprising magnetically dilute Co(II) nodes (**21** and **22** respectively). This family of five novel complexes represent the first complexes of cobalt constructed using 2,2'-biphenol, while the [Co(II)<sub>8</sub>] cluster is the second largest discrete cluster ever synthesized using this ligand. This structural and magnetic study has been published in CrystEngComm [5].

Attempts to utilize 2-hydroxypyridine (2-hpH) as a co-ligand in conjunction with 2,2'-biphenol in the synthesis of Cu(II)-Ln(III) systems led to the production of eleven heterometallic complexes containing both Cu(II) and Ln(III) ions. This family comprises a family of [Cu(II)<sub>4</sub>Ln(III)<sub>4</sub>] clusters (**23-25**), alongside a series of 1-D coordination polymers comprising {Ln(III)<sub>2</sub>Cu(II)<sub>8</sub>} nodes (**24-33**). Although 2,2'-biphenol is not present in these complexes (2-hp being the only ligand present), these complexes significantly build on previous research. The gadolinium analogues in these families are currently being investigated for their ability to perform as molecular

coolant materials, while the anisotropic terbium and dysprosium versions will be probed for SMM behaviour. Once these experiments have been completed, this study will be ready for publication.

## Publications

- [1] N. Berg, T. Rajeshkumar, S. M. Taylor, E. K. Brechin, G. Rajaraman, and L. F. Jones, "What Controls the Magnetic Interaction in bis- $\mu$ -Alkoxo Mn(III) Dimers? A Combined Experimental and Theoretical Exploration.," *Chemistry - A European Journal*, vol. 18, no. 19, pp. 5906–18, May 2012.
- [2] N. Berg, T. N. Hooper, J. Liu, C. C. Beedle, S. K. Singh, G. Rajaraman, S. Piligkos, S. Hill, E. K. Brechin, and L. F. Jones, "Synthetic, Structural, Spectroscopic and Theoretical Study of a Mn(III)-Cu(II) Dimer Containing a Jahn-Teller Compressed Mn ion," *Dalton transactions*, vol. 42, pp. 207-216, 2013.
- [3] N. Berg and L. F. Jones, "Alternating bimetallic Na/Mn covalent and ionic chains," *CrystEngComm*, vol. 12, no. 11, p. 3518, 2010.
- [4] N. Berg and L. F. Jones, "A series of alternating  $\text{Na}^+/\text{M}^{3+}$  (M = Mn, Fe) covalent and ionic chains," *CrystEngComm*, vol. 13, no. 17, p. 5510, 2011.
- [5] N. Berg, S. M. Taylor, A. Prescimone, E. K. Brechin, and L. F. Jones, "Old dog, new tricks: 2,2'-biphenol as a bridging and book-end ligand in discrete and extended Co(II) architectures," *CrystEngComm*, vol. 14, no. 8, p. 2732, 2012.

# **Chapter 1:**

## **Introduction**

## 1.1 History and background of magnetism

Thousands of years ago, human beings already knew about the fascinating properties of naturally magnetized magnetite. According to legend, these properties were first discovered by an elderly shepherd called Magnes in ancient Greece [6]. As he was herding his sheep, Magnes noticed that the nails of his sandals and the metal tip of his staff became stuck to the large black rock on which he was standing. This myth explains the origin of the terms magnet and magnetite, although according to many historians, they are named after the Grecian town of Magnesia. The English called pieces of magnetized magnetite ‘Lodestone’, which in Middle English means ‘course-stone’ or ‘leading-stone’, referring to the material’s first practical application as a compass needle. The compass was not invented by the English however, in fact many historians believe that it was used as early as the 13th century BC in China [7].

Hans Christian Ørsted was the first scientist to prove the relationship between electricity and magnetism. He made his initial discovery during a lecture in 1820 when he noticed that a compass needle moved when the electric current from a battery was switched on and off [8]. This led him to perform experiments which confirmed that an electric current produces a magnetic field as it flows through a wire. It was not until 1897, that the origin of electric current – the electron, was discovered by J. J. Thompson and his team while attempting to gain some information as to the nature of cathode rays [9]. His experiments, in which he measured the velocity and the mass to charge ratio for cathode rays, involved combining the magnetic deflection of the rays with their heating on a thermocouple. Velocities of up to 1/10th of that of light along with mass to charge ratios of only 1/1000th of that for the hydrogen ion were found. It was thus concluded that the particles might be “detached and hitherto hypothetical individual electrons or atoms of electricity themselves” [10].

In the same way that electrons moving along a wire produce a magnetic field, in magnetic materials the magnetization results from electron motion in atoms. This motion includes the electron’s orbital angular momentum (its movement about the nucleus) and also the intrinsic spin of the particle. This property of ‘spin’ was first described by Pauli in 1924 as a “peculiar not classically describable two-valuedness of the quantum properties of the valence electron” [11], in an attempt to explain the ‘anomalous’ Zeeman effect displayed by the valence electron of alkali metals. This observed spectral line splitting was then described by Goudsmit and Uhlenbeck in

1925 [12], as arising due to an intrinsic angular momentum or spin of the electron giving rise to a magnetic dipole moment, which could align parallel or antiparallel to the external magnetic field, thus giving rise to two different energy levels as observed in Zeeman splitting. At first, Pauli ridiculed the notion of an electron spinning on its axis, but later accepted the concept as a quantum mechanical property [13]. Each electron thus possesses a spin quantum number  $S = \frac{1}{2}$ , and can have a spin direction of either  $m_s = +\frac{1}{2}$  or  $-\frac{1}{2}$  (Figure 1). These  $m_s$  levels are referred to as *microstates*.

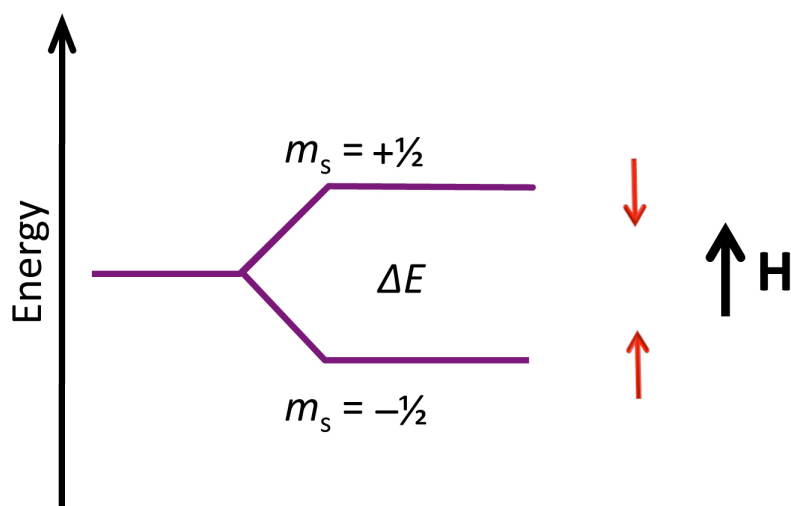


**Figure 1.** Schematic diagram depicting Zeeman Splitting. The electrons can either align themselves parallel or antiparallel with the external magnetic field ( $H$ ), leading to two energy states (microstates).

The magnetic moment of an atom in a magnetic material arises from a combination of the orbital and spin angular momenta of its individual electrons. Paired electrons in orbitals cancel out each other's moments, leaving only the unpaired electrons to contribute to the overall atomic moment. For this reason, elements belonging to the transition metal and lanthanoid series are employed in the construction of magnetic materials, as each metal ion can possess up to five ( $3d^5$ ) and seven ( $4f^7$ ) unpaired electrons respectively. Because these unpaired electrons occupy non-overlapping d- or f-orbitals, their spins align parallel to one another due to Hund's rule (intra-atomic ferromagnetic exchange), leading to a net atomic moment.

There are several ways in which the individual atomic moments in a magnetic solid or molecule can arrange themselves, dictating the overall magnetic behaviour of the material. These arrangements are listed below (section 1.2).

## 1.2 Types of magnetic behaviour

### 1.2.1 Paramagnetism

A paramagnetic material possesses unpaired electrons (unlike a diamagnetic material where all the electrons are spin paired). In pure paramagnetism the individual atomic magnetic moments do not interact with one another and are randomly oriented in the absence of an external magnetic field due to thermal agitation, resulting in a zero net magnetic moment of the material (Figure 2A). When a magnetic field is applied, the individual moments will tend to align with the applied field, resulting in a net magnetic moment in the direction of the applied field. Paramagnetic materials have a positive magnetic susceptibility and are thus attracted by an external magnetic field, whereas diamagnetic materials are repelled by an external field.

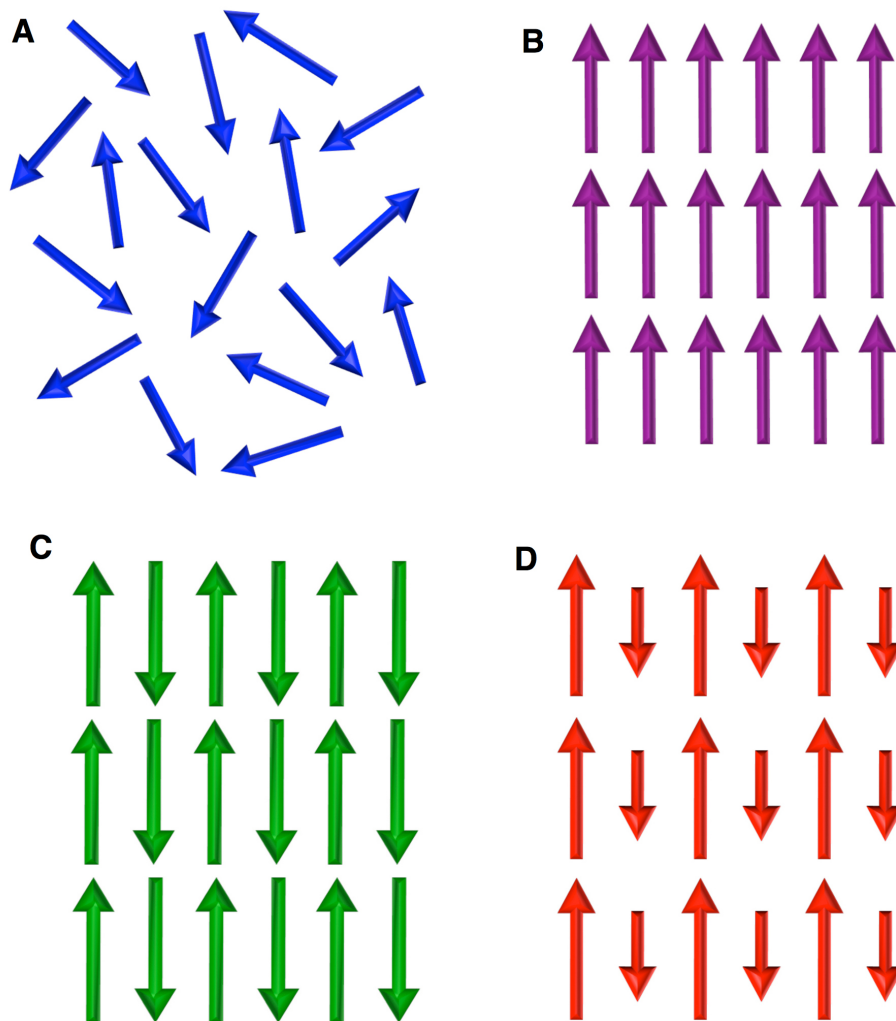


**Figure 2.** Schematic diagram depicting the alignment of individual magnetic moments in (A) paramagnetic, (B) ferromagnetic, (C) antiferromagnetic and (D) ferrimagnetic systems.

### **1.2.2 Ferromagnetism**

Ferromagnetism arises as a result of the parallel alignment of adjacent atomic moments in the absence of an applied field (Figure 2B). This type of ordering leads to a large net magnetic moment of the material. The Curie temperature ( $T_C$ ) of a ferromagnetic material is the temperature below which ferromagnetic ordering occurs. Above this Curie temperature, paramagnetic behavior is observed in the material.

### **1.2.3 Antiferromagnetism**

In antiferromagnetism, the individual magnetic moments align antiparallel to one another (Figure 2C). These dipoles are of the same magnitude, and as a result complete cancellation occurs, leading to a net magnetic moment of zero. Above their Néel temperature ( $T_N$  – the temperature below which antiferromagnetic ordering is observed, analogous to the Curie temperature in ferromagnetism), antiferromagnetic materials exhibit paramagnetic behaviour.

### **1.2.4 Ferrimagnetism**

A ferrimagnetic material is one in which the individual moments are aligned antiparallel, as seen in antiferromagnetism. However, in this case the individual moments are not of equal magnitude, and so incomplete cancellation occurs (Figure 2D). This leads to a net magnetic moment in the direction of the dipoles of greater magnitude. Magnetite ( $\text{Fe(III)}_2\text{Fe(II)O}_4$ ), the naturally occurring spontaneous magnet mentioned in section 1.1 is a ferrimagnet as the atomic moment of one Fe(III) ion orients antiparallel to the moments of the other two cations of the formula unit (Fe(III) and Fe(II)). Akin to ferromagnetism, spontaneous magnetization of a ferromagnetic material is only observed below its Curie temperature.

### **1.2.5 Superparamagnetism**

Sufficiently small ferro- or ferrimagnetic nanoparticles and a little more recently Single-Molecule Magnets (SMMs) (discussed in section 1.8.1) can exhibit a form of magnetism known as superparamagnetism. In their superparamagnetic state these particles can randomly flip their magnetization under the influence of temperature, and transition to this state can occur below the particles' Curie temperature. This behaviour is different to paramagnetism as the atoms of each individual nanoparticle

or molecule remain ferro- or ferrimagnetically ordered. The typical time between flips is called the Néel relaxation time ( $\tau_N$ ), a value that increases with increasing temperature. If the nanoparticle or molecule is magnetically anisotropic (possessing a preferred direction for its magnetic moment), its magnetic moment will have only two stable orientations antiparallel to each other, separated by an energy barrier ( $\Delta E$  or  $U_{\text{eff}}$ ). These stable orientations define the particle's so called *easy axis*.

The ***blocking temperature*** ( $T_B$ ) of a magnetic nanoparticle or SMM describes the ability of that particle to retain its magnetization in just one direction. It is the temperature at which the magnetic relaxation time of the particle becomes longer than the timescale of the magnetization measurements ( $\tau = 100$  s). At this temperature, the magnetization does not flip during the measurement and appears blocked in one direction.

The magnetic relaxation of a material is typically given as the relaxation time at infinite temperature  $\tau_0$ . This value is related to the energy barrier to magnetization reversal ( $\Delta E$ ), and the magnetic relaxation time  $\tau$  at a specific temperature ( $T$ ) by the Arrhenius law ( $k_B$  is the Boltzmann constant):

$$\tau = \tau_0 \exp(\Delta E/k_B T)$$

### 1.3 Quantifying magnetic properties

Magnetic interactions are typically characterized by their responses to variations in temperature and applied magnetic field.

The ***Magnetic Moment*** ( $\mu$ ) of a sample of magnetic material determines both how the material responds to an external magnetic field and the way that the material changes the field. A common unit is the Bohr Magneton (BM or  $\mu_B$ ), which is a physical constant and the natural unit for expressing the magnetic dipole moment of a single electron (1 BM =  $9.274 \times 10^{-24}$  J T<sup>-1</sup> or  $9.274 \times 10^{-21}$  Erg G<sup>-1</sup>). The “spin only” magnetic moment of a single atom or molecule can be calculated using the spin-only formula:

$$\mu_{\text{S.O.}} = 2[S(S+1)]^{1/2}$$

$S$  is the spin quantum number and describes the total number of unpaired electrons that contribute to the magnetic moment, where each unpaired electron contributes  $S = 1/2$ . The value of  $\mu$  obtained using this formula relates to the magnetic moment that

arises only from the spin angular momenta of the electrons, and not their orbital angular momenta. In molecules or atoms where the orbital angular momentum has been quenched (see section 1.6), this calculated value is very often close to the measured value. However in materials where orbital angular momentum is unquenched, the measured magnetic moment of a sample can deviate significantly from the calculated spin-only value.

The ***Molar Magnetization*** ( $M$ ) of a sample can be explained as the “amount of magnetic moment per mole” of material. The magnitude of the magnetization of a sample is dependent on the strength of the external magnetic field – the stronger the external field, the greater the value of the magnetization. In the field of molecular magnetism (see section 1.7), the most common unit for magnetization is  $\text{G cm}^3 \text{ mol}^{-1}$ , where Gauss is the cgs measurement of magnetic field and the  $\text{cm}^3$  and  $\text{mol}^{-1}$  entities arise in the conversion of the *Volume Magnetization* (which has units of Gauss) to the *Molar Magnetization*.

The ***Molar Magnetic Susceptibility*** ( $\chi_M$ ) is the proportionality constant between the molar magnetization ( $M$ ) and the external magnetic field ( $H$ ) in small external fields and not extremely low temperatures:

$$M = \chi_M H$$

Thus, the molar magnetic susceptibility gives greater insight into how attracted a sample is to a magnetic field as this value is independent of the external field. The most common unit for the magnetic susceptibility of a sample in the field of molecular magnetism is  $\text{cm}^3 \text{ mol}^{-1}$ . For systems in which orbital angular momentum has been quenched, and magnetic behaviour arises solely from electronic spin, the magnetic susceptibility and the spin only magnetic moment can be related by:

$$\mu_{S,O} = 2.828(\chi_M T)^{1/2}$$

The ***Curie Law*** describes the temperature dependence of the magnetic susceptibility for an ideal paramagnet. This is due to the fact that a reduction in thermal agitation leads to an increase in individual moments aligning with the external field:

$$\chi_M = C/T$$

The value  $C$  is a material specific Curie constant. This formula only applies to systems in which the individual magnetic moments are not communicating with each other (i.e. magnetically *dilute* materials). In such systems plotting  $1/\chi_M$  vs.  $T$  gives a straight line with slope  $C$  that intersects the origin. To account for magnetic interactions between neighbouring spins, a modified version called the **Curie-Weiss law** was devised:

$$\chi_M = C/(T - \theta)$$

The  $\theta$  value is the Weiss constant. Plotting  $1/\chi_M$  vs.  $T$  gives a straight line with  $C$  as the slope and  $\theta$  as the intercept. If  $\theta$  is positive, the material is ferromagnetic, while an antiferromagnetic material gives a negative value of  $\theta$ . To show deviations from Curie behaviour, and thus to reveal the strength of the magnetic coupling between atomic moments, a plot  $\chi_M T$  vs.  $T$  is commonly reported. In a system where the individual moments were magnetically dilute,  $\chi_M T$  does not vary as a function of temperature. This type of material obeys the Curie Law and  $\chi_M$  is inversely proportional to the temperature. However, in systems where magnetic coupling is observed  $\chi_M T$  can vary immensely with  $T$ , particularly at low temperature. Figure 3 shows the deviations from Curie behaviour for ferromagnetic, ferrimagnetic and antiferromagnetic materials.

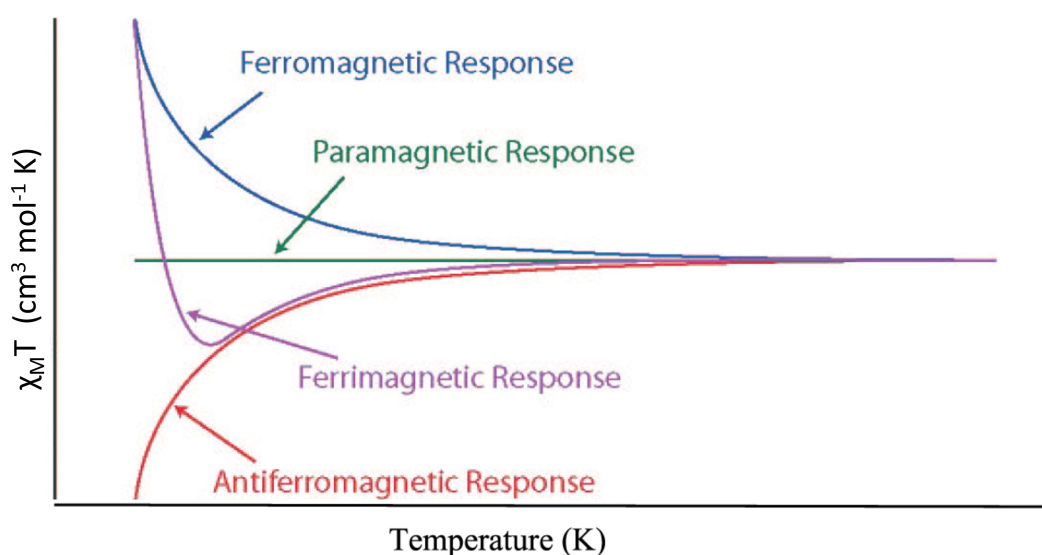


**Figure 3.** Graph depicting the variation of  $\chi_M T$  with temperature, for materials exhibiting different types of magnetic behaviour.

**Magnetic Hysteresis** measurements give insight into how ‘hard’ or ‘soft’ a magnet is. When an external magnetic field is applied to a magnetic material, the atomic dipoles align themselves with it. Upon removal of the field, part of this alignment will be retained as the material has become magnetized. Once magnetized, a ‘hard’ ferro- or ferrimagnet will stay magnetized for a long period of time, whereas a ‘soft’ ferro- or ferrimagnet will retain its magnetized state for a much shorter time. A pure paramagnet however will lose its memory of the applied magnetic field due to thermal agitation almost instantly upon removal of the field. Hysteresis measurements show the ability of a magnet to retain its magnetization when the field is removed and when the field is applied in the opposite direction. A hysteresis loop is a plot of the variation of magnetization with magnetic field for two opposing directions of the field (+H and -H). The field is gradually increased in one direction until it reaches a maximum, and then is decreased gradually until it reaches zero. The field is then gradually increased and decreased in the opposite direction in the same fashion. Magnetization measurements are carried out on the sample simultaneously. An example of hysteresis loops for both hard and soft ferromagnets is shown in Figure 4.

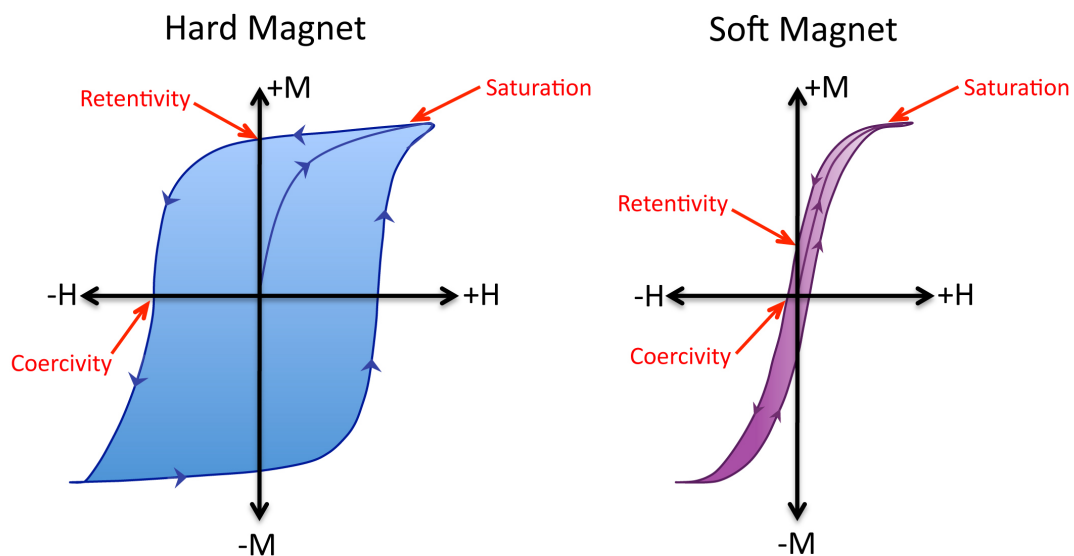


**Figure 4.** Schematic diagrams depicting hysteresis loops for a ‘hard magnet’ (left) and a ‘soft magnet’ (right). Although magnetization saturation is the same for both types, much larger values of coercivity and retentivity are exhibited by the ‘hard’ magnet.

Figure 4 shows the points of saturation, retentivity and coercivity on each hysteresis curve. These points are identical for the opposite direction of the field. The saturation magnetization for each magnet is the same in this schematic, however the ability of

the hard magnet to retain this magnetization (retentivity – often called remnance) upon removal of the external field is far greater than that of the soft magnet. The coercivity is the intensity of the opposing applied magnetic field required to reduce the magnetization of each magnet to zero after the magnetization of the sample has been driven to saturation. For a hard magnet, a strong opposing magnetic field is required to reduce its magnetization to zero, while a lower field strength is needed for a softer magnet. The area surrounded by a hysteresis loop is called the coercive field. The size of this area is a good indication of a materials magnetic hardness. A superparamagnet will exhibit magnetic hysteresis below its blocking temperature ( $T_B$ ).

## **1.4 Measuring magnetic properties**

### **1.4.1 SQUID Magnetometry**

In the field of molecular magnetism (see section 1.7), the most common instrument employed in the measurement of magnetic properties is the SQUID (Superconducting Quantum Interference Device), as it is highly sensitive and can measure very subtle changes to a magnetic field. In a SQUID the sample becomes magnetized in a field produced by a superconducting magnet. Within the device, the sample is surrounded by a superconducting sensing coil, which is coupled to a second loop. As the magnetized sample is moved through the coil, it induces a current in the double loop circuit. Due to their superconducting nature, these loops do not cause any signal loss. A change in the magnetic flux of these coils changes the current in the detection circuit, which produces a variation in the SQUID output voltage. This output voltage is directly proportional to the magnetic moment of the sample.

### **1.4.2 Electron Paramagnetic Resonance (EPR)**

EPR spectroscopy is a technique used to probe the electronic properties of magnetic materials. As we have mentioned, each electron possesses a spin quantum number  $S = \frac{1}{2}$ , with magnetic components (microstates –  $m_s$ ) of  $+\frac{1}{2}$  and  $-\frac{1}{2}$ . In the presence of an external magnetic field ( $H$ ), the electrons' magnetic moment aligns itself either parallel ( $+\frac{1}{2}$ ) or antiparallel ( $-\frac{1}{2}$ ) to the field, each alignment having a specific energy (giving rise to the Zeeman effect). The parallel alignment corresponds to the lower energy state, and the energy separation between it and the upper state is:

$$\Delta E = g_e \mu_B H$$

The symbol  $g_e$  represents the electron's so-called g-factor,  $\mu_B$  is the Bohr Magneton, and  $H$  is the applied magnetic field. The difference in energy between these two states can be determined by the absorption of a photon of the same energy, usually of microwave frequency, which causes a transition from the  $m_s = +\frac{1}{2}$  to the  $m_s = -\frac{1}{2}$  states. (Figure 5). Because the energy gap is proportional to the external field strength, either by keeping the incident photon frequency constant and varying the field strength (or vice versa), we can pinpoint  $\Delta E$  for a specific value of the field (Figure 5). Thus the electrons g-factor can be determined. The g-factor is basically a proportionality constant that relates the magnetic dipole moment and the angular momentum of an electron. For an electron that possesses only spin angular momentum (no orbital angular momentum) its g-factor is close to the free electron value of 2.0023. However, many transition metal and lanthanoid ions possess large orbital angular momentum, which changes the value of the g-factor (due to spin-orbit coupling – discussed in section 1.6). In this way, EPR measurements are extremely useful in shedding light on the electronic behaviour of an atom or molecule. In addition, the g-factor of the electron may not have the same value for all orientations of the atom, a concept known as magnetic anisotropy, also discussed in section 1.6. Because an unpaired electron will respond not only to a spectrometer's applied magnetic field, but also to any local magnetic fields arising due to neighbouring electrons, knowledge of the g-factor can give additional information about a paramagnetic center's electronic structure.

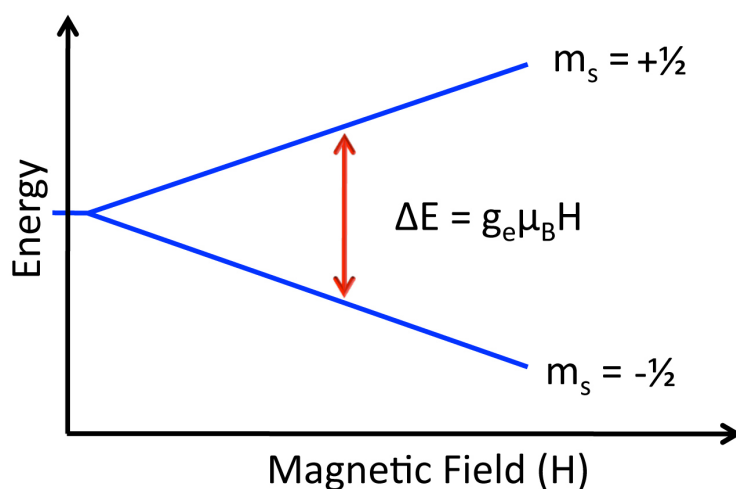


**Figure 5.** Schematic representation depicting the splitting of the  $m_s$  states in the presence of an applied magnetic field. The difference in energy ( $\Delta E$ ) between the two states increases with increasing field strength and is probed using microwave frequency radiation of energy  $h\nu$ .

## 1.5 Magnetic exchange

### 1.5.1 Introduction to magnetic exchange

When positioned in close proximity, electronic spins communicate, causing both spins to arrange themselves either parallel or antiparallel with one another. In section 1.1 we briefly mentioned intra-atomic exchange. In order to reduce the coulombic repulsion between two electrons occupying separate degenerate orbitals, they prefer to align parallel with one another so that their wavefunctions cannot overlap, due to the Pauli principle [14]. The tendency for these unpaired electrons to align parallel is described by Hund's rule of maximum multiplicity. This concept is applicable to a case of ferromagnetic coupling between neighbouring atoms. If a magnetic (half-filled) orbital on one atom is mutually orthogonal with a magnetic orbital on a neighbouring atom (no overlap), the unpaired electrons prefer to align parallel with one another to avoid the greater coulombic repulsion involved with spin pairing. However, if overlap occurs between adjacent magnetic orbitals on separate atoms, the unpaired electrons will prefer to align antiparallel in accordance with the Pauli exclusion principle, leading to an antiferromagnetic interaction. The interaction involved in these two scenarios between orbitals on two adjacent atoms is referred to as *direct exchange*, as the magnetic centres are close enough to communicate directly. The net magnetic exchange between two neighbouring atoms is a combination of the individual interactions between all magnetic orbitals on one atom with all magnetic orbitals on the other (and interactions between half-filled with filled and empty orbitals). This net interaction is described by the Isotropic Exchange Hamiltonian:

$$\hat{H} = -2J\hat{S}_1 \cdot \hat{S}_2$$

The terms  $\hat{S}_1$  and  $\hat{S}_2$  are spin operators and describe the spin quantum number of the two exchange coupled atoms. For example, high spin Mn(III) ions possess 4 unpaired electrons, and a spin quantum number  $S = 2$  (due to the fact that each electron is  $s = \frac{1}{2}$ ). The nature of the exchange coupling between two atoms (i.e. ferro- or antiferromagnetic) is described by  $J$ . This term, referred to as the  $J$ -value, is negative for antiferromagnetic exchange coupling, and positive for ferromagnetic interactions. The magnitude of this value describes the strength of the interaction, and is related to the energy difference between the ferromagnetic and antiferromagnetic states of an

exchange coupled pair.  $J$  is most commonly reported in  $\text{cm}^{-1}$  and occasionally in Kelvin (K).

This thesis is concerned with the magnetic and structural properties of inorganic polynuclear complexes comprising paramagnetic metal centers. These complexes can be discrete clusters comprising two or more paramagnetic ions (coordination clusters), or infinite 1-, 2- and 3-dimensional arrays (coordination polymers) and will be discussed in section 1.7. In these types of complexes the individual magnetic ions are separated by one or several ligand atoms, which link the ions together into the aforementioned topologies, while forming an organic sheath around the inorganic core of the molecule. Unlike the atoms in metallic or ionic solids, the magnetic centers in most molecules of these types are too far apart for direct exchange to be of any significance. However, weak exchange couplings *are* observed between magnetic ions separated by one or more diamagnetic groups, a discovery which gave rise to the theory of *superexchange*. This type of exchange can also be described by the exchange Hamiltonian for magnetically isotropic systems.

### 1.5.2 Superexchange

The phenomenon of superexchange emerged as a result of experiments carried out by Kramers in the 1930's on the cooling of paramagnetic salts under an external magnetic field [15]. He noticed weak magnetic interactions between the metal ions separated by diamagnetic atoms, and concluded that these ions could cause spin dependent perturbations in the wave functions of the intervening atoms. This occurrence, which was later termed *kinetic exchange*, is mediated by the delocalization of electrons between the two magnetic ions through the ligand orbitals. Kramers proposed a generalized scheme for this observed phenomenon which involved a partial electron transfer between magnetic orbitals and the ligand orbitals [16]. For example, in the case of manganese oxide (MnO), the largest contribution to the magnetic exchange involves the interaction between unpaired electrons in the  $d_z^2$  orbitals of the Mn(II) ions. These orbitals point directly towards the lobes of the filled  $p_z$  orbital on the oxygen ions, which lie between the metal centers (the Mn(II)–O<sup>2-</sup>–Mn(II) bond angle is 180°). Taking into account a single Mn(II)–O<sup>2-</sup>–Mn(II) entity, if partial electron transfer occurs from an electron in the  $p_z$  orbital to the  $d_z^2$  orbital on one Mn(II) centre, the electron in the receiving  $d_z^2$  orbital ion must be aligned

antiparallel to this electron in accordance with the Pauli exclusion principle. The oxygen ion from which the electron is transferred now has a net spin due to the remaining electron whose spin is antiparallel to the removed electron. Due to the overlap of the  $p_z$  orbital with the  $d_z^2$  orbital of Mn(II) ion on the other side, the remaining  $p_z$  electron and the one in the  $d_z^2$  orbital align antiparallel, again due to the Pauli exclusion principle. The net effect is the antiferromagnetic coupling of the two Mn(II) ions (Figure 6).

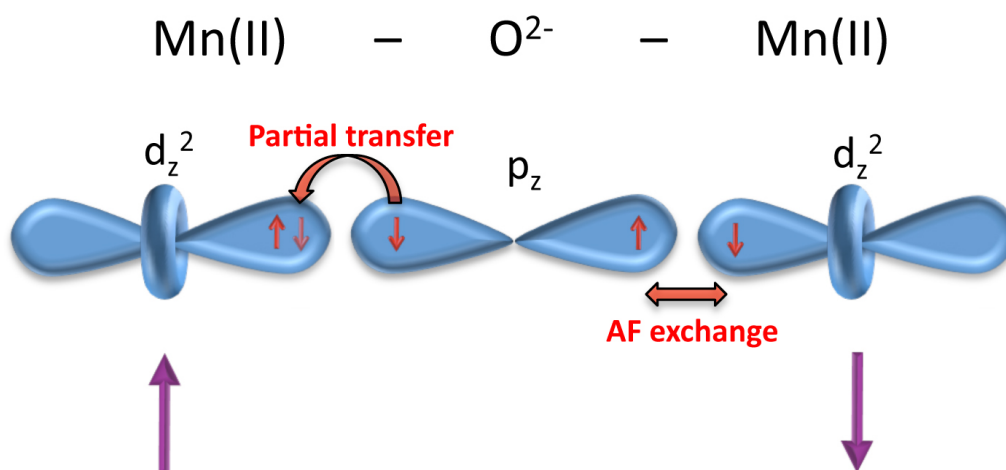


**Figure 6.** Schematic diagram depicting the kinetic exchange interaction involving the half-filled metal  $d_z^2$  orbitals of two Mn(II) ions and the  $p_z$  orbital of the intervening  $O^{2-}$  anion in a  $180^\circ$  bonding situation.

Using this model one can consider a similar  $d_z^2$ - $p_z$ - $d_z^2$  situation, where one  $d_z^2$  orbital is half filled while the other is empty. Partial electron transfer occurs from the  $p_z$  orbital to the empty  $d_z^2$  orbital and aligns itself parallel to the net spin of the cation in accordance with Hund's rule. The net spin of the oxygen atom is thus antiparallel to the spin of this cation, and also couples with the cation on the other side antiferromagnetically. This leads to an overall ferromagnetic exchange interaction between the cations. These two scenarios deal with superexchange interactions where the M-L-M bond angle is  $180^\circ$  and thus magnetic communication can occur through the lobes of the same p orbital. In a  $90^\circ$  bonding situation, the half-filled 3d orbital of one cation may overlap with a  $p_z$  orbital on the ligand atom, while the interacting half-filled 3d orbital on the other cation may overlap with a p orbital perpendicular to  $p_z$  ( $p_x$  or  $p_y$ ). Since each 3d orbital overlaps with a different ligand orbital, there is no kinetic exchange between the two cations and the interaction can be ferromagnetic. In

the case where the magnetic orbitals are mutually orthogonal (i.e. zero overlap), the interaction between them is always ferromagnetic (Figure 7).

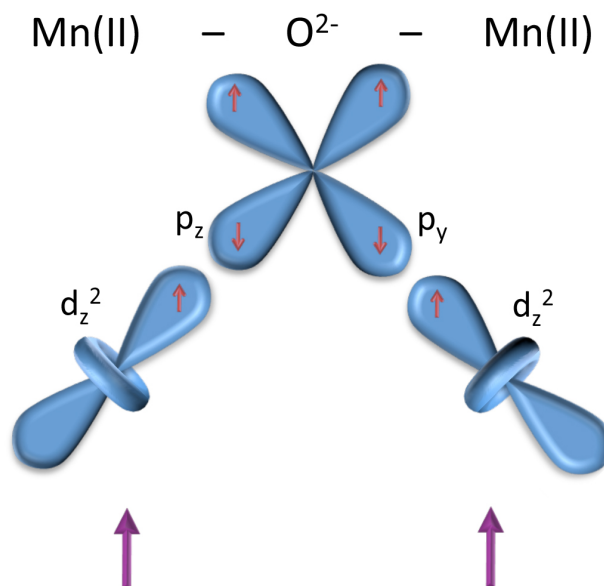


**Figure 7.** Schematic diagram depicting the ferromagnetic superexchange interaction in a hypothetical Mn(II)-O<sup>2-</sup>-Mn(II) 90° bonding scenario.

### 1.6.3 Superexchange: Developments upon Kramers' proposed mechanism

The 1950's saw an emergence of many publications concerning the mechanism of superexchange. In 1950, Anderson refined Kramers' model and reported formulae for Kramers' proposed interaction in terms of spin operators [17]. For this reason superexchange is often referred to as Kramers-Anderson superexchange. A few years later Goodenough and Loeb published a paper in which the effect of semicovalence between the cations and anions involved in superexchange was considered [18], [19]. Predictions based on their idea concerning the type of exchange (F or AF) mostly agree with those based on the Kramers/Anderson model, though in some cases they are conflicting. In 1958, Yamashita and Kondo [20] explained how non-orthogonality of orbitals could produce superexchange without any electron transfer, a phenomenon known as *spin-polarization*. For example, if a d-orbital and a p-orbital are non-orthogonal to each other, effective deformations of these orbitals will occur due to the Pauli principle, leading to communication between magnetic centers. In 1959, Kanamori published an article in which he discussed the relationship of the orbital symmetry with the magnetic exchange [21]. In the same year Anderson reported a revised version of his 1950 publication, this time taking a molecular orbital approach

in which the mixing of the 3d orbitals on the metal ion and the p orbitals on the intervening ligand give rise to bonding and antibonding MOs [22]. The two electrons originally occupying the p orbital now reside in the bonding MO, while the 3d electron(s) occupy the antibonding MO. In this way, the 3d electrons from each magnetic ion can interact. The molecular orbital diagrams of Figure 8 illustrate this concept. Both schematics represent the exchange interaction between two Cu(II) ions (possessing an unpaired electron in their  $d_{x^2-y^2}$  orbitals) separated via an intermediate oxygen atom. In a  $180^\circ$  bonding situation, just one oxygen p orbital ( $p_y$ ) overlaps with both  $d_{x^2-y^2}$  orbitals (one from each Cu(II) ion), leading to three MOs. The four electrons thus reside in the two lower energy MOs – leading to a non-magnetic ground state, or antiferromagnetic coupling between the Cu(II) ions ( $S = 0$ ). However, in a  $90^\circ$  bonding situation, each of the two  $d_{x^2-y^2}$  orbitals interacts with a different oxygen p orbital ( $p_x$  and  $p_y$ ) leading to four MOs. The magnetic ( $S = 1$ ) ground state arises due to the two higher energy MOs being degenerate, as depicted in Figure 8.

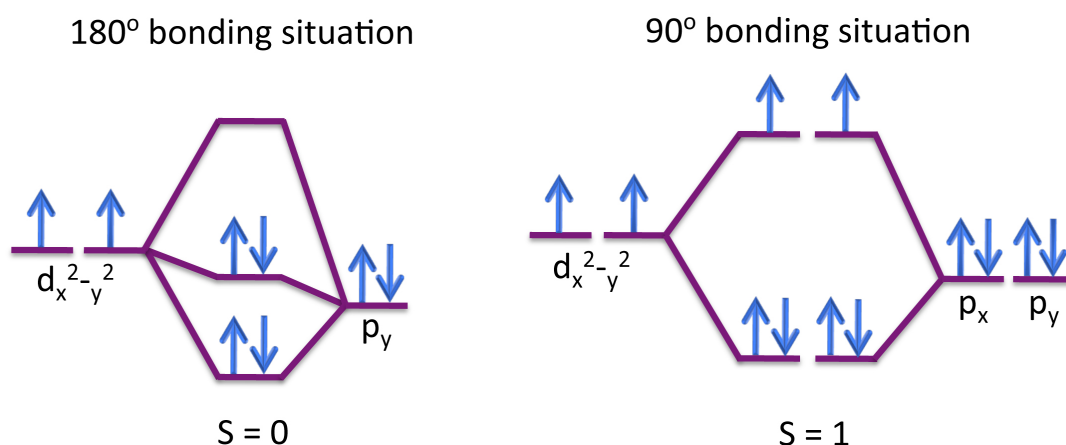


**Figure 8.** MO diagrams depicting the exchange interaction between two Cu(II) ions separated by a bridging oxygen atom. A  $180^\circ$  bond angle leads to a non-magnetic ground state (antiferromagnetic interaction), while a  $90^\circ$  bond angle leads to a ground state of  $S = 1$  (ferromagnetic interaction).

Goodenough and Kanamori developed a set of semi-empirical rules – the Goodenough-Kanamori rules [23], for rationalizing the magnetic properties of a wide range of materials on a qualitative level. By consideration of the symmetry and the electron occupancy of the interacting orbitals on neighboring magnetic centers the sign and relative magnitude of the resulting kinetic exchange can often be predicted. These rules possess roots in Kramers' original model, and basically state that if there is a large overlap between half-filled orbitals at two magnetic ions, the superexchange

mechanism is strongly antiferromagnetic; whereas overlap between partly occupied and unoccupied orbitals gives a ferromagnetic interaction. However, complications arise when the M–L–M bond angle deviates away from  $120^\circ$ , as is the case for most cluster compounds, and further complications can arise when spin-orbit coupling becomes significant. In addition, these rules inaccurately predict that the net kinetic exchange coupling between transition metal ions is always antiferromagnetic, and cases where ferromagnetic coupling is observed is assumed to be due to spin polarization or direct exchange. The rationale behind this hypothesis was that the largest contribution to the kinetic exchange is the interaction between two non-orthogonal half filled orbitals which is always antiferromagnetic. The minor (ferromagnetic) contributions are the interactions between a half-filled orbital and either a filled or empty orbital, and that of a filled orbital with an empty orbital. The sum of these ferromagnetic contributions was assumed too small to cancel out the major antiferromagnetic contribution, and so the net kinetic exchange was believed to be always antiferromagnetic. This widely held belief was found to be incorrect in 1997, when Weihe and Güdel proved that ferromagnetic exchange terms were more important than had been previously assumed [24].

#### **1.5.4 Current methods used to rationalize superexchange**

Nowadays, superexchange interactions are rationalized using a combination of spin delocalization (kinetic exchange) and spin polarization mechanisms. Both of these mechanisms lead to spin densities on ligand atoms, which can be assessed using density functional theory (DFT). For example if an unpaired electron on a metal ion has positive spin (i.e. its spin is aligned with the external field), its delocalization results in a distribution of positive spin density throughout the molecule. The amount of spin delocalization is more important for the atoms directly bonded to the paramagnetic centre and it increases with the covalent character of the metal – ligand bond [25]. The spin polarization mechanism induces negative spin density on atoms directly bonded to the metal ion with positive spin. This effect propagates through the molecule away from the paramagnetic centre thus generating densities of alternating spin at rather long distances. The net spin density at a particular atom arises from the combination of these two mechanisms. Generally, when the unpaired electrons are located in a metal  $\pi$ -type orbital ( $t_{2g}$  in an octahedral complex) spin polarization is

expected to dominate, while if it is in a  $\sigma$ -type orbital ( $e_g$ ), there is direct overlap with the ligand orbitals and a spin delocalization mechanism is expected to predominate. In chapters 2 and 3 of this thesis we have used density functional theory in order to assess the spin densities of a new family of  $[\text{Mn(III)}_2]$  dimers and a heterometallic  $[\text{Cu(II)Mn(III)}]$  dimer respectively. We have then related these spin densities to their observed exchange couplings. Considering the many exchange pathways present between the magnetic ions in these dimers, assigning each contribution to the observed spin densities is not an easy task.

## 1.6 Magnetic anisotropy, spin-orbit coupling and zero-field splitting

The magnetic anisotropy of a bulk solid, a molecule or an atom is the tendency of that material to align its magnetic moment(s) in a specific direction, i.e. the magnetic properties are not equal in all spatial directions. This effect is very important in the field of molecular magnetism (see sections 1.7 and 1.8) as magnetic anisotropy is essential in order for a molecular magnet to retain its magnetization upon removal of the external field. In transition metal and lanthanoid complexes, this effect arises mainly due to the spin-orbit coupling of the constituent metal ions (the coupling of the electronic spins with their orbital angular momenta). Dipolar spin-spin interactions also contribute to the anisotropy in these complexes, but to a much lesser extent [26]. A paramagnetic ion will possess orbital angular momentum if it possesses electrons that can move between orbitals. This occurs in orbitally degenerate states where the degenerate orbitals containing the moving electron are exchangeable via rotation about an axis. For example, an electron in degenerate  $d_{xz}$  and  $d_{yz}$  orbitals possesses angular momentum since rotation about the  $z$ -axis exchanges the two orbitals. However, an electron in degenerate  $d_z^2$  and  $d_{x^2-y^2}$  has no angular momentum since these orbitals are not exchangeable via rotation. This moving charge circulating about the atom generates a magnetic dipole moment perpendicular to the plane of motion, which the electronic spins can couple with, leading to the phenomenon of spin-orbit coupling. In metal ions whose orbital angular momentum has been quenched (due to crystal field splitting), spin-orbit coupling may be observed due to the presence of low lying excited electronic states. In this case, the ground state can interact with excited states that have different orbital occupations via spin-orbit coupling. This interaction can be interpreted as electrons in the ground state configuration ‘jumping’ into orbital

vacancies (thus giving the excited state electronic configuration) and generating orbital angular momentum and thus spin-orbit coupling. Again these transitions are only allowed if the two orbitals involved in the electron ‘jump’ are related by a rotation around a given axis, and the resultant magnetic dipole generated possesses a specific orientation.

Spin-orbit coupling introduces magnetic anisotropy to an atom, ion or molecule by making some directions preferable even in the absence of an applied magnetic field (zero-field splitting) [26]. For a state with a given spin  $S$  there are  $2S+1$  magnetic microstates ( $M_S$  levels) with  $M_S = S, S-1, \dots, -S$ , each state composed of a specific arrangement of electrons. In these different  $M_S$  levels the orientation of the electron spins differ relative to a given axis. In the  $M_S = S$  state the spins are aligned parallel with this axis, while in the  $M_S = -S$  state the spins are antiparallel. The spins are tilted in each of the intermediate  $M_S$  states. Since the orbital angular momentum generates a magnetic dipole moment that is oriented in a specific direction, each of these  $M_S$  levels interact differently with it. The  $M_S$  levels that are in close alignment with this dipole moment will be of lower energy than those that are in poor alignment with it, and thus, the microstate degeneracy is removed even in the absence of an applied magnetic field. Since the electronic spins in each  $M_S$  level possess a specific orientation, the ground state (the lowest lying pair of  $M_S$  levels) will be anisotropic. This phenomenon is known as zero-field splitting (ZFS).

ZFS can only occur in atoms or molecules that possess a ground spin state of  $S \geq 1$ . For an  $S = 3/2$  system, ZFS splits the spin microstates into  $M_S = \pm 3/2$  and  $M_S = \pm 1/2$ , where the energy separation between these two states is twice the axial zero-field splitting parameter ( $D$ ). If the doublet  $M_S = \pm 3/2$  is the lowest energy state, this means that the magnetization is preferentially aligned along an *easy axis* and  $D$  is negative. However, if the lowest energy state is  $M_S = \pm 1/2$ , the magnetization is within an *easy plane*, and  $D$  assumes a positive value [27]. These pairs of degenerate  $M_S$  levels of opposite sign are called Kramers doublets, and the energy separation between them may be probed using high-frequency high-field EPR spectroscopy (see chapter 3) [28]. A schematic representation of the zero-field splittings of several systems with  $S = 1$  to  $S = 5/2$  is shown in Figure 9.

The Co(II) ion exhibits large and negative  $D$  value and high magnetic anisotropy due to first order spin-orbit coupling. For this reason coordination clusters possessing

Co(II) ions have the potential to possess large barriers to magnetization reversal. However, due to the unpredictable nature of the magnitude of the orbital angular momentum in these complexes, their magnetic data is often quite difficult to interpret. We have dedicated chapter 5 to novel complexes of Co(II).

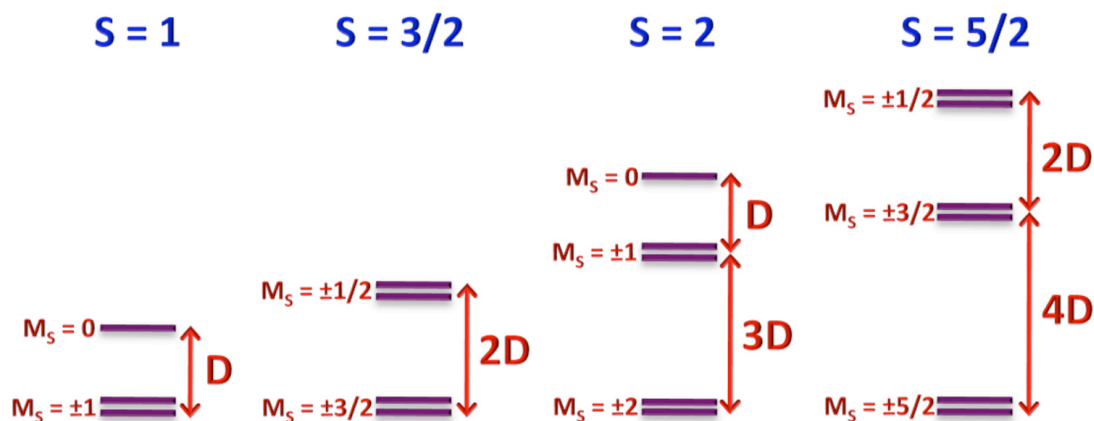


**Figure 9.** Schematic representation of the zero-field splittings of several systems with  $S = 1$  to  $S = 5/2$ . All four systems depicted in this diagram possess negative  $D$  values which are related to the energy separations between the microstates.

Complexes of many lanthanoid ions (such as Dy(III) and Tb(III)) possess large spin-orbit couplings owing to the ‘core like’ nature of their f-orbitals which are virtually unaffected by the ligand field. Gd(III) possesses no orbital angular momentum however, as it possesses one unpaired electron in each of its seven f-orbitals. As these electrons prefer to align parallel, movement of electrons between orbitals is forbidden due to the Pauli exclusion principle. Gd(III) is thus magnetically isotropic, while Dy(III) and Tb(III) are highly anisotropic. Chapter 6 details the synthesis and characterization of novel heterometallic Cu(III)-Ln(III) clusters and 1-D coordination polymers, comprising both isotropic (Gd(III)) and anisotropic (Dy(III) and Tb(III)) lanthanoid ions.

## 1.7 Molecular magnetism

The field of molecular magnetism is a vibrant area of research. Researchers in the field are concerned with the magnetic properties of individual molecules rather than bulk solids or nanoparticles, in an attempt to understand magnetic behaviour, electronic structure and the nature of magnetic exchange interactions at the atomic

and electronic level. Molecular crystals provide us with aggregates of iso-oriented magnetic objects on which we can study physical properties, offering us insight into the magnetic intricacies at this fundamental level.

Chemists in this field provide the test-beds for this type of investigation by synthesizing discrete coordination cluster compounds and 1-, 2- and 3-dimensional coordination polymers (a.k.a. metal-organic frameworks – MOFs). These topologies comprise paramagnetic metal ions linked together via various organic ligands or anions, usually containing oxygen or nitrogen donor centres. Discrete magnetic clusters are contained within ligand shells that limit the growth of the metal ion structure to an infinite mineral, while coordination polymers extend into 1-, 2- and 3-D arrays. Examples of a  $[\text{Co(II)}_8]$  coordination cluster of formula  $[\text{Co(II)}_8(\text{OMe})_2(\text{L})_4(\text{LH})_2(2\text{-hp})_4(\text{MeCN})_4]\cdot\text{MeCN}$  (**20**), and a 1-D coordination polymer containing both paramagnetic Mn(III) and diamagnetic Na(I) nodes of formula  $[\text{Na(I)}_2\text{Mn(III)}_2(\text{L})_4(\text{py})_3(\text{EtOH})_2]_n$  (**10**), are shown in Figure 10. Both structures are reported in this thesis (labeled complex **10** and **20** respectively). The magnetic properties of such clusters, which can be considered zero-dimensional, and compounds with higher dimensionalities (1-, 2- and 3-D) are dependent on several factors including the nature of the magnetic ions, the exchange mechanisms mediated by the bridging ligands (superexchange – see section 1.5.2) and the zero-field splitting of the individual ions (see section 1.6).

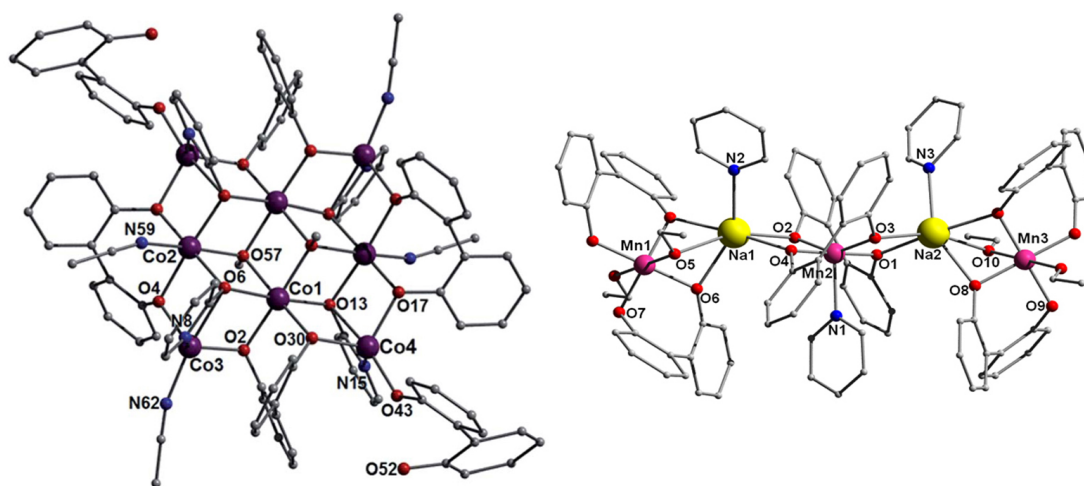


**Figure 10.** Crystal structures of  $\text{Co(II)}_8(\text{OMe})_2(\text{L})_4(\text{LH})_2(2\text{-hp})_4(\text{MeCN})_4\cdot\text{MeCN}$  (**20**) (left), and  $[\text{Na(I)}_2\text{Mn(III)}_2(\text{L})_4(\text{py})_3(\text{EtOH})_2]_n$  (**10**) (right), examples of a discrete cluster and a 1-D coordination polymer respectively.

The field of molecular magnetism is currently experiencing a renaissance due to the discovery of Single-Molecule Magnetism – the ability of a single molecule to behave as a tiny magnet and exhibit magnetic hysteresis of purely molecular origin (see section 1.8.1). Such molecules are an important sub-class of *spin clusters* – molecular cluster compounds in which ferro- or ferrimagnetic interactions between neighbouring paramagnetic ions lead to a non-zero ground spin state of the molecule. This ground spin state can be described by the spin quantum number  $S$ .

## 1.8 Applications of Molecular Magnetism

In addition to the pursuit of understanding magnetic properties and interactions at the atomic and molecular level, molecules in which the magnetic ions are ferro- or ferrimagnetically exchange coupled have many potential technological applications listed below.

### 1.8.1 Single-Molecule Magnets

Single-Molecule Magnets, (SMMs) are a class of ferro- or ferrimagnetic coordination clusters that exhibit superparamagnetic behaviour. At their blocking temperature  $T_B$  (see section 1.2.5) these individual complexes can retain their magnetic moment in one direction for 100 seconds, and for up to years at temperatures lower than  $T_B$ . At these temperatures, SMMs exhibit magnetic hysteresis of purely molecular origin. In order for a coordination cluster to exhibit SMM properties it must possess a large energy barrier to reversal of its magnetization  $\Delta E$  (or  $U$ ), which is dependent on the ground spin quantum number ( $S$ ) and the zero-field splitting parameter ( $D$ ) of the molecule. The cluster must possess a sizable and negative  $D$  value for it to be an SMM. The relationship between  $\Delta E$ ,  $S$  and  $D$  is given by the formulae:

$$\Delta E = S^2|D|$$

for integer values of  $S$ , and:

$$\Delta E = (S^2 - \frac{1}{4})|D|$$

for half integer values of  $S$ .

The spin quantum number  $S$  is the sum of all unpaired spins of the coordination cluster, where each electron possesses a spin of  $\frac{1}{2}$ , and opposing spins cancel each other out. For example, in chapter 3 we compare a ferromagnetic Cu(II)–Mn(III)

dinuclear cluster to a ferrimagnetic analogue. As the Cu(II) and Mn(III) ions possess one ( $S = 1/2$ ) and four ( $S = 2$ ) unpaired electrons respectively, ferromagnetic coupling would lead to a cluster spin ground state of  $S = 5/2$ , while ferrimagnetic coupling would give  $S = 3/2$ . The axial zero-field splitting parameter ( $D$ ) describes the systems anisotropy, and is discussed in section 1.3. In chapter 3 we report the use of high-field and high-frequency electron paramagnetic resonance (EPR) in the determination of the  $D$  value for the aforementioned Cu(II)–Mn(III) dimer.

Due to the fact that SMMs exhibit magnetic hysteresis below their blocking temperature, they are ideal candidates for information storage as each molecule can possess either a ‘spin up’ or ‘spin down’ orientation, where each orientation can represent either a ‘one’ or a ‘zero’ in binary code [29]. In today’s computer hard drives, binary units are stored in magnetic domains, where each magnetic domain is composed of hundreds of grains, each grain being typically 10 nm in size. Discrete molecules are several orders of magnitude smaller than these domains; therefore SMMs offer the alternative of much denser information storage. SMMs are also candidates as qubits in quantum computing [30], a potential technology in which the fundamental units of information are ‘one’, ‘zero’ (as in classical computing), and a quantum superposition of both these states. Having three possible units of information, coupled with the nano-scale size of SMMs, could potentially lead to further miniaturization of information storage devices.

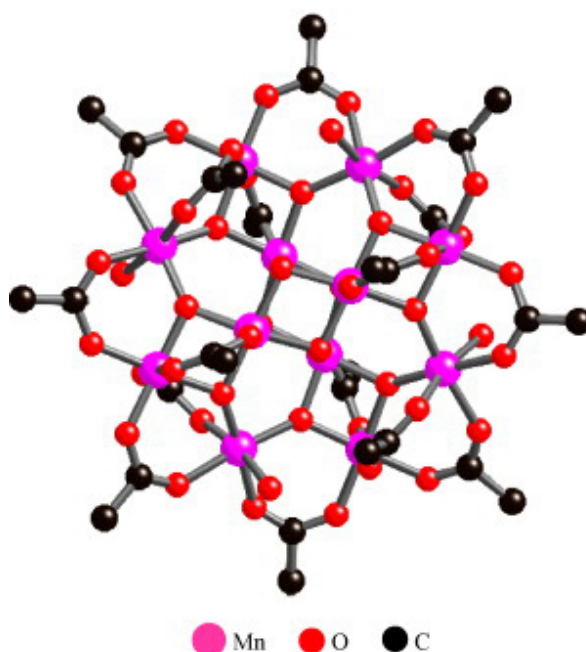


**Figure 11.** Crystal structure of the archetypal SMM – Mn<sub>12</sub>OAc, taken from ref [31].

The first molecule ever discovered to exhibit Single-Molecule Magnet behaviour is a dodecanuclear manganese cluster of formula  $[\text{Mn}_{12}\text{O}_{12}(\text{CH}_3\text{COO})_{16}(\text{H}_2\text{O})_4] \cdot 2\text{CH}_3\text{COOH} \cdot 4\text{H}_2\text{O}$ , usually shortened to  $\text{Mn}_{12}\text{OAc}$ . Its crystal structure (Figure 11) was first reported by Lis et al in 1980 [32]. However it was not until 1991 that this molecule was shown to exhibit slow magnetic relaxation below 10 K [33]. Sessoli et al reported that the cluster exhibits magnetic hysteresis of purely molecular origin [34], i.e. the observed hysteresis effect is not associated with bulk magnetic order, but arises due to the slow relaxation of the magnetization of individual  $[\text{Mn}_{12}\text{OAc}]$  molecules. Several years after the discovery that  $\text{Mn}_{12}\text{OAc}$  could exhibit hysteresis of molecular origin, the term ‘Single-Molecule Magnet’ appeared [35], suggesting that the individual molecules behave as tiny magnets.

This cluster was found to possess a ground spin state of  $S = 10$ . This is due to an inner core of four ferromagnetically coupled Mn(IV) ions, which are antiferromagnetically coupled to an external ring of eight Mn(III) ions (all aligned spin-parallel to one another). In a large fraction of the molecules in a bulk sample of  $\text{Mn}_{12}\text{OAc}$ , all eight Mn(III) ions display parallel alignment of their Jahn-Teller axes. As the anisotropic easy axis run along the Jahn-Teller axis in Mn(III) ions, this leads to a large and negative cluster anisotropy ( $D \approx -0.5 \text{ cm}^{-1}$ ). However, it is worth noting here that a number of analogues of  $\text{Mn}_{12}\text{OAc}$  possess a single misaligned Jahn-Teller axis (lying perpendicular to the other seven Mn(III) ions) [36], [37] which can be switched to a parallel conformation under the influence of pressure, thereby increasing the cluster anisotropy [37]. Rather than investigating the effect of the relative orientation of the Jahn-Teller axes on the cluster anisotropy, we have investigated its effect on the exchange coupling between Mn(III) ions in chapter 2 of this thesis.

A schematic diagram of the spin microstates ( $M_S$  levels) associated with  $\text{Mn}_{12}\text{OAc}$  is shown in Figure 12, split due to zero-field splitting (see section 1.6). As the cluster possesses a ground spin state of 10, the formula  $(2S + 1)$  tells us the number of available microstates. The equation  $\Delta E = S^2|D|$  may be used to work out the energy barrier to magnetization reversal for this cluster. However, a phenomenon known as quantum tunneling can lead to a lowering of this calculated energy barrier [38], [39], due to a small percentage of the molecules in a sample undergoing this effect and reversing their magnetization. This results in the occurrence of steps in the magnetization on the hysteresis loop, observed in  $\text{Mn}_{12}\text{OAc}$  below 3 K.

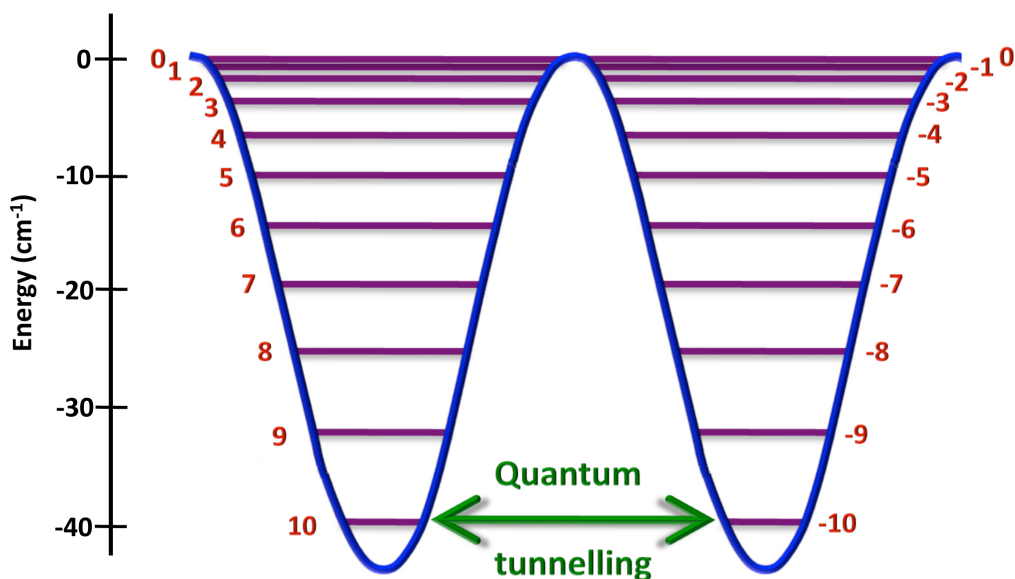


**Figure 12.** Microstates associated with the Mn<sub>12</sub>OAc SMM, which are split due to ZFS effects.

The Mn<sub>12</sub>OAc cluster kick-started an upsurge in polynuclear complex chemistry, and despite many attempts to create better SMMs, this complex and its carboxylate-substituted derivatives held the highest blocking temperatures of  $\sim 3.5$  K for almost 15 years. However in 2007, Brechin et al reported a [Mn<sub>6</sub>] cluster possessing a barrier to magnetization reversal of  $60 \text{ cm}^{-1}$ , and a blocking temperature of  $\sim 4.5$  K [40], finally breaking the long standing record held by the [Mn<sub>12</sub>] family. The current record holder is a radical bridged Tb(III) dimer, which possesses a barrier to magnetization reversal of  $227.0 \text{ cm}^{-1}$ , and a blocking temperature of 13.9 K [41].

### 1.8.2 Single-Chain Magnets

Single-Chain Magnets or SCMs are 1-D coordination polymers that exhibit long-range magnetic ordering and display slow relaxation to their magnetization. They provide, at low temperatures, a magnetic hysteretic behaviour for a single polymeric chain [42], with no inter-chain exchange interactions present.

### 1.8.3 Molecular Coolants

The magneto-caloric effect (MCE) is based on the change of the magnetic entropy ( $\Delta S_M$ ) of a material upon application of a magnetic field. When an external magnetic field is applied to a magnetic material, the individual atomic moments align

themselves with the field, and there is a reduction of the materials' magnetic entropy ( $S_M$ ) and heat capacity ( $C_p$ ). Under adiabatic conditions (insulated from the environment) this magnetic entropy change must be compensated for by an equal but opposite change in the entropy associated with the lattice, resulting in a change in temperature of the material, i.e. the material heats up. This heat can be removed via a liquid or a gas, and the material is kept under the external field to avoid re-absorption of the heat by the magnetic dipoles. The material is then returned to adiabatic conditions and the magnetic field is removed. The magnetic dipoles then absorb heat from the material in order to become randomly aligned, thus increasing the magnetic entropy of the material and lowering the temperature significantly according to a process known as adiabatic demagnetization. For a molecule to be a good magnetic coolant, it must exhibit a large value of  $\Delta S_M$ . In order to achieve this, the molecule must possess negligible anisotropy ( $D \sim 0 \text{ cm}^{-1}$ ) (unlike SMMs), and exhibit weak ferromagnetic interactions between its magnetic ions leading to a large ground spin state ( $S$ ) [43]. Isotropic clusters are favoured as they have no preferred orientation of their magnetic moment, and thus respond well to an external field in any direction. They will also continue to relax rapidly even at low temperatures (no blocking temperature). In order to achieve negligible anisotropy and weak exchange, synthesis of clusters containing both Gd(III) ions and Cu(II) ions is becoming popular [44], [45], due to the magnetically isotropic nature of Gd(III) and the ferromagnetic character of the Cu(II) – Gd(III) couple [46].

If this technology succeeds, it offers an energy efficient and environmentally friendly alternative to conventional refrigeration methods, and could also replace helium-3 for cooling in the ultra-low temperature region. For this purpose we have investigated the synthesis of Cu(II) – Gd(III) systems in chapter 6.

#### **1.8.4 Molecular Spintronic Devices**

Spintronics, also known as magnetoelectronics, is an emerging technology exploiting the intrinsic spin of the electron, in addition to its fundamental electronic charge, in solid-state devices. In electronic devices, the electronic spins are randomly aligned, however in spintronic devices, the spins are polarized in a certain direction. Hence information can be carried not only by the electron's charge, but also by its spin direction. SMMs are thought of as promising candidates for spintronic devices [47].

### 1.8.5 Spin Crossover Complexes

Spin crossover is a phenomenon exhibited by some metal complexes, in which their spin state may be changed due to external perturbations in temperature, pressure, light irradiation or the influence of a magnetic field [48]. A typical example is the transition from low-spin to high-spin in transition metal complexes comprising octahedral  $3d^4$ – $3d^7$  ions [49]. These complexes have potential technological applications as molecular switches and sensors.

## 1.9 Synthesis of magnetic clusters and coordination polymers

### 1.9.1 Choice of ligand

In the design and synthesis of cluster compounds and coordination polymers, one of the most basic steps is choosing a ligand. In this sense of the word, a ligand is a molecular moiety that possesses at least one donor atom (an atom with a non-bonding electron pair - usually oxygen or nitrogen), which can form a coordinate bond with a metal ion. Certain types of ligand can act as connecting blocks, which provide the bridges necessary to link the metal centres together, and as terminal blocks, which prevent the complex from growing to an infinite size. In the synthesis of coordination polymers, ligands taking the role of terminal blocks are obviously undesirable as they prevent the formation of infinite networks. Many different families of ligand have been employed in the production of both SMMs and coordination polymers, and the employment of these different types of ligands are usually what separates the research of many groups involved in these two fields. Examples of the ligands used in the synthesis of SMMs and coordination polymers are displayed in Figure 13.



**Figure 13.** Popular ligands employed in the field of molecular magnetism (examples taken from ref [50]). The hydroxide groups can be deprotonated under basic reaction conditions giving alkoxide anions.

Alkoxides ( $\text{OR}^-$ ), can coordinate to between one and three metal atoms via their oxygen atom, thus making them an ideal candidate for use in the synthesis of polymetallic compounds. Alkoxide linkers can be introduced to a reaction by the deprotonation of an alcohol in the presence of a base.

### 1.9.2 2,2'-Biphenol ( $\text{LH}_2$ )

In this study we have investigated of the coordination chemistry of the ligand 2,2'-biphenol (Figure 14), which can be singly- or doubly-deprotonated to form an alkoxide anion. This ligand has been severely under-investigated in the context of molecular magnetism, with only a few reported metal complexes in the literature comprising this ligand [51–53]. The most notable of these reported structures is the high-spin  $[\text{Mn}_{10}]$  cluster [53–55], synthesized by Lippard et al in 1993.

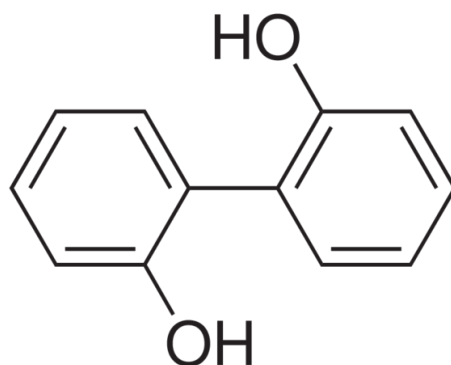


**Figure 14.** Diagram of 2,2'-biphenol ( $\text{LH}_2$ ), a ligand that has been thoroughly investigated in this work.

This thesis reports a wide variety of coordination modes exhibited by this ligand, ranging from chelating to the bridging of up to three metal ions (adopting the  $\eta^1:\eta^2,\mu_3$ -bridging motif). In addition this ligand has accessed all three possible levels of deprotonation in the complexes reported in this thesis; we will refer to each one as  $\text{LH}_2$ ,  $\text{LH}^-$  and  $\text{L}^{2-}$ .

### 1.9.3 The role of co-ligands

In the synthesis of cluster compounds and coordination polymers, a co-ligand is usually employed in the reaction scheme to work in conjunction with the original ligand. A co-ligand can assist in the bridging of metal ions, or simply help to complete coordination spheres around the ions. In this study we adopt pyridine, and many of its derivatives to assist 2,2'-biphenol in complex formation. This type of

ligand is very popular in the synthesis of coordination compounds [56–58]. Figure 15 shows just three of the pyridine ligands successfully utilized in this study.

In chapter 4 we show that even a slight change in functionality on the pyridine ligand (a  $-\text{CH}_3$  group compared with a  $-\text{CH}_2\text{CH}_3$  group), or a change in the position of the functional group (the 3- compared with the 4-position) can lead to significant differences in the topology of a series of heterometallic 1-D coordination polymers. In chapter 5 we show that by changing the co-ligand in a reaction scheme, completely different complexes can be obtained, from  $[\text{Co}(\text{II})_2]$  and  $[\text{Co}(\text{II})_8]$  discrete clusters, to 1- and 2-D coordination polymers.

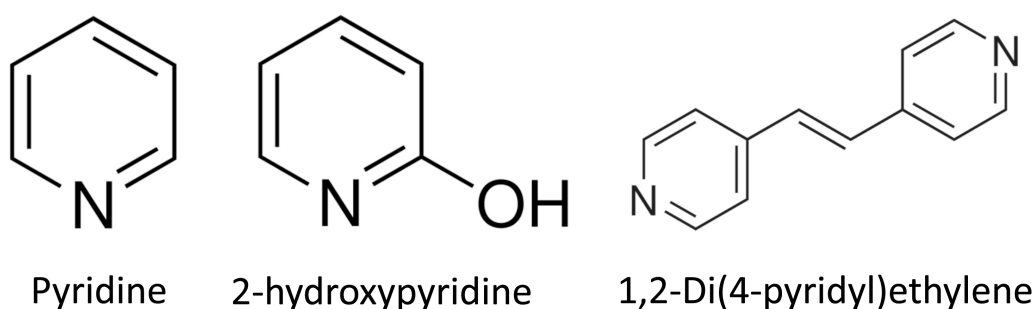


**Figure 15.** Diagrams of three pyridyl ligands successfully utilized in this work.

#### 1.9.4 Reactant ratios

In the previous section we discussed how slightly altering the functionality of the co-ligand in the synthesis of coordination compounds can drastically influence the products obtained. In a similar fashion, the ratios of the reactants in the synthesis of coordination clusters and polymers are of utmost importance in determining the outcome of the reaction. For instance in the complexes reported in chapter 6 of this thesis, the ratio of  $\text{Cu}(\text{I})\text{Br}$  to  $\text{Gd}(\text{III})(\text{NO}_3)_3 \cdot 6\text{H}_2\text{O}$  in the reaction determines whether a  $[\text{Gd}(\text{III})_4\text{Cu}(\text{II})_4]$  discrete cluster, or a 1-D coordination polymer comprising  $\{\text{Gd}(\text{III})_2\text{Cu}(\text{II})_8\}$  cluster units will be obtained.

## 1.10 Bibliography

- [6] B. E. Publishing, *The Britannica Guide to Electricity and Magnetism*. The Rosen Publishing Group, 2011, p. 3.
- [7] J. W. Jewett and R. A. Serway, *Physics for Scientists and Engineers with Modern Physics*. Cengage Learning EMEA, 2007, p. 808.
- [8] E. Purcell, *Electricity and Magnetism*. Cambridge University Press, 2011, p. 170.
- [9] J. J. Thomson, "Cathode Rays," *Philosophical Magazine*, vol. 90, pp. 25–29, Feb. 2010.
- [10] S. O. Lodge, *Electrons or the Nature and Properties of Negative Electricity*. 1906, p. 47.
- [11] D. Giulini, "Electron spin or 'classically non-describable two-valuedness'," *Studies In History and Philosophy of Science Part B: Studies In History and Philosophy of Modern Physics*, vol. 39, no. 3, pp. 557–578, Sep. 2008.
- [12] *Histories of the Electron: The Birth of Microphysics*. MIT Press, 2004, pp. 430–431.
- [13] W. Pauli, "Wolfgang Pauli - Nobel Lecture: Exclusion Principle and Quantum Mechanics," 1945. [Online]. Available: [http://www.nobelprize.org/nobel\\_prizes/physics/laureates/1945/pauli-lecture.html](http://www.nobelprize.org/nobel_prizes/physics/laureates/1945/pauli-lecture.html).
- [14] J. Frohlich and D. Ueltschi, "Hund's Rule and Metallic Ferromagnetism," *Journal of Statistical Physics*, vol. 118, no. 5–6, pp. 973–978, Mar. 2005.
- [15] W. De Haas, E. Wiersma, and H. Kramers, "Experiments on adiabatic cooling of paramagnetic salts in magnetic fields," *Physica*, vol. 1, no. 1–6, pp. 1–13, Jan. 1934.
- [16] H. Kramers, "L'interaction Entre les Atomes Magnétogènes dans un Cristal Paramagnétique," *Physica*, vol. 1, pp. 182–192, Jan. 1934.
- [17] P. Anderson, "Antiferromagnetism. Theory of Superexchange Interaction," *Physical Review*, vol. 79, no. 2, pp. 350–356, Jul. 1950.
- [18] J. Goodenough and A. Loeb, "Theory of Ionic Ordering, Crystal Distortion, and Magnetic Exchange Due to Covalent Forces in Spinel," *Physical Review*, vol. 98, no. 2, pp. 391–408, Apr. 1955.
- [19] J. B. Goodenough, "Theory of the Role of Covalence in the Perovskite-Type Manganites [La, M(II)]MnO<sub>3</sub>," *Physical Review*, vol. 100, no. 2, pp. 564–573, Oct. 1955.
- [20] J. Yamashita and J. Kondo, "Superexchange Interaction," *Physical Review*, vol. 109, no. 3, pp. 730–741, Feb. 1958.
- [21] J. Kanamori, "Superexchange interaction and symmetry properties of electron orbitals," *Journal of Physics and Chemistry of Solids*, vol. 10, pp. 87–98, Jul. 1959.
- [22] P. W. Anderson, "New Approach to the Theory of Superexchange Interactions," *Physical Review*, vol. 115, no. 1, pp. 2–13, Jul. 1959.
- [23] J. B. Goodenough, *Magnetism and the Chemical Bond*. 1963, pp. 165–184.
- [24] H. Weihe and H. U. Güdel, "Quantitative Interpretation of the Goodenough–Kanamori Rules: A Critical Analysis," *Inorganic Chemistry*, vol. 36, no. 17, pp. 3632–3639, Aug. 1997.

- [25] E. Ruiz, J. Cirera, and S. Alvarez, "Spin density distribution in transition metal complexes," *Coordination Chemistry Reviews*, vol. 249, no. 23, pp. 2649–2660, Dec. 2005.
- [26] A. Cornia, D. Gatteschi, and R. Sessoli, "New experimental techniques for magnetic anisotropy in molecular materials," *Coordination Chemistry Reviews*, vol. 219–221, pp. 573–604, Oct. 2001.
- [27] J. Cirera, E. Ruiz, S. Alvarez, F. Neese, and J. Kortus, "How to build molecules with large magnetic anisotropy.," *Chemistry (Weinheim an der Bergstrasse, Germany)*, vol. 15, no. 16, pp. 4078–4087, Jan. 2009.
- [28] J. Krzystek, A. Ozarowski, and J. Telsler, "Multi-frequency, high-field EPR as a powerful tool to accurately determine zero-field splitting in high-spin transition metal coordination complexes," *Coordination Chemistry Reviews*, vol. 250, no. 17–18, pp. 2308–2324, Sep. 2006.
- [29] M. Affronte, "Molecular nanomagnets for information technologies," *Journal of Materials Chemistry*, vol. 19, no. 12, p. 1731, 2009.
- [30] P. C. E. Stamp and A. Gaita-Ariño, "Spin-based quantum computers made by chemistry: hows and whys," *Journal of Materials Chemistry*, vol. 19, no. 12, p. 1718, 2009.
- [31] E. Coronado, C. Martí-Gastaldo, and S. Tatay, "Magnetic molecular nanostructures: Design of magnetic molecular materials as monolayers, multilayers and thin films," *Applied Surface Science*, vol. 254, no. 1, pp. 225–235, Oct. 2007.
- [32] T. Lis, "Preparation, structure, and magnetic properties of a dodecanuclear mixed-valence manganese carboxylate," *Section B: Structural Crystallography and Crystal Chemistry*, vol. 36, pp. 2042–2046, 1980.
- [33] A. Caneschi, D. Gatteschi, R. Sessoli, A. L. Barra, L. C. Brunel, and M. Guillot, "Alternating current susceptibility, high field magnetization, and millimeter band EPR evidence for a ground  $S = 10$  state in  $[\text{Mn}_{12}\text{O}_{12}(\text{CH}_3\text{COO})_{16}(\text{H}_2\text{O})_4] \cdot 2\text{CH}_3\text{COOH} \cdot 4\text{H}_2\text{O}$ ," *Journal of the American Chemical Society*, vol. 113, no. 15, pp. 5873–5874, Jul. 1991.
- [34] R. Sessoli, H. L. Tsai, A. R. Schake, S. Wang, J. B. Vincent, K. Folting, D. Gatteschi, G. Christou, and D. N. Hendrickson, "High-spin molecules:  $[\text{Mn}_{12}\text{O}_{12}(\text{O}_2\text{CR})_{16}(\text{H}_2\text{O})_4]$ ," *Journal of the American Chemical Society*, vol. 115, no. 5, pp. 1804–1816, Mar. 1993.
- [35] H. J. Eppley, S. M. J. Aubin, M. W. Wemple, D. M. Adams, H.-L. Tsai, V. A. Grillo, S. L. Castro, Z. Sun, K. Folting, J. C. Huffman, D. N. Hendrickson, and G. Christou, "Single-Molecule Magnets: Characterization of Complexes Exhibiting Out-of-Phase AC Susceptibility Signals," *Molecular Crystals and Liquid Crystals Science and Technology. Section A. Molecular Crystals and Liquid Crystals*, vol. 305, no. 1, pp. 167–179, Oct. 1997.
- [36] Z. Sun, D. Ruiz, D. N. Hendrickson, N. R. Dilley, M. Brian Maple, M. Soler, K. Folting, G. Christou, and J. Ribas, "The origin of the second relaxation process in the  $[\text{Mn}_{12}\text{O}_{12}(\text{O}_2\text{CR})_{16}(\text{H}_2\text{O})_4]$  single-molecule magnets: 'Jahn–Teller isomerism' in the  $[\text{Mn}_{12}\text{O}_{12}]$  core," *Chemical Communications*, no. 19, pp. 1973–1974, 1999.
- [37] P. Parois, S. A. Moggach, J. Sanchez-Benitez, K. V. Kamenev, A. R. Lennie, J. E. Warren, E. K. Brechin, S. Parsons, and M. Murrie, "Pressure-induced Jahn–Teller switching in a  $\text{Mn}_{12}$  nanomagnet.," *Chemical communications (Cambridge, England)*, vol. 46, no. 11, pp. 1881–1883, Mar. 2010.

- [38] E. del Barco, A. D. Kent, S. Hill, J. M. North, N. S. Dalal, E. M. Rumberger, D. N. Hendrickson, N. Chakov, and G. Christou, "Magnetic Quantum Tunneling in the Single-Molecule Magnet Mn<sub>12</sub>-Acetate," *Journal of Low Temperature Physics*, vol. 140, no. 1–2, pp. 119–174, Jul. 2005.
- [39] S. Hill, S. Datta, J. Liu, R. Inglis, C. J. Milios, P. L. Feng, J. J. Henderson, E. del Barco, E. K. Brechin, and D. N. Hendrickson, "Magnetic quantum tunneling: insights from simple molecule-based magnets.," *Dalton transactions*, vol. 39, no. 20, pp. 4693–4707, May 2010.
- [40] C. J. Milios, A. Vinslava, W. Wernsdorfer, S. Moggach, S. Parsons, S. P. Perlepes, G. Christou, and E. K. Brechin, "A record anisotropy barrier for a single-molecule magnet.," *Journal of the American Chemical Society*, vol. 129, no. 10, pp. 2754–2755, Mar. 2007.
- [41] J. D. Rinehart, M. Fang, W. J. Evans, and J. R. Long, "A N<sub>2</sub>(3-) radical-bridged terbium complex exhibiting magnetic hysteresis at 14 K.," *Journal of the American Chemical Society*, vol. 133, no. 36, pp. 14236–14239, Sep. 2011.
- [42] L. Bogani, A. Vindigni, R. Sessoli, and D. Gatteschi, "Single chain magnets: where to from here?," *Journal of Materials Chemistry*, vol. 18, no. 40, p. 4750, 2008.
- [43] M. Evangelisti and E. K. Brechin, "Recipes for enhanced molecular cooling," *Dalton Transactions*, vol. 39, no. 20, p. 4672, 2010.
- [44] A. S. Dinca, A. Ghirri, A. M. Madalan, M. Affronte, and M. Andruh, "Dodecanuclear [Cu(II)6Gd(III)6] nanoclusters as magnetic refrigerants.," *Inorganic chemistry*, vol. 51, no. 7, pp. 3935–3937, Apr. 2012.
- [45] T. N. Hooper, J. Schnack, S. Piligkos, M. Evangelisti, and E. K. Brechin, "The Importance of Being Exchanged: [Gd<sup>III</sup><sub>4</sub>M<sup>II</sup><sub>8</sub>(OH)<sub>8</sub>(L)<sub>8</sub>(O<sub>2</sub>CR)<sub>8</sub>]<sup>4+</sup> Clusters for Magnetic Refrigeration," *Angewandte Chemie*, vol. 124, no. 19, pp. 4711–4714, May 2012.
- [46] J. P. Costes, F. Dahan, and A. Dupuis, "Is ferromagnetism an intrinsic property of the CuII/GdIII couple? Structures and magnetic properties of novel trinuclear complexes with  $\mu$ -phenolato- $\mu$ -oximato (Cu-Ln-Cu) cores (Ln = La, Ce, Gd).," *Inorganic chemistry*, vol. 39, no. 26, pp. 5994–6000, Dec. 2000.
- [47] L. Bogani and W. Wernsdorfer, "Molecular spintronics using single-molecule magnets.," *Nature materials*, vol. 7, no. 3, pp. 179–86, Mar. 2008.
- [48] P. Gütlich and H. A. Goodwin, *Spin Crossover in Transition Metal Compounds, Volume 2*. Springer, 2004, p. 294.
- [49] A. Bousseksou, G. Molnár, L. Salmon, and W. Nicolazzi, "Molecular spin crossover phenomenon: recent achievements and prospects.," *Chemical Society reviews*, vol. 40, no. 6, pp. 3313–35, Jun. 2011.
- [50] R. Winpenny, Ed., *Single-Molecule Magnets and Related Phenomena*, vol. 122. Berlin/Heidelberg: Springer-Verlag, 2006.
- [51] E. W. Ainscough, A. M. Brodie, S. J. McLachlan, and K. L. Brown, "The reaction of 1,1'-biphenyl-2,2'-diol with iron(III) and the crystal structure of piperidinium bis[ $\mu$ -(1,1'-biphenyl-2,2'-diolato-O, $\mu$ -O')(1,1'-biphenyl-2,2'-diolato-O,O')ferrate(III)].ethanol," *Journal of the Chemical Society, Dalton Transactions*, no. 7, p. 1385, 1983.
- [52] J. S. Bashkin, A. R. Schake, J. B. Vincent, H. R. Chang, Q. Li, J. C. Huffman, G. Christou, and D. N. Hendrickson, "Mixed valence manganese-(II, III) and -(III, IV) dinuclear complexes: preparation, structure, magnetochemistry, and e.s.r. spectra of Mn<sub>2</sub>(biphen)<sub>2</sub>(biphenH)(bpy)<sub>2</sub> and Mn<sub>2</sub>O<sub>2</sub>Cl<sub>2</sub>(OAc)(bpy)<sub>2</sub>(biphenH<sub>2</sub> = 2,2'-biphenol, bpy = 2,2'-bipyridine),"

- Journal of the Chemical Society, Chemical Communications*, no. 11, p. 700, 1988.
- [53] D. P. Goldberg, A. Caneschi, and S. J. Lippard, "A decanuclear mixed-valent manganese complex with a high spin multiplicity in the ground state," *Journal of the American Chemical Society*, vol. 115, no. 20, pp. 9299–9300, Oct. 1993.
- [54] D. P. Goldberg, A. Caneschi, C. D. Delfs, R. Sessoli, and S. J. Lippard, "A Decanuclear Manganese Cluster with Oxo and Halide Bridging Ligands: Magnetic Behavior of an  $S = 12$  System," *Journal of the American Chemical Society*, vol. 117, no. 21, pp. 5789–5800, May 1995.
- [55] A. R. Schake, E. A. Schmitt, A. J. Conti, W. E. Stribe, J. C. Huffman, D. N. Hendrickson, and G. Christou, "Preparation and properties on mononuclear and ferromagnetically coupled dinuclear manganese complexes with 2,2'-biphenoxide," *Inorganic chemistry*, vol. 30, no. 16, pp. 3192–3199, 1999.
- [56] A. J. Amoroso, A. Thompson, M. W. Cargill, J. P. Maher, J. A. McCleverty, and M. D. Ward, "Di-, Tri-, and Tetranucleating Pyridyl Ligands Which Facilitate Multicenter Magnetic Exchange between Paramagnetic Molybdenum Centers," *Inorganic Chemistry*, vol. 34, no. 19, pp. 4828–4835, Sep. 1995.
- [57] H. R. Simmonds and D. S. Wright, "Main group pyridyl-based ligands; strategies to mixed metal complexes.," *Chemical communications (Cambridge, England)*, vol. 48, pp. 8617–8624, Jul. 2012.
- [58] J. Boeckmann, M. Wriedt, and C. Näther, "Metamagnetism and single-chain magnetic behavior in a homospin one-dimensional iron(II) coordination polymer.," *Chemistry (Weinheim an der Bergstrasse, Germany)*, vol. 18, no. 17, pp. 5284–9, Apr. 2012.

## **Chapter 2:**

# **What Controls the Magnetic Interaction in bis- $\mu$ -Alkoxo Mn(III) Dimers? A Combined Experimental and Theoretical Exploration**

## 2.1 Introduction

The construction of families of polynuclear cluster compounds containing multiple paramagnetic metal centres and the understanding and development of the relationship between structure and magnetism (magneto-structural correlations) is an area of widespread interest [59]. In practice of course this is not a trivial task, even assuming that a large number of structurally-related compounds can be synthesised, crystallized and characterized, because the super-exchange mechanisms involved are influenced by many structural factors including, for example, the type of metal ion(s) (M) and bridging ligand(s) (L) employed, and the specific M–M and M–L distances and the M-L-M and M-L-L-M angles in the molecule [59]. Despite these obstacles such studies are extremely important because the ability to control and modulate the type and magnitude of magnetic exchange within a complex has enormous ramifications for materials science and nanotechnology as discussed in section 1.8. Understanding the magneto-structural relationship in small compounds, such as dimers and trimers, is an important step towards understanding the magnetic behaviour of large or very large polymetallic complexes, since the magnetic skeletons of the latter are often made up of the same basic building blocks.

Studies on magnetic dinuclear complexes began in 1952, when Bleaney and Bowers demonstrated that the “anomalous” paramagnetism of copper acetate was due to the dimeric nature of the molecule (previously thought to be monomeric) using EPR spectroscopy [60]. The structure of this antiferromagnetically coupled Cu(II) dimer was later validated via single crystal X-ray diffraction [61]. These findings coincided with the rapid development of structure determination and soon led to the evolution of magneto-structural correlation studies within other dinuclear Cu(II) species. The first example of a quantitative relationship was developed by Hatfield and Hodgson using a large family of di- $\mu$ -OH bridged [Cu(II)<sub>2</sub>] complexes, in which the magnetic exchange ( $J$ ) was found to be governed by the magnitude of the Cu-OH-Cu angle [62–65]. These observations were then followed by other studies on dimeric cupric complexes containing, for example, symmetric halide bridging ligands [66], [67], asymmetric mixed ligand combinations [68], and a family of end-on azide-bridged complexes containing both ferro- and antiferromagnetically coupled siblings in which the magnetic exchange was very elegantly shown to depend on the Cu-N-Cu angle [69]. Thereafter, magneto-structural correlations were also attempted and established

for (dimeric) complexes containing other first row transition metal ions such as Fe(III) [70–73], Cr(III) [74–76], Mn(II) [77] and Mn(III) [78].

If the magnetic behaviour of small dimeric building blocks that can self-assemble to form larger architectures are known and understood, the magnetic behaviour of larger molecules can be more easily rationalised. Such polynuclear compounds often possess very elaborate topologies comprising multiple M-L-M and/or M-L-L-M exchange pathways that may not be accurately deciphered due to over parameterisation and/or computational limitations [79], [80]. Indeed the last few years have seen both qualitative and quantitative magneto-structural trends established for tri- [81], [82], tetra- [83–86], hexa- [87–89], and octanuclear [90] complexes of first row transition metals, as well as with mixed metal 3d– 4f species [91].

In addition to experimental observations, theoretical methods based on density functional theory (DFT) have become increasingly popular tools with which to compute magnetic exchange interactions and develop magneto-structural correlations [92]. Established theoretical protocols have provided excellent numerical estimates of  $J$  values and of the underlying electronic structure. One major advantage of the theoretical approach is that magneto-structural correlations for a particular structure type can be developed on simplified model complexes in which structural parameters can be modified in a methodical manner, offering insights into the effect of one particular structural change at a time on the sign and magnitude of  $J$ .

Due to its large single ion anisotropy the Jahn–Teller elongated Mn(III) ion is often the metal of choice for the synthesis of Single-Molecule Magnets (SMMs), an important class of compounds with potential applications in information storage (discussed in section 1.8.1). To build such molecules it is preferable to have strong ferromagnetic exchange between neighbouring Mn(III) centres and as such knowledge of what controls the pairwise magnetic exchange is vital. A literature search reveals however that the majority of di- and polynuclear Mn(III) complexes exhibit, with few exceptions [93], [94], very weak ferro- or antiferromagnetic exchange interactions and that the parameters that control the magnitude and sign of  $J$  have not been clearly established – even for simple Mn(III) dimers. The bis-alkoxo bridged dinuclear Mn(III) compounds reported in the literature to date are collected in Tables 4-6, and have  $J$  values (based on the  $2J\hat{S}_1\cdot\hat{S}_2$  formalism) ranging from  $-15.5\text{ cm}^{-1}$  to  $+19.7\text{ cm}^{-1}$ . Herein, we describe the synthesis and magnetic characterization of

a new family of bis- $\mu$ -alkoxide bridged Mn(III) dinuclear complexes of general formula  $[\text{Mn(III)}_2(\mu\text{-OR})_2(\text{L})_2(\text{ROH})_y(\text{X})_z]$  (where R = Me, Et and X = MeOH, pyridine, 2-hydroxypyridine, 3-picoline, 4-picoline) and establish a magneto-structural correlation for all known bis-alkoxo bridged dinuclear Mn(III) compounds using a combined experimental and theoretical study.

## 2.2 Results and Discussion

### 2.2.1 Structural Descriptions

All significant bond distances and angles along with single crystal X-ray diffraction data for complexes **1-5** are given in Tables 1-3, respectively. Structural parameters pertinent to our correlation studies are given in Tables 4-6. The first member of this family is  $[\text{Mn(III)}_2(\mu\text{-OMe})_2(\text{L})_2(\text{MeOH})_4]$  (**1**) formed via the reaction of  $\text{Mn}(\text{NO}_3)_2 \cdot 6\text{H}_2\text{O}$ , 2,2'-biphenol ( $\text{LH}_2$ ) and NaOH in alcohol. Complex **1** (Figure 16) crystallizes in the triclinic P-1 space group with an asymmetric unit composed of one dinuclear molecule. The two six-coordinate Mn(III) ions, which lie about an inversion centre (Mn1 and symmetry equivalent (s.e.)), are bridged via two  $\mu\text{-OMe}$  anions with a Mn1-O1-Mn1' angle of  $103.66^\circ$  and Mn1 $\cdots$ Mn1' distance of 3.071 Å. Each Mn(III) cation is ligated by two oxygen atoms from a chelating, doubly deprotonated 2,2'-biphenolate ligand ( $\text{L}^{2-}$ ). The six coordinate distorted octahedral geometries of each metal ion are completed by two terminal methanol molecules which bond on the Jahn–Teller axes at distances of 2.37 Å (Mn1–O4) and 2.27 Å (Mn1–O5). The oxidation state of the Mn(III) was confirmed through bond length and charge balance considerations and BVS calculations (as were all others described in this chapter).

**Table 1.** Selected bond lengths (Å) and angles ( $^\circ$ ) for complexes **1-3**.

<b>1</b>		<b>2</b>		<b>3</b>	
Mn1-O1	1.956(19)	Mn1-O1	1.972(6)	Mn1-O1	1.938(2)
Mn1-O1'	1.950(2)	Mn1-O2	1.936(2)	Mn1-O1'	1.935(2)
Mn1-O2	1.896(2)	Mn1-O3	1.841(6)	Mn1-O2	1.853(2)
Mn1-O3	1.852(2)	Mn1-O4	1.879(6)	Mn1-O3	1.842(2)
Mn1-O4	2.366(3)	Mn1-N1	2.321(7)	Mn1-N1	2.196(2)
Mn1-O5	2.270(2)	Mn1-N2	2.420(8)		
Mn1-O1- Mn1'	103.65(10)	Mn1-O1- Mn1'	101.1(2)	Mn1-O1- Mn1'	104.11(9)
Mn1 $\cdots$ Mn1'	3.071	Mn1 $\cdots$ Mn1'	3.007(2)	Mn1 $\cdots$ Mn1'	3.0537(9)

**Table 2.** Selected bond lengths (Å) and angles (°) for complexes **4** and **5**.

<b>4</b>		<b>5</b>	
Mn1-O1	1.9388(14)	Mn1-O1	1.9372(15)
Mn1-O1'	1.9475(14)	Mn1-O1'	1.9496(15)
Mn1-O2	1.8363(15)	Mn1-O2	1.8563(14)
Mn1-O3	1.8645(15)	Mn1-O3	1.8839(15)
Mn1-N1	2.1847(19)	Mn1-O4	2.3056(16)
		Mn1-O5	2.2839(16)
Mn1-O1-Mn1'	103.03(6)	Mn1-O1-Mn1'	102.85(6)
Mn1...Mn1'	3.0422(8)	Mn1...Mn1'	3.039

**Table 3.** Crystallographic data obtained from complexes **1-5**.

	<b>1</b>	<b>2</b>	<b>3</b>	<b>4</b>	<b>5</b>
Formula <sup>a</sup>	C <sub>30</sub> H <sub>38</sub> O <sub>10</sub> Mn <sub>2</sub>	C <sub>41</sub> H <sub>37</sub> N <sub>3</sub> O <sub>6</sub> Mn <sub>2</sub>	C <sub>38</sub> H <sub>36</sub> N <sub>2</sub> O <sub>6</sub> Mn <sub>2</sub>	C <sub>40</sub> H <sub>40</sub> N <sub>2</sub> O <sub>6</sub> Mn <sub>2</sub>	C <sub>42</sub> H <sub>48</sub> N <sub>2</sub> O <sub>10</sub> Mn <sub>2</sub>
<i>M<sub>w</sub></i>	668.48	777.62	726.57	754.62	850.70
Crystal System	Triclinic	Monoclinic	Monoclinic	Monoclinic	Monoclinic
Space group	P-1	P2 <sub>1</sub> /n	C2/c	P2 <sub>1</sub> /n	C2/c
<i>a</i> /Å	7.1410(14)	13.827(3)	18.445(4)	10.974(2)	11.772(2)
<i>b</i> /Å	10.822(2)	20.677(4)	9.0195(18)	9.3942(19)	15.946(3)
<i>c</i> /Å	10.979(2)	12.657(3)	21.421(4)	17.383(4)	21.458(4)
<i>α</i> /°	110.86(3)	90	90	90	90
<i>β</i> /°	104.73(3)	93.53(3)	104.33(3)	92.11(3)	90.77(3)
<i>γ</i> /°	95.21(3)	90	90	90	90
<i>V</i> /Å <sup>3</sup>	751.2(3)	3611.8(12)	3452.9(12)	1790.9(6)	4027.6(14)
<i>Z</i>	1	4	4	2	4
<i>T</i> /K	150(2)	150(2)	150(2)	150(2)	150(2)
<i>λ<sup>b</sup></i> /Å	0.7107	0.7107	0.7107	0.7107	0.7107
<i>D<sub>c</sub></i> /g cm <sup>-3</sup>	1.478	1.430	1.398	1.399	1.403
<i>μ</i> (Mo-Kα)/mm <sup>-1</sup>	0.896	0.752	0.780	0.755	0.687
Meas./indep.( <i>R<sub>int</sub></i> ) refl.	2647 / 1924 (0.0408)	6597 / 4818 (0.0936)	3153 / 2734 (0.0398)	3274 / 2482 (0.0300)	3682 / 3086 (0.0340)
wR2 (all data)	0.0814	0.2681	0.1250	0.0740	0.0783
<i>R</i> 1	0.0655	0.1136	0.0468	0.0498	0.0446
G.O.F on <i>F</i> <sup>2</sup>	0.982	1.221	1.099	1.055	1.085

The introduction of N-donor (pyridine type) ligands into the synthetic procedure used for the formation of **1** gives rise to the remaining members of this family. For instance, the addition of pyridine (py) and 3-picoline (3-pic) affords [Mn(III)<sub>2</sub>(μ-OMe)<sub>2</sub>(L)<sub>2</sub>(py)<sub>3</sub>] (**2**) and [Mn(III)<sub>2</sub>(μ-OMe)<sub>2</sub>(L)<sub>2</sub>(3-pic)<sub>2</sub>] (**3**), respectively. Complexes **2** and **3** (Figure 16) crystallize in the monoclinic space groups P2<sub>1</sub>/c and C<sub>2</sub>/c respectively and share many structural similarities with complex **1**. Both contain central μ-OMe ligands, this time producing Mn–O–Mn angles of 101.14° (Mn1-O1-Mn2) and 100.70° (Mn1-O2-Mn2) in **2** and 104.04° (Mn1-O1-Mn1') in **3**.

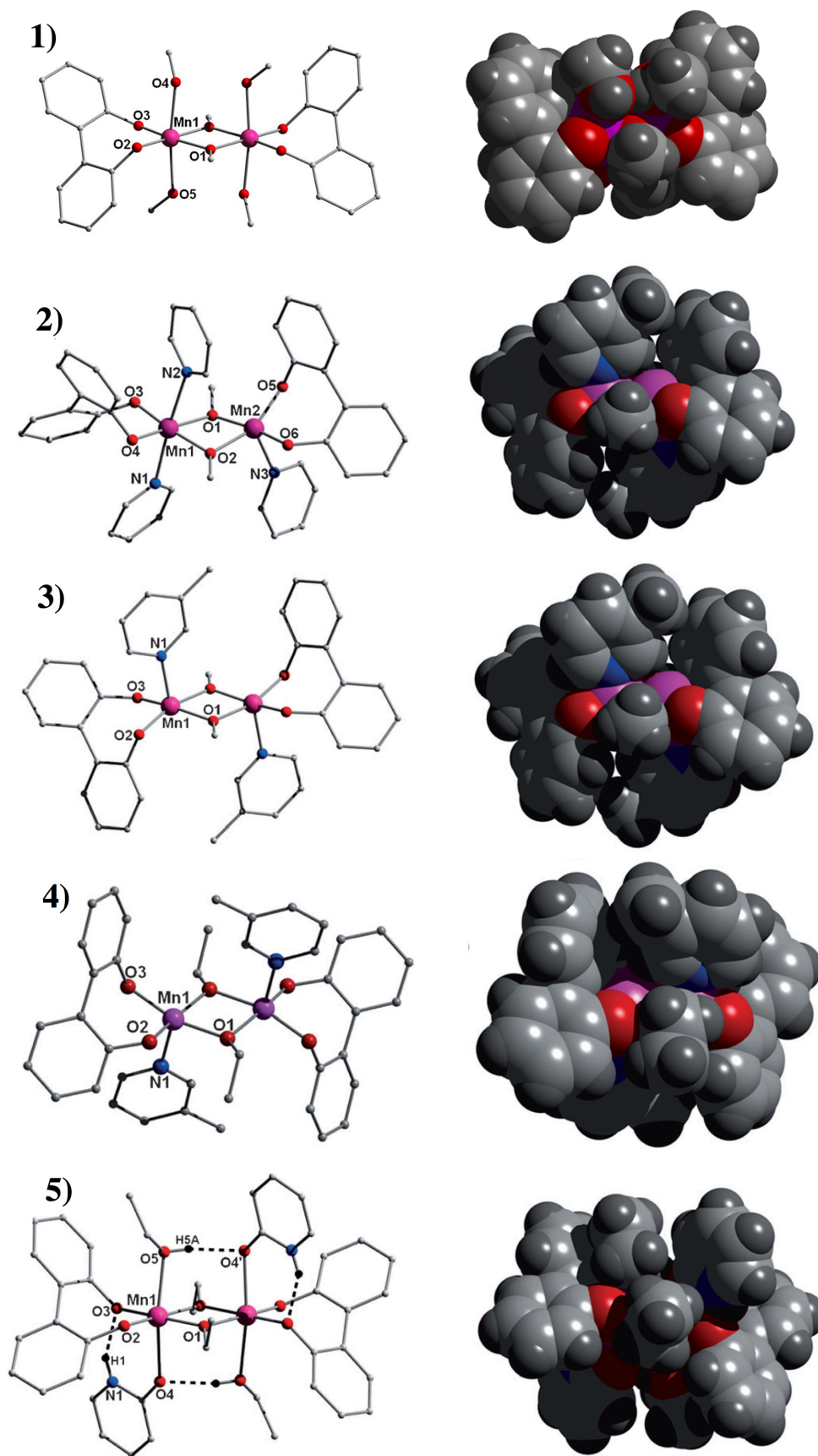


**Figure 16.** Crystal structures of the complexes **1–5** viewed as ball and stick (left) and space-fill (right). Pink = Mn, red = O, blue = N, light grey = C, dark grey = H.

Indeed **2** and **3** differ to complex **1** only due to the presence of terminally bonded N-donor ligands rather than terminally bonded alcohol. More specifically, complex **2** contains two pyridine ligands axially coordinated to the Jahn–Teller axis of [distorted octahedral] Mn1 (via N1 and N2), and one pyridine molecule attached (N3) to Mn2. The latter is in a distorted square based pyramidal geometry ( $\tau = 0.28$ ) [95], presumably due to the steric effects of the rather twisted biphenoxide ligands. The Mn1–N1 and Mn1–N2 bond lengths in **2** are 2.322 Å and 2.420 Å respectively, while the Mn–N3 distance is slightly shorter, at a value of 2.207 Å. The steric constraints present in **2** give rise to a puckering of the  $\{\text{Mn(III)}_2(\mu\text{-OMe})_2\}$  plane. This core distortion can be quantified via the Mn1-O1-Mn2-O2 torsion angle of  $15.08^\circ$  which can be directly compared to the completely flat  $\{\text{Mn(III)}_2(\mu\text{-OMe})_2\}$  plane in complex **1** (Mn1-O1-Mn1'-O1' =  $0.0^\circ$ ).

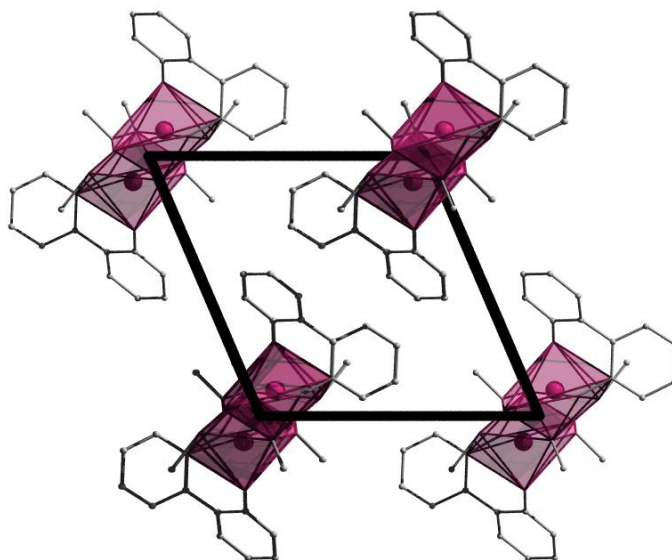


**Figure 17.** Polyhedral representation of the packing observed in the unit cell of **1** as viewed along the *a* axis.

The individual  $\{\text{Mn(III)}_2\}$  units in **1** stack in superimposable rows along the *a* axis of the unit cell (Figure 17). These 1–D rows are stabilised by two symmetry related H-bonding interactions between an O atom of a  $L^{2-}$  ligand (O2) and a nearby alcoholic proton (H4A-O4) belonging to a terminal EtOH ligand of a juxtaposed  $\{\text{Mn(III)}_2\}$  unit ( $\text{O2}\cdots\text{H4A(O4)} = 1.909$  Å). These hydrogen bonded chains arrange in the common brickwork pattern in the remaining two directions. No significant intermolecular interactions are observed between the chains in **1**. The packing arrangement in **2** also comprises superimposable 1–D rows propagating along the *c* axis of the unit cell (Figure 18). These chains are held in position by only weak

interactions; however these rows are connected in 3-dimensions via strong C–H $\cdots$  $\pi$  dipolar interactions at a distance of 2.496 Å ([C24–C29] $\cdots$ H4(C4)) emanating from L<sup>2-</sup> and pyridyl aromatic rings on neighbouring dimeric units.

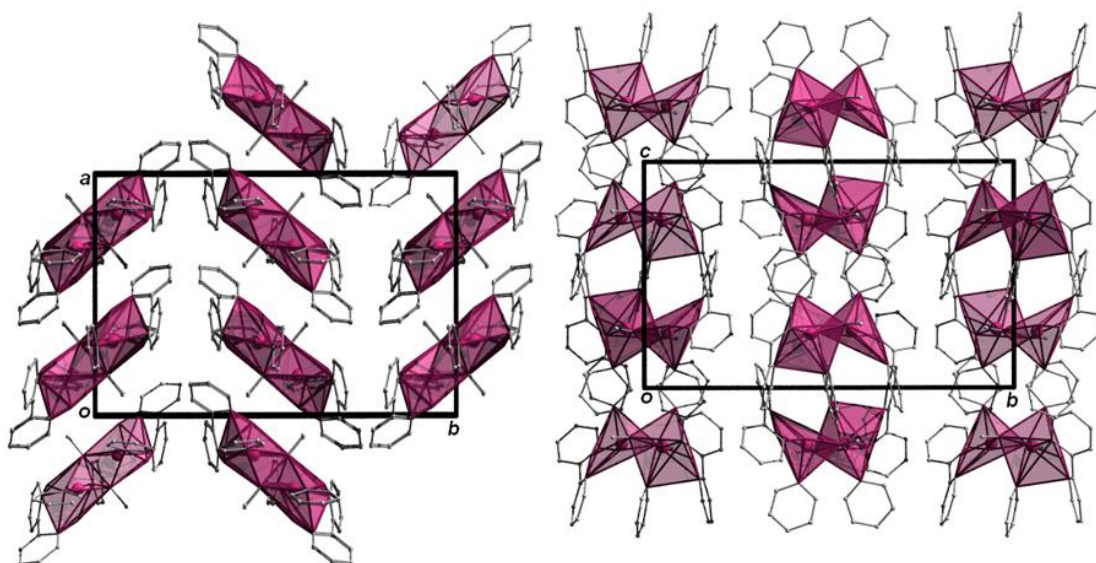


**Figure 18.** Packing diagram detailing the arrangement of individual {Mn(III)<sub>2</sub>} polyhedral units in **2** as viewed down the *c* (left) and *a* axis respectively.

In complex **3** (Figure 16) both Mn(III) ions are five coordinate and adopt square-based pyramidal geometry ( $\tau = 0.02$ ), with one 3-picoline ligand coordinated to each metal centre at a distance of 2.198 Å (Mn1–N1). This change in metal coordination number is presumably due to the presence of the bulkier 3-picoline ligand (Figure 16). This is also true for [Mn<sub>2</sub>( $\mu$ -OEt)<sub>2</sub>(biphen)<sub>2</sub>(3-pic)<sub>2</sub>] (**4**) (Figure 16), whose structure is essentially analogous to complex **3** but in which the bridging methoxide ions are replaced with bridging ethoxide ligands, as a result of the change of solvent from MeOH to EtOH. **4** crystallizes in the monoclinic space group P2<sub>1</sub>/n. The Mn–O–Mn angles in **3** and **4** are given as 104.11° and 103.03° resulting in Mn $\cdots$ Mn distances of 3.054 and 3.402 Å, respectively. Moreover the Mn–O–Mn–O torsion angles produced in **3** and **4** are both 0°. The crystal packing in the unit cells of **3** and **4** bear striking similarities (Figure 19). Both comprise 1–D superimposable chains running across (dissecting) the *ab* plane in **3** and along the *b* axis in **4**. The individual {Mn(III)<sub>2</sub>} units in these siblings are connected through intra-chain H-bonding interactions via O atoms and methyl protons belonging to 2,2'-biphenolate and 3-picoline ligands, respectively, of nearest neighbour {Mn(III)<sub>2</sub>} units (O3 $\cdots$ H18A(C18) = 2.715 Å in **3**; O2 $\cdots$ H19(C19) = 2.420 Å in **4**). In terms of 3–D connectivity the 1–D rows in **3** and **4**

each alternate in direction along the *c* axis of their unit cells. Inter-chain close contacts were observed in both structures via interactions between O and H atoms of neighbouring L<sup>2-</sup> ligands (O2⋯H9(C9) = 2.550 Å in **3**; O2⋯H19(C19) = 2.420 Å in **4**) (Figure 19).

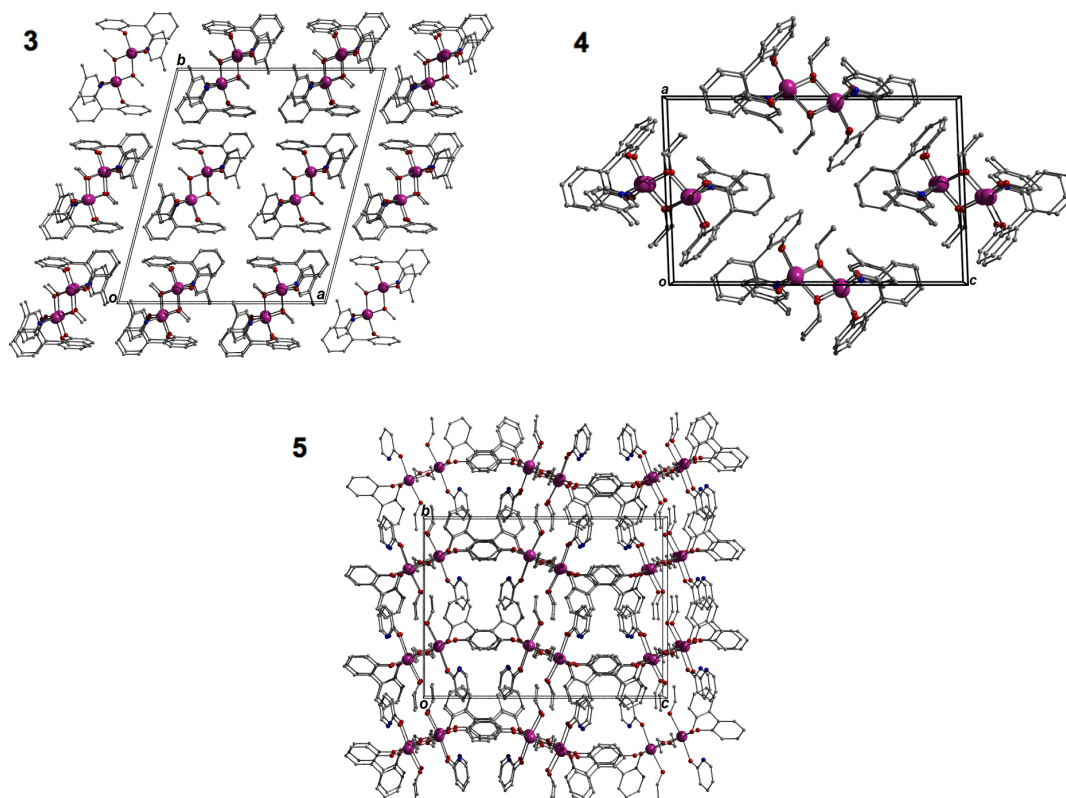


**Figure 19.** Packing diagrams for complexes **3-5**. H-atoms omitted for clarity, colour scheme as in Figure 16.

The final member of the family, [Mn(III)<sub>2</sub>(μ-OEt)<sub>2</sub>(biphen)<sub>2</sub>(EtOH)<sub>2</sub>(2-hpH)<sub>2</sub>] (**5**; Figures 16 and 19), is made from the reaction of Mn(ClO<sub>4</sub>)<sub>2</sub>·6H<sub>2</sub>O, LH<sub>2</sub>, 2-hydroxypyridine (2-hpH) and NMe<sub>4</sub>OH in EtOH. The common central {Mn-(μ-OEt)<sub>2</sub>-Mn} core is retained, with a Mn1-O1-Mn1' angle of 102.85° and a Mn⋯Mn distance of 3.039 Å (Mn-O-Mn'-O' torsion angle = 0°). Indeed the only major structural difference between **5** and its siblings lies in the nature of the bonding of the 2-hydroxypyridine ligands; the ligand bonds to the metal centre via the deprotonated phenolic O-atom (Mn1-O4, 2.306 Å), with the pyridyl N atom now protonated and H-bonding to an O-atom of the chelating biphenoxide (O3⋯H1(N1) = 1.913 Å). A second intra-molecular H-bond is observed between the terminal EtOH ligands, that complete the octahedral coordination spheres at each Mn(III) centre, and O4

O4'...H5(O5), 1.907 Å). Akin to the other family members, the {Mn(III)<sub>2</sub>} units in **5** connect into chains (dissecting the *ab* plane of the cell) via two symmetry equivalent C–H... $\pi$  close contacts ((C17–C21)...H16(C16) = 3.293 Å), derived from interactions between aromatic pyridyl ring and ethyl protons of a close by terminal EtOH molecule (Figure 19). Furthermore, these 1–D rows further connect in the remaining directions via further C–H... $\pi$  interactions comprising aromatic rings and aromatic protons of juxtaposed biphenolate ligands of neighbouring {Mn(III)<sub>2</sub>} complexes ([C9–C14]...H7(C7) = 2.583 Å).

### 2.2.2 Magnetic Susceptibility Measurements

Magnetic susceptibility measurements on complexes **1–5** were carried out in the 300–5 K temperature range in an applied field of 0.1 T (Figures 20 and 21). The room temperature  $\chi_M T$  products for **1–5** lie in the 4.03–4.55 cm<sup>3</sup> mol<sup>-1</sup> K range and are significantly lower than the expected value for two non-interacting Mn(III) ions of 6.00 cm<sup>3</sup> mol<sup>-1</sup> K, assuming *g* = 2.00. This is an indication of antiferromagnetic exchange between the metal centres, as supported by the uniform drop in  $\chi_M T$  on decreasing temperature. In each case, the *T* = 5 K value is close to zero. Fitting of these data with a simple 1–*J* isotropic Hamiltonian:  $\hat{H} = -2J\hat{S}_1 \cdot \hat{S}_2$  affords the best fit parameters documented in Table 4 and represented by the solid lines in Figures 20 and 21. The *J* values span the small range of -10.5 cm<sup>-1</sup> (in **4**) to -14.3 cm<sup>-1</sup> (in **3**).

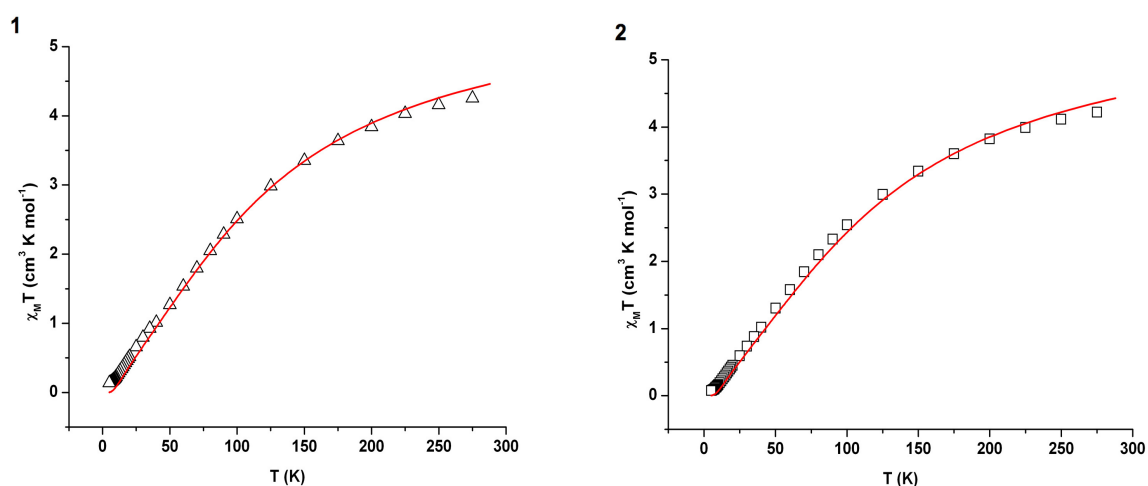


**Figure 20.** Plots of magnetic susceptibility ( $\chi_M T$ ) vs *T* for complexes **1** and **2**. Solid red lines represent the best-fit to give the parameters given in Table 4.

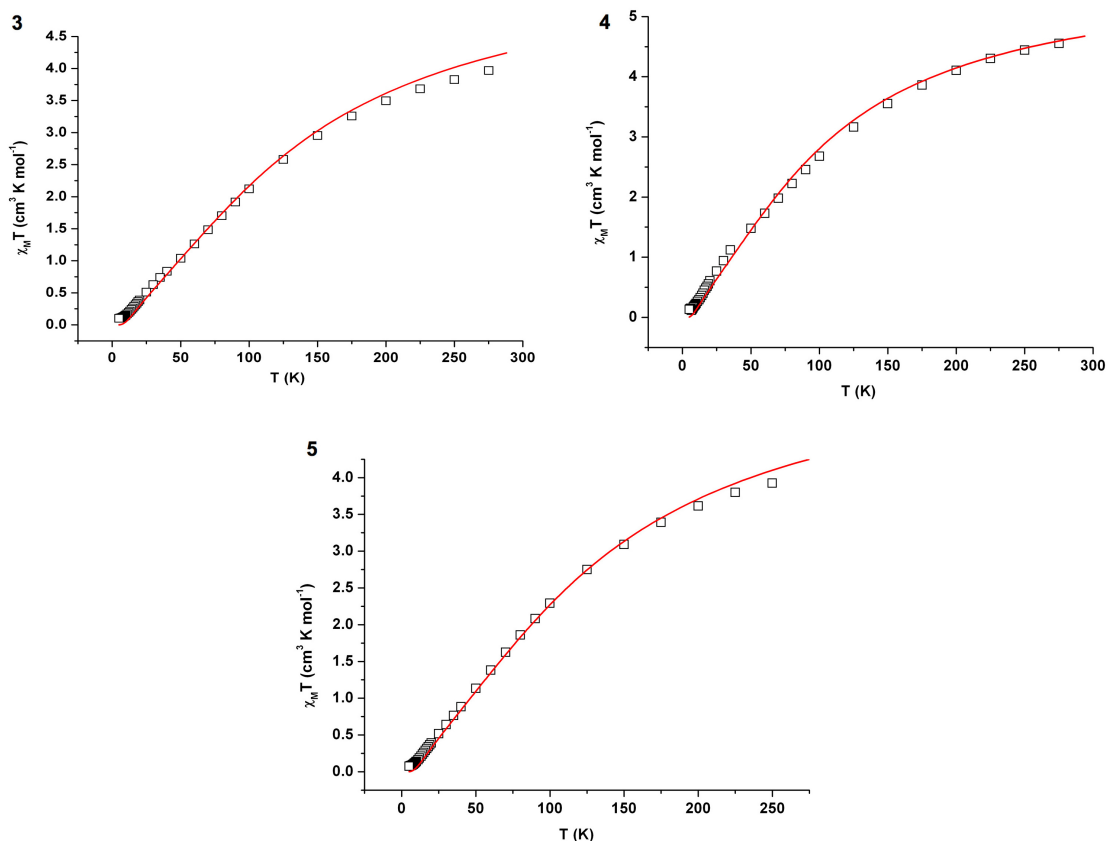


**Figure 21.** Plots of magnetic susceptibility ( $\chi_M T$ ) vs  $T$  for complexes **3–5**. Solid red lines represent the best-fit to give the parameters shown in Table 4.

## 2.3 Magneto-structural correlation study

### 2.3.1 Types I – III

To put these results into context we have compared the structural and magnetic properties of **1–5** to those of all known  $\mu$ -OR bridged  $[\text{Mn}(\text{III})_2]$  clusters reported in the literature. Each compound may be grouped in to one of three distinct categories (see type **I–III** in Figure 22) based on the orientation of the Jahn–Teller axes, using an approach proposed by Tuchagues and co-workers in 1995 [117]. Each of these three families can be categorised by noting the relative orientation of their associated Jahn–Teller axes with respect to one another as well as their orientation with respect to the  $\mu$ -OR bridging plane (Figure 22). These classifications are reported in Tables 4–6 along with their associated magnetic spin Hamiltonian parameters ( $J$ - and  $g$ - values; ground spin state  $S$ ), and all structural parameters, which may have a significant bearing on their resultant magnetic properties. These parameters were then utilised in our subsequent magneto-structural correlation studies.

**Type I:** Complexes belonging to the first category exhibit a co-linear orientation of their Jahn–Teller axes, each of which are perpendicular to the bridging plane of the dimer as observed here and elsewhere in the literature (Figure 22). Indeed the introduction of complexes **1-5** almost doubles the literature basis set for this type of dinuclear species. Magnetic exchange parameters ( $J$ ) for these compounds are all weakly antiferromagnetic with values ranging from  $-8.2 \text{ cm}^{-1}$  [103] to  $-15.5 \text{ cm}^{-1}$  [105]. Interestingly, a group of  $\text{O}^{2-}$  bridged  $[\text{Mn(III)}_2\text{O}_2]$  complexes exhibiting type I conformations are known. As these compounds possess  $\mu\text{-O}^{2-}$  bridging anions rather than  $\mu\text{-OR}$  species they are exempt from our comparative study. The  $\mu\text{-O}^{2-}$  bridging angles of these dimers are significantly more acute than the  $\mu\text{-OR}$  analogues (ca.  $93\text{--}95^\circ$ ), leading to much shorter  $\text{Mn}\cdots\text{Mn}$  distances (ca.  $2.65\text{--}2.7 \text{ \AA}$ ) and as a result these compounds exhibit strong antiferromagnetic interactions with  $J$  values of approximately  $-100 \text{ cm}^{-1}$  [96–99].

**Type II:** This is the most common conformation exhibited by alkoxide bridged dinuclear Mn(III) complexes. Here, the Jahn–Teller axes of the Mn(III) ions are parallel to one another as well as being parallel to the bridging  $\mu\text{-OR}$  plane (Figure 22). The Mn–OR bonds in these types of complexes are thus elongated and as a result the extent of orbital overlaps amongst d-based orbitals appears to be altered. Indeed this may explain the magnetic coupling observed within these species as they exhibit magnetic exchange parameters that lie on the ferro $\leftrightarrow$ antiferromagnetic interface. For instance,  $J$  values ranging from the weakly antiferromagnetic ( $-5.00 \text{ cm}^{-1}$ ) in  $[\text{Mn}_2(2\text{-OH}(5\text{-NO}_2\text{-sal})\text{pn})_2]$  [115], to weakly ferromagnetic ( $J = +6.3 \text{ cm}^{-1}$ ) in the complex  $[\text{Mn}_2(\text{salen})_2(\text{H}_2\text{O})_2](\text{ClO}_4)_2$ , where  $\text{H}_2\text{salen} = N,N'$ -bis(salicylideneaminoato)ethylene [109], have been reported (Table 5).

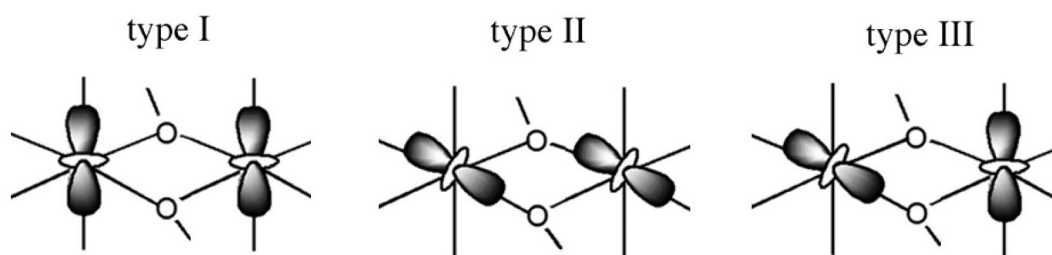


**Figure 22.** Schematic illustrating the three types of magnetic orbital spatial orientations observed within recognised  $\mu\text{-OR}$  bridged  $[\text{Mn(III)}_2]$  complexes.

**Table 4.** Selected magneto-structural parameters for type I dinuclear complexes discussed in this chapter (t.c.) and in the literature. Magnetic data is reported in the  $\hat{H} = -2J\hat{S}_1 \cdot \hat{S}_2$  formalism.

Formula	g	J-value (cm <sup>-1</sup> ) Expt	J-value (cm <sup>-1</sup> ) DFT	Mn...Mn (Å)	Av. Mn-O-Mn angle (°)	Mn-O-Mn-O torsion	Jahn-Teller Dihedral (°)	Av. Mn-O (Å)	Ref
[Mn <sub>2</sub> (OMe) <sub>2</sub> (L) <sub>2</sub> (MeOH) <sub>4</sub> ] (1)	1.98	-12.2	-10.5	3.071	103.66	0	5.4	1.953	t.c.
[Mn <sub>2</sub> (OMe) <sub>2</sub> (L) <sub>2</sub> (py) <sub>3</sub> ] (2)	1.98	-12.5	-	3.007	100.93	15.37	-	1.950	t.c.
[Mn <sub>2</sub> (OMe) <sub>2</sub> (L) <sub>2</sub> (3-pic) <sub>2</sub> ] (3)	1.98	-14.3	-	3.054	104.04	0	-	1.936	t.c.
[Mn <sub>2</sub> (OEt) <sub>2</sub> (L) <sub>2</sub> (3-pic) <sub>2</sub> ] (4)	1.98	-10.5	-12.4	3.042	103.03	0	0	1.944	t.c.
[Mn <sub>2</sub> (OEt) <sub>2</sub> (L) <sub>2</sub> (hpy) <sub>2</sub> (EtOH) <sub>2</sub> ] (5)	1.98	-13.5	-11.6	3.039	102.85	0	0	1.944	t.c.
[Mn <sub>2</sub> (L)(OMe)(OAc)(MeOH) <sub>2</sub> ]Br	1.90	-13.1	-	2.942	97.86	14.85	0.6	1.952	[100]
[Mn <sub>2</sub> (3-OMe-salpentO)(OMe)(OAc)(MeOH) <sub>2</sub> ]Br	1.98	-13.7	-	2.928	98.11	15.10	3.3	1.938	[101]
[Mn <sub>2</sub> (5-NO <sub>2</sub> -salpentO)(OMe)(OAc)(MeOH) <sub>2</sub> ]I <sub>3</sub>	1.98	-12.4	-	2.911	97.95	15.75	4.5	1.930	[102]
[Mn <sub>2</sub> (L <sup>5a</sup> ) <sub>2</sub> (OMe) <sub>2</sub> (MeOH) <sub>2</sub> ]	2.00	-11.8	-	3.038	102.57	7.06	6.5	1.947	[103]
[Mn <sub>2</sub> (L <sup>5b</sup> ) <sub>2</sub> (OMe) <sub>2</sub> (MeOH) <sub>2</sub> ]	2.00	-8.2	-	n.c.a	n.c.a	n.c.a	-	n.c.a	[103]
[Mn <sub>2</sub> (3-Me-salpentO)(OMe)(OAc)(MeOH) <sub>2</sub> ]Br	2.02	-15.1	-	2.929	98.22	16	0	1.937	[104]
[Mn <sub>2</sub> (L)(OMe)Cl <sub>2</sub> (MeOH) <sub>2</sub> ]	2.00	-15.5	-	3.006	101.50	n.c.a	-	1.941	[105]
[Mn <sub>2</sub> (OMe) <sub>2</sub> (sal) <sub>2</sub> (MeOH) <sub>4</sub> ]	2.00	-10.3	-	3.025	102.97	0	5.2	1.934	[106]

**Table 5.** Selected magneto-structural parameters for type II dinuclear complexes discussed in this chapter (t.c.) and in the literature. Magnetic data is reported in the  $\hat{H} = -2J\hat{S}_1 \cdot \hat{S}_2$  formalism.

Formula	g	J-value (cm <sup>-1</sup> ) Expt	J-value (cm <sup>-1</sup> ) DFT	Mn...Mn (Å)	Av. Mn-O-Mn angle	Mn-O-Mn-O torsion	Jahn-Teller Dihedral (°)	Av. Mn-O (Å)	Ref
[Mn <sub>2</sub> (bbml) <sub>2</sub> (acac) <sub>2</sub> ](BF <sub>4</sub> ) <sub>2</sub>	1.97	-0.18	-	3.178	105.27	n.c.a	-	1.99	[107]
[Mn <sub>2</sub> (saltmen) <sub>2</sub> (ReO <sub>4</sub> ) <sub>2</sub> ]	2.00	+2.65K	-	3.330	98.00	0	-	2.193	[108]
[Mn <sub>2</sub> (salen) <sub>2</sub> (H <sub>2</sub> O) <sub>2</sub> ](ClO <sub>4</sub> ) <sub>2</sub>	2.00	+6.30	-	3.334	100.59	0	180	2.156	[109]
[Mn <sub>2</sub> (saltmen) <sub>2</sub> (O <sub>2</sub> CMe) <sub>2</sub> ]	1.98	+1.35	0.73	3.641	99.57	0	152.5	2.352	[110]a
[Mn <sub>2</sub> (saltmen) <sub>2</sub> (N <sub>3</sub> ) <sub>2</sub> ]	1.98	+0.60	-	3.922	98.39	0	180	2.527	[110]b
[Mn <sub>2</sub> (salen) <sub>2</sub> (NCO) <sub>2</sub> ]	2.03	+0.73	-	3.584	97.82	0	180	2.346	[110]c
[Mn(3,5-Br-salen)(3,5-Br-salicylal)] <sub>2</sub>	2.00	+0.55	-	3.597	100.00	0	180	2.323	[110]d
[Mn <sub>2</sub> (5-Br-salen) <sub>2</sub> (MeOH) <sub>2</sub> ](ClO <sub>4</sub> ) <sub>2</sub>	1.96	-0.45	-0.62	3.307	99.85	0	180	2.152	[110]e
[Mn <sub>2</sub> (L) <sub>2</sub> (H <sub>2</sub> O) <sub>2</sub> ](ClO <sub>4</sub> ) <sub>2</sub>	2.01	-1.68	-	3.318	103.38	0	180	2.109	[111]
[Mn <sub>2</sub> (Hthme) <sub>2</sub> (bpy) <sub>2</sub> ](ClO <sub>4</sub> ) <sub>2</sub>	1.71	+2.13	-	3.096	101.56	0	180	1.996	[112]
[Mn <sub>2</sub> (L <sub>1</sub> ) <sub>2</sub> (N <sub>3</sub> ) <sub>2</sub> ]	2.04	-0.55	-	3.341	101.84	0	180	2.144	[113]a
[Mn <sub>2</sub> (L <sub>2</sub> ) <sub>2</sub> (N <sub>3</sub> ) <sub>2</sub> ]	1.99	+1.32	-	3.361	96.76	0	180	2.375	[113]b
[Mn <sub>2</sub> (OMe) <sub>2</sub> (dbm) <sub>4</sub> ]	1.98	+0.28	-	3.104	101.21	0	180	2.005	[114]
[Mn <sub>2</sub> (2-OH(5-NO <sub>2</sub> -sal)pn) <sub>2</sub> ]	1.95	-5.0	-	3.247	99.07	0	180	2.127	[115]
[Mn <sub>2</sub> (bbml) <sub>2</sub> (tol) <sub>2</sub> ](ClO <sub>4</sub> ) <sub>2</sub>	1.97	-1.19	-	3.209	106.29	0	177.9	2.004	[116]
[Mn <sub>2</sub> (saltmen) <sub>2</sub> (H <sub>2</sub> O) <sub>2</sub> ](ClO <sub>4</sub> ) <sub>2</sub>	1.93	+1.79	-	3.381	101.58	0	180	2.172	[108]a
[Mn <sub>2</sub> (naphmen) <sub>2</sub> (H <sub>2</sub> O) <sub>2</sub> ](ClO <sub>4</sub> ) <sub>2</sub>	1.96	+1.20	-	3.541	100.59	0	180	2.279	[108]b
[Mn <sub>2</sub> (saltmen) <sub>2</sub> (NCS) <sub>2</sub> ](ClO <sub>4</sub> ) <sub>2</sub>	1.99	+0.55	-	4.092	96.24	0	180	2.657	[108]c
[Mn <sub>2</sub> (naphmen) <sub>2</sub> (NCS) <sub>2</sub> ](ClO <sub>4</sub> ) <sub>2</sub>	2.03	+0.12	-	4.388	96.57	0	180	2.818	[108]d
[Mn <sub>2</sub> (naphmen) <sub>2</sub> (Cl) <sub>2</sub> ](ClO <sub>4</sub> ) <sub>2</sub>	2.04	+0.38	-	4.102	94.20	0	180	2.699	[108]e
[Mn <sub>2</sub> (3-NO <sub>2</sub> -salpro) <sub>2</sub> (H <sub>2</sub> O)] <sub>2</sub> ·H <sub>2</sub> O	2.04	-1.62	-	3.223	100.52	0	180	2.095	[117]
[Mn <sub>2</sub> (salpn) <sub>2</sub> (NCO) <sub>2</sub> ]	2.02	0.42	-	3.429	100.58	0	180	2.241	[118]a
[Mn <sub>2</sub> (salmen) <sub>2</sub> (N <sub>3</sub> ) <sub>2</sub> ]	2.00	0.58	-	3.433	98.54	0	180	2.246	[118]b
[Mn <sub>2</sub> (acphpn) <sub>2</sub> (N <sub>3</sub> ) <sub>2</sub> ]	2.00	-0.20	-	3.425	101.23	0	180	2.202	[118]c
[Mn <sub>2</sub> (L) <sub>2</sub> (N <sub>3</sub> ) <sub>2</sub> ]	2.03	0.59	-	3.368	98.06	0	180	2.215	[119]
[Mn <sub>2</sub> (salpn) <sub>2</sub> (N <sub>3</sub> ) <sub>2</sub> ]	2.00	0.90	-	3.388	98.42	0	180	2.221	[120]a
[Mn <sub>2</sub> (salpn) <sub>2</sub> (NCS) <sub>2</sub> ]	2.01	0.14	-	3.369	99.39	0	180	2.192	[120]b
[Mn <sub>2</sub> (sapln) <sub>2</sub> (H <sub>2</sub> O) <sub>2</sub> ]	2.00	1.10	-	3.315	99.50	0	180	2.158	[120]c
[Mn <sub>2</sub> (acphen) <sub>2</sub> (NCS) <sub>2</sub> ]	2.00	-0.79	-	3.374	102.14	0	180	2.159	[121]

**Type III:** In this conformation the Jahn–Teller axes of the metal ions are perpendicular to one another: one lying parallel to the bridging plane, the other perpendicular to it (Figure 22). Just two alkoxide bridged  $[\text{Mn(III)}_2]$  complexes exhibiting this conformation have been reported to date. Furthermore both complexes exhibit relatively strong ferromagnetic coupling, proposed due to the non-colinearity of their respective elongated axes [93], [94]. The rarity of these compounds is perhaps due to the low level of symmetry this conformation requires, with the complexes possessing different ligands at each of their two Mn(III) centres (Table 6).

**Table 6.** Selected magneto-structural parameters for type III dinuclear complexes discussed this chapter (t.c.) and in the literature. Magnetic data is reported in the  $\hat{H} = -2J\hat{S}_1 \cdot \hat{S}_2$  formalism.

Formula	g	J-value (cm <sup>-1</sup> ) Expt	J-value (cm <sup>-1</sup> ) DFT	Mn...Mn (Å)	Av. Mn-O-Mn angle	Mn-O-Mn-O torsion	Jahn-Teller Dihedral (Å)	Av. Mn-O (Å)	Ref
$[\text{Mn}_2(\text{OMe})_2(\text{L})(\text{MeOH})](\text{ClO}_4)$	2.00	+6.25	+9.45	3.122	101.10	7.32	81.9	2.022	[93]
$[\text{Mn}_2(\text{OMe})_2(\text{HL})_4]$	1.90	+9.85	+9.8	3.084	102.51	2.20	117.1	1.976	[94]

Since only the orientation between the two planes differs in the three types, we have defined a dihedral plane between the two Jahn–Teller axes which emerges as the key structural factor governing the differences in magnetic behaviour between types I–III and this parameter clearly defines the three categories of structures noted above. The collected experimental structures are plotted in Figure 23 as  $J$  versus dihedral plane.

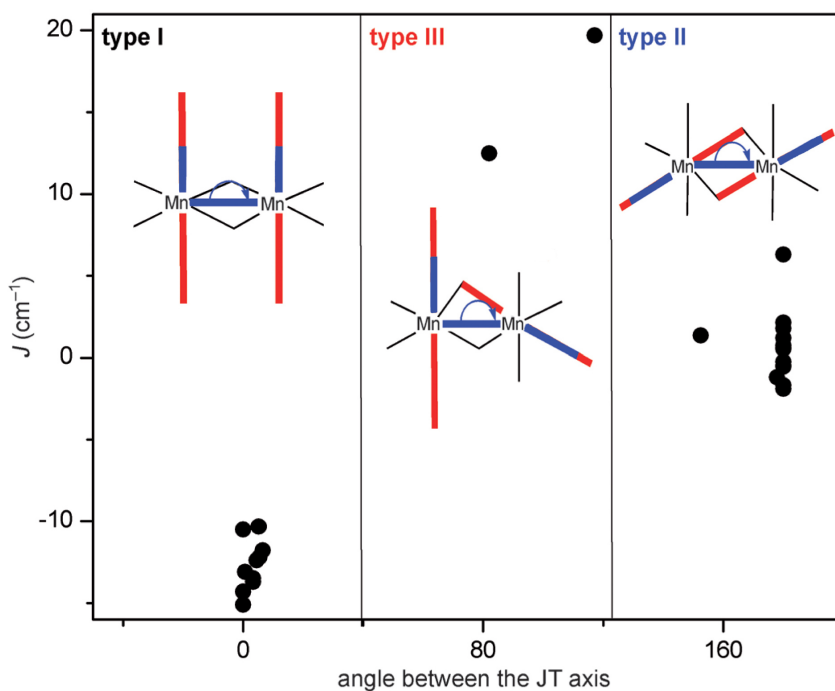


**Figure 23.** Plot of  $J$  (cm<sup>-1</sup>) versus the angle forged between the two Jahn-Teller axes in  $[\text{Mn(III)}_2]$  dimers of types I–III.

The way the dihedral angle has been measured within the dihedral plane is shown in Figure 23 (solid blue lines). As per our classification, all three types can be clearly distinguished. This is not true for any other structural parameters such as short/long Mn–O distances (where a scattered picture emerges). Accordingly, type I structures have dihedral planes  $< 10^\circ$ , type II structures fall into the  $152 - 180^\circ$  range and type III structures (where a strong ferromagnetic exchange has been observed) fall in the middle ground with dihedral angles of  $81.9$  and  $117.1^\circ$  for the two structures reported. As is apparent from Tables 4-6 and Figure 23 the magnitude of the exchange interaction  $J$  varies across the three types I–III. To understand in detail the difference in sign and magnitude of  $J$  observed among these structures and also to develop magneto-structural correlations based on other structural parameters, an extensive theoretical study based on density functional methods has been undertaken. Figure 24 shows one dimer (taken from the crystal data) from each of the three types (highlighting Jahn-Teller orientations) that have been used in our theoretical studies.

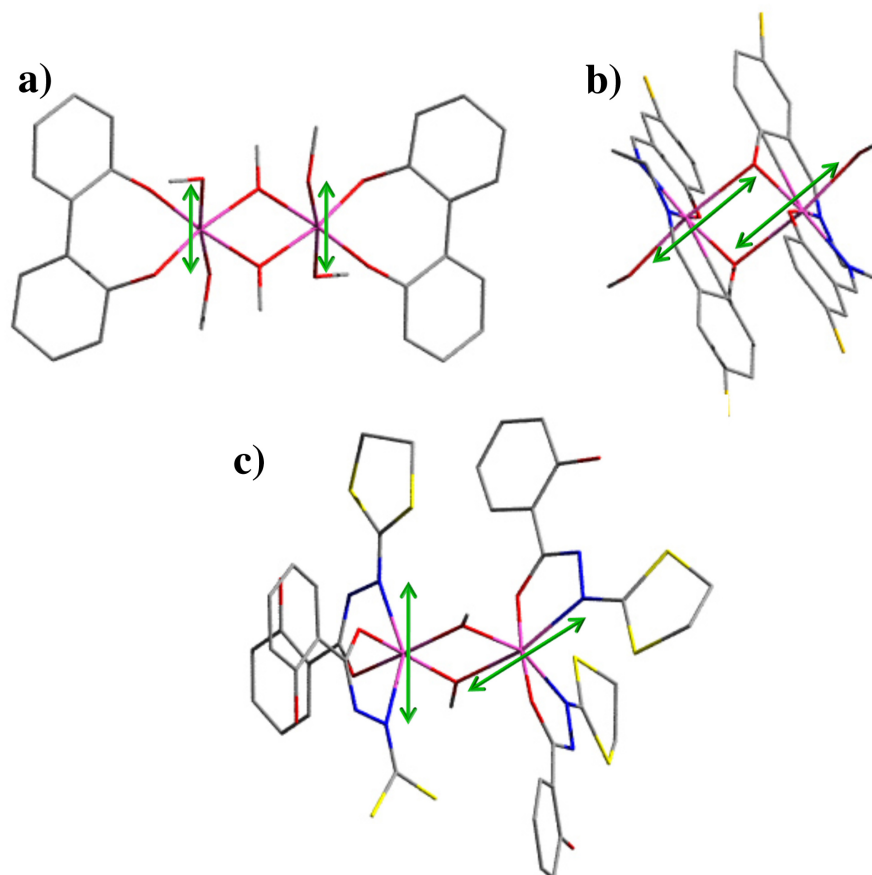


**Figure 24.** Crystal structures of complex **1** (a), complex **II-2** (b) and complex **III-2**. Green arrows highlight the orientation of each Jahn-Teller axis. The structures of complexes **II-2** and **III-2** have been taken from cif data obtained from references [110] and [94] respectively. All three complexes have been studied extensively using DFT.

## 2.3.2 Theoretical Studies

### 2.3.2.1 DFT calculations

To explain the variation in magnetic behaviour between the three types of complexes presented here, we have carried out DFT calculations on selected structures from type I (**1**, **4** and **5**) type II (II-1 [110]a, II-2 [110]e) and type III (III-1 [93], III-2 [94]). The computed  $J$  values are given in Tables 4-6. As is evident from the presented data the  $J$  values calculated are in good agreement with the experimentally reported values for these complexes. In fact, apart from complex III-2, excellent agreement in terms of the sign and magnitude of  $J$  has been observed in all the computed cases. The chosen method and the theoretical level are also able to effectively reproduce the magnitude and values of  $J$  even in borderline cases where the  $J$  values are less than  $1 \text{ cm}^{-1}$ .

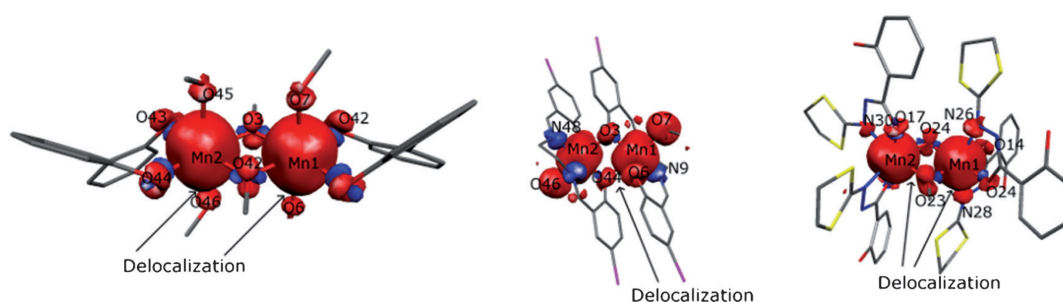


**Figure 25.** B3LYP computed spin density plot for **1**, II-2 [110]e and III-2 [94] with a cut-off value of 0.005 a.u. Red regions represent positive (up) spin density, while blue represents regions of negative (down) spin density.

To probe the electronic origin of the differences between the three types, a spin density plot has been computed for one structure from each type (**1**, II-2 [110]e and III-2 [94]), as shown in Figure 25. As previously mentioned in section 1.5.4, positive spin density refers to regions of electron density whose spin is aligned parallel with the external field, while negative spin density refers to antiparallel alignment with the field. The computed spin densities of the metal atoms and the atoms which are coordinated to Mn(III) for complexes **1**, II-2 and III-2 are listed in Table 7. The modulus of the spin densities on each manganese atom is calculated to be  $>3.7$  in all three types, indicating that the magnetic orbitals are centred on the metals and that there is some unpaired spin density on the ligands. Generally, when the unpaired electrons are located in a metal  $\pi$ -type orbital spin polarization is expected to dominate, while if it is in a  $\sigma$ -type orbital a spin delocalization mechanism is expected to predominate. However this also then depends on the nature of the donor atoms [122]. For Mn(III) ions, since the unpaired electrons are located in three  $t_{2g}$ -like

orbitals and in the  $d_z^2$  orbital, a mechanism encompassing a mixture of spin delocalization and spin polarization is expected. As the Jahn–Teller axis coincides with the  $d_z^2$  orbital direction, the ligand atoms which are coordinated via the Jahn–Teller axis are expected to have the positive spin density as here the spin delocalization will be predominant. In other directions, a mechanism comprising a mixture of spin delocalization and spin polarization is found, leading to either positive or negative spin densities on the donor atoms. In all three cases (**1**, **II-2** and **III-2**) the superexchange propagates through the two bridging  $\mu$ -alkoxo groups and the spin density on these bridging oxygen atoms is expected to influence the sign and magnitude of the  $J$  values.

**Table 7.** DFT computed spin densities of selected atoms of complex **1**, **II-2** and **III-2**.

Complex (1)		Complex (II-2)		Complex (III-2)	
Atom specification	Spin densities	Atom specification	Spin densities	Atom specification	Spin densities
Mn1	3.9414	Mn1	3.7468	Mn1	3.8862
Mn2	3.9414	Mn2	3.7468	Mn2	3.8738
O3	0.0026	O3	0.0278	O11	-0.0028
O4	-0.0023	O6	0.0220	O14	-0.0045
O5	0.0114	O7	0.2793	O17	-0.0141
O6	0.0082	N8	-0.0833	O20	-0.0297
O7	0.0166	N9	-0.0561	O23	0.0379
O42	0.0026	O44	0.0278	O24	0.0069
O43	-0.0023	O45	0.0220	N26	0.0258
O44	0.0114	O46	0.2793	N28	0.0205
O45	0.0082	N47	-0.0803	N30	0.0040
O46	0.0166	N48	-0.0561	N32	0.0283

For type I structures, both  $\mu$ -O-atoms have a very small positive spin density indicating that both the spin polarization and delocalization mechanisms compete, leading to very small spin densities on both oxygen atoms. In type II structures, since the Jahn-Teller axis points towards the  $\mu$ -O-atoms, a predominant spin delocalization from one of the Mn atoms and a mixture from the second Mn atom is expected, leading to a significant increase in the spin density compared to type I structures. In type III structures, since the Jahn-Teller axes are perpendicular, behaviour lying in-between that of types I and II is observed, where one of the oxygen atoms (O23) has significant spin density, while the other (O24) has negligible spin density. These differences in the mechanism and differing magnitude of spin densities on the  $\mu$ -alkoxo group is expected to be exemplified in the computed exchange interaction (Figure 25) [122].

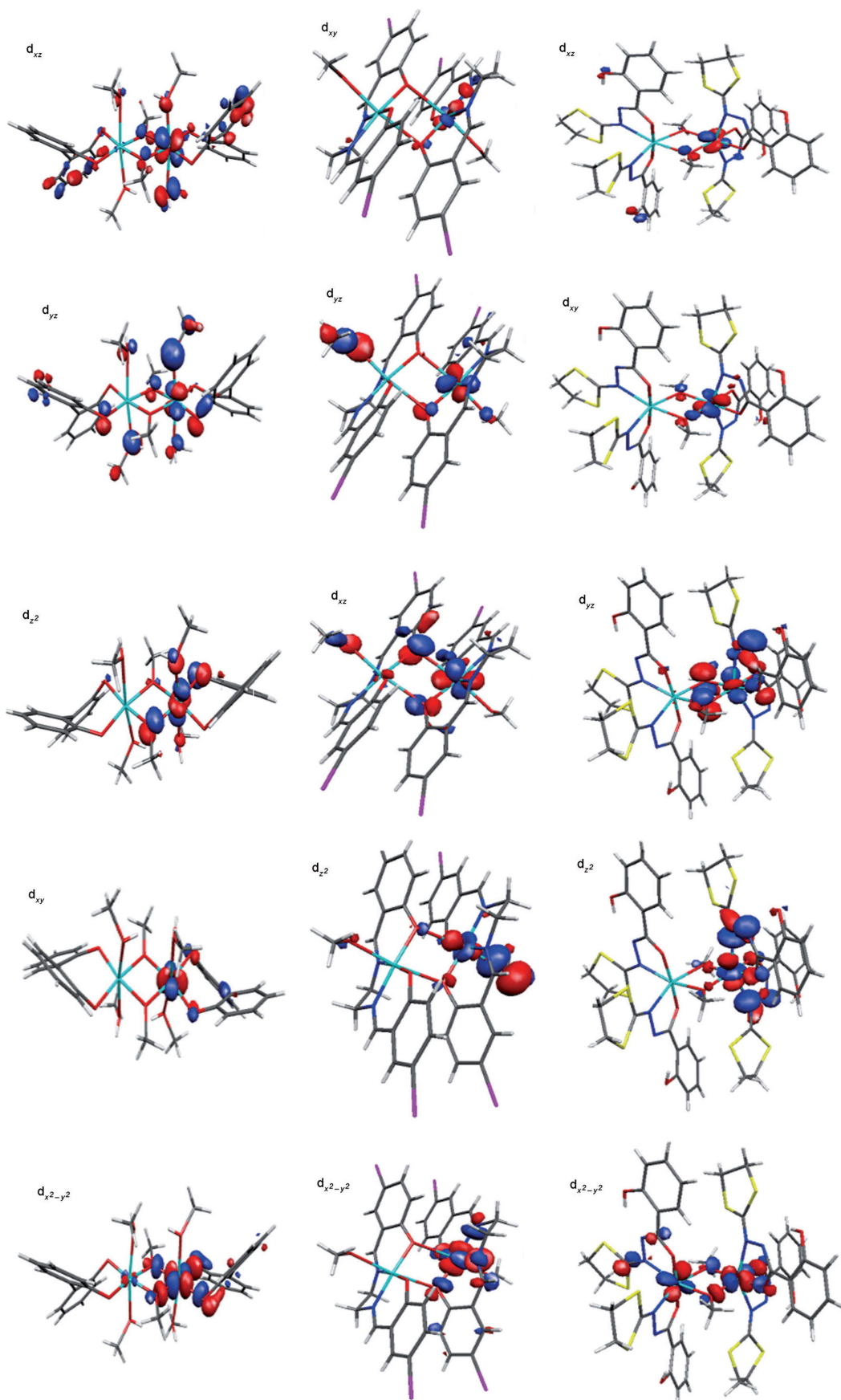


**Figure 26.** Alpha magnetic orbitals of complexes **1**, **II-2** and **III-2** in order of decreasing energy (top to bottom).

### 2.3.2.2 Orbital analysis

To probe the electronic origin further, molecular orbital (MO) analysis has been performed on complexes **1**, II-2 and III-2. The DFT Kohn–Sham orbitals are very useful for qualitatively analysing the  $J$  values, and for providing some insight into the coupling mechanism. The qualitative model of Kahn-Briat [123] takes into consideration the overlap between the non-orthogonal magnetic orbitals and relates it to the  $J$  values. Even though types I – III differ in their net  $J$  values, the net exchange interactions have contributions from both the antiferromagnetic ( $J_{AF}$ ) and ferromagnetic ( $J_F$ ) parts. The computed overlap integral between the singly occupied orbitals is directly proportional to  $J_{AF}$ . It has been noted in several instances that the so-called cross-interaction between the empty  $d_x^2-y^2$  orbitals and the singly occupied orbitals leads to ferromagnetic interactions and this has been qualitatively studied to rationalise the weak interactions observed in Mn(III) dimers in general [124]. We have decided to compute the overlap integral for this pair, since its magnitude is expected to reveal the strength of the ‘cross-interaction’ that exists in these molecules and thus can be translated as the contribution to  $J_F$ . The d-based orbitals of the alpha set (Mn1) for types I–III are shown in Figure 26. The results of the overlap integral calculation are summarised in the computed energy level diagram of Figure 27. A double-headed arrow connecting the alpha (3d orbitals of Mn1) and beta (3d orbitals of Mn2 or Mn1’) sets indicates a significant overlap between the two orbitals (the grey arrows indicate significant cross-interaction). As is evident from the graph, type I structures experience significant overlap between the singly occupied orbitals or SOMOs ( $d_{xy}$ ,  $d_{yz}$ ,  $d_{xz}$  and  $d_z^2$  in Jahn-Teller elongated Mn(III)), leading to antiferromagnetic exchange interactions (see section 1.5.2). The  $d_x^2-y^2$  orbitals of type I structures, which are empty do not experience significant interaction leading to a decrease in the  $J_F$  contribution (See Appendix A for the complete list of computed overlap integrals). Among others, the  $d_{yz}-d_{yz}$ ,  $d_z^2-d_{yz}$ ,  $d_{yz}-d_z^2$ ,  $d_{yz}-d_{xy}$ ,  $d_z^2-d_{xy}$ ,  $d_{xy}-d_z^2$ , interactions are notable. A larger  $J_{AF}$  contribution and a negligible  $J_F$  contribution lead to a large antiferromagnetic net  $J$  for this type of complex. For type II structures, both the  $J_F$  and  $J_{AF}$  contributions exist with the significant exchanges being  $d_{yz}-d_{yz}$ ,  $d_{xz}-d_{yz}$ ,  $d_{yz}-d_{xz}$ ,  $d_{xz}-d_{xz}$  and  $d_{xy}-d_{xy}$  along with some significant cross-interactions. Here the  $J_{AF}$  and  $J_F$  contributions essentially cancel each other out, leading to a very weak net exchange. The sign of the exchange (ferro- or antiferromagnetic) in this type of

complex is determined by the predominant factor. For type III structures on the other hand, fewer  $J_{AF}$  interactions are observed and the cross-interactions play a vital role. A large cross-interaction is evident from the broken symmetry  $d_{x^2-y^2}$  orbital plotted in Figure 26. A stronger  $J_F$  and weaker  $J_{AF}$  leads to relatively strong net ferromagnetic exchange. As mentioned before, the differences in the magnitude and the sign of  $J$  arise due to the difference in the orientation of the  $d_z^2$  orbital – which coincides with the Jahn–Teller axis. On several occasions the Jahn–Teller orientation has been evoked to explain the reduction in the cluster anisotropy and here for the first time with quantitative calculations and qualitative analysis, we provide direct evidence that the Jahn–Teller orientation is important in determining the sign as well as magnitude of the coupling in Mn(III) dimers. A perpendicular alignment of the Jahn–Teller axes for the dinuclear unit is expected to exhibit a relatively strong ferromagnetic interaction. However we point out that this orientation is also likely to lead to a decrease in the cluster anisotropy, an important parameter to consider when designing molecular nanomagnets.

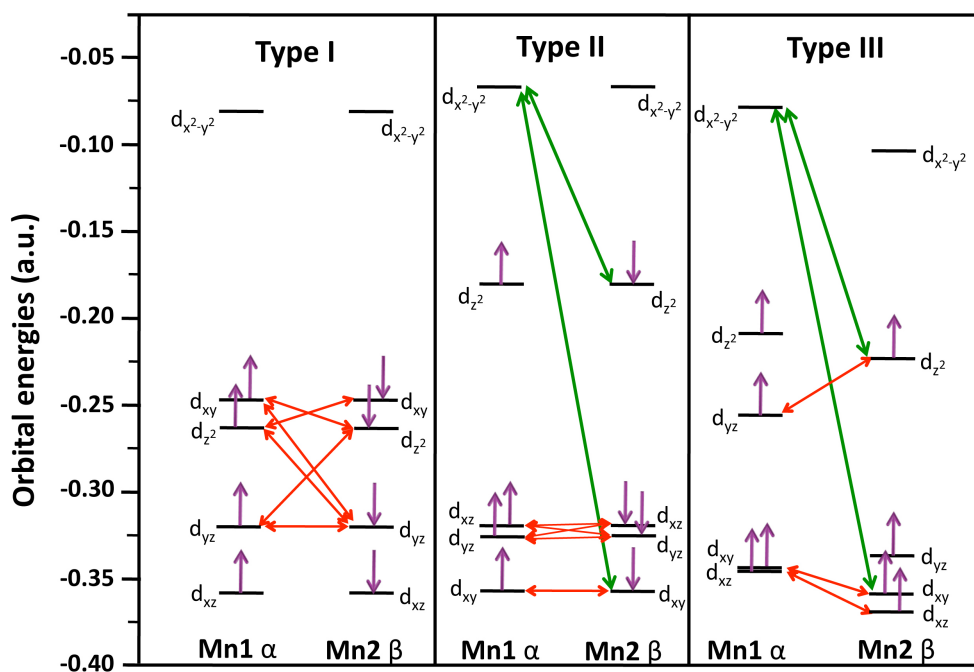


**Figure 27.** Dominant interactions between the magnetic orbitals in type I – III structures. Anti-ferromagnetic interactions are shown as black lines and ferromagnetic interactions as grey arrows.

Since all of the complexes in this study possess different terminal ligands we then sought to determine the effect of a change in the nature of the terminal ligands on the

$J$  values. Thus we have modelled two complexes, in which the terminal ligands of complexes **1** and III-**2** were interchanged. This gives  $J = -8.4 \text{ cm}^{-1}$  and  $+21.6 \text{ cm}^{-1}$  compared to  $-10.2 \text{ cm}^{-1}$  and  $+9.8 \text{ cm}^{-1}$  for their original complexes, respectively. This clearly indicates that the terminal ligands have negligible contribution to the exchange coupling constant.

### 2.3.3 Other structural factors

Although the experimental studies and the theoretical analysis presented in this work strongly suggest that the orientation of the Jahn–Teller axis is the most important parameter in controlling  $J$  across the three types presented, within a particular type other structural parameters are expected to influence the final observed  $J$  value. Indeed, to our knowledge, no theoretical correlations have been developed for this topology to understand the unique structural features that are expected to affect the resultant  $J$  values. We have thus decided to develop correlations for a type I structure in the shape of our own complex **1** (Figure 16). There are four structural parameters deemed vital in influencing and determining the  $J$  value: Mn-O-Mn angle, Mn-O distance, Mn-O-Mn'-O' dihedral angle and the out-of-plane shift of the alkyl group ( $\mu$ -OR) of the compound in question (described by  $\tau$ ). The developed correlations for these four parameters are given in Figure 28. The experimental parameters listed in Table 4 along with the experimental  $J$  have also been plotted along with the computed points (solid squares). For the data obtained from the experimental structure, the three types I–III are distinguished in different colours.

#### 2.3.3.1 Bond angle

By varying the average Mn-O-Mn angle from  $80.1^\circ$  to  $119.8^\circ$ , a correlation has been developed for  $J$  and its value varies exponentially, as represented in Figure 28. The  $J$  parameter decreases and become less antiferromagnetic upon increasing Mn-O-Mn angle. At an acute angle, relatively strong antiferromagnetic exchange has been encountered with the steep increase in negative  $J$  due to significant overlap of the  $d_{xy}$  orbital with other orbitals, as evidenced from the overlap integral values (Table A3 in Appendix A). Since the Mn-O-Mn angle decreases with a decrease in the Mn...Mn distance, this effect is somewhat expected. However at large angles, an overall drop in the overlap values is detected and this leads to smaller negative  $J$  values. There is no switch from antiferromagnetic to ferromagnetic and this is essentially due to

negligibly small cross-interactions at all the computed angles. The experimental type I data points lie within the computed points, revealing that this is a rather reliable parameter. As expected, type II and type III structures deviate from the computed data and this once again suggests that the Jahn-Teller orientation is more important than any other structural parameter.

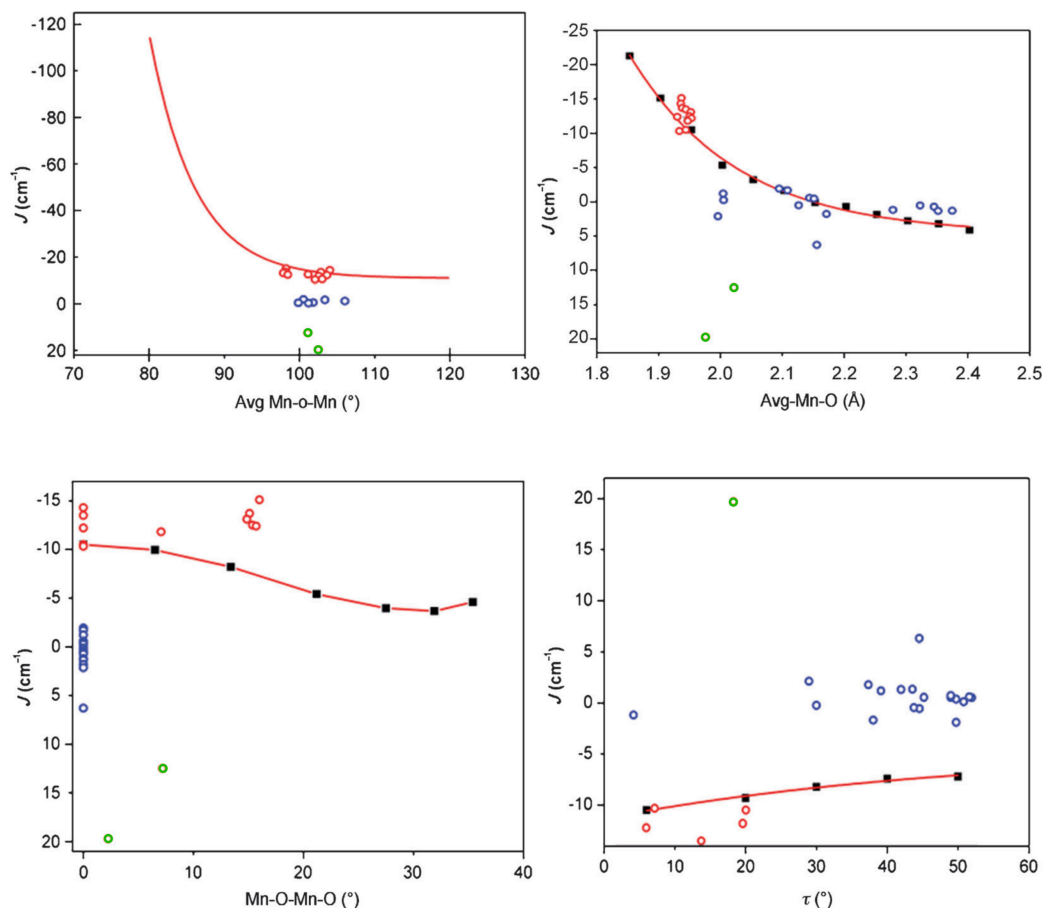


**Figure 28.** Magneto-structural correlations developed by varying structural parameters Mn-O-Mn and Mn-O-Mn-O angles, Mn-O distance and  $\tau$  using DFT calculations. Experimental values are represented in coloured circles, red = type I, blue = type II, and green = type III.

### 2.3.3.2 Bond distance

The second correlation is carried out by varying the average Mn–O distances from 1.853 to 2.403  $\text{\AA}$ . This parameter also exhibits an exponential relationship (Figure 28) whereby the  $J$  value steadily decreases (becomes less antiferromagnetic) with increasing average distance. Moreover as the Mn–O distance passes a value of 2.103  $\text{\AA}$  the interaction becomes ferromagnetic. This is because as the Mn–O distance increases, the type I structure will be converted into other types (II and III for example) and this leads to significant increase in cross-interaction and a predominant ferromagnetic exchange. The experimental data points fit with the type I structures at

shorter Mn–O distances and type II structures at longer Mn–O distances. For the full list of overlap integrals, see Table A4 in Appendix A.

### 2.3.3.3 Dihedral angle

The Mn-O-Mn-O dihedral angle in **1** is varied from 0 to 35.4° to obtain the third correlation. The plot of dihedral angle versus  $J$  is shown in Figure 28. Only a small variation in  $J$  is detected and the complex becomes less antiferromagnetic as the dihedral angle increases. This is as a result of the reduction in the  $d_z^2$ - $d_z^2$  overlap. Here the experimental data points are rather scattered, suggesting that this parameter may not be particularly significant. For the full list of overlap integrals, see Table A5 in Appendix A.

### 2.3.3.4 Out-of-plane displacement of alkyl groups ( $\tau$ )

The fourth correlation analysis involved monitoring  $J$  when the out-of-plane displacement parameter ( $\tau$ ) of the bridging alkyl O atoms was manipulated in the 6 to 50° range. The  $\tau$  versus  $J$  plot (Figure 28) shows a linear relationship. As in the case of the dihedral correlation, an increase in the out-of-plane displacement of the alkyl group also leads to less antiferromagnetic  $J$  values, due to a reduction in overlap between the singly occupied orbitals of the Mn(III) ions (Table A6 in Appendix A).

## 2.4 Conclusion

Based on the structural variation observed among the reported Mn(III) dimeric structures having two alkoxide-bridges, a unique structural feature which distinguishes the type of magnetic interaction observed is proposed. This parameter, based on the orientation of the Jahn–Teller axes of the two Mn(III) atoms, sharply categorises three different types of dimers where type I represent moderately strong antiferromagnetic exchange, type III structures exhibit moderately strong ferromagnetic interactions and type II structures are classified as borderline where a weak ferro- or antiferromagnetic interaction is detected. These three types of classification are supplemented with the synthesis and characterization of a new family of alkoxide-bridged Mn(III) dimers of general formula  $[\text{Mn(III)}_2(\mu\text{-OR})_2(\text{L})_2(\text{ROH})_y(\text{X})_z]$  (where R = Me, Et;  $\text{LH}_2$  = 2,2'-biphenol and X = terminally bonded MeOH or N-donor ligand). All five structures reported here belong to type I

and help us to extend the database to validate the proposed correlations. Additionally, a detailed computational study on all three types was undertaken to probe the electronic origin of the differences in the magnetic behaviour observed. Our computations reveal that the magnetic exchange interaction has two contributions,  $J_{AF}$  and  $J_F$ , with the  $J_F$  contribution arising due to the cross-interaction between the SOMOs and the unoccupied d orbitals. The strength of  $J_F$  is vital as it determines the sign and magnitude of the  $J$  observed in all three types. However the strength of  $J$  is related to the orientation of the  $d_z^2$  orbitals in a particular structure. Since the orientation of the  $d_z^2$  orbital is related to the Jahn–Teller elongation, our study reveals that a perpendicular orientation of the  $d_z^2$  orbitals enhances  $J_F$  significantly, leading to a strong ferromagnetic interaction (type III). A parallel orientation of the two Jahn–Teller axes which lie in the bridging plane is found to be a borderline case (type II). If these axes do not form the  $\mu$ -alkoxide bridges, then a moderately strong antiferromagnetic interaction is encountered (type I). The electronic origins of these differences were traced back to the orbital overlaps and this has been quantitatively analysed using overlap integral computation. In the field of molecular magnetism a strong ferromagnetic interaction is a highly sought-after parameter as the ferromagnetic interaction maximises the ground state S value and its strength helps to promote an isolated ground state. Although a plethora of SMMs comprising Mn(III) ions have been reported, there have been no extensive studies undertaken to pinpoint the unique structural features, which would yield this highly sought-after parameter. The combined experimental and theoretical study undertaken here reveals that the orientation of Jahn-Teller axes plays an important role in the magnetic coupling, with a perpendicular orientation leading to a strong ferromagnetic exchange. However, it is well known that a perpendicular orientation of Jahn-Teller axes leads to a decrease in the anisotropy of the cluster, which is an important parameter in designing molecular nanomagnets. Our study therefore suggests that large anisotropy and a strong ferromagnetic interaction are unlikely to coexist in Mn(III) clusters containing only  $[Mn(\mu\text{-OR})_2]$  building blocks.

Following our investigation into the magnetic exchange coupling in homometallic  $[Mn(III)_2]$  dimers, we move on to explore the exchange interaction in a heterometallic Mn(III)-Cu(II) dimer. Surprisingly, this complex possesses a Jahn-Teller compressed Mn(III) ion and exhibits 2,2'-biphenol in a bridging mode (rather than chelating as

observed in this chapter). The rarity of this type of structural distortion is highlighted by the fact that in our thorough literature search of all known bis- $\mu$ -alkoxo Mn(III) dimers, not a single Mn(III) ion in a tetragonally compressed environment was encountered.

## **2.5 Experimental Section**

### **2.5.1 Physical measurements**

Infrared spectra were recorded on a Perkin–Elmer FT-IR Spectrum One spectrometer equipped with a Universal ATR Sampling accessory (NUI Galway). Elemental analysis detailed was carried out by Marion Vignoles of the School of Chemistry microanalysis service at NUI Galway. Variable-temperature, solid-state direct current (dc) magnetic susceptibility data down to 1.8 K were collected on a Quantum Design MPMS-XL SQUID magnetometer equipped with a 7 T dc magnet (University of Edinburgh). Diamagnetic corrections were applied to the observed paramagnetic susceptibilities using Pascal’s constants.

### **2.5.2 X-Ray crystallography**

The structures of **1–5** were collected on an Xcalibur S single crystal diffractometer (Oxford Diffraction) using an enhanced Mo source. Each data reduction was carried out on the CrysAlisPro software package. The structures were solved by direct methods (SHELXS-97) [125] and refined by full matrix least squares using SHELXL-97 [126]. SHELX operations were automated using the OSCAIL software package [127]. All hydrogen atoms were placed in calculated positions. The non-hydrogen atoms were all refined anisotropically.

### **2.5.3 Computational details**

All calculations were performed using the hybrid B3LYP [128] functional with Ahlrich [129] triple- $\zeta$  basis set as implemented in the Gaussian 09 suite of programs. The  $J$  values were computed from the energy differences between the high spin (EHS) state calculated using single determinant wave functions, and the low spin (EBS) state determined using the Broken Symmetry (BS) approach developed by Noodleman [130]. Negative and positive values for  $J$  correspond to antiferromagnetic and

ferromagnetic interactions, respectively. Details of the computational method employed to compute the exchange interaction is discussed elsewhere [131–135].

#### 2.5.4 Syntheses

All reactions were performed under aerobic conditions at room temperature and all reagents and solvents were used as purchased.

##### Preparation of [Mn(III)<sub>2</sub>(μ-OMe)<sub>2</sub>(L)<sub>2</sub>(MeOH)<sub>4</sub>] (**1**)

A 1.456 M aqueous solution of Mn(NO<sub>3</sub>)<sub>2</sub>·6H<sub>2</sub>O (2 cm<sup>3</sup>, 2.9 mmol) and 2,2'-biphenol (0.54 g, 2.9 mmol) were dissolved in MeOH (30 cm<sup>3</sup>). NaOH (0.115 g, 2.9 mmol) was then added and the solution was left stirring for 10 min. The resultant deep brown solution was then filtered and allowed to stand. X-ray quality crystals of **1** were obtained in ~30% yield upon slow evaporation of the mother liquor overnight. FT-IR (cm<sup>-1</sup>): 3056.0(w), 1587.6(w), 1488.8(m), 1469.2(m), 1430.8(s), 1250.6(s), 1220.9(s), 1154.1(w), 1118.1(w), 1096.2(w), 1046.8(w), 1007.6(w), 934.0(w), 857.8(s), 836.6(m), 753.1(vs), 728.0(s), 710.0 cm<sup>-1</sup>(m). Elemental analysis calculated (found) (%) for C<sub>30</sub>H<sub>38</sub>O<sub>10</sub>Mn<sub>2</sub> (**1**): C: 53.90 (53.82), H: 5.73 (5.93).

##### Preparation of [Mn(III)<sub>2</sub>(μ-OMe)<sub>2</sub>(L)<sub>2</sub>(py)<sub>3</sub>] (**2**)

MnBr<sub>4</sub>·4H<sub>2</sub>O (0.5 g, 1.74 mmol) and 2,2'-biphenol (0.32 g, 1.74 mmol) were dissolved in MeOH (40 cm<sup>3</sup>). NaOPh<sub>3</sub>·3H<sub>2</sub>O (0.15 g, 0.87 mmol) and NaOH (0.035 g, 0.87 mmol) were then added and the resultant deep brown solution was stirred for 15 min. After this time an excess of pyridine was added (12 cm<sup>3</sup>, 149 mmol) and the mixture was left stirring for a further 10 min. The solution was then filtered and left to stand in a fume-cupboard covered by a perforated lid. X-ray quality crystals of **2** were obtained in ~15% yield upon slow evaporation of the mother liquor after two days. FT-IR (cm<sup>-1</sup>): 3060.7(w), 3003.3(w), 2920.9(w), 2815.5(w), 1595.7(m), 1585.2(w), 15578.0(w), 1486.7(m), 1464.3(m), 1443.2(m), 1431.3(s), 1357.5(w), 1292.4(w), 1256.9(s), 1212.0(s), 1152.2(w), 1113.3(w), 1096.5(w), 1053.4(s), 1035.6(m), 1003.4(m), 932.8(w), 857.4(s), 832.7(m), 768.1(s), 755.0(m), 731.8(m), 698.6 cm<sup>-1</sup>(s). Elemental analysis calculated (found) (%) for C<sub>41</sub>H<sub>37</sub>O<sub>6</sub>N<sub>3</sub>Mn<sub>2</sub> (**2**): C: 63.33 (63.28), H: 4.80 (4.76), N: 5.40 (5.48).

### **Preparation of [Mn(III)<sub>2</sub>(μ-OMe)<sub>2</sub>(L)<sub>2</sub>(3-pic)<sub>2</sub>] (3)**

MnBr<sub>2</sub>·4H<sub>2</sub>O (0.167 g, 0.58 mmol) and 2,2'-biphenol (0.11 g, 0.59 mmol) were dissolved in MeOH (20 cm<sup>3</sup>). NaOPh·3H<sub>2</sub>O (0.05 g, 0.43 mmol) and NaOH (0.012 g, 0.3 mmol) were then added in sequence, and the solution was left stirring for 5 min. After this time an excess of 3-picoline (2 cm<sup>3</sup>, 20.55 mmol) was added and the reactant mixture was allowed to stir for a further 15 min. The resultant deep brown solution was then filtered, covered with a perforated lid and allowed to stand in the fume-cupboard. X-ray quality crystals of **3** were obtained in ~20% yield upon slow evaporation of the mother liquor after 24 h. FT-IR (cm<sup>-1</sup>): 3050.9(w), 2922.7(w), 2819.7(w), 1738.3(w), 1581.9(w), 1485.0(m), 1461.6(m), 1428.0(s), 1272.1(m), 1255.8(s), 1221.8(s), 1193.0(m), 1096.6(w), 1053.0(m), 1003.7(m), 935.9(w), 866.8(m), 832.7(m), 798.2(m), 761.4(vs), 726.3(s), 703.5 cm<sup>-1</sup>(s). Elemental analysis calculated (found) (%) for C<sub>38</sub>H<sub>36</sub>O<sub>6</sub>N<sub>2</sub>Mn<sub>2</sub> (**3**): C: 62.82 (62.77), H: 4.99 (5.02), N: 3.86 (4.08).

### **Preparation of [Mn(III)<sub>2</sub>(μ-OEt)<sub>2</sub>(L)<sub>2</sub>(3-pic)<sub>2</sub>] (4)**

MnBr<sub>2</sub>·4H<sub>2</sub>O (0.5 g, 1.74 mmol) and 2,2'-biphenol (0.32 g, 1.72 mmol) were dissolved in EtOH (40 cm<sup>3</sup>). Sequentially, NaOMe (0.28 g, 5.2 mmol) and 3-picoline (2 cm<sup>3</sup>, 20.55 mmol) were added and the solution was left stirring for 10 min. The resultant deep brown solution was then filtered, covered with a perforated lid and allowed to stand in the fume-cupboard. X-ray quality crystals of **4** were obtained in ~15% yield upon slow evaporation of the mother liquor after 24 h. FT-IR (cm<sup>-1</sup>): 3052.2(w), 2969.6(w), 2927.7(w), 1625.2(w), 1581.9(m), 1486.6(m), 1464.6(m), 1427.4(s), 1382.7(m), 1273.5(m), 1258.4(s), 1225.5(s), 1194.0(m), 1152.5(w), 1127.4(w), 1087.8(m), 1037.5(s), 1003.5(m), 935.4(w), 889.1(m), 869.2(s), 858.9(m), 835.3(m), 797.1(m), 763.7(vs), 728.7(m), 712.9(m), 703.6(s), 653.1 cm<sup>-1</sup>(m). Elemental analysis calculated (found) (%) for C<sub>40</sub>H<sub>40</sub>O<sub>6</sub>N<sub>2</sub>Mn<sub>2</sub> (**4**): C: 63.66 (63.82), H: 5.34 (5.28), N: 3.71 (4.04).

### **Preparation of [Mn(III)<sub>2</sub>(μ-OEt)<sub>2</sub>(L)<sub>2</sub>(EtOH)<sub>2</sub>(2-hpH)<sub>2</sub>] (5)**

Mn(ClO<sub>4</sub>)<sub>2</sub>·6H<sub>2</sub>O (0.35 g, 0.96 mmol) and 2,2'-biphenol (0.26 g, 1.4 mmol) were dissolved in EtOH (40 cm<sup>3</sup>). The ligand 2-hydroxypyridine (0.26 g, 2.74 mmol) and NMe<sub>4</sub>(OH) (0.25 g, 2.75 mmol) were then added in sequence and the resultant deep

brown solution was left to stir for 10 min. After this time the solution was filtered, covered with a perforated lid and allowed to stand in the fume hood for several days. X-ray quality crystals of **5** were obtained in ~15% yield upon slow evaporation of the mother liquor after two days. FT-IR ( $\text{cm}^{-1}$ ): 3254.6(w), 3047.6(w), 2920.5(w), 1695.8(w), 1642.8(vs), 1606.9(s), 1537.4(m), 1487.1(m), 1470.0(m), 1430.7(s), 1406.1(m), 1376.1(m), 1274.6(s), 1261.4(m), 1233.2(s), 1154.3(m), 1093.0(m), 1044.4(s), 992.2(m), 963.4(w), 933.1(w), 895.0(m), 866.6(m), 841.3(m), 762.6(vs), 727.8(s), 711.6(m), 669.0  $\text{cm}^{-1}$ (w). Elemental analysis calculated (found) (%) for  $\text{C}_{42}\text{H}_{48}\text{O}_{10}\text{N}_2\text{Mn}_2$  (**5**): C: 59.30 (59.35), H: 5.69 (5.67), N: 3.29 (3.16).

## 2.6 Bibliography

- [59] O. Kahn, "Dinuclear Complexes with Predictable Magnetic Properties," *Angewandte Chemie International Edition in English*, vol. 24, no. 10, pp. 834–850, Oct. 1985.
- [60] B. Bleaney and K. D. Bowers, "Anomalous Paramagnetism of Copper Acetate," *Proceedings of the Royal Society A: Mathematical, Physical and Engineering Sciences*, vol. 214, no. 1119, pp. 451–465, Oct. 1952.
- [61] J. N. van Niekerk and F. R. L. Schoening, "A new type of copper complex as found in the crystal structure of cupric acetate,  $\text{Cu}_2(\text{CH}_3\text{COO})_4 \cdot 2\text{H}_2\text{O}$ ," *Acta Crystallographica*, vol. 6, no. 3, pp. 227–232, Mar. 1953.
- [62] Hatfield W. E., *Extended Interactions between Metal Ions*, vol. 5. Washington D. C.: American Chemical Society, 1974, pp. 108–141.
- [63] K. T. McGregor, N. T. Watkins, D. L. Lewis, R. F. Drake, D. J. Hodgson, and W. E. Hatfield, "Magnetic properties of di- $\mu$ -hydroxobis(2,2'-bipyridyl) dicopper(II) nitrate, and the correlation between the singlet-triplet splitting and the Cu-O-Cu angle in hydroxo-bridged copper(II) complexes," *Inorganic and Nuclear Chemistry Letters*, vol. 9, no. 4, pp. 423–428, Apr. 1973.
- [64] D. L. Lewis, K. T. McGregor, W. E. Hatfield, and D. J. Hodgson, "Preparation and structural and magnetic characterization of beta.-di- $\mu$ -hydroxo-bis [2-(2-dimethylaminoethyl)pyridine]dicopper(II) perchlorate," *Inorganic Chemistry*, vol. 13, no. 5, pp. 1013–1019, May 1974.
- [65] E. D. Estes, W. E. Hatfield, and D. J. Hodgson, "Structural characterization of di- $\mu$ -hydroxo-bis(N,N,N',N'-tetraethylethylenediamine)dicopper(II) perchlorate,  $[\text{Cu}(\text{teen})\text{OH}]_2(\text{ClO}_4)_2$ ," *Inorganic Chemistry*, vol. 13, no. 7, pp. 1654–1657, Jul. 1974.
- [66] W. E. Marsh, K. C. Patel, W. E. Hatfield, and D. J. Hodgson, "Magnetic interactions in chloro-bridged copper(II) dimers. Structural and magnetic characterization of bis( $\mu$ -chloro)bis[chloro(N,N,N'-triethylethylenediamine) copper(II)],  $[\text{Cu}(\text{Et}_3\text{en})\text{Cl}_2]_2$ ," *Inorganic Chemistry*, vol. 22, no. 3, pp. 511–515, Feb. 1983.
- [67] C. P. Landee and R. E. Greeney, "Strong antiferromagnetic exchange in a bromide-bridged copper dimer, bis( $\mu$ -bromo)bis[bromobis(tetramethylene sulfoxide)copper(II)]. Structure, susceptibility, and magnetostructural correlations," *Inorganic Chemistry*, vol. 25, no. 21, pp. 3771–3775, Oct. 1986.
- [68] R. Costa, I. de P. R. Moreira, S. Youngme, K. Siriwong, N. Wannarit, and F. Illas, "Toward the design of ferromagnetic molecular complexes: magnetostructural correlations in ferromagnetic triply bridged dinuclear Cu(II) compounds containing carboxylato and hydroxo bridges.," *Inorganic chemistry*, vol. 49, no. 1, pp. 285–294, Jan. 2010.
- [69] S. S. Tandon, L. K. Thompson, M. E. Manuel, and J. N. Bridson, "Magnetostructural Correlations in  $\mu_2$ -1,1-N<sub>3</sub> Bridged, Dinuclear Copper(II) Complexes.," *Inorganic Chemistry*, vol. 33, no. 24, pp. 5555–5570, Nov. 1994.
- [70] S. M. Gorun and S. J. Lippard, "Magnetostructural correlations in magnetically coupled ( $\mu$ -oxo)diiron(III) complexes," *Inorganic Chemistry*, vol. 30, no. 7, pp. 1625–1630, Apr. 1991.
- [71] H. Weihe and H. U. Güdel, "Angular and Distance Dependence of the Magnetic Properties of Oxo-Bridged Iron(III) Dimers," *Journal of the American Chemical Society*, vol. 119, no. 28, pp. 6539–6543, Jul. 1997.

- [72] H. Weihe and H. U. Güdel, "Magneto-Structural Correlations in Linear and Bent Oxo-Bridged Transition-Metal Dimers: Comparisons, Interpretations, and Predictions of Ground-State Magnetic Properties," *Journal of the American Chemical Society*, vol. 120, no. 12, pp. 2870–2879, Apr. 1998.
- [73] R. Werner, S. Ostrovsky, K. Griesar, and W. Haase, "Magnetostructural correlations in exchange coupled phenoxo-, alkoxo-, and hydroxo-bridged dinuclear iron(III) compounds," *Inorganica Chimica Acta*, vol. 326, no. 1, pp. 78–88, Dec. 2001.
- [74] W. E. Hatfield, J. J. MacDougall, and R. E. Shepherd, "Exchange coupling in the hydroxo-bridged chromium dimer di- $\mu$ -hydroxo-bis(ethylenediamine-N,N'-diacetato)dichromium(III) tetrahydrate. Observations on the effect of structure on superexchange interactions," *Inorganic Chemistry*, vol. 20, no. 12, pp. 4216–4219, Dec. 1981.
- [75] S. J. Cline, D. J. Hodgson, S. Kallsoe, S. Larsen, and E. Pedersen, "Low-temperature structural and magnetic characterization of the chromium(III) dimers bis( $\mu$ -hydroxo)bis[tetraamminechromium(III)] dithionate tetrahydrate and bis( $\mu$ -hydroxo)bis[tetraamminechromium(III)] chloride tetrahydrate,  $[\text{Cr}(\text{NH}_3)_4\text{OH}]_2(\text{S}_2\text{O}_6)_2 \cdot 4\text{H}_2\text{O}$ ," *Inorganic Chemistry*, vol. 22, no. 4, pp. 637–642, Feb. 1983.
- [76] R. P. Scaringe, D. J. Hodgson, and W. E. Hatfield, "Exchange coupling in di- $\mu$ -hydroxo-bridged chromium(III) dimers," *Transition Metal Chemistry*, vol. 6, no. 6, pp. 340–344, Dec. 1981.
- [77] T. K. Karmakar, B. K. Ghosh, A. Usman, H.-K. Fun, E. Rivière, T. Mallah, G. Aromí, and S. K. Chandra, "Magneto-structural correlations: synthesis of a family of end-on azido-bridged manganese(II) dinuclear compounds with  $S = 5$  spin ground state.," *Inorganic chemistry*, vol. 44, no. 7, pp. 2391–2399, Apr. 2005.
- [78] D. A. Pantazis, V. Krewald, M. Orio, and F. Neese, "Theoretical magnetochemistry of dinuclear manganese complexes: broken symmetry density functional theory investigation on the influence of bridging motifs on structure and magnetism.," *Dalton transactions (Cambridge, England : 2003)*, vol. 39, no. 20, pp. 4959–4967, May 2010.
- [79] N. Kaltsoyannis and J. E. McGrady, *Principles and Applications of Density Functional Theory in Inorganic Chemistry II*, vol. 113. Berlin, Heidelberg: Springer Berlin Heidelberg, 2004.
- [80] T. Cauchy, E. Ruiz, and S. Alvarez, "Magnetostructural correlations in polynuclear complexes: the  $\text{Fe}_4$  butterflies.," *Journal of the American Chemical Society*, vol. 128, no. 49, pp. 15722–15727, Dec. 2006.
- [81] S. Gehring, P. Fleischhauer, H. Paulus, and W. Haase, "Ferromagnetic exchange coupling and magneto-structural correlations in mixed-bridged trinuclear copper(II) complexes. Magnetic data and theoretical investigations and crystal structures of two angled  $\text{Cu}^{\text{II}}_3$  complexes," *Inorganic Chemistry*, vol. 32, no. 1, pp. 54–60, Jan. 1993.
- [82] Y.-Q. Zhang and C.-L. Luo, "Theoretical study of magnetostructural correlations in a family of triangular manganese(III) complexes.," *Dalton transactions (Cambridge, England : 2003)*, no. 29, pp. 5627–5636, Aug. 2009.
- [83] J. Tercero, E. Ruiz, S. Alvarez, A. Rodriguez-Forteza, and P. Alemany, "Density functional study of magnetostructural correlations in cubane complexes containing the  $\text{Cu}_4\text{O}_4$  core," *Journal of Materials Chemistry*, vol. 16, no. 26, p. 2729, 2006.

- [84] L. Gregoli, C. Danieli, A.-L. Barra, P. Neugebauer, G. Pellegrino, G. Poneti, R. Sessoli, and A. Cornia, "Magnetostructural correlations in Tetrairon(III) single-molecule magnets.," *Chemistry (Weinheim an der Bergstrasse, Germany)*, vol. 15, no. 26, pp. 6456–6467, Jun. 2009.
- [85] S. Sasmal, S. Hazra, P. Kundu, S. Majumder, N. Aliaga-Alcalde, E. Ruiz, and S. Mohanta, "Magneto-structural correlation studies and theoretical calculations of a unique family of single end-to-end azide-bridged Ni(II)<sub>4</sub> cyclic clusters.," *Inorganic chemistry*, vol. 49, no. 20, pp. 9517–9526, Oct. 2010.
- [86] M. A. Palacios, A. J. Mota, J. E. Perea-Buceta, F. J. White, E. K. Brechin, and E. Colacio, "Antiferromagnetic versus ferromagnetic exchange interactions in bis( $\mu$ -O(oximate))dinickel(II) units for a series of closely related cube shaped carboxamideoximate-bridged Ni<sub>4</sub> complexes. A combined experimental and theoretical magneto-structural study.," *Inorganic chemistry*, vol. 49, no. 21, pp. 10156–10165, Nov. 2010.
- [87] C. J. Milios, R. Inglis, A. Vinslava, R. Bagai, W. Wernsdorfer, S. Parsons, S. P. Perlepes, G. Christou, and E. K. Brechin, "Toward a magnetostructural correlation for a family of Mn<sub>6</sub> SMMs.," *Journal of the American Chemical Society*, vol. 129, no. 41, pp. 12505–12511, Oct. 2007.
- [88] A. Prescimone, C. J. Milios, J. Sanchez-Benitez, K. V. Kamenev, C. Loose, J. Kortus, S. Moggach, M. Murrie, J. E. Warren, A. R. Lennie, S. Parsons, and E. K. Brechin, "High pressure induced spin changes and magneto-structural correlations in hexametallc SMMs.," *Dalton transactions (Cambridge, England : 2003)*, no. 25, pp. 4858–67, Jul. 2009.
- [89] R. Inglis, L. F. Jones, C. J. Milios, S. Datta, A. Collins, S. Parsons, W. Wernsdorfer, S. Hill, S. P. Perlepes, S. Piligkos, and E. K. Brechin, "Attempting to understand (and control) the relationship between structure and magnetism in an extended family of Mn<sub>6</sub> single-molecule magnets.," *Dalton transactions (Cambridge, England : 2003)*, no. 18, pp. 3403–3412, May 2009.
- [90] O. Waldmann, R. Koch, S. Schromm, J. Schülein, P. Müller, I. Bernt, R. W. Saalfrank, F. Hampel, and E. Balthes, "Magnetic Anisotropy of a Cyclic Octanuclear Fe(III) Cluster and Magneto-Structural Correlations in Molecular Ferric Wheels †," *Inorganic Chemistry*, vol. 40, no. 13, pp. 2986–2995, Jun. 2001.
- [91] J. Bartolomé, G. Filoti, V. Kuncser, G. Schinteie, V. Mereacre, C. Anson, A. Powell, D. Prodius, and C. Turta, "Magnetostructural correlations in the tetranuclear series of {Fe<sub>3</sub>LnO<sub>2</sub>} butterfly core clusters: Magnetic and Mössbauer spectroscopic study," *Physical Review B*, vol. 80, no. 1, Jul. 2009.
- [92] *Magnetism: Molecules to Materials V*. John Wiley & Sons, 2006, pp. 310–319.
- [93] M. F. Anderlund, J. Zheng, M. Ghiladi, M. Kritikos, E. Rivière, L. Sun, J.-J. Girerd, and B. Åkermark, "A new, dinuclear high spin manganese(III) complex with bridging phenoxy and methoxy groups. Structure and magnetic properties," *Inorganic Chemistry Communications*, vol. 9, no. 12, pp. 1195–1198, Dec. 2006.
- [94] C. Beghidja, G. Rogez, J. Kortus, M. Wesolek, and R. Welter, "Very strong ferromagnetic interaction in a new binuclear  $\mu$ -methoxo-bridged Mn(III) complex: synthesis, crystal structure, magnetic properties, and DFT calculations.," *Journal of the American Chemical Society*, vol. 128, no. 10, pp. 3140–1, Mar. 2006.

- [95] A. W. Addison, T. N. Rao, J. Reedijk, J. van Rijn, and G. C. Verschoor, "Synthesis, structure, and spectroscopic properties of copper(II) compounds containing nitrogen/sulphur donor ligands; the crystal and molecular structure of aqua[1,7-bis(N-methylbenzimidazol-2'-yl)-2,6-dithiaheptane]copper(II) perchlorate," *Journal of the Chemical Society, Dalton Transactions*, no. 7, p. 1349, 1984.
- [96] J. Glerup, P. A. Goodson, A. Hazell, R. Hazell, D. J. Hodgson, C. J. McKenzie, K. Michelsen, U. Rychlewska, and H. Toftlund, "Synthesis and Characterization of Bis( $\mu$ -oxo)dimanganese(III,III), -(III,IV), and -(IV,IV) Complexes with Ligands Related to N,N'-Bis(2-pyridylmethyl)-1,2-ethanediamine (Bispicen)," *Inorganic Chemistry*, vol. 33, no. 18, pp. 4105–4111, Aug. 1994.
- [97] Y. Mikata, H. So, A. Yamashita, A. Kawamura, M. Mikuriya, K. Fukui, A. Ichimura, and S. Yano, "Quinoline-based tetradentate nitrogen ligands stabilize the bis(micro-oxo) dinuclear manganese(III,III) core.," *Dalton transactions (Cambridge, England : 2003)*, no. 30, pp. 3330–3334, Aug. 2007.
- [98] R. Celenligil-Cetin, P. Paraskevopoulou, N. Lalioti, Y. Sanakis, R. J. Staples, N. P. Rath, and P. Stavropoulos, "Metalloradical complexes of manganese and chromium featuring an oxidatively rearranged ligand.," *Inorganic chemistry*, vol. 47, no. 23, pp. 10998–11009, Dec. 2008.
- [99] L. Dubois, J. Pécaut, M.-F. Charlot, C. Baffert, M.-N. Collomb, A. Deronzier, and J.-M. Latour, "Carboxylate ligands drastically enhance the rates of oxo exchange and hydrogen peroxide disproportionation by oxo manganese compounds of potential biological significance.," *Chemistry (Weinheim an der Bergstrasse, Germany)*, vol. 14, no. 10, pp. 3013–3025, Jan. 2008.
- [100] H. Biava, C. Palopoli, S. Shova, M. De Gaudio, V. Daier, M. González-Sierra, J.-P. Tuchagues, and S. Signorella, "New dimanganese(III) complexes of pentadentate ( $N_2O_3$ ) Schiff base ligands with the  $[Mn_2(\mu-OAc)(\mu-OR)_2]^{3+}$  core: synthesis, characterization and mechanistic studies of  $H_2O_2$  disproportionation.," *Journal of inorganic biochemistry*, vol. 100, no. 10, pp. 1660–1671, Oct. 2006.
- [101] C. Palopoli, M. González-Sierra, G. Robles, F. Dahan, J.-P. Tuchagues, and S. Signorella, "Synthesis and characterisation of dimanganese(III) complexes of 1,5-bis(X-salicylidenamino)pentan-3-ol (X = 3- or 5-methoxy) and their catalytic activity towards hydrogen peroxide disproportionation," *Journal of the Chemical Society, Dalton Transactions*, no. 20, p. 3813, 2002.
- [102] V. Daier, H. Biava, C. Palopoli, S. Shova, J.-P. Tuchagues, and S. Signorella, "Synthesis, characterisation and catalase-like activity of dimanganese(III) complexes of 1,5-bis(5-X-salicylidenamino)pentan-3-ol (X=nitro and chloro).," *Journal of inorganic biochemistry*, vol. 98, no. 11, pp. 1806–1817, Nov. 2004.
- [103] T. K. Paine, T. Weyhermuller, E. Bothe, K. Wieghardt, and P. Chaudhuri, "Manganese complexes of mixed O, X, O-donor ligands (X = S or Se): synthesis, characterization and catalytic reactivity," *Dalton Transactions*, no. 15, p. 3136, 2003.
- [104] D. Moreno, C. Palopoli, V. Daier, S. Shova, L. Vendier, M. G. Sierra, J.-P. Tuchagues, and S. Signorella, "Synthesis, structure and catalase-like activity of dimanganese(III) complexes of 1,5-bis(X-salicylidenamino)pentan-3-ol (X = 3- and 5-methyl). Influence of phenyl-ring substituents on catalytic activity.," *Dalton transactions (Cambridge, England : 2003)*, no. 43, pp. 5156–5166, Nov. 2006.

- [105] M. Mikuria, Y. Yamamoto, and T. Tokii, "A binuclear manganese(III) complex with 1,5-bis(salicylideneamino)-3-pentanol which contains chloride ions," *Inorganica chimica acta*, vol. 181, no. 1, pp. 1–2, 1991.
- [106] X. Shi Tan, W. Xia Tang, and J. Sun, "Synthesis, structure and magnetic properties of a new manganese(III) dimer  $[\text{Mn}_2(\mu\text{-OCH}_3)_2(\text{SAL})_2(\text{CH}_3\text{OH})_4]$  bridged by two  $\mu\text{-OCH}_3$  groups," *Polyhedron*, vol. 15, no. 16, pp. 2671–2675, Aug. 1996.
- [107] J. J. Zhang, Q. H. Luo, C. Y. Duan, Z. L. Wang, and Y. H. Mei, "Synthesis, crystal structure and properties of a new dinuclear manganese(III) complex: a mimic for catalase.," *Journal of inorganic biochemistry*, vol. 86, no. 2–3, pp. 573–579, Sep. 2001.
- [108] H. Miyasaka, R. Clérac, W. Wernsdorfer, L. Lecren, C. Bonhomme, K. Sugiura, and M. Yamashita, "A Dimeric Manganese(III) Tetradentate Schiff Base Complex as a Single-Molecule Magnet," *Angewandte Chemie*, vol. 116, no. 21, pp. 2861–2865, May 2004.
- [109] H.-L. Shyu, H.-H. Wei, and Y. Wang, "Structure and magnetic properties of dinuclear  $[\text{Mn}(\text{III})(\text{salen})(\text{H}_2\text{O})]_2(\text{ClO}_4)_2$  and polynuclear  $[\text{Mn}(\text{III})(\text{salen})(\text{NO}_3)]_n$ ," *Inorganica Chimica Acta*, vol. 290, no. 1, pp. 8–13, Jun. 1999.
- [110] Z. Lü, M. Yuan, F. Pan, S. Gao, D. Zhang, and D. Zhu, "Syntheses, crystal structures, and magnetic characterization of five new dimeric manganese(III) tetradentate Schiff base complexes exhibiting single-molecule-magnet behavior.," *Inorganic chemistry*, vol. 45, no. 9, pp. 3538–3548, May 2006.
- [111] N. Matsumoto, Z. J. Zhong, H. ōkawa, and S. Kida, "Crystal structure and magnetic property of the binuclear manganese(III) complex  $[\text{Mn}(\text{L})\text{H}_2\text{O}]_2(\text{ClO}_4)_2$  (L = N-(acetylaceto nyridene)-N'-( $\alpha$ -methylsalicylidene)-ethylenediamine)," *Inorganica Chimica Acta*, vol. 160, no. 2, pp. 153–157, Jun. 1989.
- [112] G. Rajaraman, E. C. Sañudo, M. Helliwell, S. Piligkos, W. Wernsdorfer, G. Christou, and E. K. Brechin, "Magnetic and theoretical characterization of a ferromagnetic Mn(III) dimer," *Polyhedron*, vol. 24, no. 16–17, pp. 2450–2454, Nov. 2005.
- [113] S. Saha, D. Mal, S. Koner, A. Bhattacharjee, P. Gütllich, S. Mondal, M. Mukherjee, and K.-I. Okamoto, "Synthesis, X-ray structure and magnetic properties of the azido adducts of quadridentate Schiff base manganese(III) complexes," *Polyhedron*, vol. 23, no. 10, pp. 1811–1817, Jun. 2004.
- [114] G. L. Abbati, A. Cornia, A. C. Fabretti, A. Caneschi, and D. Gatteschi, "Structure and Magnetic Properties of a Mixed-Valence Heptanuclear Manganese Cluster," *Inorganic Chemistry*, vol. 37, no. 15, pp. 3759–3766, Jul. 1998.
- [115] A. Gelasco, M. L. Kirk, J. W. Kampf, and V. L. Pecoraro, "The  $[\text{Mn}_2(2\text{-OHSalpn})_2]^{(2-,0,+)}$  System: Synthesis, Structure, Spectroscopy, and Magnetism of the First Structurally Characterized Dinuclear Manganese Series Containing Four Distinct Oxidation States.," *Inorganic chemistry*, vol. 36, no. 9, pp. 1829–1837, Apr. 1997.
- [116] J.-J. Zhang, Y.-Y. Tang, Q.-H. Luo, C.-Y. Duan, Z.-L. Wang, and Y.-H. Mei, "Synthesis, crystal structure and activity for  $\text{H}_2\text{O}_2$  disproportionation of a binuclear manganese(III) complex  $[(\text{tol})\text{Mn}(\text{bbml})_2\text{Mn}(\text{tol})](\text{ClO}_4)_2$ ," *Polyhedron*, vol. 20, no. 18, pp. 2285–2291, Aug. 2001.

- [117] Z.-Y. Zhang, C. Brouca-Cabarrecq, C. Hemmert, F. Dahan, and J.-P. Tuchagues, "Manganese complexes of 1,3-bis(3-nitrosalicylideneamino)-propan-2-ol. Structure and magnetic and electrochemical properties," *Journal of the Chemical Society, Dalton Transactions*, no. 9, p. 1453, 1995.
- [118] G. Bhargavi, M. V. Rajasekharan, J.-P. Costes, and J.-P. Tuchagues, "Synthesis, crystal structure and magnetic properties of dimeric Mn(III) Schiff base complexes including pseudohalide ligands: Ferromagnetic interactions through phenoxo bridges and single molecule magnetism," *Polyhedron*, vol. 28, no. 7, pp. 1253–1260, May 2009.
- [119] S. Mandal, G. Rosair, J. Ribas, and D. Bandyopadhyay, "Synthesis, crystal structure and magnetic characterization of a new phenoxo-bridged binuclear manganese(III) Schiff base complex exhibiting single-molecule-magnet behavior," *Inorganica Chimica Acta*, vol. 362, no. 7, pp. 2200–2204, May 2009.
- [120] Y. Feng, C. Wang, Y. Zhao, J. Li, D. Liao, S. Yan, and Q. Wang, "Out-of-plane dimeric Mn(III) quadridentate Schiff-base complexes: Synthesis, structure and magnetic properties," *Inorganica Chimica Acta*, vol. 362, no. 10, pp. 3563–3568, Aug. 2009.
- [121] G. Bhargavi, M. V. Rajasekharan, and J.-P. Tuchagues, "Antiferromagnetic interactions through phenoxo bridges and lattice water: Synthesis, structure, and magnetic properties of new Mn(III) Schiff base complexes in combination with thiocyanate ligand," *Inorganica Chimica Acta*, vol. 362, no. 9, pp. 3247–3252, Jul. 2009.
- [122] O. Kahn and B. Briat, "Exchange interaction in polynuclear complexes. Principles, model and application to the binuclear complexes of chromium(III)," *Journal of the Chemical Society, Faraday Transactions 2*, vol. 72, p. 268, 1976.
- [123] A. D. Becke, "Density-functional thermochemistry. III. The role of exact exchange," *The Journal of Chemical Physics*, vol. 98, no. 7, p. 5648, Apr. 1993.
- [124] R. Hotzelmann, K. Wieghardt, U. Floerke, H. J. Haupt, D. C. Weatherburn, J. Bonvoisin, G. Blondin, and J. J. Girerd, "Spin exchange coupling in asymmetric heterodinuclear complexes containing the  $\mu$ -oxo-bis( $\mu$ -acetato)dimetal core," *Journal of the American Chemical Society*, vol. 114, no. 5, pp. 1681–1696, Feb. 1992.
- [125] G. M. Sheldrick, "Phase annealing in SHELX-90: direct methods for larger structures," *Acta Crystallographica Section A Foundations of Crystallography*, vol. 46, no. 6, pp. 467–473, Jun. 1990.
- [126] G. M. Sheldrick, "SHELXL-97, A computer program for crystal structure determination." 1997.
- [127] P. McArdle, P. Daly, and D. Cunningham, "CHKSYM - a PC program that checks the symmetry properties of the unit cell and its contents," *Journal of Applied Crystallography*, vol. 35, no. 3, pp. 378–378, May 2002.
- [128] A. Schafer, H. Horn, and R. Ahlrichs, "Fully optimized contracted Gaussian basis sets for atoms Li to Kr," *The Journal of Chemical Physics*, vol. 97, no. 4, p. 2571, Aug. 1992.
- [129] A. Schafer, C. Huber, and R. Ahlrichs, "Fully optimized contracted Gaussian basis sets of triple zeta valence quality for atoms Li to Kr," *The Journal of Chemical Physics*, vol. 100, no. 8, p. 5829, Apr. 1994.

- [130] L. Noodleman, "Valence bond description of antiferromagnetic coupling in transition metal dimers," *The Journal of Chemical Physics*, vol. 74, no. 10, p. 5737, May 1981.
- [131] E. Ruiz, J. Cano, S. Alvarez, and P. Alemany, "Broken symmetry approach to calculation of exchange coupling constants for homobinuclear and heterobinuclear transition metal complexes," *Journal of Computational Chemistry*, vol. 20, no. 13, pp. 1391–1400, Oct. 1999.
- [132] E. Ruiz, A. Rodríguez-Forteza, J. Cano, S. Alvarez, and P. Alemany, "About the calculation of exchange coupling constants in polynuclear transition metal complexes." *Journal of computational chemistry*, vol. 24, no. 8, pp. 982–989, Jun. 2003.
- [133] P. Christian, G. Rajaraman, A. Harrison, M. Helliwell, J. J. W. McDouall, J. Raftery, and R. E. P. Winpenny, "Synthesis and studies of a trinuclear Mn(II) carboxylate complex.," *Dalton transactions (Cambridge, England : 2003)*, no. 16, pp. 2550–2555, Aug. 2004.
- [134] G. Rajaraman, J. Cano, E. K. Brechin, and E. J. L. McInnes, "Density functional calculations of a tetradecametalllic iron(III) cluster with a very large spin ground state.," *Chemical communications (Cambridge, England)*, no. 13, pp. 1476–1477, Jul. 2004.
- [135] G. Rajaraman, M. Murugesu, E. C. Sañudo, M. Soler, W. Wernsdorfer, M. Helliwell, C. Muryn, J. Raftery, S. J. Teat, G. Christou, and E. K. Brechin, "A family of manganese rods: syntheses, structures, and magnetic properties.," *Journal of the American Chemical Society*, vol. 126, no. 47, pp. 15445–15457, Dec. 2004.

## **Chapter 3:**

# **Synthetic, Structural, Spectroscopic and Theoretical Study of a Mn(III)-Cu(II) Dimer Containing a Jahn-Teller Compressed Mn(III) ion**

## 3.1 Introduction

### 3.1.1 Jahn-Teller effects

Just over seventy-five years have passed since the well known theorem of Jahn and Teller emerged [136], which was formulated using group theory. Seven decades later, this theorem and its related physical phenomena, referred to by the term ‘Jahn–Teller effects’, continue to be the subjects of active research. In coordination chemistry the most commonly observed Jahn-Teller effect is the tetragonal distortion of octahedral complexes with degenerate electronic ground states. In the previous chapter, this effect was observed as the axial elongation of the octahedral coordination environment of the Mn(III) ions in forty-four Mn(III)-(OR<sup>-</sup>)<sub>2</sub>-Mn(III) dinuclear complexes. Due to its d<sup>4</sup> electronic configuration, the octahedral Mn(III) ion possesses three electrons in the t<sub>2g</sub> set of orbitals (one in each) and just one in the e<sub>g</sub> set. Without a Jahn-Teller distortion this state is doubly degenerate (<sup>5</sup>E<sub>g</sub>), as this e<sub>g</sub> electron can reside in either the d<sub>z<sup>2</sup></sub> or the d<sub>x<sup>2</sup>-y<sup>2</sup></sub> orbitals. Jahn and Teller proved that such a doubly degenerate arrangement is unstable, thus a structural distortion occurs in order to remove the degeneracy. In the Jahn-Teller elongated Mn(III) ions described in chapter 2, the four equatorial bonds (that lie along the lobes of the d<sub>x<sup>2</sup>-y<sup>2</sup></sub> orbital) are shorter than in a perfect octahedron, while the two axial bonds (that lie along the lobes of the d<sub>z<sup>2</sup></sub> orbital), are longer. Due to the fact that these bonds are lengthened, an electron in the d<sub>z<sup>2</sup></sub> orbital will experience less coulombic repulsion with the (axially bonded) ligand lone pairs than it would with those of the equatorially bonded ligands if it occupied the d<sub>x<sup>2</sup>-y<sup>2</sup></sub> orbital. The e<sub>g</sub> electron thus occupies the more stable d<sub>z<sup>2</sup></sub> orbital in these Jahn-Teller elongated Mn(III) ions (Figure 29).

A much less common type of distortion that Mn(III) ions can exhibit is known as Jahn-Teller compression. This type of distortion *shortens* the axial bonds, while lengthening the equatorial bonds. In this scenario, the e<sub>g</sub> electron resides in the d<sub>x<sup>2</sup>-y<sup>2</sup></sub> orbital, as it is lower in energy than the d<sub>z<sup>2</sup></sub> orbital (Figure 29). One of the reasons for the predominance of Jahn-Teller elongated octahedral Mn(III) complexes is due to the symmetry allowed mixing of the 3d<sub>z<sup>2</sup></sub> orbital with the empty 4s orbital, leading to greater stability [137]. The unusual occurrence of a compressed Mn(III) ion may be due to steric strain imposed by the coordinating ligands [138].

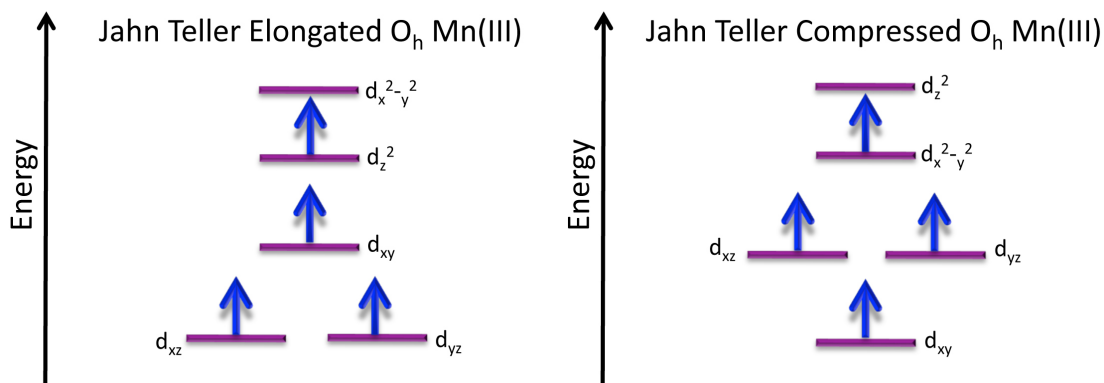


**Figure 29.** Schematic diagram showing the relative energies (not to scale) of the 3d orbitals in a Jahn-Teller elongated octahedral Mn(III) ion (left), and a Jahn-Teller compressed octahedral Mn(III) ion (right).

### 3.1.2 Relationships between magnetic coupling and Jahn-Teller effects

In chapter 2 we illustrated how the relative orientation of the Jahn-Teller axes influences the sign and strength of the magnetic exchange interaction ( $J$ ) in bis- $\mu$ -alkoxide bridged Mn(III) dimers. During our thorough literature search of all complexes of this type, not a single complex exhibiting Jahn-Teller compression was encountered, highlighting the rarity of this type of distortion. However, several Mn(III) dimers possessing the ‘( $\mu$ -oxo)bis( $\mu$ -carboxylato)dimanganese(III)’ core (Figure 30) have been reported to exhibit Jahn-Teller compression of both metal ions [124], [139–141]. Interestingly, these dimers exhibit weak ferromagnetic, or negligibly small antiferromagnetic ( $J = -0.2 - -0.7 \text{ cm}^{-1}$ ) interactions between the Mn(III) centres. This is partially due to the absence of electron density in the  $3d_z^2$  orbital of each ion, both of which point their lobes towards the single  $\mu$ -oxo bridge [139]. Due to the fact that the carboxylato bridges separate the magnetic centres by three atoms, the  $\mu$ -oxo bridge is mainly responsible for the superexchange interaction in these complexes [139]. A direct comparison of the magnetic exchange interaction in compressed ( $\mu$ -oxo)bis( $\mu$ -carboxylato)dimanganese(III) complexes with the Jahn-Teller elongated versions is not straightforward. This is due to the fact that the Jahn-Teller axis of the distortion possesses a different orientation in each type of complex; the compression axis goes through the bridging oxide, while the elongation axis passes through a carboxylate oxygen (Figure 30). In the elongated versions, the  $d_{x^2-y^2}$  orbital points its lobes towards the  $\mu$ -oxo bridge. Since this orbital is empty (akin to the  $d_z^2$  orbital in the compressed complexes), weak net interactions are also observed, although they are usually antiferromagnetic in nature [142–146].

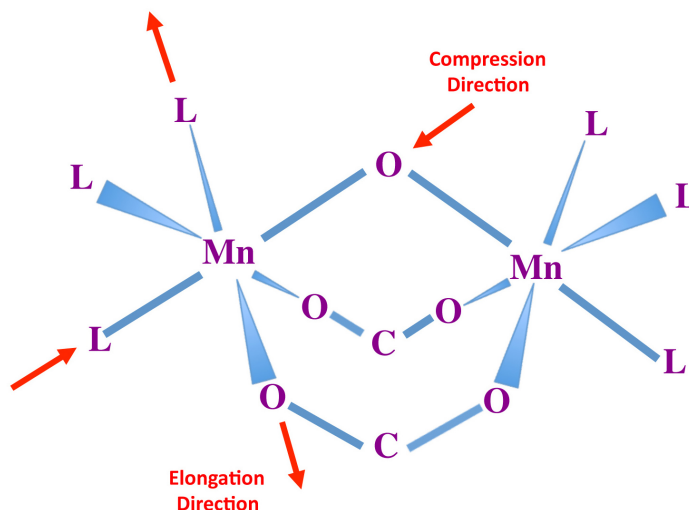


**Figure 30.** Schematic of the ( $\mu$ -oxo)bis( $\mu$ -carboxylato)dimanganese(III) core showing the axes of distortion for both elongated and compressed  $[\text{Mn(III)}_2]$  complexes.

The Cu(II) ion, being a  $d^9$  system ( $t_{2g}^6 e_g^3$ ) is also subject to Jahn-Teller distortion. In 2004 a very interesting comparative study was published highlighting how a change in distortion (compression vs elongation) can lead to a switch in the net exchange interaction (ferro- vs antiferromagnetic) [147]. The two Cu(II) dimers reported in this study possess the same core and their axes of distortion are in the same orientation; the only difference being the type of distortion. In the elongated Cu(II) dimer ( $[\text{Cu}_2(\text{dpyam})_2(\mu\text{-C}_2\text{O}_4)(\text{NO}_3)_2(\text{DMF})_2]$ , (dpyam = di-2-pyridylamine)), the electron pair occupies the lower energy  $d_z^2$  orbital while the unpaired electron resides in the  $d_{x^2-y^2}$  orbital. As the  $d_{x^2-y^2}$  orbital of each Cu(II) ion points its lobes toward the oxygen atoms of the oxalato bridge, an antiferromagnetic superexchange involving the two half-filled  $d_{x^2-y^2}$  orbitals dictates the overall magnetic coupling between the two Cu(II) ions. In the compressed complex ( $[\text{Cu}_2(\text{dpyam})_4(\mu\text{-C}_2\text{O}_4)](\text{PF}_6)_2(\text{H}_2\text{O})_2$ ) the opposite scenario is observed, and the  $d_z^2$  is the magnetic orbital in each Cu(II) ion. These orbitals are perpendicular to the bridging plane, leading to negligible overlap with ligand orbitals. The net magnetic interaction in this compressed complex is thus ferromagnetic.

In another study published in 2001 [148], the exchange interactions of the complexes  $\text{K}_2\text{Cu(II)F}_4:\text{Mn(II)}$  and  $\text{KZnF}_3:\text{Cu(II)-Mn(II)}$  are compared. Both compounds possess the same linear Cu(II)–F–Mn(II) unit, however, the two systems exhibit magnetic coupling strengths that are considerably different. The exchange interaction was found to be  $J = -65 \pm 5 \text{ cm}^{-1}$ , for  $\text{KZnF}_3:\text{Cu(II)-Mn(II)}$  [149] which is about two

times larger than that for  $\text{K}_2\text{Cu(II)F}_4\text{:Mn(II)}$ ;  $J = -26 \pm 1 \text{ cm}^{-1}$  [150]. This is attributed to the Jahn-Teller distortion of the Cu(II) ion; compression is observed in  $\text{KZnF}_3\text{:Cu(II)-Mn(II)}$  while elongation is observed in  $\text{K}_2\text{CuF}_4\text{:Mn(II)}$ . As the axis of distortion runs along the Cu(II)–F–Mn(II) direction in both complexes, it is possible to make a direct comparison. It was concluded that the main contribution to the observed magnetic coupling in  $\text{KZnF}_3\text{:Cu(II)-Mn(II)}$  is the Cu(II)( $d_z^2$ )–Mn(II)( $d_z^2$ ) interaction which is strongly antiferromagnetic due to the unpaired electron residing in the  $d_z^2$  orbital of the Jahn-Teller compressed Cu(II) ion. To explore this further, the elongated version of  $\text{KZnF}_3\text{:Cu(II)-Mn(II)}$  was modeled by Xiao-Yu et al. and the resultant exchange coupling was calculated as  $J \sim -0.05 \text{ cm}^{-1}$  [148].

In this chapter, we compare the magnetic interaction of two Cu(II)–Mn(III) dimers; one novel complex constructed using 2,2'-biphenol ( $\text{LH}_2$ ) ( $[\text{MnCu(L)}_2(\text{py})_4](\text{ClO}_4)\cdot\text{MeOH}$  – complex **6**), of which we report the synthesis and structural characterization, and one previously reported by Oshio et al built using the ligand 5-bromo-2-salicylideneamino-1-propanol ( $\text{H}_2\text{5-Br-sap}$ ) [151]. Surprisingly, our novel dimer possesses a Mn(III) ion in a Jahn-Teller compressed environment which is antiferromagnetically coupled to the Cu(II) ion ( $S = 3/2$ ,  $J_{\text{CuMn}} = -33.4 \text{ cm}^{-1}$ ), while the complex synthesized by Oshio et al. possesses an elongated Mn(III) ion which is ferromagnetically coupled to the Cu(II) ion ( $S = 5/2$ ,  $J_{\text{CuMn}} = +78 \text{ cm}^{-1}$ ). The Cu(II) and Mn(III) ions in both dimers are linked via alkoxide bridges, the Cu(II) ions possess square planar geometry, and the M···M distances and M-OR-M bond angles are comparable, thus a direct comparison between the exchange interactions in the two complexes can be made. In addition, we use SQUID magnetometry, DFT and high-field and high-frequency EPR to determine the zero-field splitting parameter of the compressed Mn(III) ion ( $D$  – see section 1.6). In Jahn-Teller compressed Mn(III) ions, the  $D$  parameter is always positive [152–154], whereas in elongated Mn(III) ions this value is negative [155], [156], with the exception of  $\text{trans-}[\text{Mn(III)(cyclam)}]_2\text{I}$  (cyclam = 1, 4, 8, 11-tetraazacyclotetradecane) [157]. We have used DFT to examine the spin-orbit coupling excitations (discussed in section 1.6) of the Mn(III) ion in order to rationalize the observed positive ZFS parameter. In this chapter we also report the synthesis and characterization of an isostructural Cu(II)–Mn(III) dimer ( $[\text{MnCu(L)}_2(4\text{-pic})_4](\text{ClO}_4)(\text{LH}_2)$  – complex **7**) and an analogous homometallic  $[\text{Cu(II)}_2]$  complex ( $[\text{Cu}_2(\text{LH})_2(3\text{-pic})_4](\text{ClO}_4)_2\cdot 2\text{EtOH}$  – complex **8**)

## 3.2 Results and Discussion

### 3.2.1 Structural Descriptions

Complex **6**  $[\text{MnCu}(\text{L})_2(\text{py})_4](\text{ClO}_4)\cdot\text{EtOH}$  (Figure 31) is readily prepared *via* the reaction of  $\text{Mn}(\text{II})(\text{ClO}_4)_2\cdot 6\text{H}_2\text{O}$ , anhydrous  $\text{Cu}(\text{I})\text{Cl}$ , 2,2'-biphenol and  $\text{NEt}_4(\text{OH})$  in an EtOH / pyridine solvent mixture. The resultant green / black solution, upon filtration and slow evaporation, gives rise to X-ray diffraction quality crystals of **6** in ~20% yield that crystallize in the triclinic space group P-1 (see Table 8 for crystallographic data). The structure of the cation in **6** comprises a single distorted square planar Cu(II) ion (Cu1) linked to a single six coordinate Jahn-Teller compressed Mn(III) ion (Mn1) by two bridging  $\text{O}_{\text{phen}}$  donor atoms (Mn1-O1-Cu1, 99.62°; Mn1-O3-Cu1, 101.10°) belonging to two distinct doubly deprotonated 2,2'-biphenolate ( $\text{L}^{2-}$ ) ligands. Their remaining  $\text{O}_{\text{phen}}$  atoms (O2 and O4) are terminally

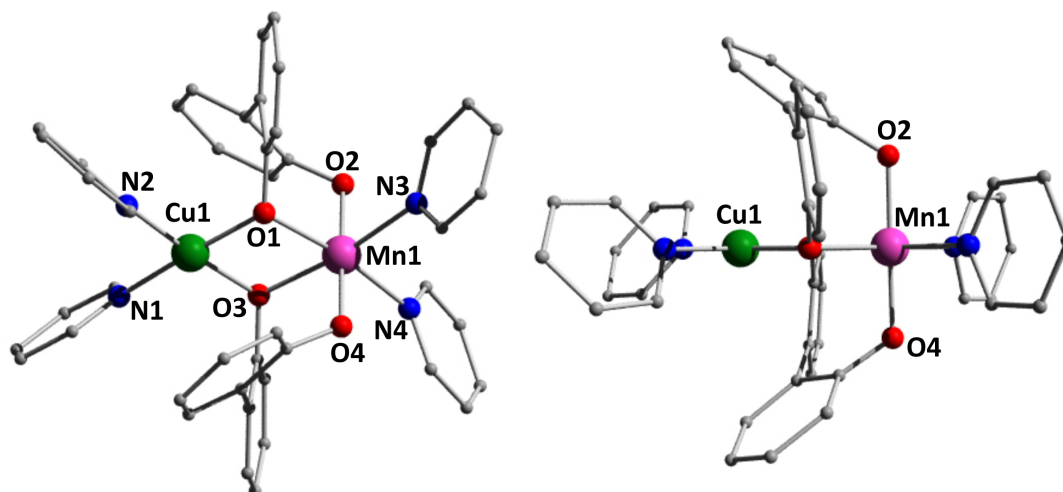


**Figure 31.** Molecular structure of the cationic heterobimetallic unit in **6** as viewed off-set (left) and perpendicular (right) to the Jahn-Teller compressed axis of the Mn(III) ion. Colour code: green (Cu), purple (Mn), red (O), blue (N) and grey (C). Hydrogen atoms and counter anions have been omitted for clarity.

bonded, providing the short axial bonds to the sole Mn(III) ion that define the Jahn-Teller compressed axis (Mn1-O2, 1.879 Å; Mn1-O4, 1.870 Å). The longer equatorial bonds range between 2.053 Å (Mn1-O3) and 2.209 Å (Mn1-N4). The “free” axial sites of the square planar Cu(II) ion are blocked by the presence of the phenyl rings of the rather twisted  $\text{L}^{2-}$  ligands ( $\text{Cu}\cdots\text{Ph}(\text{centroid}) = 3.559$  and 3.578 Å); indeed the dihedral (torsion) angles between the Ph rings on the same ligand are 49.86° [C5-C8] and 51.60° [C17-C20]. Four terminal pyridine ligands complete the coordination spheres at the six coordinate Mn(III) centre (N3 and N4) and at the four coordinate

Cu(II) site (N1 and N2) affording  $\{\text{Mn(III)O}_4\text{N}_2\}$  and  $\{\text{Cu(II)O}_2\text{N}_2\}$  coordination spheres, respectively. The resultant  $\{\text{Cu(II)Mn(III)(L)}_2(\text{py})_4\}^+$  cation is charge balanced by the presence of a single  $\text{ClO}_4^-$  ion. Despite many efforts, the modelling of an EtOH solvent molecule of crystallization gives rise to a short C-C bond (C50-C51) length. In order to confirm that this electron density was indeed due to an EtOH solvent molecule, a SQUEEZE [158] analysis was carried out. The result (42 electrons per void with 1 void in cell) confirmed the partial occupancy of approximately 0.8 EtOH molecules per  $[\text{CuMn(L)}_2(\text{py})_4]$  unit in **6**. To rule out the possibility of any dynamic Jahn-Teller effects, a crystal structure of complex **6** was collected at 250 K (as opposed to 150 K). The same bond lengths were also observed in this structure. The individual cationic  $\{\text{Cu(II)Mn(III)(L)}_2(\text{py})_4\}^+$  cluster units pack in superimposable rows along the *a* unit cell direction and are separated at a  $\text{M}\cdots\text{M}$  distance of  $\sim 12$  Å. These 1-D rows pack in the common brickwork formation in the *bc* plane (Figure 32).

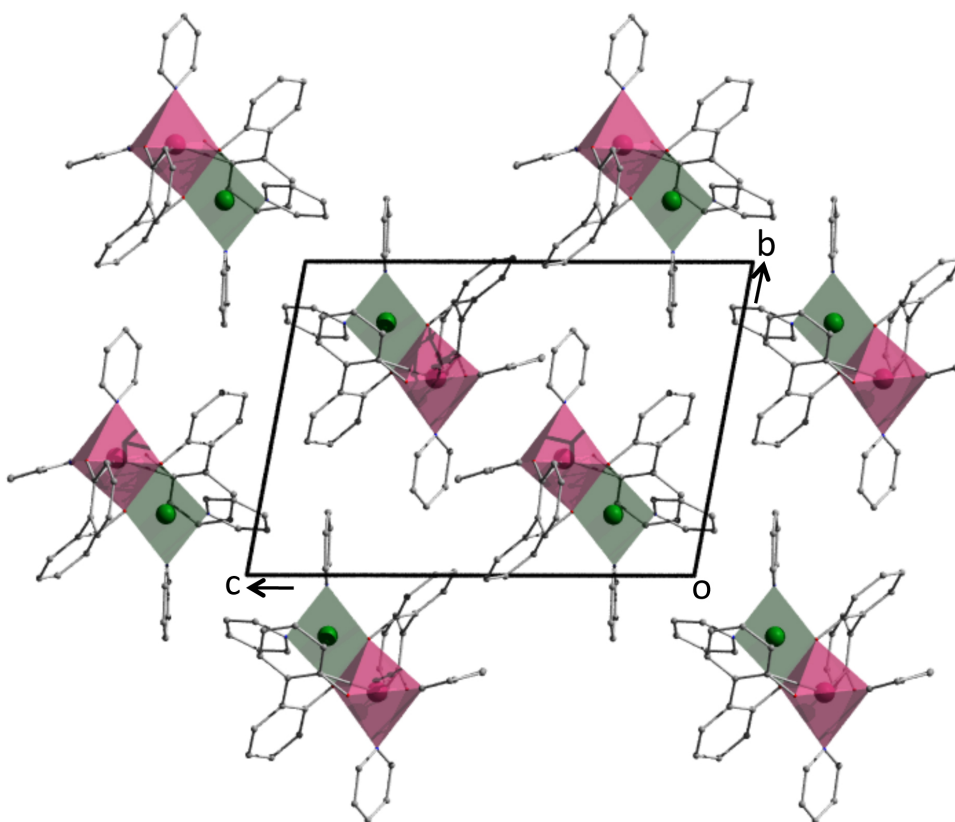


**Figure 32.** Packing diagram of **6** as viewed along the *a* direction of the unit cell. The EtOH solvent molecules of crystallization and  $\text{ClO}_4^-$  counter anions have been omitted for clarity.

The replacement of pyridine with 4-picoline (in the synthesis of **6**) leads to the formation of  $[\text{Mn(III)Cu(II)(L)}_2(4\text{-pic})_4](\text{ClO}_4)(\text{LH}_2)$  (**7**) (Figure 33). The structure of the cation in **7** is almost identical to that of **6**, comprising a single distorted square planar Cu(II) ion (Cu1) linked to a single six coordinate Jahn-Teller compressed Mn(III) ion (Mn1) by two bridging  $\text{O}_{\text{phen}}$  donor atoms ( $\text{Mn1-O1-Cu1} = 101.94^\circ$ ;  $\text{Mn1-O3-Cu1} = 99.35^\circ$ ) belonging to two distinct doubly deprotonated  $\text{L}^{2-}$  ligands. Akin to complex **6**, the remaining  $\text{O}_{\text{phen}}$  atoms (O2 and O4) are terminally bonded along the Jahn-Teller compressed axis ( $\text{Mn1-O2} = 1.884 \text{ \AA}$ ;  $\text{Mn1-O4} = 1.853 \text{ \AA}$ ). The longer equatorial bonds range between  $2.032 \text{ \AA}$  ( $\text{Mn1-O1}$ ) and  $2.219 \text{ \AA}$  ( $\text{Mn1-N4}$ ). The +1 charge of the  $\{\text{Cu(II)Mn(III)(L)}_2(4\text{-pic})_4\}^+$  cationic unit is balanced by the presence of a single  $\text{ClO}_4^-$  anion. There are no solvent molecules in the lattice, although the unit cell contains highly disordered  $\text{LH}_2$  units (one per  $[\text{Mn(III)Cu(II)(L)}_2(4\text{-pic})_4]^+$  cation), which despite numerous efforts could not be modeled satisfactorily. Again, this was treated using the *PLATON SQUEEZE* routine [158]. The void region contained approximately 74 electrons, which indicates the partial occupancy of approximately 0.75  $\text{LH}_2$  molecules per formula unit.

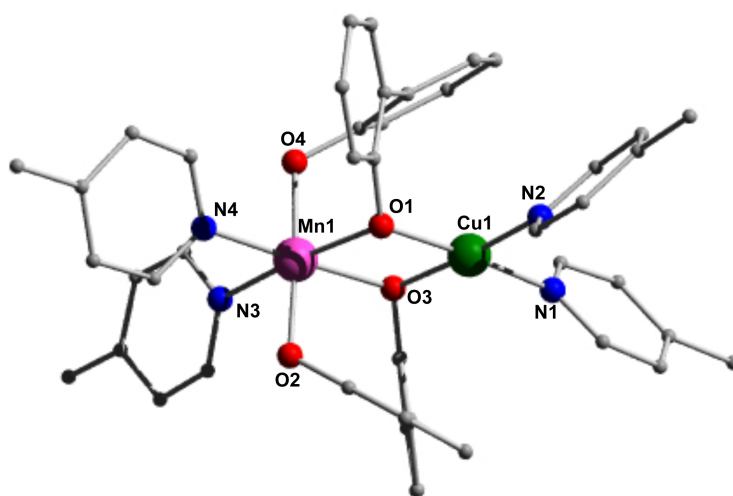


**Figure 33.** Molecular structure of the cationic heterobimetallic unit in **7**. Colour scheme as in Figure 31, hydrogen atoms are omitted for clarity.

The cationic  $\{\text{Cu(II)Mn(III)(L)}_2(4\text{-pic})_4\}^+$  dimeric units in **7** pack into superimposable rows along the  $b$  direction of the unit cell. These rows pack together in a zig-zag fashion along the  $a$  axis (Figure 34). Due to the isostructural nature of the  $\text{Mn(III)-(OR)}_2\text{-Cu(II)}$  core in **7** with that of **6**, magnetic studies on this complex were deemed unnecessary.

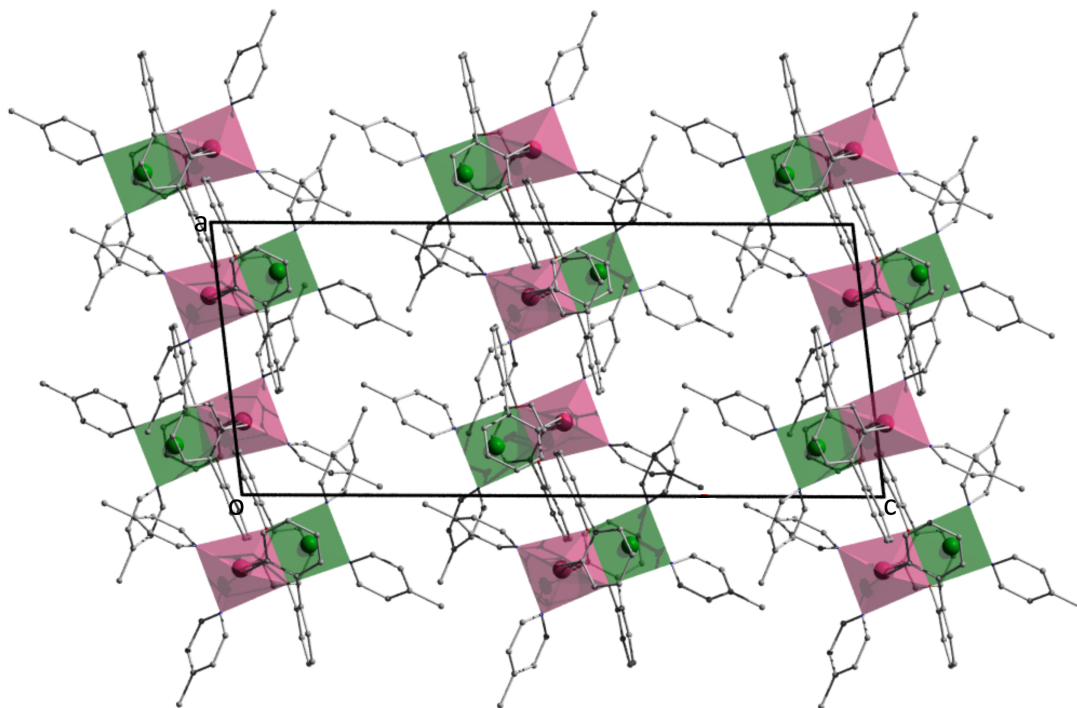


**Figure 34.** Packing diagram of **6** as viewed along the *b* direction of the unit cell.  $\text{ClO}_4^-$  counter anions and disordered  $\text{LH}_2$  units have been omitted for clarity.

The homometallic Cu(II) analogue to complexes **6** and **7** is readily prepared *via* the reaction of  $\text{Cu(I)Cl}$ ,  $\text{LH}_2$  and  $\text{NMe}_4(\text{OH})$  in an  $\text{EtOH} / 3\text{-picoline}$  solvent mixture. The copper dimer  $[\text{Cu}_2(\text{LH})_2(3\text{-pic})_4](\text{ClO}_4)_2 \cdot 2\text{EtOH}$  (**8**), shown in Figure 35, crystallizes in the monoclinic spacegroup  $\text{P}2_1/c$ . The cationic dimeric unit in **8** comprises two symmetrically equivalent square based pyramidal Cu(II) ions linked via two  $\text{O}_{\text{phen}}$  donor atoms ( $\text{Cu1-O1-Cu1}' = 102.1^\circ$ ) belonging to two *singly* deprotonated  $\text{LH}^-$  ligands. The protonated oxygen atoms of the two  $\text{LH}^-$  moieties coordinate axially to one Cu(II) ion each ( $\text{Cu1-O2} = 2.372 \text{ \AA}$ ). The remaining two equatorial bonding positions of each Cu(II) ion are occupied by the nitrogen atoms two 3-picoline ligands. The resultant  $\{\text{Cu(II)}_2(\text{LH})_2(3\text{-pic})_4\}^{2+}$  cation is charge balanced by the presence of two  $\text{ClO}_4^-$  ions, both of which hydrogen bond through O3 to the protons of the hydroxyl groups on  $\text{LH}^-$  moieties ( $\text{H1}\cdots\text{O3} = 2.015 \text{ \AA}$ ). Two  $\text{EtOH}$  solvent molecules of crystallization per cationic unit reside in the crystal structure and hydrogen bond through their hydroxyl groups to the perchlorate oxygen atoms ( $\text{H7}\cdots\text{O6} = 2.677 \text{ \AA}$ ). In complexes **6-8** both the singly and doubly deprotonated forms of  $\text{LH}_2$  adopt the  $\eta^1:\eta^2,\mu$ -bridging motif. This bridging mode is quite different from the chelating mode observed in the  $[\text{Mn(III)}_2]$  complexes of chapter 2.

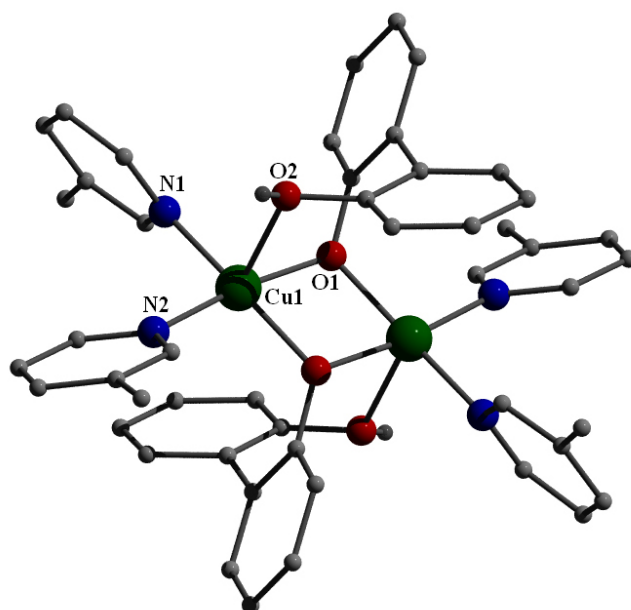


**Figure 35.** Molecular structure of the cationic unit in **8**. With the exception of the  $\text{LH}^-$  hydroxyl protons, hydrogen atoms have been omitted for clarity. Colour scheme as in Figure 31.

Figure 36 shows the crystal packing of complex **8** as viewed along the  $a$  axis of the unit cell. The superimposable rows that run along the  $a$  axis pack in the common brickwork formation in the  $bc$  plane (Figure 36).

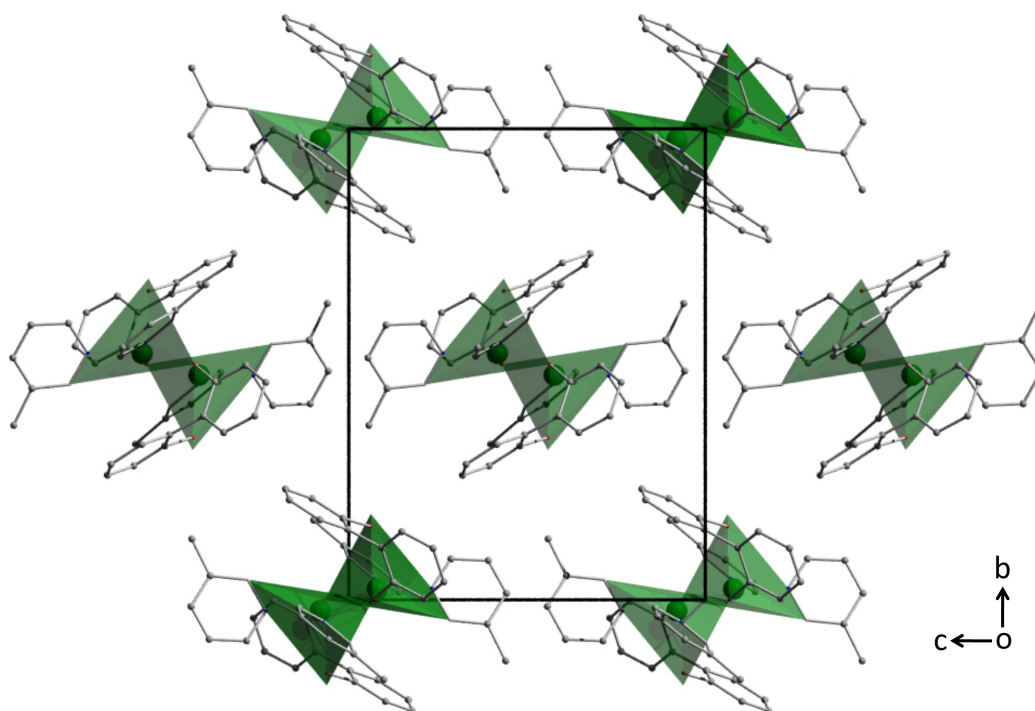


**Figure 36.** Crystal packing diagram of complex **8** as viewed along the  $a$  axis of the unit cell. The EtOH solvent molecules of crystallization and  $\text{ClO}_4^-$  counter anions have been omitted for clarity.

Although a number of Cu(II)-Mn(II) dinuclear complexes are known in the literature [159–162], an extensive CSD search reveals that **6** and **7** represent two members of an elite group that possess the Cu(II)-Mn(III) oxidation state distribution [151], [163], [164], and are indeed the first to possess a Mn(III) ion exhibiting a Jahn-Teller compression.

**Table 8.** Crystal data for complexes **6-8**

	(6)	(7)	(8)
Formula <sup>a</sup>	C <sub>45</sub> H <sub>40</sub> N <sub>4</sub> O <sub>9</sub> CuMn	C <sub>60</sub> H <sub>54</sub> ClCuMnN <sub>4</sub> O <sub>10</sub>	C <sub>52</sub> H <sub>58</sub> Cl <sub>2</sub> Cu <sub>2</sub> N <sub>4</sub> O <sub>14</sub>
<i>M<sub>w</sub></i>	934.74	1145.03	1161.04
Crystal System	Triclinic	Monoclinic	Monoclinic
Space group	P-1	P2 <sub>1</sub> /c	P2 <sub>1</sub> /c
<i>a</i> /Å	10.686(2)	11.780(2)	12.179(2)
<i>b</i> /Å	12.392(3)	16.071(3)	17.116(3)
<i>c</i> /Å	17.360(4)	27.552(6)	12.956(3)
<i>α</i> /°	97.99(3)	90.00	90.00
<i>β</i> /°	100.99(3)	96.77(3)	92.27(3)
<i>γ</i> /°	101.10(3)	90.00	90.00
<i>V</i> /Å <sup>3</sup>	2177.2(8)	5179.68	2698
<i>Z</i>	2	4	2
<i>T</i> /K	150(2)	150(2)	150(2)
<i>λ</i> <sup>b</sup> /Å	0.7107	0.7107	0.7107
<i>D<sub>c</sub></i> /g cm <sup>-3</sup>	1.426	1.229	1.429
<i>μ</i> (Mo-Kα)/ mm <sup>-1</sup>	0.899	0.756	0.955
Meas./indep.( <i>R</i> <sub>int</sub> ) refl.	7945 / 4906 (0.0553)	9453 / 3877 (0.1068)	4939 / 3422 (0.0411)
wR2 (all data)	0.2134	0.2403	0.1200
<i>R</i> <sup>d,e</sup>	0.0741	0.0893	0.0507
Goodness of fit on <i>F</i> <sup>2</sup>	1.023	0.912	1.092

### 3.2.2 SEM Images

Interestingly, the presence of solvent molecules of crystallization in complexes **6** and **8** is perhaps the cause of observed cracks in the crystals upon prolonged exposure to the atmosphere, as seen in the SEM images of Figure 37. Complex **7** possesses no solvent molecules in the lattice, and exhibits negligible cracking under the same conditions.

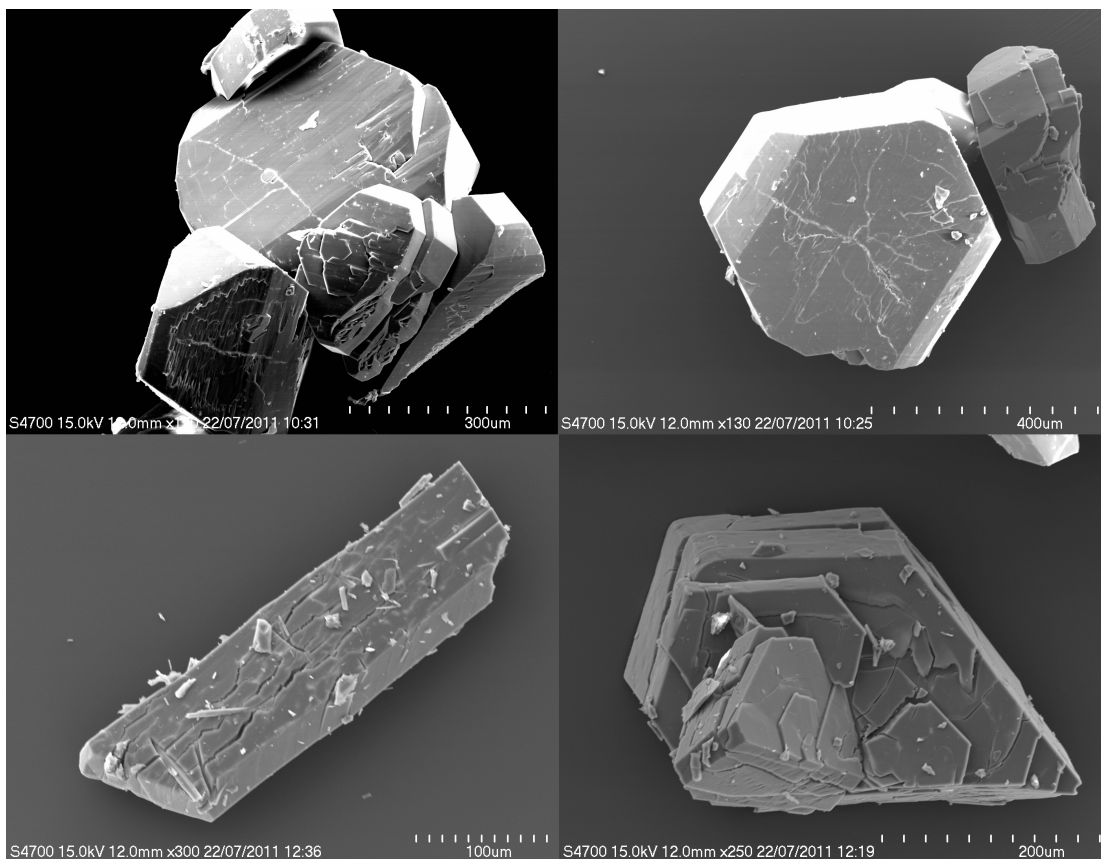


**Figure 37.** SEM images showing the crystals of **6** (bottom left), **7** (top left and right) and **8** (bottom right).

### 3.2.3 SQUID Magnetometry

Dc magnetic susceptibility measurements were performed on a powdered microcrystalline sample of **6** in an applied magnetic field of 0.1 T and in the temperature range 250 to 5 K. The results are plotted as the  $\chi_M T$  product vs.  $T$  in Figure 38. The high temperature  $\chi_M T$  value of  $2.27 \text{ cm}^3 \text{ K mol}^{-1}$  is lower than that expected from the spin-only value ( $3.38 \text{ cm}^3 \text{ K mol}^{-1}$ ) for non-interacting high-spin Mn(III) ( $3d^4$ ) and Cu(II) ( $3d^9$ ) ions, assuming  $g = 2$ . This reflects the existence of a strong intra-molecular antiferromagnetic interaction in **6**. The  $\chi_M T$  product decreases in a sigmoidal-like fashion with decreasing temperature until it reaches a plateau of around  $1.75 \text{ cm}^3 \text{ K mol}^{-1}$  in the 45 to 20 K temperature interval. The  $\chi_M T$  product at this low temperature plateau is consistent with the existence of a thermally isolated  $S = 3/2$  spin-state. For the modelling of the  $\chi_M T$  product we used spin-Hamiltonian:

$$\hat{H} = -2J\hat{S}_{Cu} \cdot \hat{S}_{Mn} + D_{Mn}[\hat{S}_{z,Mn}^2 - S_{Mn}(S_{Mn} + 1)/3] + \mu_B \sum_{i=Cu,Mn} \{g_i \vec{B}_i \cdot \hat{S}_i\}$$

where  $J$  is the Cu(II)-Mn(III) isotropic exchange interaction parameter,  $\hat{S}$  is a spin-operator,  $D_{\text{Mn}}$  is the single-ion uniaxial anisotropy of Mn(III),  $S = 2$  is the single-ion spin of Mn(III),  $\mu_{\text{B}}$  is the Bohr magneton,  $g_{\text{Mn}} = 2.0$  and  $g_{\text{Cu}} = 2.1$  are the employed  $g$ -factors of the Mn(III) and Cu(II) ions, respectively, and  $\vec{B}$  is the applied magnetic field vector. The  $\chi_{\text{M}}T$  product of **6** was numerically fitted, by use of the simplex algorithm [165], to the spin-Hamiltonian (above) by numerical diagonalisation of the spin-Hamiltonian matrix of dimension 10 by 10. While fitting the  $\chi_{\text{M}}T$  product, it became apparent that inclusion of the Mn(III) single-ion anisotropy term does not significantly improve the quality of fit, as measured by the  $\chi^2$  statistics. This is as expected since anisotropy effects are predominant at very low temperatures and thus, do not weight significantly in the fitting of the  $\chi_{\text{M}}T$  product. The best-fit parameter of the spin Hamiltonian (above) to the  $\chi_{\text{M}}T$  product of **6** was  $J = -33.4 \text{ cm}^{-1}$ , affording an  $S = 3/2$  spin ground state with the  $S = 5/2$  excited state some  $167 \text{ cm}^{-1}$  higher in energy. The determined strong antiferromagnetic interaction is consistent with the above qualitative description of the thermal dependence of the  $\chi_{\text{M}}T$  product of **6**. In addition, intermolecular interactions were taken into account in the frame of mean-field theory, by use of the Curie-Weiss temperature  $\theta$ . A Curie-Weiss constant of  $\theta = -0.9 \text{ K}$ , was necessary to reproduce the small drop of the  $\chi_{\text{M}}T$  product below  $\sim 20 \text{ K}$ .

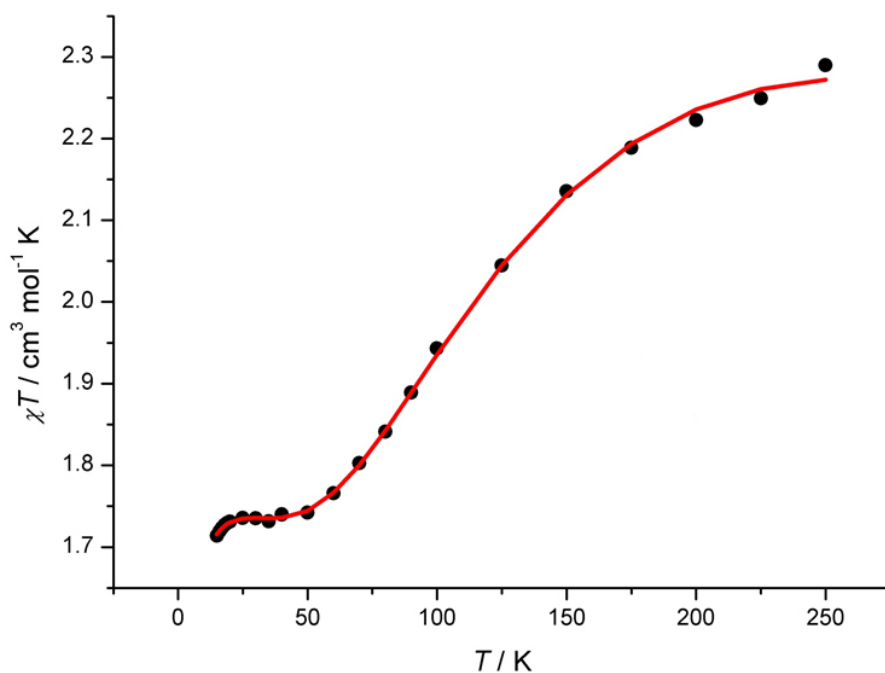


**Figure 38.** Plot of the  $\chi_{\text{M}}T$  product of **6** vs.  $T$  in the 250 - 5 K temperature range in an applied field of 0.1 T. The solid red line is the best-fit of the data with  $J = -33.4 \text{ cm}^{-1}$  as described in the text.

In order to determine, by magnetisation measurements, the single-ion axial anisotropy parameter for the Mn(III) centre in **6**, variable-temperature-variable-field magnetisation measurements were performed in the  $T = 2.0\text{--}7.0$  K and  $B = 0.5\text{--}5.0$  T temperature and dc magnetic field ranges, respectively. These experimental data are presented as reduced magnetisation ( $M/N\mu_B$  vs.  $\mu_B B/kT$ , with  $N$  being Avogadro's number and  $k$  the Boltzmann constant) in Figure 39. They were again numerically fitted, by use of the simplex algorithm [165], to the same spin-Hamiltonian, by numerical diagonalisation of the 10 by 10 spin-Hamiltonian matrix. The best fit parameter, keeping  $J$  fixed to  $J = -33.4$   $\text{cm}^{-1}$  (as determined by fitting the  $\chi_M T$  product), was  $D_{\text{Mn}} = +4.95$   $\text{cm}^{-1}$ . Forcing the  $D_{\text{Mn}}$  parameter to vary only in the negative-values semi-axis, leads to  $\chi^2$  values that are two orders of magnitude higher than those obtained by letting  $D_{\text{Mn}}$  vary freely to give  $D_{\text{Mn}} = +4.95$   $\text{cm}^{-1}$ . The positive value of  $D_{\text{Mn}}$  is in good agreement with the axially compressed nature of the coordination sphere of the Mn(III) ion [152–154].

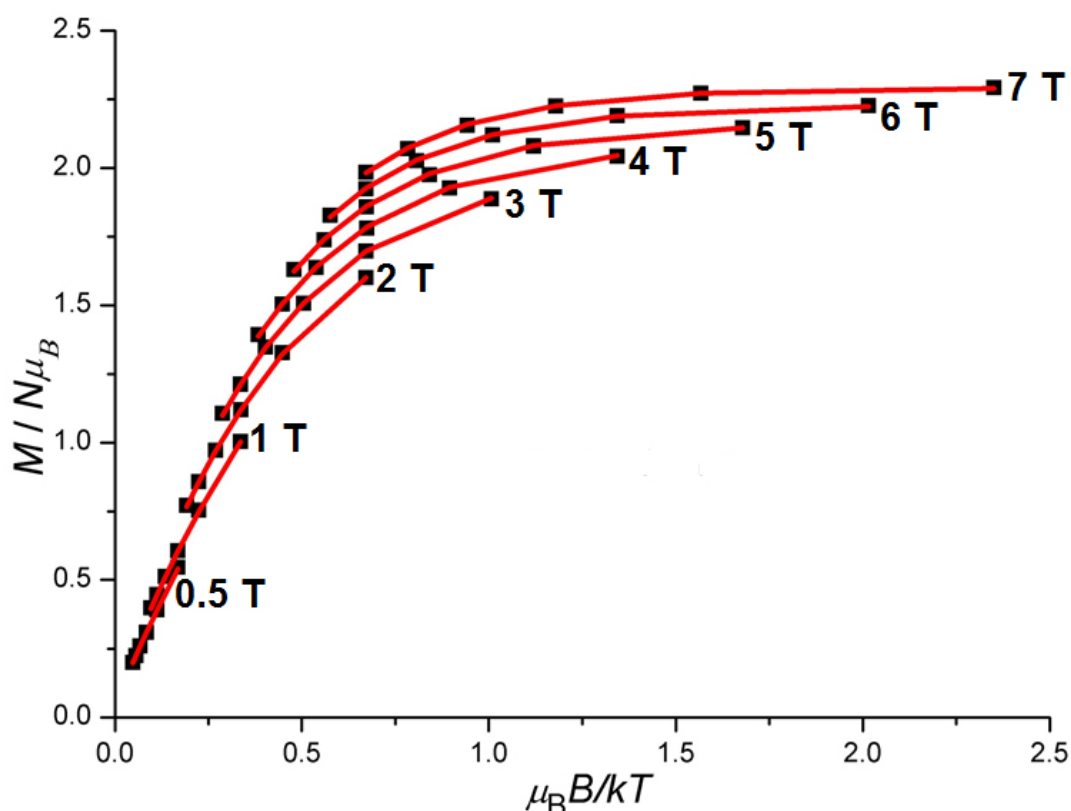


**Figure 39.** Plot of reduced magnetisation of **6** in the 2.0 to 7.0 K temperature range and at the indicated field strengths. The solid red lines are the best-fit of the data with  $J$  fixed to  $-33.4$   $\text{cm}^{-1}$  and  $D_{\text{Mn}} = +4.95$   $\text{cm}^{-1}$ , as described in the text.

Magnetic susceptibility measurements performed on the [Cu(II)<sub>2</sub>] dimer (**8**), reveal an antiferromagnetic interaction between the Cu(II) ions so strong, that signal loss occurs upon decreasing the temperature. In general, antiferromagnetic coupling is observed in alkoxide bridged Cu(II) dimers where the bridging angle is greater than 97° [166].

### 3.2.4 EPR Spectroscopy

Powder EPR data were collected for complex **6** in order to determine the magnetic anisotropy of the dimer. Given the spin states of the constituent ions ( $S = 2$  and  $1/2$  for Mn(III) and Cu(II) respectively), one expects a half integer ground state spin of either  $S = 3/2$  or  $5/2$  for the dimer. The low-energy spectrum should thus consist of either two or three [*i.e.*  $(2S + 1)/2$ ] Kramers doublets, split by any associated magnetic anisotropy. Figure 40 displays representative frequency-dependent powder EPR spectra for complex **6** collected between 100.6 and 406 GHz at a relatively low temperature of 5 K. All of the labelled resonances persist to the lowest temperatures investigated (not shown), indicating that they involve transitions either within or from the lowest Kramers doublet. At frequencies below 200 GHz, the spectra are dominated by three strong resonance branches that we assign to the x, y and z-transitions within the ground-state Kramers doublet; these are marked by open red, blue and black circles, respectively. As can be seen in the frequency versus field map in Figure 41, the peak positions corresponding to these transitions each lie on simulated curves (*vide infra*) that intersect the origin, as expected for intra-Kramers transitions. At frequencies above 200 GHz, additional resonance branches appear at low fields (solid black squares and circles). As can be seen in Figure 41, these resonances all lie on lines/curves that meet at a unique finite-frequency offset on the zero-field axis. We thus assign them as inter-Kramers transitions, and the intercept on the ordinate corresponds exactly to the zero-field energy splitting between the two lowest Kramers doublets. We note that this splitting of  $381 \pm 5$  GHz is rather substantial for a complex comprised of just Mn(III) and Cu(II) ions. The solid circles in Figure 41 correspond to the usual  $\Delta M_S = \pm 1$  perpendicular-mode EPR transitions, while the solid squares correspond to  $\Delta M_S = \pm 2$  resonances (see below). The simulations assume that the applied field,  $B$ , is parallel to  $z$ . However, all three inter-Kramers components (*i.e.*  $B//x$ ,  $y$  and  $z$ ) generate  $\Delta M_S = \pm 1$  and  $\pm 2$  resonances at

similar locations, provided the applied field is relatively weak ( $< 3$  T), which may account for the appreciable intensity of the lowest field 406.4 GHz peak in Figure 40.

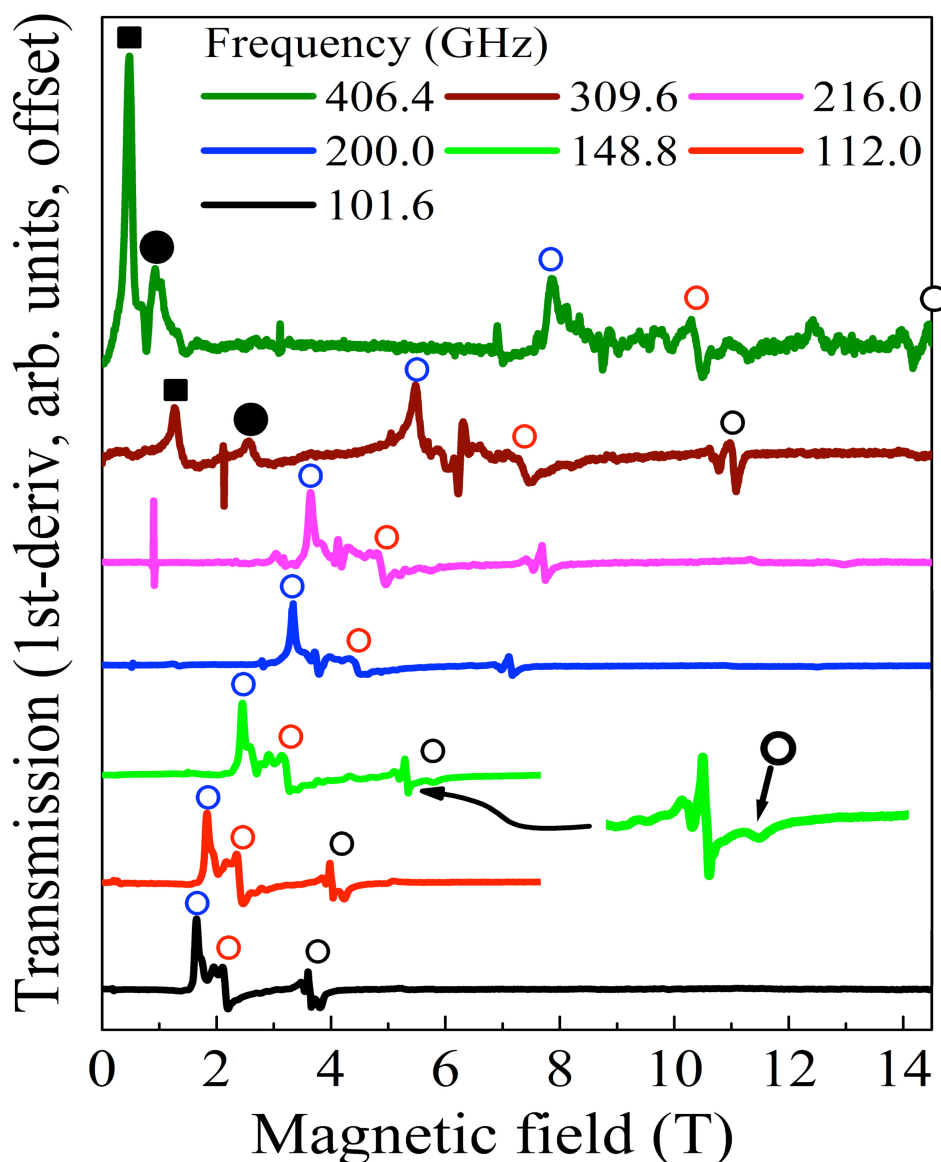


**Figure 40.** Representative frequency dependent powder EPR spectra collected at 5 K: the red, blue and black open circles denote the intra-Kramers  $x$ ,  $y$  and  $z$ -components of the spectra, while the solid circles ( $\Delta M_s = \pm 1$ ) and squares ( $\Delta M_s = \pm 2$ ) denote transitions between Kramers doublets; the inset displays an expanded portion of the 200 GHz spectrum in the vicinity of the  $z$ -component (see main text for explanation). The extremely sharp features seen in some of the spectra (e.g. at  $\sim 1$  T in the 216 GHz spectrum) correspond to known signals from oxygen adsorbed in the sample holder.

While analysis of susceptibility data enables reliable estimates of the exchange coupling within a simple spin system, especially a dimer, EPR measurements provide much more robust constraints on both the sign and magnitude of the magneto-anisotropy. The EPR data presented in Figure 41 clearly reveal the presence of a pair

of low-energy Kramers doublets. However, they do not rule out the possibility of a third higher-lying doublet. Thus, a determination of the ground state spin from the EPR data is not entirely straightforward. This would require careful analysis of much weaker transitions observed at elevated temperatures, and we do not pursue this here because the susceptibility measurements clearly indicate that the coupling within the dimer is antiferromagnetic. Therefore, in the following analysis, we assume that the ground state spin value is  $S = 3/2$ . In doing so, we will see that the obtained anisotropy is quite consistent with expectations, thus providing indirect confirmation of the  $S = 3/2$  ground state spin value.

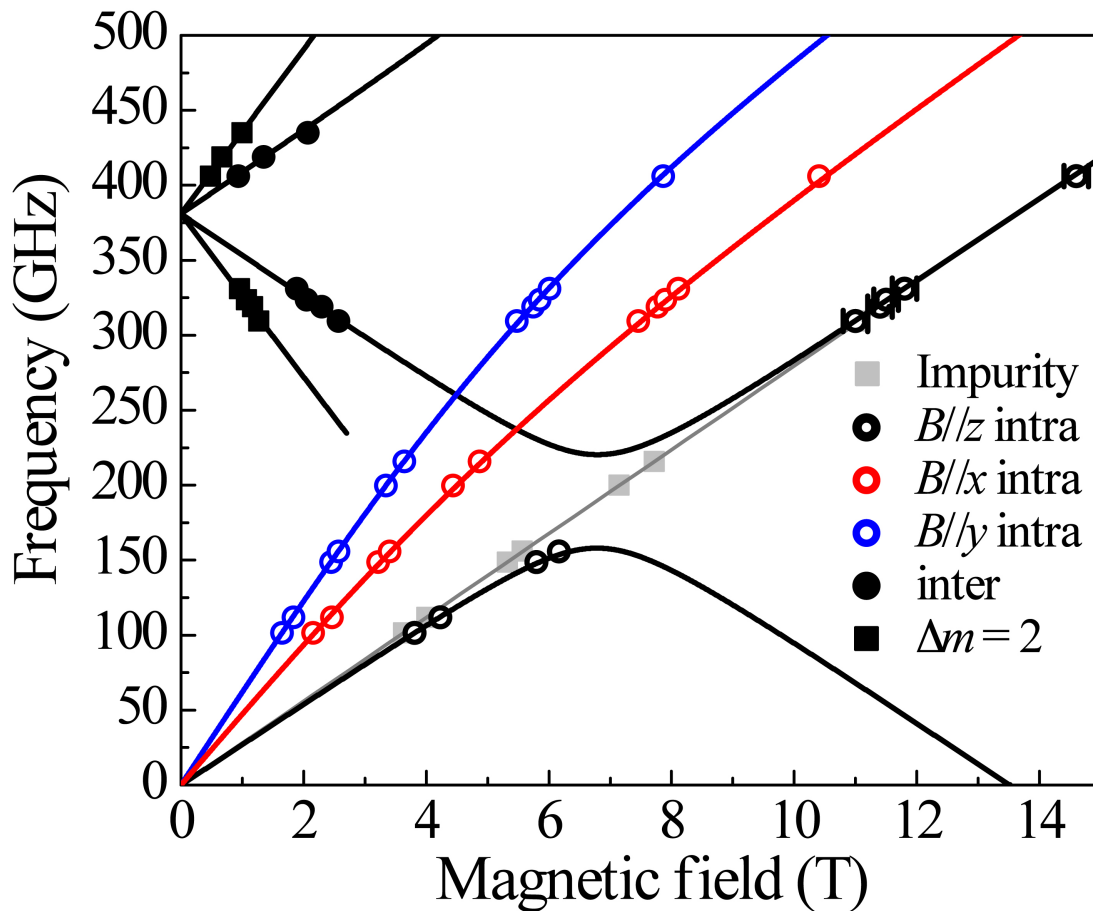


**Figure 41.** Plot of the frequency dependent EPR peak positions as a function of the applied magnetic field strength. The solid curves (same colour coding as the data) correspond to the simulations described in the main text. Note that the grey data points and the grey line correspond to an impurity signal with  $g = 2.003(2)$ .

We first turn our attention to the sign of the second-order axial zero-field splitting parameter  $D_S$  associated with the  $S = 3/2$  ground state. In the presence of easy-plane type anisotropy ( $D_S > 0$ ), the  $B//x$ - and  $y$ -components of the spectrum associated with the lowest Kramers doublet (red and blue circles, respectively, Figure 41) possess

effective  $g$ -values that are substantially larger than 2.00, *i.e.* slopes that substantially exceed 28 GHz/T as  $B \rightarrow 0$ ; meanwhile, the  $B//z$ -component has an effective  $g$ -value (slope) very close to 2.00 (or 28 GHz/T, denoted by the grey line in Figure 41). The opposite holds for the easy-axis case ( $D < 0$ ) [167], [168]. Thus, the powder EPR data clearly support the presence of an easy-plane type anisotropy ( $D > 0$ ), which one would expect in a Jahn-Teller compressed Mn(III) system, since this represents the main source of anisotropy within the dimer. The magnitude of  $D_S$  is approximately constrained by the intercept of the inter-Kramers resonance branches. For a purely axial system, this intercept corresponds exactly to  $2D_S$ , hence  $D_S \approx 381/2$  GHz =  $6.35$  cm<sup>-1</sup>. However, as can clearly be seen from Figures 40 and 41, there is a considerable splitting between the  $x$  and  $y$  components of the spectrum, signifying a rhombic distortion and, hence, a rhombic  $E_S$  parameter. In such situations,  $D_S$  can only be determined precisely *via* diagonalisation of the following effective spin Hamiltonian:

$$\hat{H}_S = D_S \hat{S}_z^2 + E_S (\hat{S}_x^2 - \hat{S}_y^2) + \mu_B \vec{B} \cdot \mathbf{g}_S \cdot \hat{S}$$

where  $\hat{S}$  represents the total spin operator and  $\hat{S}_i$  ( $i = x, y, z$ ) its components, the subscript  $S = 3/2$  defines the total spin-state on which the effective spin-Hamiltonian (2) is applied and  $g_S$  is the Landé tensor of the total spin-state  $S$ . The best simulation of the data in Figure 4 was obtained with the following parameters:  $D_S = +6.27$  cm<sup>-1</sup>,  $E_S = \pm 0.57$  cm<sup>-1</sup>,  $g_{S,x} = 1.97$ ,  $g_{S,y} = 1.97$  and  $g_{S,z} = 1.98$ . The main constraint on the  $E_S$  parameter is the splitting between the  $x$ - and  $y$ -components of the intra-Kramers transitions (red and blue curves in Figure 41), *i.e.* its value is well constrained. While one might expect a corresponding difference between  $g_{S,x}$  and  $g_{S,y}$ , this leads to an over parameterization of the model. Therefore, we have assumed these parameters to have the same value.

The transverse anisotropy ( $E$ ) leads naturally to an avoided-crossing between the  $m_S = -3/2$  and  $m_S = -1/2$  components of the two Kramers doublets, which meet at  $\sim 7$  T when  $B//z$ . It is this interaction that is the reason for the  $\sim 60$  GHz ( $2$  cm<sup>-1</sup>) gap between the inter- and intra-Kramers  $z$ -component resonance branches at  $\sim 7$  T in Figure 41 (solid black lines). Surprisingly, spectra recorded at frequencies close to 200 GHz (*e.g.* the blue curve in Figure 40) still show weak resonances in this gapped region of the  $B//z$  simulations. Closer inspection of the spectra reveals that the  $z$

component appears to consist of a narrow derivative (*i.e.* a sharp peak followed by a sharp minimum) superimposed on a broad dip; this contrasts the  $x$  and  $y$  components that each consist of a single feature, *i.e.* a peak for  $y$  and a shoulder for  $x$ , as expected for such a powder spectrum. The narrow and broad  $z$ -components are separately plotted in Figure 41 as grey squares and open black circles. The sharp components lie on a straight (grey) line passing through the origin, having a slope corresponding to  $g = 2.003(2)$ . At most frequencies, the broad dip lies very close to this line. However, one clearly sees that the broad component moves appreciably to the high-field side of the  $g = 2.003$  position (the sharp peak) as the frequency approaches the gapped region; the relevant portion of the 148.8 GHz spectrum has been enlarged in Figure 40 (green curve) to emphasize this point. Indeed, if one assumes that it is this broad dip that corresponds to the  $z$ -component of the dimer spectrum, one finds excellent agreement with the simulations in Figure 41. Meanwhile, we believe that the sharp component corresponds to an impurity phase within the powder, possibly containing isotropic Mn(II); this is often found to be the case in Mn-containing polynuclear clusters, and explains why a resonance is still observed in the gapped region of the  $B//z$  spectrum. In fact, it is notable that the 200 GHz spectrum exhibits only a sharp component, the broad dip appears to be absent, which is why an open circle is not included in Figure 41 for this frequency.

Due to the strong Cu(II)-Mn(III) exchange interaction ( $J \sim -33.4 \text{ cm}^{-1}$ ), we can make a reliable estimation of the anisotropy parameters associated with the individual ions using the projection method [169]. According to Kramers' theorem, any zero-field splitting interaction associated with the Cu(II) ion ( $S_{\text{Cu}} = 1/2$ ) is strictly forbidden; hence, the zero-field splitting parameters of the molecule are determined only by the anisotropy parameters of the Mn(III) ion. The projection method gives  $D_{S=3/2} = 1.4 D_{\text{Mn}}$ , where  $D_{S=3/2}$  and  $D_{\text{Mn}}$  are the anisotropy tensors of the molecule and the Mn(III) ion, respectively. Therefore, we estimate that  $D_{\text{Mn}} = +4.45 \text{ cm}^{-1}$  and  $E_{\text{Mn}} = \pm 0.41 \text{ cm}^{-1}$ . We note that these zero-field interaction parameters obtained *via* EPR data are in excellent agreement with the parameters obtained via the reduced magnetization measurements, and are consistent with values found for related Mn(III) compounds. Finally, we comment on the  $g$ -values obtained from the EPR measurements. Again, using projection methods, one can estimate that  $g_{S=3/2} = 1.2 g_{\text{Mn}} - 0.2 g_{\text{Cu}}$ .

Consequently, the obtained  $g$ -values for the molecule should be dominated by the Mn(III) ion, which is consistent with the obtained values that are very close to 2.00.

### 3.3 Magneto-structural correlation

The aforementioned ferromagnetic Cu(II)-Mn(III) dimer possessing an elongated Mn(III) ion reported by Oshio et al [151], of formula  $[\text{CuMnCl}(\text{5-Br-sap})_2(\text{MeOH})]$  will be referred to as complex **9** for our comparative study (Figure 42). Complexes **6** and **9** are structurally very similar. Both contain  $[\text{Cu}(\text{II})(\text{OR})_2\text{Mn}(\text{III})]$  magnetic cores (albeit with different R-groups), resulting in very similar Cu(II)-O(R)-Mn(III) bond angles;  $100.36^\circ$  (avg.) in **6**, and  $101.28^\circ$  in **9** (Mn-O2-Cu – see Figure 42). Indeed the only difference in terms of magnetic structure is the presence of a Jahn-Teller compressed Mn(III) ion in **6** and a Jahn-Teller elongated Mn(III) ion in **9**. The synthesis of **6** therefore represents an ideal opportunity to investigate the magneto-structural relationship in these two types of complex.

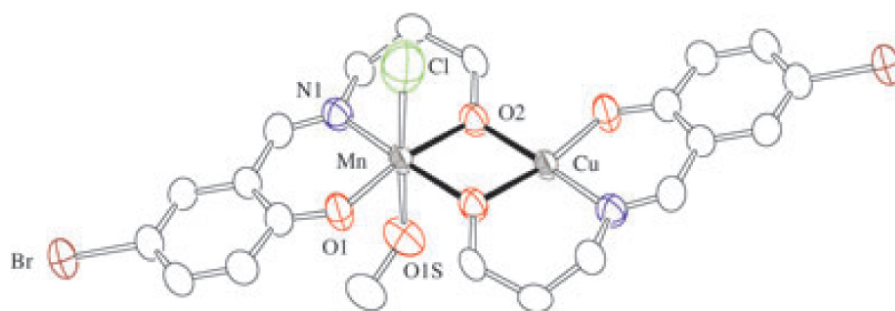


**Figure 42.** ORTEP diagram of **9** with 30% probability showing Jahn-Teller elongation of Mn(III) ion, taken from reference [151].

#### 3.3.1 DFT Analysis

Density functional studies have been performed on complex **6** to compute the  $J$  value and to explore the origin of the nature of the interaction observed experimentally. The B3LYP/TZV combination (see computational details in the experimental section) yields a  $J$  value of  $-71 \text{ cm}^{-1}$ . Although the sign of  $J$  has been correctly reproduced, the magnitude is overestimated compared to experiment ( $J_{\text{exp}} = -33.4 \text{ cm}^{-1}$ ). Although the employed methodology generally offers good numerical estimates of  $J$  values, there are instances where overestimation of the  $J$  has been noted [170], [135]. Calculations performed incorporating the counter-anion did not lead to any significant

improvement ( $-71 \text{ cm}^{-1}$  vs.  $-83 \text{ cm}^{-1}$ ; see Table B2 in Appendix B). Since our aim is to probe the origin of antiferromagnetic coupling in the Cu(II)-Mn(III) pair of **6**, we have analysed the wave function and the magnetic orbitals of the Mn(III) and Cu(II) ions (Figure 43). The Cu(II) ion is in a square planar environment, with the unpaired electron residing in the  $d_{x^2-y^2}$  orbital ( $b_{1g}$ ). For Mn(III) the following configuration has been detected from the computed wave function:  $b_{2g}(d_{xy})^1 e_g(d_{xz})^1 e_g(d_{yz})^1 b_{1g}(d_{x^2-y^2})^1$  where the  $a_{1g}(d_z^2)$  orbital is found to be empty and lies  $1.12 \text{ eV}$  higher in energy than the  $b_{1g}$  orbital. This splitting is related to the strength of the distortion and significant splitting demonstrates that the Mn(III) ion is undergoing relatively strong Jahn-Teller compression [27], [171–173].

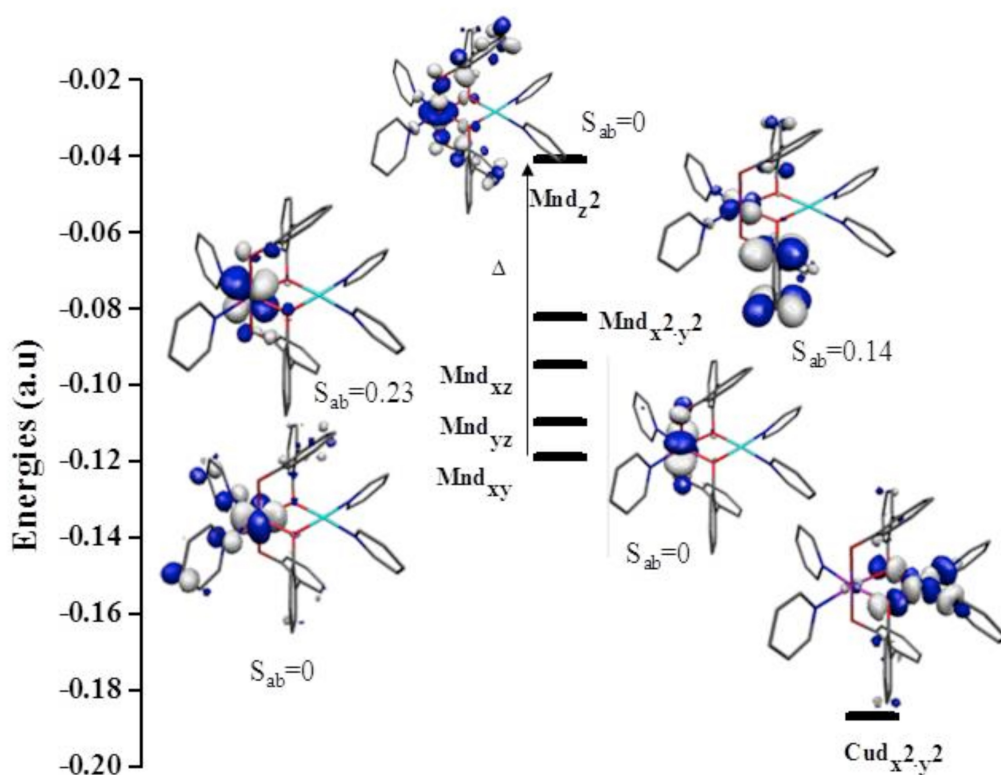


**Figure 43.** DFT calculated magnetic orbitals of Mn(III) and Cu(II) in complex **6** with computed  $S_{ab}$  (overlap integral) values. The isodensity surface represented corresponds to a value of  $0.05 \text{ e}^-/\text{bohr}^3$ .

Qualitatively  $\Delta(E_{d_{xy}} - E_{d_z^2})$  – calculated to be  $\sim 2.12 \text{ eV}$  for **6** (Figure 43) – is related to the anisotropy by the following equation for a Jahn-Teller compressed Mn(III) ion:

$$D = D_{zz} - \frac{(D_{xx} + D_{yy})}{2} \approx + \frac{3\xi_{eff}^2}{16\Delta}$$

$\zeta_{\text{eff}}$  is the effective covalently reduced one-electron spin-orbit coupling (SOC) constant of the metal ion under investigation, and  $\Delta$  is as defined in Figure 43. Since in both the metal ions the  $b_{1g}(d_{x^2-y^2})$  orbital is singly occupied, a significant interaction between these two magnetic orbitals is expected, leading to antiferromagnetic coupling. To prove this hypothesis, overlap integrals between pairs of magnetic orbitals have been computed. Our overlap integral analysis reveals a significant overlap between  $\text{Mn}(d_{x^2-y^2})$  and  $\text{Cu}(d_{x^2-y^2})$ . Additionally  $\text{Mn}(d_{xz})$  has non-negligible overlap with the  $\text{Cu}(d_{x^2-y^2})$  orbital. The  $\text{Mn}(d_{x^2-y^2})$ - $\text{Cu}(d_{x^2-y^2})$  interaction is very significant (Figure 43) and this leads to a moderate antiferromagnetic interaction in complex **6**. The other dinuclear Cu(II)-Mn(III) complex (**9**) reported in the literature [151] exhibits ferromagnetic coupling. In this complex the Mn(III) is Jahn-Teller elongated, the  $d_{x^2-y^2}$  orbital is empty and the significant  $\text{Mn}(d_{x^2-y^2})$ - $\text{Cu}(d_{x^2-y^2})$  antiferromagnetic interaction present in **6**, is absent in **9**, leading to moderate ferromagnetic coupling. This pair of complexes illustrates rather nicely how the magnetic coupling can be tuned from ferromagnetic to antiferromagnetic by altering the nature of the distortion (elongation vs. compression) on the Mn(III) site.

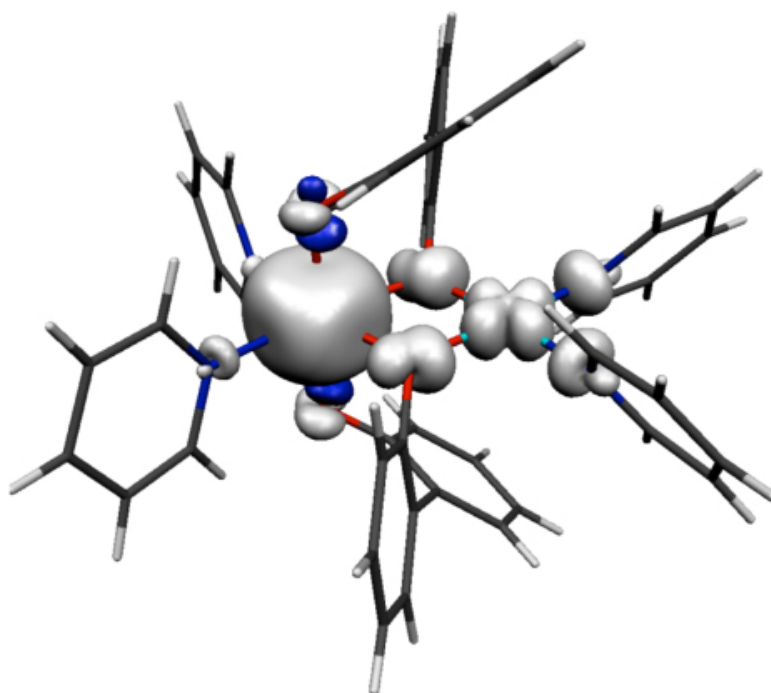


**Figure 44.** DFT computed spin density plot of **6** for the  $S = 2$  state. The isodensity surface represented corresponds to a value of  $0.005 \text{ e}^-/\text{bohr}^3$ . The white and blue regions indicate positive and negative spin populations, respectively.

The spin density values on the Mn(III) (1.663) and Cu(II) (0.59) ions of complex **6**, clearly indicate strong spin delocalization to other atoms. The spin densities on the bridging O-atoms (O1 and O2) are found to be positive (0.11 and 0.12) while the N-atoms coordinated to Cu(II) and Mn(III) are also found to have positive spin densities (see Appendix B). On the other hand, the spin densities on the O-atoms lying in the axial direction are found to be negative (Figure 44). This is in line with our expectation where the empty  $d_z^2$  orbital of the Mn(III) ion propagates spin polarization rather than spin delocalization. We have witnessed such a mixture of delocalization and polarization in chapter 2, and this has also been reported previously in the literature [174].

We have also computed the ZFS parameter of complex **6** using the methodology established by Neese et al [172]. We have performed calculations on complex **6** and also on a fictitious Zn(II)-Mn(III) model complex of **6** to estimate the  $S = 3/2$  ZFS of **6** and the  $S = 2$  single-ion anisotropy of the Mn(III) ion, in order to compare to the experimentally extracted parameters. The calculated single ion anisotropy of the Mn(III) ion is  $+1.94 \text{ cm}^{-1}$ , while the cluster anisotropy is computed to be  $+2.35 \text{ cm}^{-1}$ . The HF-EPR estimates of the ZFS are  $+4.28$  and  $+6.35 \text{ cm}^{-1}$ , respectively. Our DFT calculations reproduce the sign and the trend correctly, but clearly underestimate the magnitude quite considerably. Such underestimation by DFT methods has been well documented: accurate reproduction demands inclusion of excited state contributions and this is possible only by means of ab initio calculations. Analysis of the contributions to the net D-tensor suggest the main source arises from spin-orbit coupling ( $D_{\text{SOC}}$ ), while the spin-spin contribution ( $D_{\text{SS}}$ ) is found to be small, and significantly less than that reported for complexes in which the Mn(III) ion is Jahn-Teller elongated [27], [171–173]. The significant contributions to the ZFS are listed in Table 9. For  $D_{\text{SOC}}$  the spin-flip excitations account for nearly 65% of the contribution. Multiple contributions to the D-tensor listed in Table 10 reveal some distinct differences between the single-ion and the cluster anisotropy. The  $\alpha \rightarrow \beta$  (spin-up to spin-down) excitations are pronounced for the Mn(III) single-ion ( $S = 2$  state) anisotropy, while other contributions are very small. However for the dinuclear Cu(II)-Mn(III) compound **6** ( $S = 3/2$  ground state), very large  $\beta \rightarrow \alpha$  and  $\alpha \rightarrow \alpha$  contributions were detected, in addition to the expected  $\alpha \rightarrow \beta$  spin flip.

**Table 9.** DFT computed spin flip/spin-conserved excitations for the Cu(II)-Mn(III) (**6**) and Zn(II)-Mn(III) complexes. SOMO = singly occupied molecular orbital, DOMO = doubly occupied molecular orbital and VMO = virtual molecular orbital (unoccupied).

spin flip/spin conserved excitations	single ion anisotropy (cm <sup>-1</sup> )	cluster anisotropy (cm <sup>-1</sup> )
<b>SOMO-SOMO</b> $\alpha \rightarrow \beta$	1.215	1.484
<b>DOMO-SOMO</b> $\beta \rightarrow \beta$	0.028	0.059
<b>SOMO-VMO</b> $\alpha \rightarrow \alpha$	0.339	-2.729
<b>DOMO-VMO</b> $\beta \rightarrow \alpha$	0.002	3.554

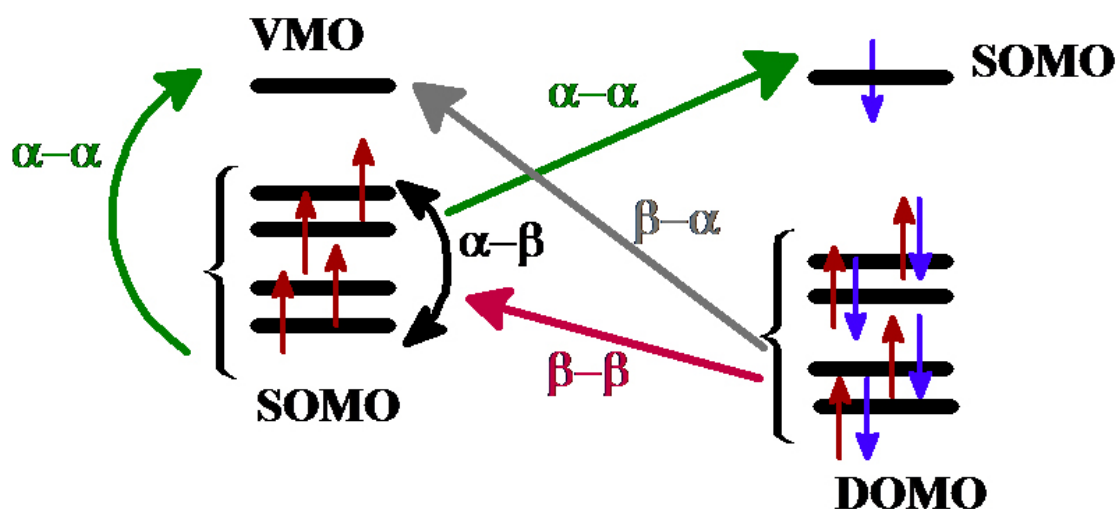


**Figure 45.** Schematic diagram illustrating the different contribution to anisotropy in complex **6**.

Analysing the wave function (see Figure 43 and related discussion on  $\Delta$ ), reveals that the main reason for the difference between the single-ion and the cluster anisotropy is that the Mn(III) ion has one empty  $\alpha$  type orbital (for  $S = 3/2$  ground state) and this leads to large singly occupied molecular orbitals (SOMO) to virtual molecular orbitals (VMO) contribution. The term *virtual molecular orbitals* describes unoccupied MOs. Another significant contribution to the cluster anisotropy is due to the  $\beta \rightarrow \alpha$  excitation from the doubly occupied orbitals (DOMO) of Cu(II) to the VMO of Mn(III). These two contributions are minimal for the mononuclear Mn(III) ions. This is illustrated in Figure 45. It is apparent from the break-up contributions given for the Cu(II)-Mn(III) complex that the DOMO  $\rightarrow$  VMO excitation which has the largest positive value determines the net sign of the anisotropy. Since this parameter is related to the mixing of Mn(III) and Cu(II) d-orbitals, efforts to vary the ligand field are expected to

significantly affect the magnitude of the anisotropy. The computed  $D$ -tensor orientation for the Cu(II)-Mn(III) complex (**6**) is shown in Figure 46. As expected the  $D_{zz}$  axis is aligned along Jahn-Teller axis with a deviation of approximately  $5^\circ$ .

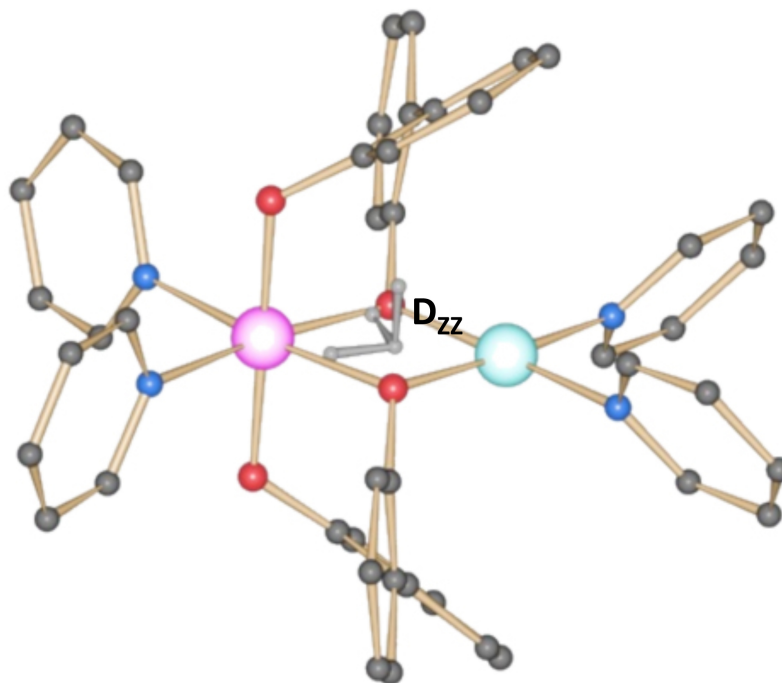


**Figure 46.** DFT calculated orientation of  $D$ -tensor in **6**. H-atoms have been omitted for clarity.

**Table 10.** Experimental versus DFT computed single-ion and cluster anisotropies with SOC and SS contributions.

Complex	$D$ total ( $\text{cm}^{-1}$ )	$D_{\text{SOC}}$ ( $\text{cm}^{-1}$ )	$D_{\text{SS}}$ ( $\text{cm}^{-1}$ )	$E/D$	$g$ -tensor
DFT on <b>6</b> ( $S=3/2$ )	2.35	2.369	-0.009	0.06	1.98
DFT on Zn(II)-Mn(III)	1.94	1.58	0.35	0.06	1.99
HF-EPR on <b>6</b>	6.27			0.09	----
HF-EPR Mn(III) ion	4.78			0.08	1.98

### 3.4 Conclusion

Complexes **6** and **7** are two rare examples of dimeric [Cu(II)-Mn(III)] cluster compound and are the first examples to exhibit a Jahn-Teller compressed Mn(III) centre. Magnetic susceptibility and magnetization studies conclude that **6** is a ferrimagnet with an isolated  $S = 3/2$  ground spin state, with  $J = -33.4 \text{ cm}^{-1}$ ,  $g = 2.0$  and  $D_{\text{Mn}} = +4.95 \text{ cm}^{-1}$ . High-field and high-frequency EPR studies on both powdered and single-crystal samples of **6** corroborate these findings, giving rise to the spin Hamiltonian parameters  $D_{\text{Mn}} = +4.78 \text{ cm}^{-1}$  and  $E_{\text{Mn}} = +0.405 \text{ cm}^{-1}$ . DFT calculations

offer insights into the mechanism of magnetic coupling where the origin of the antiferromagnetic interaction is related to the nature of the Jahn-Teller distortion. Calculations also yield a reasonable estimate of the anisotropy for complex **6** and explain how the mixing of the Mn(III) and Cu(II) d-based orbitals leads to dramatic changes in the sign as well as the magnitude of the anisotropy for **6**.

We have also successfully produced two analogues to complex **6**; one isostructural Cu(II)-Mn(III) dimer (**7**) and one homometallic [Cu(II)<sub>2</sub>] complex (**8**). All three novel compounds reported in this chapter highlight the ability of 2,2'-biphenol (LH<sub>2</sub>) to bridge metal ions, adopting the  $\eta^1:\eta^2,\mu$ -bridging motif. These observations are quite different from the chelating mode exhibited by this ligand in the [Mn(III)<sub>2</sub>] complexes of chapter 2. Continuing on the theme of heterometallic chemistry, in the next chapter we report a structurally interesting and unique family of 1-D M(III)/Na(I) extended structures (M = Mn / Fe), in which the 2,2'-biphenol ligand adopts both chelating and bridging modes.

## 3.5 Experimental Section

### 3.5.1 Physical measurements

Infra-red spectra were recorded on a Perkin Elmer FT-IR Spectrum One spectrometer equipped with a Universal ATR Sampling accessory (NUI Galway). Elemental analysis was carried out by the School of Chemistry microanalysis service at NUI Galway. Variable-temperature, solid-state direct current (dc) magnetic susceptibility data down to 5 K were collected on powdered samples using a Quantum Design MPMS-XL SQUID magnetometer equipped with a 7 T dc magnet (University of Edinburgh). Diamagnetic corrections were applied to the observed paramagnetic susceptibilities using Pascals' constants. Complex **6** was set in eicosane to avoid torquing of the crystallites. A phase-locked oscillator, in conjunction with a series of multipliers and amplifiers, was employed as a microwave source capable of providing quasi-continuous frequency coverage up to 600+ GHz; a cold bolometer was used for detection [175].

### 3.5.2 X-ray crystallography

The structure of **6** was collected on an Xcalibur S single crystal diffractometer (Oxford Diffraction) using an enhanced Mo source. Each data reduction was carried

out on the CrysAlisPro software package. The structures were solved by direct methods (SHELXS-97) [125] and refined by full matrix least squares using SHELXL-97 [126]. SHELX operations were automated using the OSCAIL software package [127].

### 3.5.3 Computational Details

DFT calculations combined with the Broken Symmetry (BS) approach [130] were employed to compute the  $J$  values. The BS method has a proven record of yielding good numerical estimates of  $J$  constants for a variety of complexes [131], [132], [134], [176], [177]. A detailed technical discussion of the computational details can be found elsewhere [133]. Here, we have performed most of our calculations using the Gaussian 09 suite of programs with the fragment approach. We have employed a hybrid B3LYP functional [123] with TZV basis sets on all atoms [129]. A very tight SCF convergence was employed throughout. DFT calculations for the estimation of the D-tensor used the ORCA suite of programs [178], employing the non-hybrid BP86 functional [179] using quasi-degenerate theory [180] with CP approach [181], [182]. The Alhrichs TZVPPP basis set was used for the Mn(III) and Cu(II) ions, while for the remaining atoms we have used the TZVP basis set. The RI approximations were considered during calculation with auxiliary TZV/J columbic fitting basis set [183]. Increased integration grids (Grid 5 in ORCA convention) along with tight SCF convergence were used.

### 3.5.4 Syntheses

All reactions were performed under aerobic conditions and all reagents and solvents were used as purchased. *Caution:* Although we encountered no problems care should be taken when using the potentially explosive perchlorate salts. The  $\text{NEt}_4(\text{OH})$  solution employed was a 40% by weight aqueous solution which was used as purchased.

#### Preparation of $[\text{MnCu}(\text{L})_2(\text{py})_4](\text{ClO}_4)_2 \cdot \text{MeOH}$ (**6**)

$\text{Mn}(\text{II})(\text{ClO}_4)_2 \cdot 6\text{H}_2\text{O}$  (0.25 g, 0.98 mmol) and anhydrous  $\text{Cu}(\text{I})\text{Cl}$  (0.39 g, 3.94 mmol) were dissolved in 25  $\text{cm}^3$  EtOH along with 1  $\text{cm}^3$  of pyridine. 2,2'-biphenol (0.73 g, 3.94 mmol) was then added along with 2 drops of a 40% (by weight) aqueous solution

of  $\text{NEt}_4(\text{OH})$  The resultant solution was stirred for 5-7 minutes before being filtered to give a green / black solution. Brown block-like crystals of **6** were obtained in ~20% yield upon slow evaporation of the mother liquor over a period of 24 hours. *Note:* Attempts at repeating the reaction employing Cu(II) salts have all been unsuccessful. FT-IR ( $\text{cm}^{-1}$ ): 3508.2(w), 3043.5(w), 2970.4(w), 1605.5(m), 1585.3(w), 1484.2(m), 1465.7(m), 1446.4(m), 1432.4(m), 1288.4(w), 1272.5(w), 1250.0(m), 1213.6(m), 1153.7(w), 1080.7(vs), 1066.8(vs), 1043.2(s), 1015.6(m), 956.7(w), 940.4(w), 869.4(w), 852.8(m), 833.7(m), 756.0(vs), 731.3(m), 695.1(vs). Elemental analysis calculated (found) (%) for  $\text{C}_{45}\text{H}_{40}\text{N}_4\text{O}_9\text{ClMnCu}$  (**6**): C: 57.82 (57.98), H: 4.31 (3.81), N: 5.99 (6.05).

#### **Preparation of $[\text{MnCu}(\text{L})_2(\text{4-pic})_4](\text{ClO}_4)(\text{LH}_2)$ (**7**)**

$\text{Mn}(\text{ClO}_4)_2 \cdot 6\text{H}_2\text{O}$  (0.5g) and an excess of 2,2'-biphenol (0.73g, 3.9mmol) were dissolved in 30  $\text{cm}^3$  EtOH. Two drops of a 40% ethanolic solution of TEA(OH) was added, followed by Cu(I)Br (0.28g, 1.95mmol) and an excess of 4-picoline (2  $\text{cm}^3$ , 20.54 mmol). The resultant deep brown solution was stirred for 8 minutes, filtered, covered with a perforated lid and allowed to stand in the fumehood. X-ray quality crystals were obtained in in ~15% yield upon slow evaporation of the mother liquor. FT-IR ( $\text{cm}^{-1}$ ): 3350.55 (w), 3061.97 (w), 2969.14 (w), 1618.91 (m), 1585.38 (w), 1555.08 (w), 1507.93 (w), 1484.38 (m), 1465.08 (m), 1432.82 (vs), 1380.76 (w), 1288.23 (w), 1273.31 (m), 1252.99 (vs), 1226.72 (s), 1211.15 (m), 1092.79 (vs), 1066.89 (s), 1039.53 (s), 1015.89 (m), 1005.04 (m), 932.66 (w), 853.53 (s), 834.56 (m), 811.10 (s), 769.08 (vs), 758.62 (vs), 730.75 (s), 708.67 (m). Elemental analysis calculated (found) (%) for  $\text{C}_{60}\text{H}_{58}\text{N}_4\text{O}_{10}\text{ClMnCu}$  (**7**): C: 62.72 (62.40), H: 5.09 (5.23), N: 4.88 (4.67).

#### **Preparation of $[\text{Cu}_2(\text{LH})_2(\text{3-pic})_4](\text{ClO}_4)_2 \cdot 2\text{EtOH}$ (**8**)**

To a 30 $\text{cm}^3$  ethanolic solution containing  $\text{Cu}(\text{ClO}_4) \cdot 4\text{H}_2\text{O}$  (0.75g, 1.91mmol) and 2,2'-biphenol (0.73g, 3.9 mmol) was added TMA(OH)  $\cdot 4\text{H}_2\text{O}$  (0.047g, 0.26mmol), followed by an excess of 3-picoline (1  $\text{cm}^3$ , 10.27mmol). The resultant brown solution was stirred for 10 minutes, after which time it was filtered and allowed to stand. Dark brown X-ray quality crystals were obtained in ~25% yield after 24 hours. FT-IR ( $\text{cm}^{-1}$ ): 3549.33 (w), 3179.69 (w), 2969.98 (w), 1610.66 (w), 1586.90 (w), 1505.56 (w),

1476.27 (w), 1435.13 (m), 1384.68 (w), 1294.61 (w), 1269.31 (w), 1252.77 (m), 1223.65 (m), 1199.76 (w), 1108.16 (s), 1096.61 (s), 1032.59 (vs), 924.82 (m), 878.94 (w), 845.85 (m), 823.77 (m), 804.54 (w), 774.05 (m), 761.40 (s), 734.03 (m), 702.36 (s), 658.14 (m). Elemental analysis calculated (found) (%) for  $C_{48}H_{58}N_4O_{14}Cl_2MnCu$  (**8**): C: 52.20 (51.86), H: 5.29 (5.56), N 5.07 (5.12).

### 3.6 Bibliography

- [136] H. A. Jahn and E. Teller, "Stability of Polyatomic Molecules in Degenerate Electronic States," *Proceedings of the Royal Society London A*, vol. 161, pp. 220–235, 1937.
- [137] H. Yersin, Ed., *Transition Metal and Rare Earth Compounds: Excited States, Transitions, Interactions, Volume 214*. Springer, 2001, p. 59.
- [138] P. L. W. Tregenna-Piggott, "Origin of compressed Jahn-Teller octahedra in sterically strained manganese(III) complexes.," *Inorganic chemistry*, vol. 47, no. 2, pp. 448–453, Jan. 2008.
- [139] M. Corbella, R. Costa, J. Ribas, P. H. Fries, J.-M. Latour, L. Öhrström, X. Solans, and V. Rodríguez, "Structural and Magnetization Studies of a New ( $\mu$ -Oxo)bis( $\mu$ -carboxylato)dimanganese(III) Complex with a Terminal Hydroxo Ligand," *Inorganic Chemistry*, vol. 35, no. 7, pp. 1857–1865, Jan. 1996.
- [140] J. E. Sheats, R. S. Czernuszewicz, G. C. Dismukes, A. L. Rheingold, V. Petrouleas, J. Stubbe, W. H. Armstrong, R. H. Beer, and S. J. Lippard, "Binuclear manganese(III) complexes of potential biological significance," *Journal of the American Chemical Society*, vol. 109, no. 5, pp. 1435–1444, Mar. 1987.
- [141] K. Wieghardt, U. Bossek, D. Ventur, and J. Weiss, "Assembly and structural characterization of binuclear  $\mu$ -oxo-di- $\mu$ -acetato bridged complexes of manganese(III). Analogues of the di-iron(III) centre in hemerythrin," *Journal of the Chemical Society, Chemical Communications*, no. 6, p. 347, 1985.
- [142] C. Cañada-Vilalta, J. C. Huffman, W. E. Streib, E. R. Davidson, and G. Christou, "Use of the dicarboxylate ligand *m*-phenylenedipropionate for the synthesis of new Mn/O clusters. Synthesis, characterization and magnetic properties," *Polyhedron*, vol. 20, no. 11–14, pp. 1375–1380, May 2001.
- [143] G. Fernández, M. Corbella, M. Alfonso, H. Stoeckli-Evans, and I. Castro, "A comparative XAS and X-ray diffraction study of new binuclear Mn(III) complexes with catalase activity. indirect effect of the counteranion on magnetic properties.," *Inorganic chemistry*, vol. 43, no. 21, pp. 6684–6698, Oct. 2004.
- [144] G. Fernández, M. Corbella, G. Aullón, M. A. Maestro, and J. Mahía, "New Dinuclear Mn(III) Compounds with 2-MeC<sub>6</sub>H<sub>4</sub>COO and 2-FC<sub>6</sub>H<sub>4</sub>COO Bridges – Effect of Terminal Monodentate Ligands (H<sub>2</sub>O, ClO<sub>4</sub><sup>-</sup> and NO<sub>3</sub><sup>-</sup>) on the Magnetic Properties," *European Journal of Inorganic Chemistry*, vol. 2007, no. 9, pp. 1285–1296, Mar. 2007.
- [145] V. Gómez, M. Corbella, and G. Aullón, "Two temperature-independent spinomers of the dinuclear Mn(III) compound [ $\{\text{Mn}(\text{H}_2\text{O})(\text{phen})\}_2(\mu\text{-}2\text{-ClC}_6\text{H}_4\text{COO})_2(\mu\text{-O})\}(\text{ClO}_4)_2$ ," *Inorganic chemistry*, vol. 49, no. 4, pp. 1471–1480, Mar. 2010.
- [146] J. B. Vincent, H. L. Tsai, A. G. Blackman, S. Wang, P. D. W. Boyd, K. Foltz, J. C. Huffman, E. B. Lobkovsky, D. N. Hendrickson, and G. Christou, "Models of the manganese catalase enzymes. Dinuclear manganese(III) complexes with the  $[\text{Mn}_2(\mu\text{-O})(\mu\text{-O}_2\text{CR})_2]^{2+}$  core and terminal monodentate ligands: preparation and properties of  $[\text{Mn}_2\text{O}(\text{O}_2\text{CR})_2\text{X}_2(\text{bpy})_2]$  (X = chloride, azide, water)," *Journal of the American Chemical Society*, vol. 115, no. 26, pp. 12353–12361, Dec. 1993.

- [147] S. Youngme, P. Gunnasoot, N. Chaichit, and C. Pakawatchai, "Dinuclear copper(II) complexes with ferromagnetic and antiferromagnetic interactions mediated by a bridging oxalato group: structures and magnetic properties of  $[\text{Cu}_2\text{L}_4(\mu\text{-C}_2\text{O}_4)](\text{PF}_6)_2(\text{H}_2\text{O})_2$  and  $[\text{Cu}_2\text{L}_2(\mu\text{-C}_2\text{O}_4)(\text{NO}_3)_2((\text{CH}_3)_2\text{NCOH})_2]$  (L = di-2-pyridylamine)," *Transition Metal Chemistry*, vol. 29, no. 8, pp. 840–846, Nov. 2004.
- [148] X.-Y. Kuang and K.-W. Zhou, "Analysis of exchange interaction for heterodinuclear Cu–F–Mn clusters in  $\text{K}_2\text{CuF}_4:\text{Mn}^{2+}$  and  $\text{KZnF}_3:\text{Cu}^{2+}\text{-Mn}^{2+}$  systems," *Physica B: Condensed Matter*, vol. 307, no. 1–4, pp. 34–39, Dec. 2001.
- [149] J. Ferguson, H. J. Guggenheim, and E. R. Krausz, "Optical absorption by Cu–Mn pairs in  $\text{KZnF}_3$ ," *Journal of Physics C: Solid State Physics*, vol. 4, no. 13, pp. 1866–1873, Sep. 1971.
- [150] J. Ferré and M. Régis, "Optical determination of the Cu–Mn — Exchange interaction in  $\text{K}_2\text{Cu}_{1-x}\text{Mn}_x\text{F}_4$ ," *Solid State Communications*, vol. 26, no. 4, pp. 225–228, Apr. 1978.
- [151] H. Oshio, M. Nihei, A. Yoshida, H. Nojiri, M. Nakano, A. Yamaguchi, Y. Karaki, and H. Ishimoto, "A dinuclear  $\text{Mn}^{\text{III}}\text{-Cu}^{\text{II}}$  single-molecule magnet.," *Chemistry (Weinheim an der Bergstrasse, Germany)*, vol. 11, no. 3, pp. 843–848, Jan. 2005.
- [152] C. Mantel, A. K. Hassan, J. Pécaut, A. Deronzier, M.-N. Collomb, and C. Duboc-Toia, "A high-frequency and high-field EPR study of new azide and fluoride mononuclear Mn(III) complexes.," *Journal of the American Chemical Society*, vol. 125, no. 40, pp. 12337–12344, Oct. 2003.
- [153] S. Romain, C. Duboc, F. Neese, E. Rivière, L. R. Hanton, A. G. Blackman, C. Philouze, J.-C. Leprêtre, A. Deronzier, and M.-N. Collomb, "An unusual stable mononuclear Mn(III) bis-terpyridine complex exhibiting Jahn-Teller compression: electrochemical synthesis, physical characterisation and theoretical study.," *Chemistry (Weinheim an der Bergstrasse, Germany)*, vol. 15, no. 4, pp. 980–988, Jan. 2009.
- [154] Q. Scheifele, C. Riplinger, F. Neese, H. Weihe, A.-L. Barra, F. Juranyi, A. Podlesnyak, and P. L. W. Tregenna-Piggott, "Spectroscopic and theoretical study of a mononuclear manganese(III) complex exhibiting a tetragonally compressed geometry.," *Inorganic chemistry*, vol. 47, no. 2, pp. 439–447, Jan. 2008.
- [155] D. P. Goldberg, J. Telser, J. Krzystek, A. G. Montalban, L.-C. Brunel, A. G. M. Barrett, and B. M. Hoffman, "EPR Spectra from 'EPR-Silent' Species: High-Field EPR Spectroscopy of Manganese(III) Porphyrins," *Journal of the American Chemical Society*, vol. 119, no. 37, pp. 8722–8723, Sep. 1997.
- [156] J. Krzystek, J. Telser, L. A. Pardi, D. P. Goldberg, B. M. Hoffman, and L.-C. Brunel, "High-Frequency and -Field Electron Paramagnetic Resonance of High-Spin Manganese(III) in Porphyrinic Complexes," *Inorganic Chemistry*, vol. 38, no. 26, pp. 6121–6129, Dec. 1999.
- [157] S. Mossin, H. Weihe, and A.-L. Barra, "Is the Axial Zero-Field Splitting Parameter of Tetragonally Elongated High-Spin Manganese(III) Complexes Always Negative?," *Journal of the American Chemical Society*, vol. 124, no. 30, pp. 8764–8765, Jul. 2002.
- [158] A. L. Spek, "Single-crystal structure validation with the program PLATON," *Journal of Applied Crystallography*, vol. 36, no. 1, pp. 7–13, Jan. 2003.

- [159] L. Bo, Z. Hong, P. Zhi-Quan, S. You, W. Cheng-Gang, Z. Han-Ping, H. Jing-Dong, and C. Ru-An, "Synthesis, characterization, magnetic and electrochemical studies of an asymmetric heterodinuclear macrocyclic complex," *Journal of Coordination Chemistry*, vol. 59, no. 11, pp. 1271–1280, Jul. 2006.
- [160] A. Hori, Y. Mitsuka, M. Ohba, and H. Ōkawa, "Heterodinuclear  $M^II Cu^II$  complexes of a constrained macrocyclic compartmental ligand. EPR studies of spin-coupled  $Mn^II Cu^II$  ( $S_T=2$ ) and  $Ni^II Cu^II$  ( $S_T=1/2$ )," *Inorganica Chimica Acta*, vol. 337, pp. 113–121, Sep. 2002.
- [161] C. J. O'Connor, D. P. Freyberg, and E. Sinn, "Relation between structure and magnetic exchange interactions in bis(hexafluoroacetylacetonato){N,N'-ethylenebis[2-hydroxypropiophenone iminato-N,O<sup>2-</sup>]copper(II)}M'(II),  $Cu((prp)_2en)M'(hfa)_2$ , where  $M' = Cu, Ni,$  and  $Mn$ . Crystal structures of the complexes," *Inorganic Chemistry*, vol. 18, no. 4, pp. 1077–1088, Apr. 1979.
- [162] H. Okawa, J. Nishio, M. Ohba, M. Tadokoro, N. Matsumoto, M. Koikawa, S. Kida, and D. E. Fenton, "Heterodinuclear copper(II)-lead(II) and copper(II)-M(II) ( $M = manganese, iron, cobalt, nickel, copper, zinc$ ) complexes of macrocycles with dissimilar 4- and 5-coordination sites: synthesis, structures, and properties," *Inorganic Chemistry*, vol. 32, no. 13, pp. 2949–2957, Jun. 1993.
- [163] F. Birkelbach, M. Winter, U. Floerke, H.-J. Haupt, C. Butzlaff, M. Lengen, E. Bill, A. X. Trautwein, K. Wieghardt, and P. Chaudhuri, "Exchange Coupling in Homo- and Heterodinuclear Complexes  $Cu^II M$  [ $M = Cr(III), Mn(III), Mn(II), Fe(III), Co(III), Co(II), Ni(II), Cu(II), Zn(II)$ ]. Synthesis, Structures, and Spectroscopic Properties," *Inorganic Chemistry*, vol. 33, no. 18, pp. 3990–4001, Aug. 1994.
- [164] Z.-W. Li, P.-P. Yang, L.-C. Li, and D.-Z. Liao, "A new  $Cu^II-Mn^{III}$  heterobinuclear complex exhibiting magnetization relaxation," *Inorganica Chimica Acta*, vol. 362, no. 9, pp. 3381–3384, Jul. 2009.
- [165] W. H. Press, B. P. Flannery, S. A. Teukolsky, and W. T. Vetterling, *Numerical Recipes in C: The Art of Scientific Computing, Second Edition*. Cambridge University Press, 1992, p. 994.
- [166] M. Handa, N. Koga, and S. Kida, "Study of the effect of structural factors on magnetism of di- $\mu$ -alkoxodicopper(II) complexes by ab initio MO calculations," *Bulletin of the Chemical Society of Japan*, vol. 61, no. 11, pp. 3853–3857.
- [167] J. M. Zadrozny, J. Liu, N. A. Piro, C. J. Chang, S. Hill, and J. R. Long, "Slow magnetic relaxation in a pseudotetrahedral cobalt(II) complex with easy-plane anisotropy.," *Chemical communications (Cambridge, England)*, vol. 48, no. 33, pp. 3927–3929, Apr. 2012.
- [168] X. Feng, J. Liu, T. D. Harris, S. Hill, and J. R. Long, "Slow magnetic relaxation induced by a large transverse zero-field splitting in a  $Mn(II)Re(IV)(CN)_2$  single-chain magnet.," *Journal of the American Chemical Society*, vol. 134, no. 17, pp. 7521–9, May 2012.
- [169] A. Bencici and D. Gatteschi, *Electron Paramagnetic Resonance of Exchange Coupled Clusters*. 1990.
- [170] A.-A. H. Abu-Nawwas, J. Cano, P. Christian, T. Mallah, G. Rajaraman, S. J. Teat, R. E. P. Winpenny, and Y. Yukawa, "An  $Fe^{III}$  wheel with a zwitterionic ligand: the structure and magnetic properties of  $[Fe(OMe)_2(proline)]_{12}$

- [ClO<sub>4</sub>]<sub>12</sub>,” *Chemical communications (Cambridge, England)*, no. 3, pp. 314–5, Mar. 2004.
- [171] C. Duboc, D. Ganyushin, K. Sivalingam, M.-N. Collomb, and F. Neese, “Systematic theoretical study of the zero-field splitting in coordination complexes of Mn(III). Density functional theory versus multireference wave function approaches.,” *The journal of physical chemistry. A*, vol. 114, no. 39, pp. 10750–10758, Oct. 2010.
- [172] F. Neese, “Importance of direct spin-spin coupling and spin-flip excitations for the zero-field splittings of transition metal complexes: a case study.,” *Journal of the American Chemical Society*, vol. 128, no. 31, pp. 10213–10222, Aug. 2006.
- [173] D. Maganas, S. Sottini, P. Kyritsis, E. J. J. Groenen, and F. Neese, “Theoretical analysis of the spin Hamiltonian parameters in Co(II)S<sub>4</sub> complexes, using density functional theory and correlated ab initio methods.,” *Inorganic chemistry*, vol. 50, no. 18, pp. 8741–8754, Oct. 2011.
- [174] L. F. Jones, G. Rajaraman, J. Brockman, M. Murugesu, E. C. Sanudo, J. Raftery, S. J. Teat, W. Wernsdorfer, G. Christou, E. K. Brechin, and D. Collison, “New routes to polymetallic clusters: fluoride-based tri-, deca-, and hexaicosametallic Mn<sup>III</sup> clusters and their magnetic properties.,” *Chemistry (Weinheim an der Bergstrasse, Germany)*, vol. 10, no. 20, pp. 5180–5194, Oct. 2004.
- [175] R. Herchel, R. Boca, J. Krzystek, A. Ozarowski, M. Durán, and J. van Slageren, “Definitive determination of zero-field splitting and exchange interactions in a Ni(II) dimer: investigation of [Ni<sub>2</sub>(en)<sub>4</sub>Cl<sub>2</sub>]Cl<sub>2</sub> using magnetization and tunable-frequency high-field electron paramagnetic resonance.,” *Journal of the American Chemical Society*, vol. 129, no. 34, pp. 10306–10307, Aug. 2007.
- [176] E. Ruiz, J. Cano, S. Alvarez, A. Caneschi, and D. Gatteschi, “Theoretical study of the magnetic behavior of hexanuclear Cu(II) and Ni(II) polysiloxanolato complexes.,” *Journal of the American Chemical Society*, vol. 125, no. 22, pp. 6791–6794, Jul. 2003.
- [177] S. Piligkos, G. Rajaraman, M. Soler, N. Kirchner, J. van Slageren, R. Bircher, S. Parsons, H.-U. Güdel, J. Kortus, W. Wernsdorfer, G. Christou, and E. K. Brechin, “Studies of an enneanuclear manganese single-molecule magnet.,” *Journal of the American Chemical Society*, vol. 127, no. 15, pp. 5572–5580, May 2005.
- [178] F. Neese, “The ORCA program system,” *Wiley Interdisciplinary Reviews: Computational Molecular Science*, vol. 2, no. 1, pp. 73–78, Jan. 2012.
- [179] J. Perdew, “Density-functional approximation for the correlation energy of the inhomogeneous electron gas,” *Physical Review B*, vol. 33, no. 12, pp. 8822–8824, Jun. 1986.
- [180] D. Ganyushin and F. Neese, “First-principles calculations of zero-field splitting parameters.,” *The Journal of chemical physics*, vol. 125, no. 2, p. 24103, Jul. 2006.
- [181] F. Neese, “Calculation of the zero-field splitting tensor on the basis of hybrid density functional and Hartree-Fock theory.,” *The Journal of chemical physics*, vol. 127, no. 16, p. 164112, Oct. 2007.
- [182] K. Ray, A. Begum, T. Weyhermüller, S. Piligkos, J. van Slageren, F. Neese, and K. Wieghardt, “The electronic structure of the isoelectronic, square-planar complexes [Fe<sup>II</sup>(L)<sub>2</sub>]<sup>2-</sup> and [Co<sup>III</sup>(L Bu)<sub>2</sub>]<sup>-</sup> (L<sup>2-</sup> and (L Bu)<sup>2-</sup> = benzene-1,2-

- dithiolates): an experimental and density functional theoretical study.," *Journal of the American Chemical Society*, vol. 127, no. 12, pp. 4403–4415, Mar. 2005.
- [183] F. Weigend, "Accurate Coulomb-fitting basis sets for H to Rn.," *Physical chemistry chemical physics : PCCP*, vol. 8, no. 9, pp. 1057–1065, Mar. 2006.

## **Chapter 4:**

### **A Series of Alternating Na(I)/M(III) (M = Mn, Fe) Covalent and Ionic Chains**

## 4.1 Introduction

Coordination polymers (a.k.a. Metal-Organic Frameworks – MOFs) [184] contain metal ions (nodes) linked into infinite 1-, 2- or 3-dimensional arrays via organic bridging ligands and/or anion donors [185]. The first man-made coordination polymer (and in fact the first known synthetic coordination compound) was discovered by Diesbach, a German dye maker in the early seventeen hundreds [186]. He was trying to make a well-known red pigment using iron sulfate and potash. However, instead of turning red, the mixture became pale, and then deep blue upon concentration. By using cheap contaminated potash, Diesbach had created the 3-dimensional coordination polymer Prussian Blue, and over 270 years later its structure ( $\text{Fe}_4[\text{Fe}(\text{CN})_6]_3 \cdot x\text{H}_2\text{O}$ ) was determined [187].

Up until quite recently coordination polymers have received very little attention, with just a few notable publications in the literature before the end of the 1980s [188–196]. A new fascination with these compounds slowly began to grow towards the end of the 1980s – particularly in the field of molecular magnetism [197], and surged following the pioneering work of Hoskins and Robson [198], [199].

In addition to their relevance in the field of molecular magnetism, coordination polymers have received attention in many areas of research including catalysis, conductivity, Non-linear Optics (NLO), and luminescence [198–202]. In the design and synthesis of coordination polymers, the choice of metal ion (which form the nodes of the infinite structure) is dependent on the target polymer being pursued [203]. For instance Ln(III) and / or Zn(II)/Cd(II) ions are commonly utilised to promote photoactive properties within such architectures [204–206] while singular or multiple (polynuclear) paramagnetic metal ion nodes would warrant selection towards the production of magnetically interesting polymeric materials such as Single-Chain Magnets (SCMs) [207]. In addition, the correct choice of connector ligand can synergistically enhance such properties by 1) dictating the resultant structural topology (although this is *not* always the case as interpenetration can testify) [208], 2) controlling metal ion(s) node-node distance and therefore the level of physical (i.e. magnetic) communication [209] or 3) acting as magnetic exchange modulators or photophysical enhancers [210], [211]. We present in this chapter the synthesis and characterization of a unique series of alternating 1-D M(III) / Na(I) (M = Mn and Fe) polymers linked covalently or ionically via a combination of the 2,2'-biphenol ligand

(LH<sub>2</sub>) and N-donor co-ligands such as pyridine, 3-picoline and their derivatives. Interestingly, this alternating 1-D M<sup>III</sup>Na<sup>I</sup>M<sup>III</sup>Na structural motif is an extremely rare architectural arrangement [212]. We also show how the type of polymer (covalent or ionic) produced depends on which N-donor co-ligand is selected. We also point out how strongly directional hydrogen bonding interactions are imperative in the formation of certain members of this family.

## 4.2 Results and Discussion

### 4.2.1 Results

Our first synthon in this work involved the reaction of Mn(II)(ClO<sub>4</sub>)<sub>2</sub>·6H<sub>2</sub>O along with a four-fold excess of LH<sub>2</sub> followed by four equivalents of NaOH base in EtOH. It was noted that no distinguishable product was formed from this mixture (or by utilising equimolar amounts of LH<sub>2</sub>), however on addition of an excess of pyridine (1 cm<sup>3</sup>, 12 eq.) followed by agitation and then slow evaporation of the resultant mother liquor, X-ray quality crystals of the chain [Na(I)<sub>2</sub>Mn(III)<sub>2</sub>(L)<sub>4</sub>(py)<sub>3</sub>(EtOH)<sub>2</sub>]<sub>n</sub> (**10**) were harvested in ~20 % yield (Figure 47).

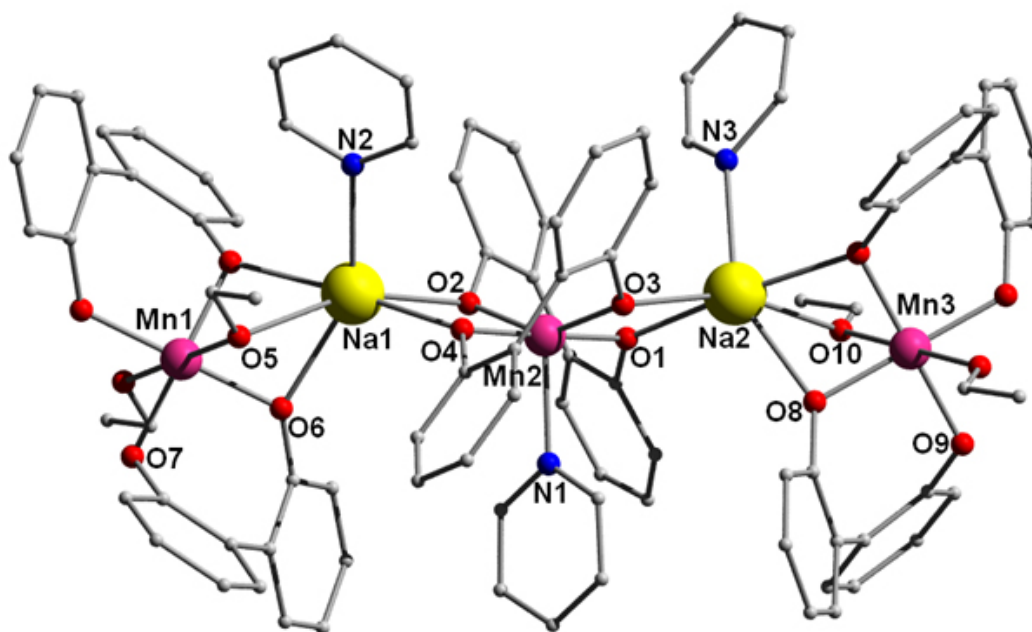


**Figure 47.** Crystal structure of the chain in **10**. Colour code: Purple (Mn), Yellow (Na), Red (O), Blue (N) and Grey (C). Hydrogen atoms omitted for clarity.

The 1-D structure in **10** crystallises in the triclinic P-1 space group and exhibits a zig-zag chain topology comprising alternate Na(I) and Mn(III) metal centres that are connected predominantly by doubly deprotonated L<sup>2-</sup> ligands. These ligands adopt the  $\eta^2:\eta^2:\mu_3$ -bonding mode (Figure 48), in contrast to the  $\eta^1:\eta^2:\mu_2$ -bridging mode observed in chapter 3, and the chelating mode adopted in chapter 2. As previously mentioned, this alternating Na<sup>+</sup>M<sup>3+</sup>Na<sup>+</sup>M<sup>3+</sup> 1-D motif is an extremely rare [212]. Bridging EtOH molecules also help construct the 1-D array in **10** by connecting Na1 to Mn1 and Na2 to Mn3 via O5 and O10 respectively (Figure 47). The two crystallographically unique Na(I) ions (Na1 and Na2) exhibit distorted octahedral geometries with sensible Na-O bond distances ranging from 2.330-2.641 Å.

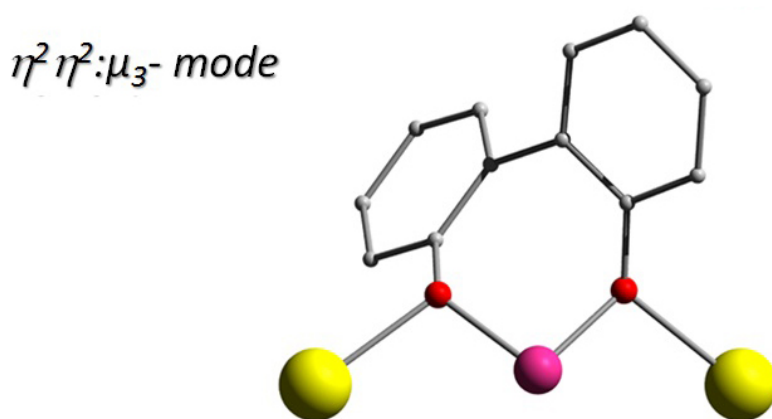


**Figure 48.**  $\eta^2:\eta^2:\mu_3$ -bonding motif observed in many complexes described in this chapter.

This coordination geometry is also observed for Mn1 and Mn3 whose Jahn-Teller elongated axes lie along the Mn1-O5 (and s.e) and Mn3-O10 (and s.e) vertices with distances of 2.358 and 2.372 Å respectively. Bond Valence Sum (BVS) calculations were employed to confirm the Mn(III) oxidation state assignments in **10** as were all other Mn(III) containing members of this series (see Table C1 in Appendix C). Similarly the crystallographic data for all members of this series are located in Tables 11 and 12. The shorter equatorial Mn-O bonds at Mn1 and Mn3 (via the 2,2'-biphenolate O6-O9 atoms) range from 1.897 to 1.906 Å. The Mn2 metal ion in **10** is five coordinate and gives a calculated  $\tau$  value of 0.51, thus lying at the midway point between ideal trigonal bipyramidal ( $\tau = 1$ ) and square based pyramidal ( $\tau = 0$ ) geometry. The terminal pyridine ligand at the Mn2 site binds at the axial locale via N1 (Mn2-N1 = 2.192 Å). The coordination geometries at the Na(I) (Na1 and Na2) are also satisfied by terminal pyridines and produce the bond lengths Na1-N2 = 2.484 Å and Na2-N3 = 2.501 Å (Figure 47).

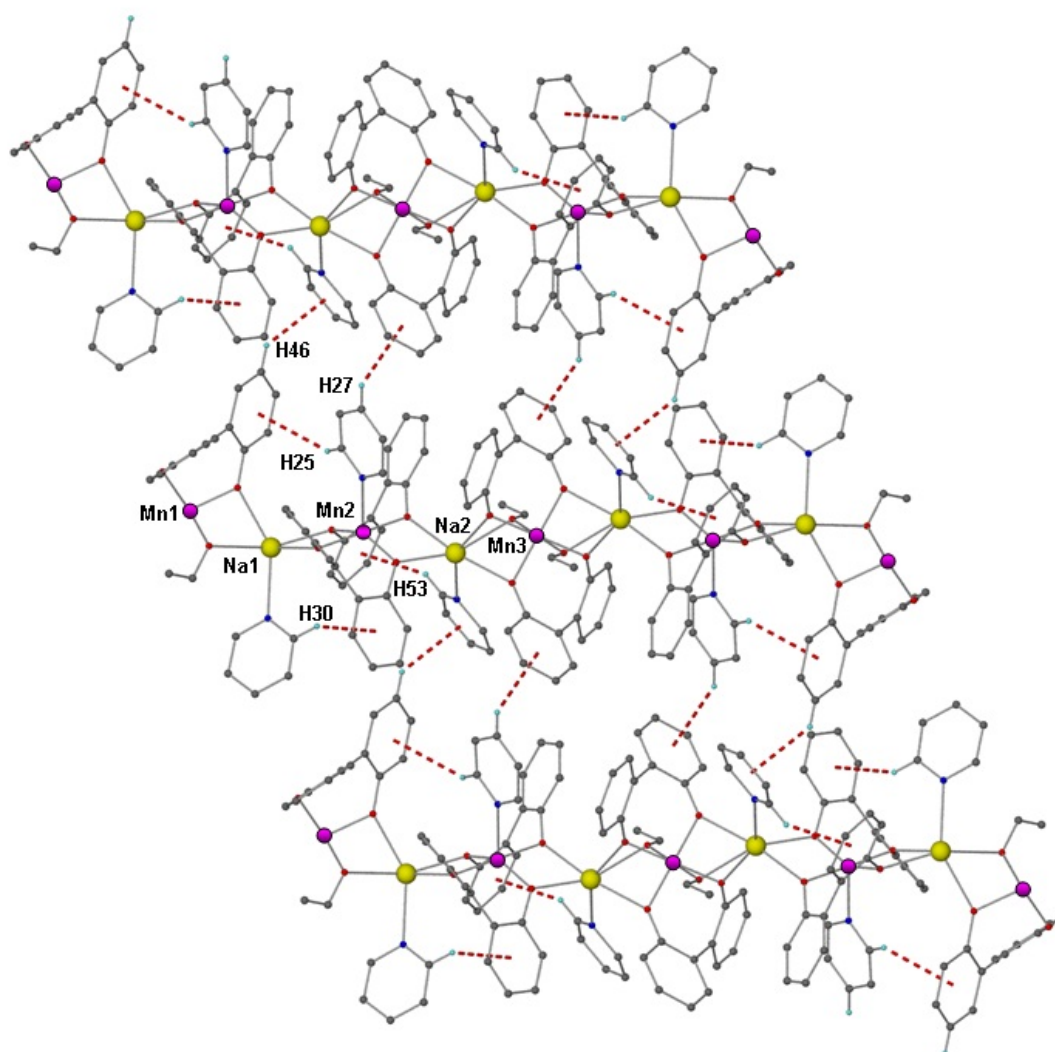


**Figure 49.** Crystal packing observed in the structure of **10**. Dashed lines highlight the inter- and intra-chain interactions observed in the crystal.

The 1-D arrays in **10** propagate along the *bc* diagonal (0 1 1) of the cell and due to their close proximity, three unique intra-chain C-H... $\pi$  interactions further stabilize the 1-D chain via the aromatic protons H25, H30 and H53 with contact distances of  $\text{H25}\cdots\pi_{\text{centroid}} = 2.998 \text{ \AA}$ ,  $\text{H30}\cdots\pi_{\text{centroid}} = 2.912 \text{ \AA}$  and  $\text{H53}\cdots\pi_{\text{centroid}} = 2.769 \text{ \AA}$  (Figure 49). The chains in **10** arrange via two unique C-H... $\pi$  intermolecular interactions ( $\text{H27}\cdots\pi_{\text{centroid}} = 2.910 \text{ \AA}$  and  $\text{H46}\cdots\pi_{\text{centroid}} = 2.846 \text{ \AA}$ ) to create a layer running parallel to the *bc* plane (Figure 50).

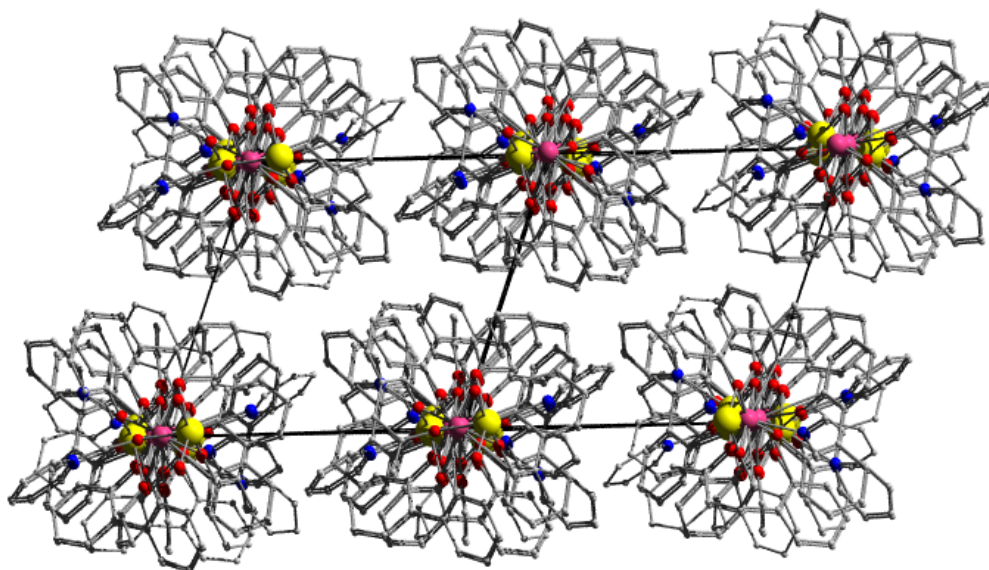


**Figure 50.** Crystal packing observed in **10** as viewed along the [011] cell face.

By using 3-picoline (3-methylpyridine) as our N donor co-ligand we produce an ionic chain in the form of  $[\text{Na}(\text{I})(\text{LH}_2)(\text{EtOH})_3][\text{Mn}(\text{III})(\text{L})_2(3\text{-pic})_2]$  (**11**) (Figure 51). Although built with very similar ligands the structures of polymers **10** and **11** are very different. As detailed earlier the chains in  $[\text{Na}(\text{I})_2\text{Mn}(\text{III})_2(\text{L})_4(\text{py})_3(\text{EtOH})_2]_n$  (**10**) are predominantly covalent in bonding character however the chains in **11** are comprised of strongly directional hydrogen bonding interactions. The chain in **11** crystallizes in the triclinic  $P\bar{1}$  space group and comprises  $[\text{Na}(\text{LH}_2)(\text{EtOH})_3]^+$  and  $[\text{Mn}(\text{L})_2(3\text{-pic})_2]^-$  ionic units which have assembled to create a one-dimensional chain by means of

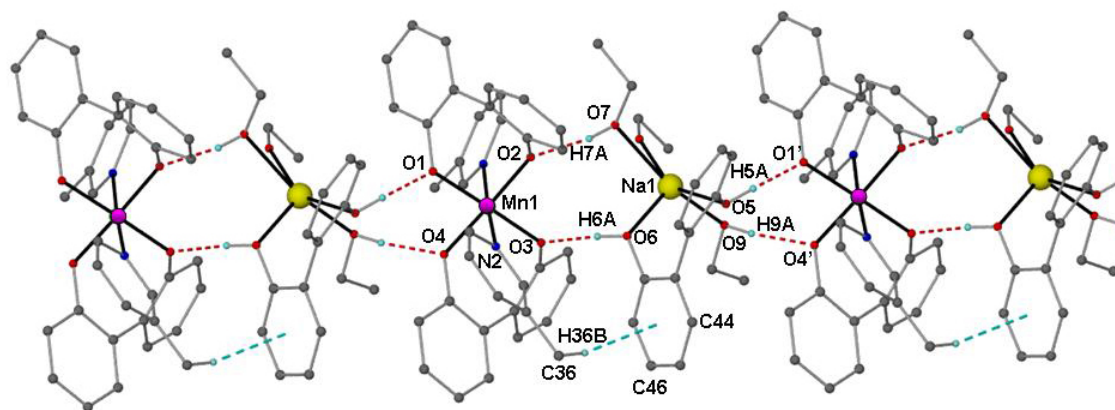


**Figure 51.** The H-bonded chain in **11**. The dashed lines represent the intra-chain interactions within the structure.

strong  $\text{O}-\text{H}\cdots\text{O}$  hydrogen bonds (Figure 51). Interactions are given as  $\text{O1}\cdots\text{H5A}(\text{O5}) = 1.692 \text{ \AA}$ ,  $\text{O2}\cdots\text{H7A}(\text{O7}) = 1.838 \text{ \AA}$ ,  $\text{O3}\cdots\text{H6A}(\text{O6}) = 1.674 \text{ \AA}$  and  $\text{O4}\cdots\text{H9A}(\text{O9}) = 1.842 \text{ \AA}$ . Moreover  $\text{C}-\text{H}\cdots\pi$  interactions (i.e.  $\text{H36B}\cdots\pi_{\text{centroid}} = 2.903 \text{ \AA}$ ) are also

observed and run along the  $a$  axis of the unit cell in **11** while a sole C-H $\cdots\pi$  edge-to-face interaction exists in between the individual 1-D rows in **11** ( $\text{H54B}\cdots\pi_{\text{centroid}} = 3.245 \text{ \AA}$ ). In complex **10**, the ligand  $\text{LH}_2$  exists in its doubly deprotonated form ( $\text{L}^{2-}$ ) and exhibits the  $\eta^2:\eta^2,\mu_3$ -bonding motif as seen in Figure 48, each ligand coordinating to three metal ions. In complex **11**, each  $\text{LH}_2$  ligand chelates to just one metal centre: two doubly deprotonated ( $\text{L}^{2-}$ ) ligands chelate to Mn1, while one neutral ( $\text{LH}_2$ ) ligand chelates to Na1. Both chelating modes observed in complex **11** are illustrated in Figure 52.

### Chelating mode

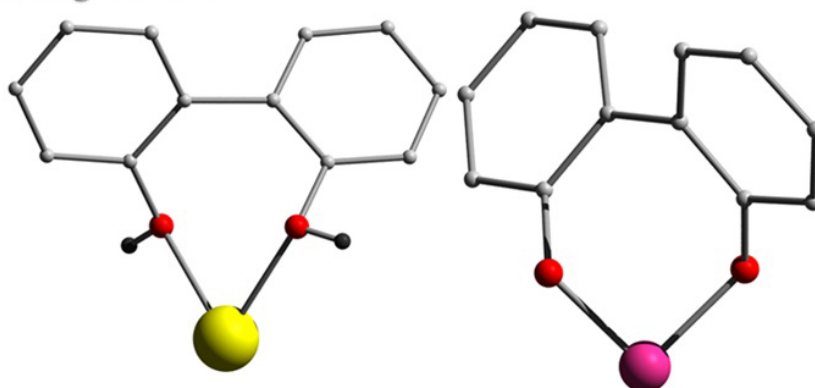


**Figure 52.** The chelating mode adopted by  $\text{LH}_2$  in the structure of the ionic chains.

The Na(I)/Fe(III) analogue to **11** is readily formed via the introduction of the  $\text{Fe(II)Cl}_2 \cdot 4\text{H}_2\text{O}$  salt to give the ionic chain  $[\text{Na(I)(LH}_2)(\text{EtOH})_3][\text{Fe(III)(L)}_2(3\text{-pic})_2]_n$  (**12**) (Figure 53). For comparative purposes all the main bonding atoms in the crystal

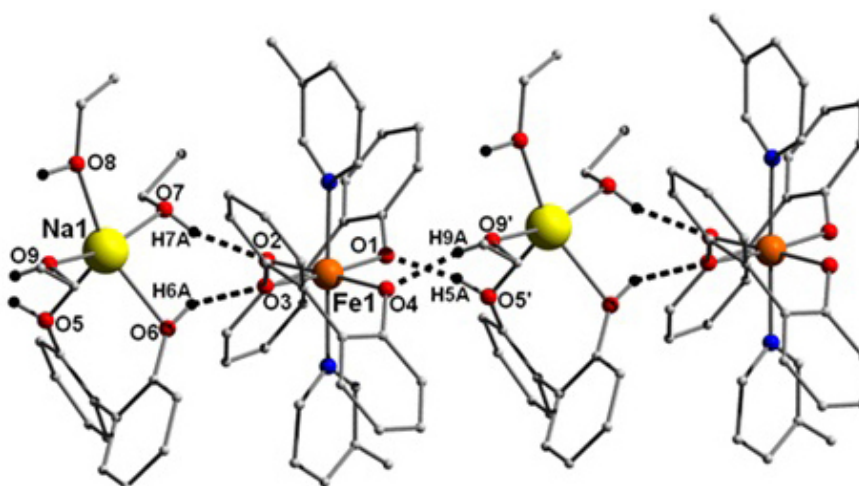


**Figure 53.** The H-bonded chain in **12**. Colour code: Orange (Fe), Yellow (Na), Red (O), Blue (N) and Grey (C). Dashed lines represent hydrogen bonding interactions.

structure of **12** (and **13** *vide supra*) were labelled identically to that of **11**. Strong directional hydrogen bonds connect the  $[\text{Na}(\text{LH}_2)(\text{EtOH})_3]^+$  and  $[\text{Fe}(\text{L})_2(3\text{-pic})_2]^-$  moieties in **12** via the donor phenolic (H5A and H6A) and ethanolic protons (H7A and H9A) and the acceptor O atoms O1-O4. These H-bonding distances were found to be  $\text{O1}\cdots\text{H5A}(\text{O5}) = 1.716 \text{ \AA}$ ,  $\text{O2}\cdots\text{H7A}(\text{O7}) = 1.894 \text{ \AA}$ ,  $\text{O3}\cdots\text{H6A}(\text{O6}) = 1.980 \text{ \AA}$  and  $\text{O4}\cdots\text{H9A}(\text{O9}) = 1.867 \text{ \AA}$ . Apart from these linker H-bonds no other significant interactions are apparent within these chains which align in superimposable rows along the *a* axis of the cell in **12** (Figure 54). Inter-chain close contacts take the form of just one long C-H $\cdots$  $\pi$  edge-to-face interaction ( $\text{C50}(\text{H50B})\cdots\pi_{\text{centroid}} = 3.205 \text{ \AA}$ ).

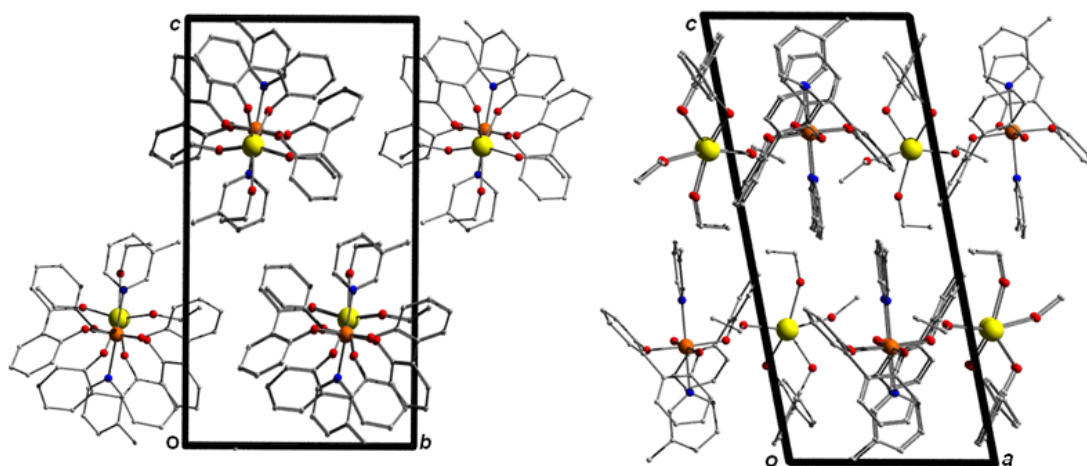


**Figure 54.** Crystal packing observed in **12** as viewed down the *a* (left) and *b* axis (right) respectively.

In order to promote the potential formation of 2 or 3-D extended nets we decided to replace the terminal N-donor ligand in **10-12** with the occasionally ditopic 4-cyanopyridine (4-cnp) [213], [214]. This in fact leads to another ionic chain in the form of  $[\text{Na}(\text{I})(\text{LH}_2)(\text{EtOH})_2(\text{H}_2\text{O})][\text{Mn}(\text{III})(\text{L})_2(4\text{-cnp})_2]_n$  (**13**). The polymer in **13** crystallizes in the monoclinic space group  $\text{P2}_1/\text{n}$  and the a.s.u contains one anionic  $\{\text{Mn}(\text{L})_2(4\text{-cnp})_2\}^-$  and one cationic  $[\text{Na}(\text{LH}_2)(\text{EtOH})_2(\text{H}_2\text{O})]^+$  monomeric unit (Figure 55). The anionic  $[\text{Mn}(\text{L})_2(4\text{-cnp})_2]^-$  unit possesses a Jahn-Teller axially elongated distorted octahedral Mn(III) ion (Mn1) at its centre. At the equatorial sites of this unit are situated four oxygen atoms of two chelating doubly deprotonated  $\text{L}^{2-}$  ligands. As regularly noted in coordination chemistry [215–217], the two 4-cnp ligands bond terminally to Mn1 at the axial positions via their ring nitrogen atoms ( $\text{Mn1-N2} =$

2.371 Å and Mn1-N3 = 2.372 Å), while the equatorial Mn-O<sub>biphen</sub> distances range between 1.888 – 1.935 Å. A five coordinate Na(I) ion (Na1) lies at the centre of the monomeric [Na(LH<sub>2</sub>)(EtOH)<sub>2</sub>(H<sub>2</sub>O)]<sup>+</sup> unit in **13** which possesses a +1 charge. The role of charge balancing lies with the anionic manganese monomer to form the neutral species. Two oxygen atoms belonging to the neutral LH<sub>2</sub> ligand chelate to the alkali metal ion. The Na-O<sub>biphen</sub> bond lengths are Na1-O5 = 2.358 Å and Na1-O6 = 2.330 Å

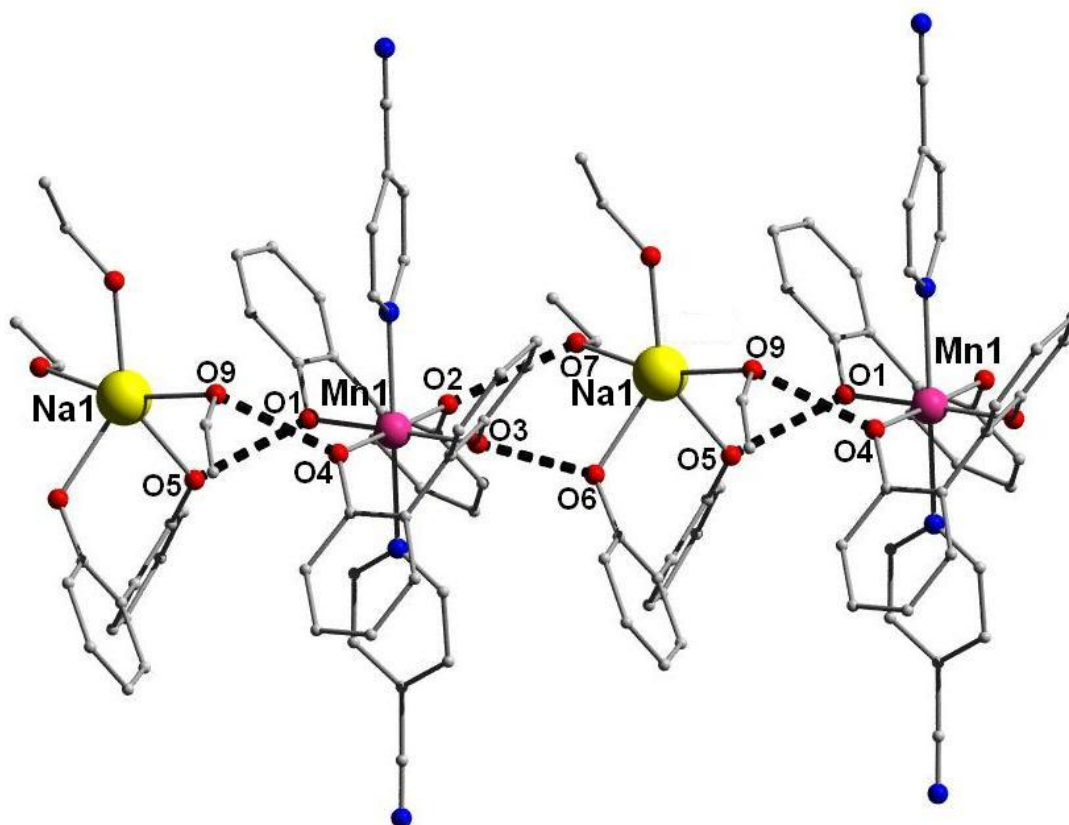


**Figure 55.** The H-bonded chain in **13**. Colour code as in Figure 47. Dashed lines represent hydrogen bonding interactions.

while the three remaining coordination sites are each occupied by two terminally ligated ethanol ligands (via O7 and O8) and a terminal water molecule (O9). These Na-O<sub>(ethanol)</sub> bond lengths are given as 2.323 Å (Na1-O7) and 2.335 Å (Na1-O8) while the Na1-O9 distance is shown to be 2.316 Å. Akin to the ionic Na/Mn and Na/Fe chains **11** and **12** respectively, the two mononuclear units in **13** partake in strong H-bonding interactions to form infinite 1-D arrays of alternating Mn(III) and Na(I) units which propagate along the *a* axis of the unit cell (Figure 56a). These assemblies arise due to intra-chain H-bonding between the deprotonated L<sup>2-</sup> oxygen atoms (O1-O4) of the [Mn(L)<sub>2</sub>(4-cnp)<sub>2</sub>]<sup>-</sup> unit, and the protons belonging to the EtOH and H<sub>2</sub>O terminal

ligands around the sodium monomer. More specifically these H-bonding donor protons originate from the chelating protonated  $LH_2$  ligand (via H5A and H6A) and via the protons from the terminal EtOH (via O7(H7A)) and  $H_2O$  ligands (O9). These H-bond distances are highlighted by the dashed lines in Figure 55 (as well as Figure 56a) and the distances are:  $O1\cdots H5A(O5) = 1.773 \text{ \AA}$ ,  $O2\cdots H7A(O7) = 1.863 \text{ \AA}$ ,  $O3\cdots H6A(O6) = 1.742 \text{ \AA}$  and  $O4\cdots O9 = 2.748 \text{ \AA}$ . The chains in **13** are further connected through O-H $\cdots$ N hydrogen bonds via the terminal bound EtOH ligands (O8(H8A)) and the nitrile N atoms (N4'') of a nearby 4-cnp ligands ((O8)H8A $\cdots$ N4'' = 2.276  $\text{\AA}$ ). These inter-chain interactions create a 2-D layer parallel to the *ac* plane (Figure 56a).

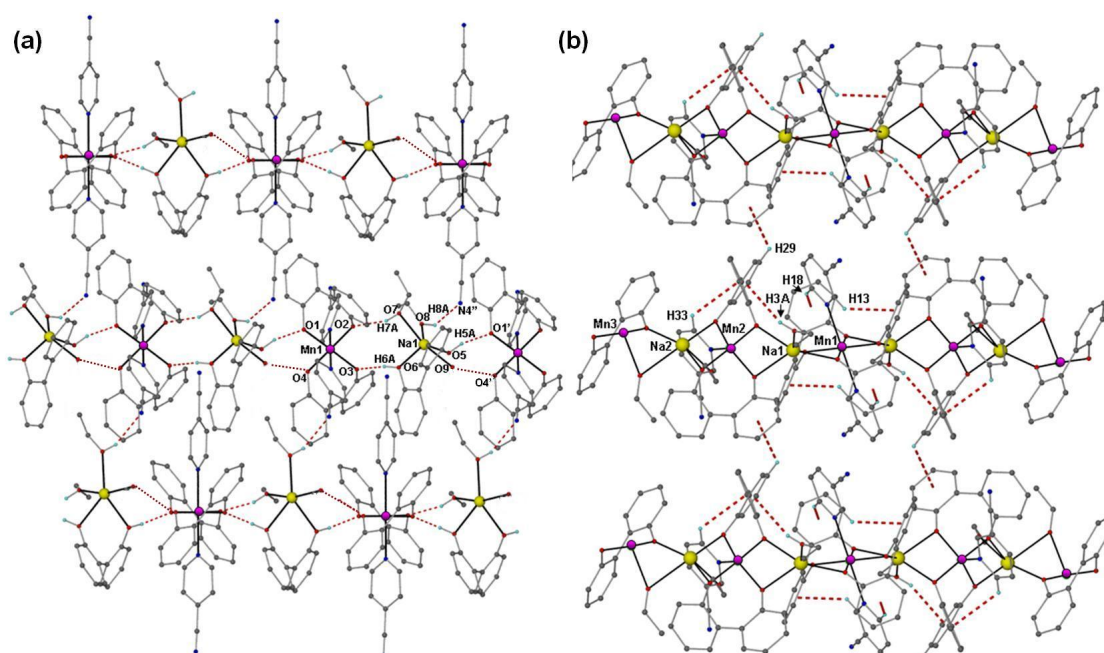


**Figure 56.** The H-bonded chains in **13** (a) and covalent chains in **14** (b). The dashed lines represent both the intra- and inter-chain interactions within the structures.

The replacement of the 4-cyanopyridine ligand with 3-cyanopyridine (3-cnp) produces our second example of an covalently assembly chain of formula  $[Na(I)_2Mn(III)_2(L)_4(3-cnp)_2(EtOH)_3]_n$  (**14**) (Figure 56b, Figure 57): a polymeric assembly structurally very similar to that of  $[Na(I)_2Mn(III)_2(L)_4(py)_3(EtOH)_2]_n$  (**10**). For comparative purposes the bonding atoms in the crystal structure of **14** were labelled identically to that of **10**. As seen in the structure of **10** the asymmetric unit in **14** contains three Mn(III) centres (Mn1-3) and two Na(I) ions (Na1 and Na2) (Figure 56b, Figure 57). These metal ions are connected into a 1-D topology via bridging  $LH_2$  ligands in the same vein as previously seen in **10** (via the  $\eta^2:\eta^2,\mu_3$ -bonding motif;

Figure 47). Likewise the Mn2 (and s.e) metal centre is five coordinate with a calculated  $\tau$  value of 0.54 and therefore also lies midway between ideal trigonal bipyramidal ( $\tau = 1$ ) and distorted square based pyramid ( $\tau = 0$ ) geometry. The coordination spheres at the Na and Mn metal centres are completed by terminal EtOH solvent molecules and the 3-cnp ligands (Figure 57). When comparing the structures of **10** and **14** it becomes clear that the only major difference between the two architectures lies at the Na(I) centres (Na1 and Na2). In **10** each of the Na(I) ions are coordinated to a single terminal pyridine ligand while in **14** all Na(I) centres are

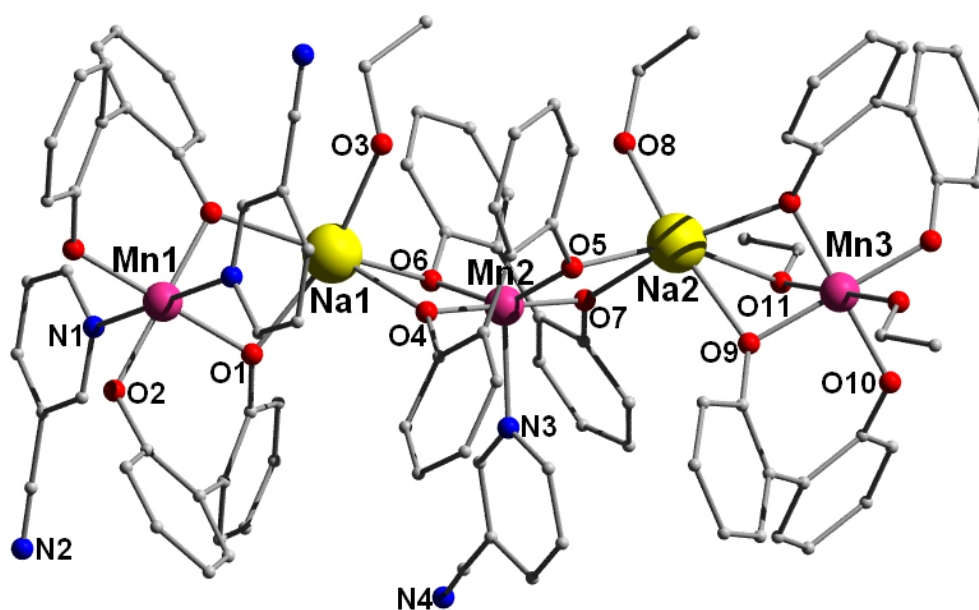


**Figure 57.** Asymmetric unit in the covalent polymer **14** illustrating its structural similarities (although *not* isostructural) to that of **10**. Colour code as in Figure 47, hydrogen atoms have been omitted for clarity.

each coordinated to one EtOH ligand (Figure 47 cf. Figure 57). The individual components in **14** have assembled to create a chain structure along the [1-1-1] line, which is stabilised by four unique intra-chain C-H $\cdots$  $\pi$  interactions. These distances are represented by dashed lines in Figure 56b and are given as ( $\text{\AA}$ ): H13 $\cdots$  $\pi_{\text{centroid}} = 2.738$ , H3A $\cdots$  $\pi_{\text{centroid}} = 2.754$  and H18 $\cdots$  $\pi_{\text{centroid}} = 2.747$   $\text{\AA}$ .

The introduction of the co-ligand 4-Ethyl pyridine (4-Et-py) into the Mn(II) / LH<sub>2</sub> / base ethanolic reaction mixture also produces a covalent chain of molecular formula  $[\{\text{Na(I)}_2\text{Mn(III)}_2(\text{biphen})_4(4\text{-Et-py})_3(\text{EtOH})_2\}.\text{EtOH}]_n$  (**15**) (Figure 58). The asymmetric unit in **15** contains two Na(I) (Na1 and Na2) and Mn(III) ions (Mn1 and Mn2) which are linked into the -Na-Mn-Na- alternating topology via four  $\eta^2:\eta^2:\mu_3$ -

bonding  $L^{2-}$  ligands. The coordination spheres at the five coordinate distorted square based pyramidal Na1 site ( $\tau = 0.15$ ) is completed by a terminal EtOH ligand (via O1T). The second Na(I) centre in the a.s.u (Na2) has four of its six coordinate distorted octahedral sites occupied by O donor atoms (O1A, O1D, O1E and O14B) from the bridging  $L^{2-}$  ligands, while the final two places are occupied by one terminal EtOH (via O1U) solvent molecule (disorder over two sites) and one terminal 4-Et-pyridine ligand at a sizeable distance of Na2-N1V = 2.987 Å. As a result of this long contact this pyridyl ligand does not sit parallel to the Na2-N1V plane, choosing

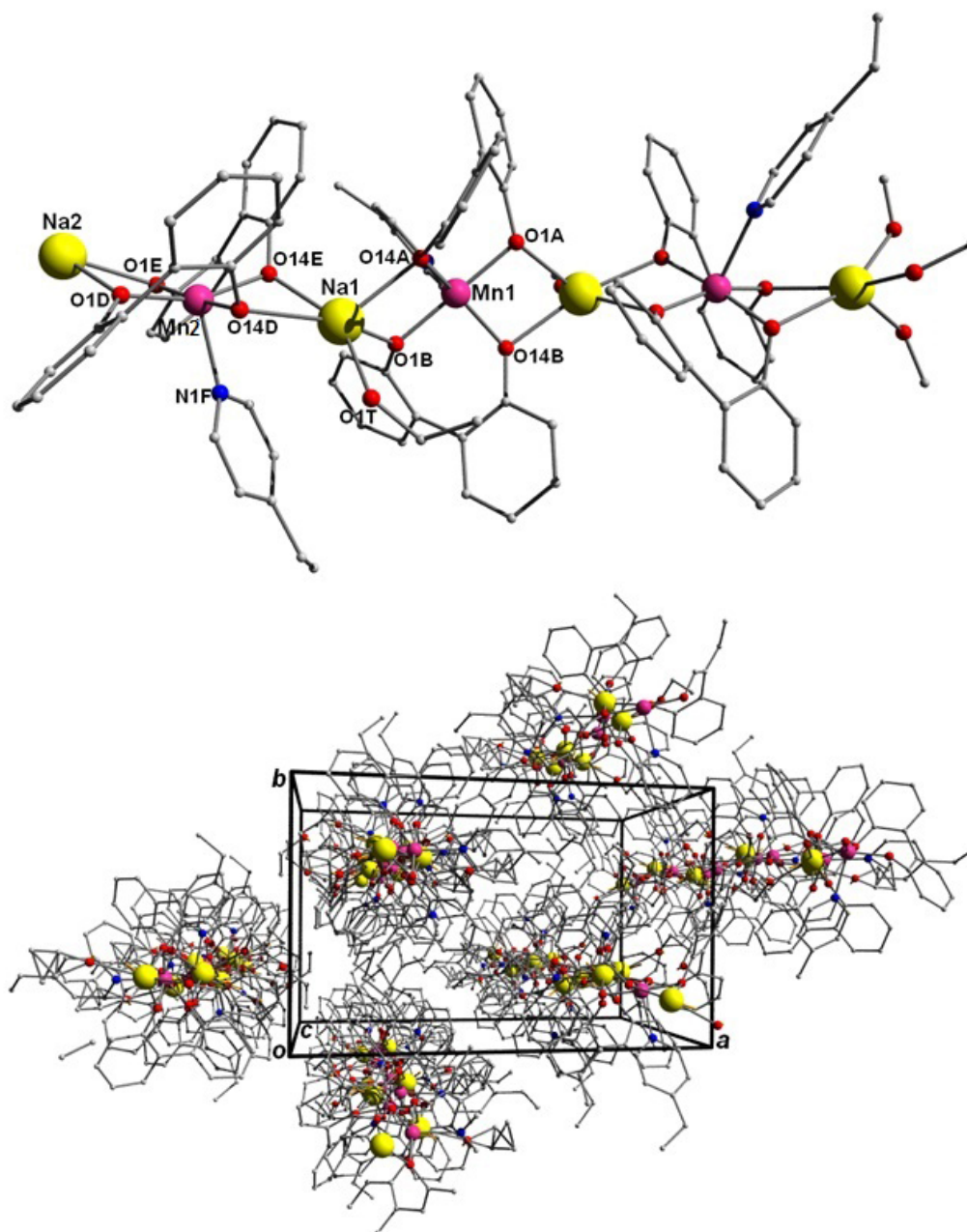


**Figure 58.** (top) Part of a 1-D row in chain **15**. Hydrogen atoms have been omitted for clarity. (bottom) View of the chains in **15** propagating along the *c* cell direction.

to lie off kilter to give an Na2-N1V-C4V angle of 132.64°. The two Mn(III) sites in **15** are five coordinate and give calculated  $\tau$  values of 0.55 (Mn1) and 0.27 (Mn2) respectively to highlight the more square bipyramidal nature of Mn2 and the intermediate nature of Mn1. Four of the five coordination sites on both these Mn(III) centres are occupied by O donor atoms (via L<sup>2-</sup> ligands) while the final spots are taken by terminal 4-Et-pyridine ligands to give the distances (Å): Mn1-N1C = 2.213 and Mn2-N1F = 2.224. An EtOH solvent molecule of crystallisation lies near the terminally coordinated EtOH ligand. The resultant hydrogen bond stems from the EtOH ligand proton (H1T) interacting with the nearby unattached EtOH solvent molecule (O1S) at a distance of (O1T)H1T...O1S = 1.838 Å. The proton of this very same EtOH solvent molecule (H1S bonded to O1S) also interacts with a nearby proton of a bridging L<sup>2-</sup> ligand (via O14D) to give a H-bond distance of 2.050 Å. The 1-D rows in **15** propagate along the *c* axis of the unit cell. The individual rows exhibit intra-chain contacts which include the (C2U)H2U2... $\pi_{\text{centroid}}$  = 2.546 Å and (C2T)H2T2... $\pi_{\text{centroid}}$  = 2.766 Å interactions, each emanating from terminal EtOH alkyl protons and juxtaposed L<sup>2-</sup> aromatic rings (Figure 58).

**Table 11.** Crystallographic data for complexes **10-13**

	<b>10</b>	<b>11</b>	<b>12</b>	<b>13</b>
Formula <sup>a</sup>	C <sub>67</sub> H <sub>59</sub> N <sub>3</sub> O <sub>10</sub> Mn <sub>2</sub> Na <sub>2</sub>	C <sub>54</sub> H <sub>58</sub> N <sub>2</sub> O <sub>9</sub> MnNa	C <sub>54</sub> H <sub>58</sub> N <sub>2</sub> O <sub>9</sub> FeNa	C <sub>52</sub> H <sub>46</sub> N <sub>4</sub> O <sub>9</sub> MnNa
<i>M</i> <sub>w</sub>	1222.03	956.95	957.86	948.86
Crystal System	Triclinic	Triclinic	Triclinic	Monoclinic
Space group	P-1	P-1	P-1	P2 <sub>1</sub> /n
<i>a</i> /Å	11.814(2)	10.350(2)	10.342(2)	10.377(2)
<i>b</i> /Å	12.513(3)	11.989(2)	12.133(2)	21.331(4)
<i>c</i> /Å	22.786(5)	21.671(4)	21.457(4)	23.121(5)
$\alpha$ /°	96.06(3)	86.90(3)	86.03(3)	90.00
$\beta$ /°	98.11(3)	78.51(3)	78.40(3)	99.53(3)
$\gamma$ /°	115.49(3)	69.14(3)	68.86(3)	90.00
<i>V</i> /Å <sup>3</sup>	2957.6(10)	2462.1(9)	2459.9(9)	5047.4(18)
<i>Z</i>	2	2	2	4
<i>T</i> /K	150(2)	150(2)	150(2)	150(2)
$\lambda$ <sup>b</sup> /Å	0.7107	0.7107	0.7107	0.7107
<i>D</i> <sub>c</sub> /g cm <sup>-3</sup>	1.372	1.291	1.293	1.249
Meas./indep.( <i>R</i> <sub>int</sub> )	10822 / 6185	9016 / 6299	9008 / 3555	9233 / 5854
refl.	(0.0599)	(0.0610)	(0.1151)	(0.0725)
wR2 (all data)	0.1225	0.0941	0.1951	0.1069
<i>R</i> <sub>1</sub> <sup>d,e</sup>	0.1411	0.1454	0.0863	0.2473
Goodness of fit on <i>F</i> <sup>2</sup>	0.966	1.065	0.951	1.059

**Table 12.** Crystallographic data for complexes **14-17**

	<b>14</b>	<b>15</b>	<b>16</b>	<b>17</b>
Formula <sup>a</sup>	C <sub>66</sub> H <sub>58</sub> N <sub>4</sub> O <sub>11</sub> Mn <sub>2</sub> Na <sub>2</sub>	C <sub>75</sub> H <sub>77</sub> N <sub>3</sub> O <sub>11</sub> Mn <sub>2</sub> Na <sub>2</sub>	C <sub>44</sub> H <sub>34</sub> N <sub>4</sub> O <sub>4</sub> Mn	C <sub>38</sub> H <sub>36</sub> N <sub>2</sub> O <sub>6</sub> FeNa
<i>M<sub>w</sub></i>	1239.02	1352.26	737.69	695.53
Crystal System	Triclinic	Monoclinic	Tetragonal	Orthorhombic
Space group	P-1	P2 <sub>1</sub> /c	I4 <sub>1</sub> /a	Pbca
<i>a</i> /Å	11.293(2)	21.3738(6)	16.357(2)	20.326(4)
<i>b</i> /Å	15.606(3)	12.8753(4)	16.357(2)	12.942(3)
<i>c</i> /Å	17.596(4)	24.8333(8)	26.747(5)	24.997(5)
<i>α</i> <sup>o</sup>	84.81(3)	90	90	90
<i>β</i> <sup>o</sup>	77.73(3)	104.246(3)	90	90
<i>γ</i> <sup>o</sup>	81.07(3)	90	90	90
<i>V</i> /Å <sup>3</sup>	2988.3(10)	6623.8(3)	7156(2)	6576(2)
<i>Z</i>	2	4	8	8
<i>T</i> /K	150(2)	150(2)	150(2)	150(2)
<i>λ</i> <sup>b</sup> /Å	0.7107	1.5418	0.7107	0.7107
<i>D<sub>c</sub></i> /g cm <sup>-3</sup>	1.377	1.356	1.369	1.405
Meas./indep.( <i>R</i> <sub>int</sub> )	10920 / 5906	13175 / 8935	3076 / 1770	6010 / 2535
refl.	(0.0814)	(0.0391)	(0.0497)	(0.0314)
w <i>R</i> 2 (all data)	0.1580	0.0906	0.1043	0.1229
<i>R</i> 1 <sup>d,e</sup>	0.1366	0.0635	0.0917	0.0358
Goodness of fit on <i>F</i> <sup>2</sup>	1.036	0.895	0.868	0.661

The replacement of the unidentate pyridine type ligands in **10-15** with the chelating ligand 2,2'-bipyridine in the general Mn(II) salt / LH<sub>2</sub> / NaOH synthon used so far in this work, leads to the formation of the discrete mononuclear [Mn(II)(LH)<sub>2</sub>(2,2'-bipy)<sub>2</sub>] (**16**) species whose asymmetric unit comprises one metal centre, one singly deprotonated LH<sub>2</sub> ligand (LH<sup>-</sup>) and one 2,2'-bipyridine ligand only. Complex **16**

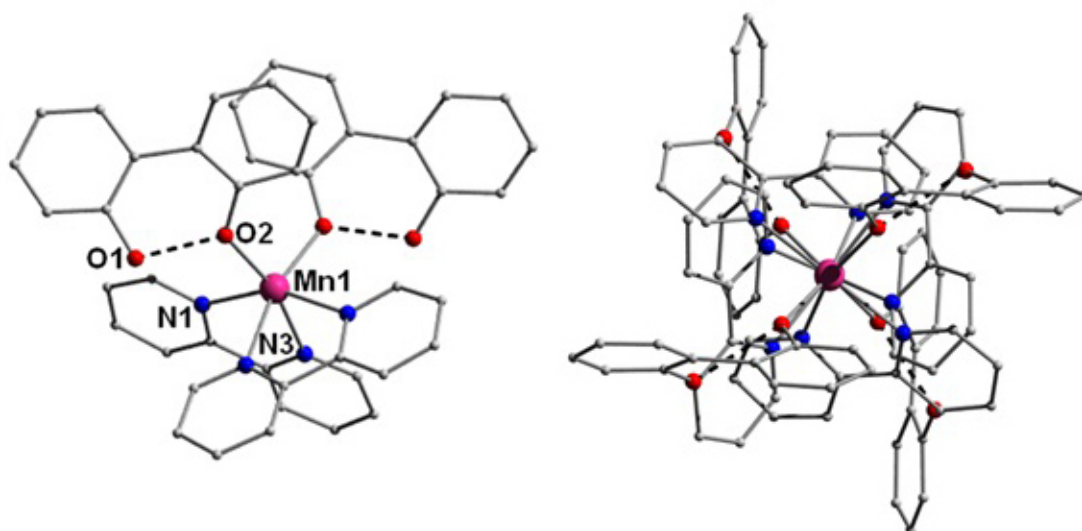


**Figure 59.** Crystal structure of the monomeric complex **16**. Dashed lines represent the intramolecular H-bonding interactions. (bottom) View of **16** down the *c* axis of the unit cell. Colour code as in Figure 47.

crystallizes in the tetragonal  $I4_1/a$  space group and comprises of a distorted octahedral Mn(II) metal centre (Mn1) bonded to two crystallographically identical singly deprotonated  $\text{LH}^-$  ligands via the phenolic oxygen atoms O2. The second  $\text{LH}^-$  oxygen remains protonated (H1-O1 and s.e) and hydrogen bonds to O2 in an intramolecular fashion at a distance of 1.695 Å (Figure 59). The coordination sphere at Mn1 is completed by two chelating 2,2'-bipyridine ligands via the nitrogen donor atoms N1 and N3 (Mn1-N1 = 2.261 Å, Mn1-N3 = 2.326 Å). The oxidation state of Mn1 was confirmed using bond length and charge balancing considerations while BVS calculations were then employed to confirm our assignment (Table C1 in Appendix C). The crystal packing in **16** is driven by the formation of 1-D zig-zag chains of  $[\text{Mn}(\text{II})(\text{LH})_2(\text{bipy})_2]$  units linked by two supramolecular interactions. The first is a weak hydrogen bond between a protonated phenolic oxygen (O1) of the  $\text{LH}^-$  ligands with an aromatic proton of a 2,2'-bipy ligand on an adjacent  $[\text{Mn}(\text{II})(\text{LH})_2(\text{bipy})_2]$  unit ( $\text{O1}\cdots\text{H20}(\text{C20}) = 2.600 \text{ \AA}$ ). The second intermolecular linkage forging these 1-D chains are  $\pi$ - $\pi$  (off-set) stacking interactions again via neighbouring 2,2'-bipyridine ligands ( $\pi_{\text{centroid}}\cdots\pi_{\text{centroid}} = 3.872 \text{ \AA}$ ) (Figure 60).

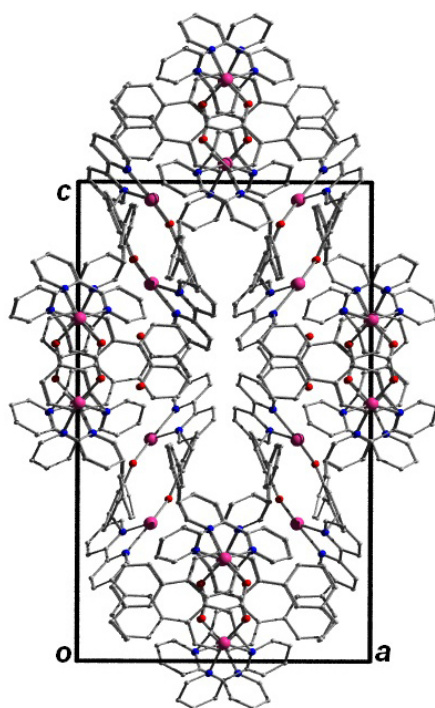


**Figure 60.** Crystal packing observed in complex **16** as viewed along the  $b$  axis. The 1-D zig zag rows of  $[\text{Mn}(\text{LH})_2(\text{bipy})_2]$  units propagate along the  $a$  axis and therefore across the page.

By simply replacing the Mn(II) salt precursor with Fe(II)Cl<sub>2</sub>·6H<sub>2</sub>O we once again produce a 1-D covalent chain: [Na(I)Fe(III)(L)<sub>2</sub>(2,2-bipy)(EtOH)<sub>2</sub>]<sub>n</sub> (**17**) (Figure 61), which crystallizes in the orthorhombic Pbc<sub>a</sub> space group. The asymmetric unit in **8** contains one Na(I) ion (Na1) and a single Fe(III) metal centre (Fe1). The six coordinate Na(I) ion is bonded entirely to oxygen donor atoms donated by doubly deprotonated  $\eta^2:\eta^2\mu_3$ -bonding L<sup>2-</sup> ligands (via O1-O4) and two terminal EtOH solvent molecules (via O5 and O6) to give a distorted octahedral geometry. Beyond the asymmetric unit, the compound exists as an infinite 1-D chain, comprising alternating Fe(III) and Na(I) components that propagate along [010]. Na1 and Fe1 are bridged via two oxygen atoms (O2 and O4), one from each doubly deprotonated L<sup>2-</sup>, generating Na1–O2–Fe1 and Na1–O4–Fe1 angles of 101.71° and 102.93° respectively.

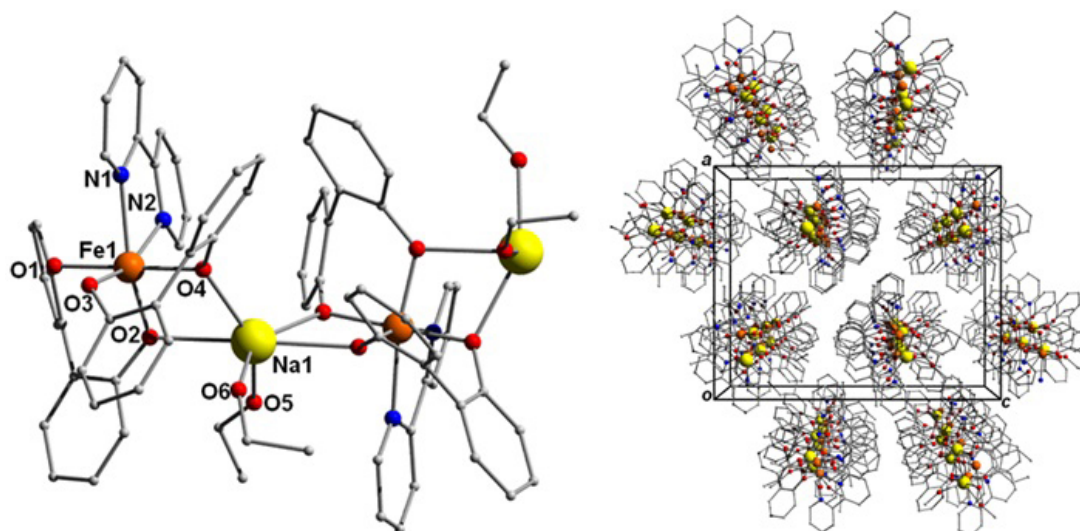


**Figure 61.** Crystal structure of the Na(I)/Fe(III) covalent chain of **17**. All pertinent bonding atoms in the asymmetric unit are labelled. (bottom) Crystal packing in **17** viewed along the *b* cell axis. Colour code: Orange (Fe), Yellow (Na), Red (O), Blue (N) and Grey (C).

The two residual deprotonated oxygen atoms (O1 and O3) of these L<sup>2-</sup> ligands are involved in bridging Fe1 to the next Na(I) ion (Na1') along the chain to produce Fe1–O1–Na1' and Fe1–O3–Na1' angles of 98.17° and 113.17° respectively. The six-coordinate distorted octahedral geometry of Na1 is completed by two terminal ethanol ligands. The Fe(III) cations are also six coordinate; chelated by the bidentate ligand 2,2'-bipyridine via N1 and N2 (Fe1–N1 = 2.240 Å, Fe1–N2 = 2.220 Å) and completing their distorted octahedral geometry (Figure 61). A sole intra-chain H-bonding interaction is observed via a proton of a terminal EtOH molecule (H5H) and a

phenolic oxygen atom (O1) of an adjacent bridging  $L^{2-}$  anion ( $H5H(O5)\cdots O1 = 1.842$  Å). Other intra-chain short contacts are observed which include  $C37(H37A)\cdots\pi_{\text{centroid}} = 2.715$  Å and  $O6(H6H)\cdots\pi_{\text{centroid}} = 2.817$  Å; as highlighted by the dashed black lines in Figure 62. Furthermore the dashed blue lines represent the sole interchain close contacts observed in **17**, giving the distance  $C35(H35A)\cdots C22_{(\text{aromatic})} = 2.895$  Å. The 1-D assemblies in **17** propagate along the *b* axis while the individual chains arrange in the common brickwork pattern within the unit cell (Figure 61).

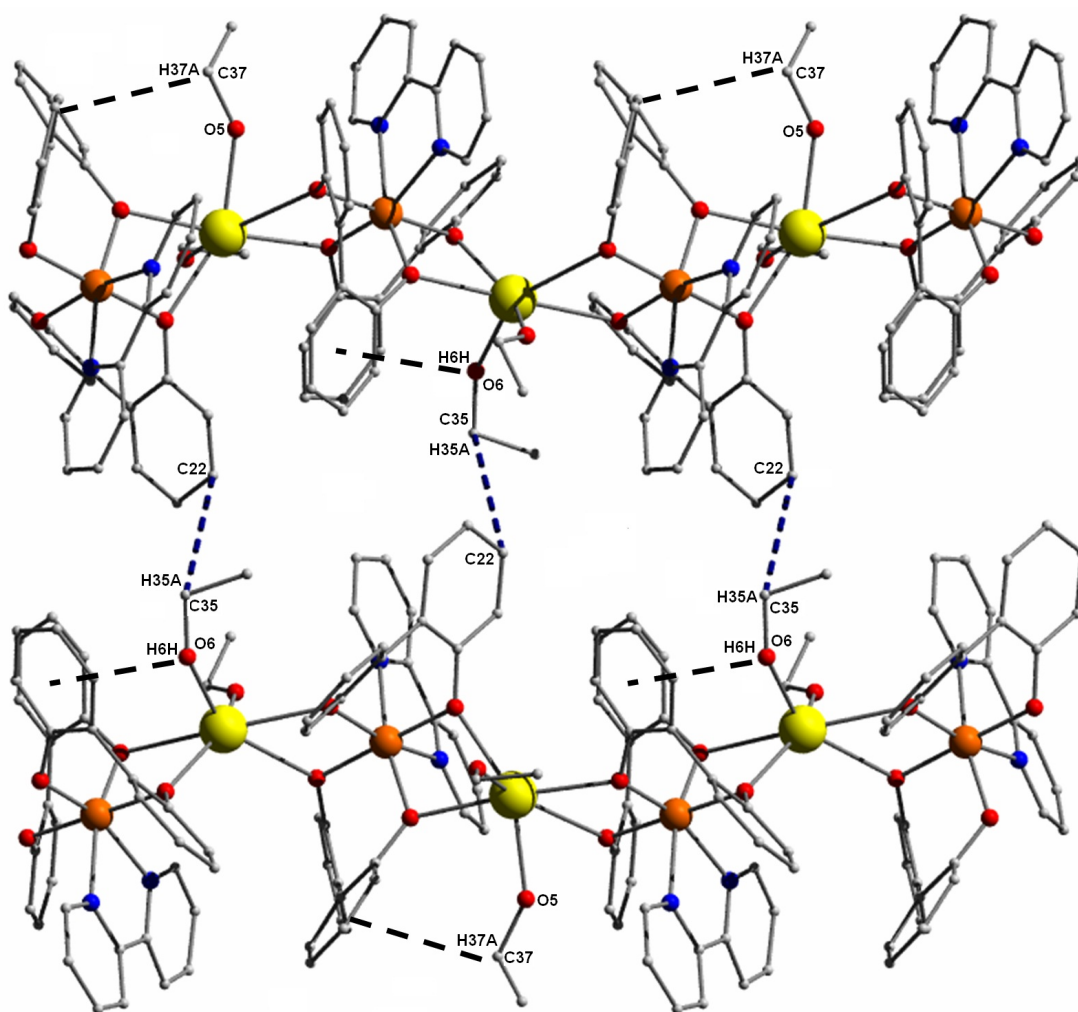


**Figure 62.** Crystal structure of **17** showing various intra- and inter-chain interactions exhibited within the crystal. H atoms have been omitted for clarity. Colour code as in Figure 61.

#### 4.2.2 Discussion

Attempt to rationalise which factors determines whether an H-bonded or covalent chain is produced here is aided by the fact that the type of N-donor pyridyl ligand used is the only variable in the synthetic procedures adopted in this work. Thus on

close inspection of all members we can first conclude that regardless of whether the pyridyl ligand used is functionalised at the 3- or 4-position, both H-bonded and covalent chains can be produced (as illustrated in Figure 63). More specifically the ligands 3-picoline and 3-cyanopyridine have produced 1 × covalent chain ( $[\text{Na(I)}_2\text{Mn(III)}_2(\text{L})_4(3\text{-cnp})_2(\text{EtOH})_3]_n$  (**14**)) and 2 × H-bonded 1-D polymers ( $[\text{Na(I)}(\text{LH}_2)(\text{EtOH})_3][\text{Mn(III)}(\text{L})_2(3\text{-pic})_2]_n$  (**11**) and  $[\text{Na(I)}(\text{LH}_2)(\text{EtOH})_3][\text{Fe(biphen)}_2(3\text{-pic})_2]_n$  (**12**)), while the 4-cyanopyridine and 4-Ethylpyridine ligands form 1 × hydrogen bonded chain (**13**) and 1 × covalent 1-D polymer in the shape of

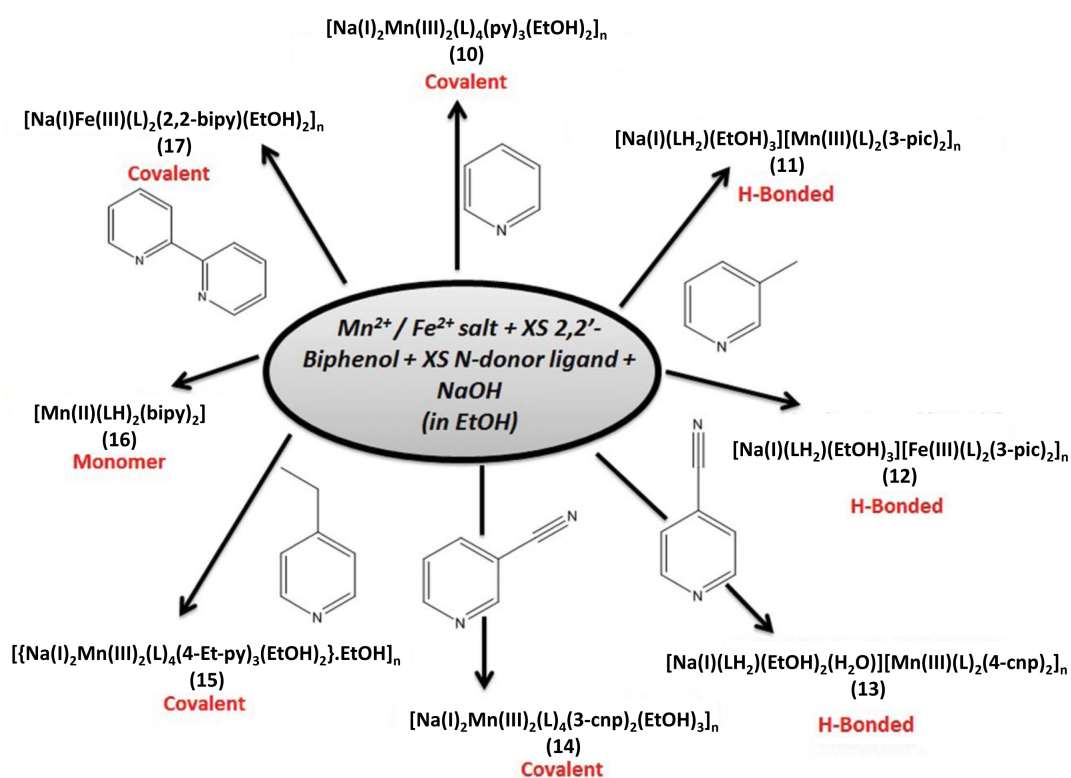


**Figure 63.** Schematic highlighting the different types of chains (covalent vs. H-bonded) observed in this work depending on the ligands employed.

**15** respectively. These findings effectively rule out any steric arguments for the domination of one chain type over another. Secondly we notice that H-bonded chain structures rely on protonated  $\text{LH}_2$  ligands (in part) to produce their unique structures while covalent chains exhibit completely deprotonated  $\text{L}^{2-}$  ligands. This prompted analysis of the  $\text{pK}_b$  values of the pyridyl ligands employed here, as a *competition for ligand protons* scenario was hypothesised to affect the final products obtained. However this theory was quickly discounted as the 3- and 4-cyanopyridine moieties of comparable ligand basicities ( $\text{pK}_b = 12.61$  and  $12.08$  respectively) produce

covalent and H-bonded chains in the form of  $[\text{Na(I)}_2\text{Mn(III)}_2(\text{L})_4(3\text{-cnp})_2(\text{EtOH})_3]_n$  (**14**) and  $[\text{Na(I)}(\text{LH}_2)(\text{EtOH})_2(\text{H}_2\text{O})][\text{Mn(L)}_2(4\text{-cnp})_2]_n$  (**13**) respectively. Indeed we cannot see any discernable scientific trends within this series in terms of their specific structure and must concede that the nature of the 1-D polymer produced here must depend on the finely balanced interplay between a number of crystallisation factors such as: 1) reaction solution concentrations; 2) the specific crystallisation conditions (temperature, pressure, pH); 3) the number and strength of inter-molecular interactions involved and 4) product(s) solubility. Furthermore we cannot rule out that both types of chain structures (H-bonded vs. covalent) may be present in these complex mixtures and the more stable moieties are formed / crystallised first.

All the  $\text{LH}_2$  ligands aiding the construction of chains **10-15** and **17** exhibit a twisting with respect to their aromatic rings, presumably being forced into this configuration due to steric effects. Upon scrutinising their crystal structures it becomes clear that the optimum torsion angle forged by the two connected rings lie at an average of  $\sim 49^\circ$  (range:  $40.06\text{-}57.57^\circ$ ) (Figure 64), regardless of which bonding motif is employed ( $\eta^2:\eta^2\mu_3^-$ ,  $\eta^2:\eta^1:\mu^-$  or chelating). Moreover we should also note that when  $\text{LH}_2$

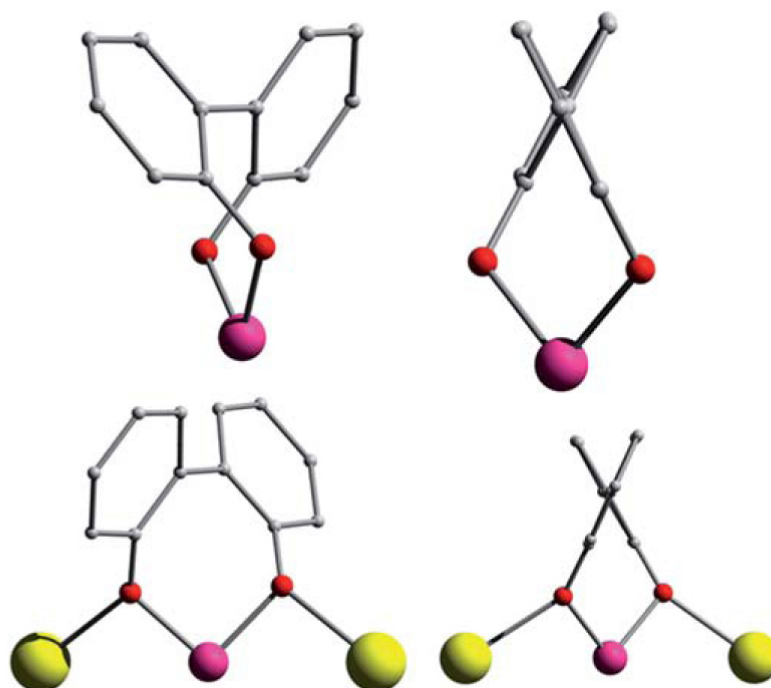


**Figure 64.** Schematics (taken from the crystal structures detailed here) illustrating the twisting of the 2,2'-biphenolate aromatic rings when ligated to Mn(III) (purple) and Na(I) (yellow) ions in this study.

exhibits a unidentate bonding motif as exhibited in the mononuclear complex  $[\text{Mn}(\text{II})(\text{LH})_2(\text{bipy})_2]$  (**16**), the torsion angle is as expected rather more acute ( $35.42^\circ$ ). All members of this series of chains show three sharp resonances in the  $1400\text{-}1500\text{ cm}^{-1}$  region as expected for aromatic, polycyclic and / or pyridine rich complexes. In addition IR resonances in the  $850\text{-}750\text{ cm}^{-1}$  range and are indicative of out-of-plane aromatic C-H stretching. The IR peaks at  $2238\text{ cm}^{-1}$  in **13** and  $2237\text{ cm}^{-1}$  in **14** are attributable to the  $\text{C}\equiv\text{N}$  stretches of the 4- and 3-cnp ligands respectively. The ionic nature of the supramolecular chains in **11**, **12** and **13** results in their solubility in solvents MeOH, EtOH and MeCN. UV-vis studies on all member complexes in each of these solvents give rise to very similar spectra (see Figures C4-C6 in Appendix C). More specifically the absorptions centred at around  $205\text{nm}$  ( $\pi\rightarrow\pi^*$ ),  $240\text{nm}$  ( $\pi\rightarrow\pi^*$ ) and  $290\text{nm}$  ( $n\rightarrow\pi^*$ ) are the result of the multiple aromatic groups present in all of these three ionic chains.

### 4.3 Conclusion

We have reported here the first 1-D architectures constructed using the 2,2'-biphenol ( $\text{LH}_2$ ) ligand. Interestingly, we cannot see any correlation between the type of chain formed (covalent or H-bonded) and the kind of N-donor pyridyl ligand utilized in their syntheses. The ionic chains in **11-13** are soluble in a range of solvents and have been assessed using UV-vis studies (see Figures C1-C6 in Appendix C). The ionic chains **11-13** are almost identical with respect to their intra-chain  $\text{M}\cdots\text{M}$  distances with  $\text{M}\cdots\text{Na}$  values of ( $\text{\AA}$ ):  $5.251$  (**11**),  $5.242$  (**12**) and  $5.257$  (**13**). The  $\text{M}\cdots\text{Na}$  distances within the covalent chains of **10**, **14**, **15** and **17** are as expected much closer and lie between  $3.142\text{ - }3.339\text{ \AA}$  in **10**,  $3.074\text{ - }3.295\text{ \AA}$  in **14** and  $3.273\text{ - }3.327\text{ \AA}$  in **15**, while the one crystallographically unique Fe1-Na1 bond in **17** has a length of  $3.439\text{ \AA}$  (see Table C2 in Appendix C). Both these intra-chain  $\text{M}\cdots\text{M}$  distance ranges render the Mn(III) and Fe(III) ions in this series as magnetically isolated or *dilute* due to the presence of the  $\{\text{Na}(\text{I})\}$  spacer units.

In addition, we have observed all three accessible levels of deprotonation of 2,2'-biphenol ( $\text{L}^{2-}$ ,  $\text{LH}^-$  and  $\text{LH}_2$ ) in the complexes detailed in this chapter. We have also witnessed a variety of coordination modes exhibited by this ligand; from chelating and unidentate in the ionic chains and the monomeric complex **16** respectively, to bridging three metal ions in the covalent chains (adopting the  $\eta^2:\eta^2,\mu_3$ -bonding motif).

The versatility of this ligand is further highlighted in the following chapter, in which we report the first complexes of Co(II/III) built using 2,2'-biphenol. Continuing on the theme of coordination polymers, this chapter includes 1- and 2-D infinite structures comprising Co(II) nodes. These are accompanied by the Co(II) analogues to complex **8** ( $[\text{Cu}_2(\text{LH})_2(3\text{-pic})_4](\text{ClO}_4)_2 \cdot 2\text{EtOH}$  – described in chapter 3) and most notably, a beautiful ferromagnetic  $[\text{Co}(\text{II})_8]$  cluster.

## 4.4 Experimental Section

### 4.4.1 Physical measurements

Infra-red spectra were recorded on a Perkin Elmer FT-IR *Spectrum One* spectrometer equipped with a Universal ATR Sampling accessory (NUI Galway). UV-visible studies were carried out on a Cary *100 Scan* (Varian) spectrophotometer. Elemental analysis was carried by Marion Vignoles and Gerard Fahy at the School of Chemistry microanalysis service NUI Galway.

### 4.4.2 Syntheses

All reactions were performed under aerobic conditions and all reagents and solvents were used as purchased. **Caution:** Although no problems were encountered during the synthesis of the following compounds, due care and attention should be paid when using the potentially explosive perchlorate and nitrate salts.

#### Preparation of $[\text{Na}(\text{I})_2\text{Mn}(\text{III})_2(\text{L})_4(\text{py})_3(\text{EtOH})_2]_n$ (**10**)

To a solution containing  $\text{Mn}(\text{ClO}_4)_2 \cdot 6\text{H}_2\text{O}$  (0.25 g, 0.985 mmol) in  $40\text{cm}^3$  EtOH, was added an excess of 2,2'-biphenol (0.73 g, 3.94 mmol). NaOH (0.157 g, 3.94 mmol) and pyridine ( $1\text{cm}^3$ , 12.4 mmol) were added in quick succession and the solution was stirred for 15 minutes. The resultant deep brown solution was then filtered and left to stand in the fume-cupboard covered by a perforated lid. X-ray quality crystals of **10** were obtained in ~20 % yield upon slow evaporation of the mother liquor. FT-IR ( $\text{cm}^{-1}$ ): 3534(w), 3049(w), 1586(w), 1556(m), 1486(s), 1469(s), 1428(s), 1393(m), 1272(s), 1250(s), 1233(s), 1231(sh), 1149(w), 1117(w), 1093(w), 1065(w), 1032(m), 1003(m), 931(m), 854(s), 754(s), 730(s), 707(s). Elemental analysis calculated (found) (%) for  $\text{C}_{67}\text{H}_{59}\text{N}_3\text{O}_{10}\text{Na}_2\text{Mn}_2$  (**10**): C: 65.85 (65.62), H: 4.87 (4.55), N: 3.44 (3.07).

### Preparation of [Na(I)(LH<sub>2</sub>)(EtOH)<sub>3</sub>][Mn(III)(L)<sub>2</sub>(3-pic)<sub>2</sub>]<sub>n</sub> (**11**)

To a solution containing Mn(ClO<sub>4</sub>)<sub>2</sub>·6H<sub>2</sub>O (0.25 g, 0.985 mmol) in 40 cm<sup>3</sup> EtOH, was added an excess of 2,2'-biphenol (0.73 g, 3.94 mmol). NaOH (0.157 g, 3.94 mmol) and 3-picoline (1 cm<sup>3</sup>, 12.4 mmol) were added in quick succession and the solution was stirred for 15 minutes. The resultant deep brown solution was then filtered and left to stand in the fume-cupboard covered by a perforated lid. X-ray quality crystals of **11** were obtained upon slow evaporation of the mother liquor in ~20 % yield. FT-IR (cm<sup>-1</sup>): 3548(w), 3050(w), 2968(w), 1585(w), 1556(m), 1487(s), 1469(s), 1428(s), 1391(m), 1273(s), 1250(s), 1233(sh), 1231(sh), 1150(w), 1118(w), 1094(w), 1035(w), 1002(m), 929(m), 854(s), 753(s), 728(s), 706(s). UV/vis (MeOH): λ<sub>max</sub> [nm] (ε<sub>max</sub> 10<sup>3</sup> dm<sup>3</sup> mol<sup>-1</sup> cm<sup>-1</sup>): 204 (104.0), 240 (39.0), 284 (24.4). (EtOH): 205 (119.6), 241 (43.0), 285 (26.4). (MeCN): 204 (98.9), 247(sh), 285 (25.2), 335 (11.4). Elemental analysis calculated (found) (%) for C<sub>54</sub>H<sub>60</sub>N<sub>2</sub>O<sub>10</sub>NaMn (**11**)·H<sub>2</sub>O: C: 66.52 (66.40), H: 6.20 (6.30), N: 2.87 (2.92).

### Preparation of [Na(I)(LH<sub>2</sub>)(EtOH)<sub>3</sub>][Fe(III)(L)<sub>2</sub>(3-pic)<sub>2</sub>]<sub>n</sub> (**12**)

FeCl<sub>2</sub>·4H<sub>2</sub>O (0.20 g, 1.0 mmol) and an excess of 2,2'-biphenol (0.73 g, 3.94 mmol) were dissolved in 40 cm<sup>3</sup> EtOH. NaOH (0.157 g, 3.94 mmol) and 3-picoline (1 cm<sup>3</sup>, 12.4 mmol) were added in quick succession and the solution was stirred for 15 minutes. The resultant deep red / purple solution was then filtered and left to stand in the fume-cupboard covered by a perforated lid. X-ray quality crystals of **12** were obtained upon slow evaporation of the mother liquor in ~25 % yield. FT-IR (cm<sup>-1</sup>): 3051(w), 2967(w), 2865(w), 2480(wb), 1739(w), 1584(m), 1484(s), 1467(s), 1428(s), 1379(m), 1271(s), 1231(s), 1236(s), 1231(s), 1147(w), 1091(m), 1039(m), 1002(m), 928(m), 878(w), 851(s), 751(s), 733(s), 700(s). UV/vis (MeOH): λ<sub>max</sub> [nm] (ε<sub>max</sub> 10<sup>3</sup> dm<sup>3</sup> mol<sup>-1</sup> cm<sup>-1</sup>): 208 (116.6), 243 (36.3), 269(sh), 285 (22.4) 314(sh). (EtOH): 207 (118.3), 243 (36.3), 270(sh), 284 (24.3). (MeCN): 204 (109.7), 240 (38.3), 267(sh), 281 (33.2). Elemental analysis calculated (found) (%) for C<sub>54</sub>H<sub>58</sub>N<sub>2</sub>O<sub>9</sub>NaFe (**12**): C: 67.71 (67.35), H: 6.10 (6.28), N: 2.92 (2.98).

### Preparation of [Na(I)(LH<sub>2</sub>)(EtOH)<sub>2</sub>(H<sub>2</sub>O)][Mn(III)(L)<sub>2</sub>(4-cnp)<sub>2</sub>]<sub>n</sub> (**13**)

A 1.456 M aqueous solution of Mn(NO<sub>3</sub>)<sub>2</sub>·4H<sub>2</sub>O (1 cm<sup>3</sup>, 1.45 mmol) and an excess of 2,2'-biphenol (1.08 g, 5.8 mmol) were dissolved in 40 cm<sup>3</sup> EtOH. NaOH (0.23 g, 5.8

mmol) and 4-cyanopyridine (4-cnp) (0.6 g, 5.8 mmol) were then added in quick succession. The resultant deep brown solution was stirred for 1 h before being filtered and allowed to stand. X-ray quality needle-like crystals of **13** were obtained in ~15 % yield upon slow evaporation of the mother liquor. FT-IR (cm<sup>-1</sup>): 3584(w), 3205(wb), 3051(w), 3002(w), 2967(w), 2547(wb), 2238(s), 1663(w), 1596(m), 1557(w), 1545(w), 1489(s), 1468(s), 1452(s), 1430(s), 1410(s), 1381(m), 1273(m), 1250(s), 1222(s), 1153(m), 1117(m), 1094(m), 1043(m), 1004(m), 966(w), 935(m), 853(s), 827(s), 755(s), 735(s), 708(s). UV/vis (MeOH):  $\lambda_{\text{max}}$  [nm] ( $\epsilon_{\text{max}}$  10<sup>3</sup> dm<sup>3</sup> mol<sup>-1</sup> cm<sup>-1</sup>): 205 (134.2), 241 (41.8), 281(29.3). (EtOH): 204 (117.5), 241 (38.1), 283 (27.3). (MeCN): 210 (90.6), 245(sh), 281 (22.7), 339 (8.6). Elemental analysis calculated (found) (%) for C<sub>52</sub>H<sub>47</sub>N<sub>4</sub>O<sub>9</sub>NaMn (**13**): C: 65.75 (66.13), H: 4.99 (4.98), N: 5.90 (6.04).

#### **Preparation of [Na(I)<sub>2</sub>Mn(III)<sub>2</sub>(L)<sub>4</sub>(3-cnp)<sub>2</sub>(EtOH)<sub>3</sub>]<sub>n</sub> (**14**)**

A 1.456 M aqueous solution of Mn(NO<sub>3</sub>)<sub>2</sub>·4H<sub>2</sub>O (1 cm<sup>3</sup>, 1.45 mmol) and an excess of 2,2'-biphenol (1.08g, 5.8mmol) were dissolved in 40cm<sup>3</sup> EtOH. NaOH (0.23 g, 5.8 mmol) and 3-cyanopyridine (3-cnp) (0.6 g, 5.8 mmol) were then added in quick succession. The resultant deep brown solution was stirred for 1 h before being filtered and allowed to stand. X-ray quality needle-like crystals of **14** were obtained in ~15 % yield upon slow evaporation of the mother liquor after 24 hours. FT-IR (cm<sup>-1</sup>): 3546(w), 3240(wb), 3060(w), 2966(w), 2545(wb), 2237(s), 1592(m), 1555(w), 1543(w), 1488(s), 1468(s), 1430(s), 1380(m), 1273(m), 1250(s), 1226(s), 1189(m), 1151(m), 1117(m), 1095(m), 1049(m), 1004(m), 964(vw), 932(m), 878(w), 851(s), 839(s), 763(s), 750(s), 734(s), 709(s), 695(s). Elemental analysis calculated (found) (%) for C<sub>66</sub>H<sub>58</sub>N<sub>4</sub>O<sub>11</sub>Na<sub>2</sub>Mn<sub>2</sub> (**14**): C 63.98 (63.67), H: 4.72 (4.41), N: 4.52 (4.92).

#### **Preparation of [Na(I)<sub>2</sub>Mn(III)<sub>2</sub>(L)<sub>4</sub>(4-Et-py)<sub>3</sub>(EtOH)<sub>2</sub>·EtOH]<sub>n</sub> (**15**)**

To a solution containing Mn(ClO<sub>4</sub>)<sub>2</sub>·6H<sub>2</sub>O (0.25g, 0.985 mmol) in 40cm<sup>3</sup> EtOH, was added an excess of 2,2'-biphenol (0.73 g, 3.94 mmol). NaOH (0.157 g, 3.94 mmol) and 4-Ethyl-pyridine (~ 1cm<sup>3</sup>, 12.4 mmol) were added in quick succession and the solution was stirred for 15 minutes. The resultant deep brown solution was then filtered and left to stand in the fume-cupboard covered by a perforated lid. X-ray quality crystals of **15** were obtained in ~15 % yield upon slow evaporation of the

mother liquor. FT-IR ( $\text{cm}^{-1}$ ): 3560(s), 3351(s), 3055(m), 3012(m), 1592(s), 1576(s), 1565(m), 1552(m), 1489(s), 1470(s), 1431 (s), 1298(s), 1274(s), 1257(s), 1241(s), 1146(w), 1150(m), 1117(w), 1091(w), 1050(w), 1027(m), 1018(m), 1003(w), 969(w), 930(m), 850(s), 832(m), 758(s), 732(s), 708(s), 689(m). Elemental analysis calculated (found) (%) for  $\text{C}_{66}\text{H}_{62}\text{N}_2\text{O}_{10}\text{Mn}_2\text{Na}_2$  (**15**): C: 66.11 (65.92), H: 5.21 (5.25), N: 2.34 (2.68).

#### **Preparation of $[\text{Mn(II)(LH)}_2(\text{bipy})_2]$ (**16**)**

$\text{Mn}(\text{ClO}_4)_2 \cdot 6\text{H}_2\text{O}$  (0.25 g, 0.985 mmol) and an excess of 2,2'-biphenol (0.73 g, 3.94 mmol) were dissolved in  $40\text{cm}^3$  EtOH. 2,2'-bipyridine (0.5 g, 3.21 mmol) and the base NaOH (0.157 g, 3.94 mmol) were then swiftly added and the solution was stirred for 15 minutes. The resultant deep brown solution was then filtered and left for slow evaporation. After 24 hours X-ray quality crystals of **16** were obtained in 25 % yield. FT-IR ( $\text{cm}^{-1}$ ): 3563(s), 3350(s), 3052(m), 3009(m), 1594(s), 1577(s), 1566(m), 1550(m), 1486(s), 1468(s), 1428(s), 1301(s), 1276(s), 1256(s), 1241(s), 1169(w), 1149(m), 1115(w), 1093(w), 1051(w), 1039(m), 1016(m), 1001(w), 968(w), 931(m), 852(s), 835(m), 757(s), 730(s), 704(s), 696(m). Elemental analysis calculated (found) (%) for  $\text{C}_{44}\text{H}_{34}\text{N}_4\text{O}_4\text{Mn}$  (**16**): C: 71.64 (72.01), H: 4.65 (4.26), N: 7.59 (7.66).

#### **Preparation of $[\text{Na(I)Fe(III)(L)}_2(2,2\text{-bipy})(\text{EtOH})_2]_n$ (**17**)**

To a solution of  $\text{FeCl}_2 \cdot 4\text{H}_2\text{O}$  (0.2 g, 1 mmol) in  $30\text{cm}^3$  EtOH, was added an excess of 2,2'-biphenol (0.75 g, 4 mmol). NaOH (0.16 g, 4.0 mmol) was added to the solution, followed by 2,2-bipyridine (0.62 g, 4.0 mmol). The mixture was left stirring for 30 minutes. The resultant blood red solution was then filtered and allowed to stand. X-ray quality needle-like crystals of **17** were obtained in 20 % yield upon slow evaporation of the mother liquor. FT-IR: 3633(w), 3054(w), 1597(m), 1567(m), 1485(s), 1468(s), 1429(vs), 1275(vs), 1169(w), 1152(w), 1116(w), 1094(w), 1044(w), 1021(w), 1000(m), 926(w), 853(m), 835(m), 752(s), 728(s), 705(m). Elemental analysis calculated (found) (%) for  $\text{C}_{38}\text{H}_{36}\text{N}_2\text{O}_6\text{NaFe}$  (**17**): C: 65.62 (65.74), H: 5.22 (5.41), N: 8.03 (7.83).

## 4.5 Bibliography

- [184] C. Janiak, "Engineering coordination polymers towards applications," *Dalton Transactions*, no. 14, p. 2781, 2003.
- [185] R. Robson, "Design and its limitations in the construction of bi- and poly-nuclear coordination complexes and coordination polymers (aka MOFs): a personal view.," *Dalton transactions (Cambridge, England : 2003)*, no. 38, pp. 5113–31, Oct. 2008.
- [186] S. R. Batten, S. M. Neville, and D. R. Turner, *Coordination Polymers: Design, Analysis and Application*, vol. 2008. Royal Society of Chemistry, 2008, p. 1.
- [187] H. J. Buser, D. Schwarzenbach, W. Petter, and A. Ludi, "The crystal structure of Prussian Blue:  $\text{Fe}_4[\text{Fe}(\text{CN})_6]_3 \cdot x\text{H}_2\text{O}$ ," *Inorganic Chemistry*, vol. 16, no. 11, pp. 2704–2710, Nov. 1977.
- [188] F. Shugam and H. Zhdanov, "No Title," *Acta Phisicochimica URSS*, vol. 20, p. 247, 1945.
- [189] H. M. Powell and J. H. Rayner, "Clathrate Compound Formed by Benzene with an Ammonia–Nickel Cyanide Complex," *Nature*, vol. 163, no. 4145, pp. 566–567, Apr. 1949.
- [190] J. H. Rayner and H. M. Powell, "Crystal structure of a hydrated nickel cyanide ammoniate," *Journal of the Chemical Society (Resumed)*, p. 3412, 1958.
- [191] Y. Kinoshita, I. Matsubara, T. Higuchi, and Y. Saito, "The Crystal Structure of Bis(adiponitrilo)copper(I) Nitrate," *Bulletin of the Chemical Society of Japan*, vol. 32, no. 11, pp. 1221–1226, 1959.
- [192] R. G. Vranka and E. L. Amma, "Metal Ion-Aromatic Complexes. II. The Crystal Structure of the 1:1 Silver Nitrate-Pyrazine Complex," *Inorganic Chemistry*, vol. 5, no. 6, pp. 1020–1025, Jun. 1966.
- [193] T. Iwamoto, T. Nakano, M. Morita, T. Miyoshi, T. Miyamoto, and Y. Sasaki, "The Hofman-type clathrate:  $\text{M}(\text{NH}_3)_2\text{M}'(\text{CN})_4 \cdot 2\text{G}$ ," *Inorganica Chimica Acta*, vol. 2, pp. 313–316, Mar. 1968.
- [194] T. Miyoshi, T. Iwamoto, and Y. Sasaki, "The crystal structure of the benzene clathrate with the ethylenediamine-bridge host lattice;  $\text{Cd}(\text{en})\text{Ni}(\text{CN})_4 \cdot 2\text{C}_6\text{H}_6$ ," *Inorganic and Nuclear Chemistry Letters*, vol. 6, no. 1, pp. 21–24, Jan. 1970.
- [195] A. Santoro, a. D. Mighell, and C. W. Reimann, "The crystal structure of a 1:1 cupric nitrate–pyrazine complex  $\text{Cu}(\text{NO}_3)_2 \cdot (\text{C}_4\text{N}_2\text{H}_4)$ ," *Acta Crystallographica Section B Structural Crystallography and Crystal Chemistry*, vol. 26, no. 7, pp. 979–984, Jul. 1970.
- [196] P. W. Carreck, M. Goldstein, E. M. McPartlin, and W. D. Unsworth, "Far-infrared spectra of bis(pyrazine) complexes of transition metal(II) halides. The crystal and molecular structure of dichlorobis(pyrazine)cobalt(II)," *Journal of the Chemical Society D: Chemical Communications*, no. 24, p. 1634, 1971.
- [197] D. M. L. Goodgame, D. J. Williams, and R. E. P. Winpenny, "Novel Bimetallic Macrocyclic Polymer Structures Incorporating Deprotonated 2-Pyrrolidone Bridges: The Crystal Structures of  $[\{\text{Hg}_2\text{Cu}(\text{C}_4\text{H}_6\text{NO})_4\}\text{X}_2]_n\text{X}$   $\text{NO}_3$  or  $\text{ClO}_4$ ," *Angewandte Chemie International Edition in English*, vol. 26, no. 10, pp. 1044–1045, Oct. 1987.
- [198] B. F. Hoskins and R. Robson, "Infinite polymeric frameworks consisting of three dimensionally linked rod-like segments," *Journal of the American Chemical Society*, vol. 111, no. 15, pp. 5962–5964, Jul. 1989.

- [199] B. F. Hoskins and R. Robson, "Design and construction of a new class of scaffolding-like materials comprising infinite polymeric frameworks of 3D-linked molecular rods. A reappraisal of the zinc cyanide and cadmium cyanide structures and the synthesis and structure of the diamond-related frameworks," *Journal of the American Chemical Society*, vol. 112, no. 4, pp. 1546–1554, Feb. 1990.
- [200] P. Brandt, A. K. Brimah, and R. D. Fischer, "Partially Reversible Intercalation of Ferrocene in a Zeolite-like Host Lattice Consisting of  $\text{Fe}(\text{CN})_6$  and  $\text{Me}_3\text{Sn}$  Units," *Angewandte Chemie International Edition in English*, vol. 27, no. 11, pp. 1521–1522, Nov. 1988.
- [201] B. F. Abrahams, B. F. Hoskins, D. M. Michail, and R. Robson, "Assembly of porphyrin building blocks into network structures with large channels," *Nature*, vol. 369, no. 6483, pp. 727–729, Jun. 1994.
- [202] S. R. Batten, B. F. Hoskins, and R. Robson, "Two Interpenetrating 3D Networks Which Generate Spacious Sealed-Off Compartments Enclosing of the Order of 20 Solvent Molecules in the Structures of  $\text{Zn}(\text{CN})(\text{NO}_3)(\text{tpt})_{2/3} \cdot \text{solv}$  (tpt = 2,4,6-tri(4-pyridyl)-1,3,5-triazine, solv =  $\text{C}_2\text{H}_2\text{Cl}_4$ )," *Journal of the American Chemical Society*, vol. 117, no. 19, pp. 5385–5386, May 1995.
- [203] C. Janiak and J. K. Vieth, "MOFs, MILs and more: concepts, properties and applications for porous coordination networks (PCNs)," *New Journal of Chemistry*, vol. 34, no. 11, p. 2366, 2010.
- [204] Z. Wang, Y.-H. Xing, C.-G. Wang, L.-X. Sun, J. Zhang, M.-F. Ge, and S.-Y. Niu, "Synthesis, structure and luminescent properties of coordination polymers with 1,2-benzenedicarboxylic acid and a series of flexible dicarboxylate ligands," *CrystEngComm*, vol. 12, no. 3, p. 762, 2010.
- [205] C. Gao, S. Liu, L. Xie, Y. Ren, R. Cao, J. Cao, and X. Zhao, "A three-dimensional microporous coordination polymer with fluorescent property," *Journal of Molecular Structure*, vol. 891, no. 1–3, pp. 384–387, Nov. 2008.
- [206] H. Adams, W. Z. Alsindi, G. M. Davies, M. B. Duriska, T. L. Easun, H. E. Fenton, J.-M. Herrera, M. W. George, K. L. Ronayne, X.-Z. Sun, M. Towrie, and M. D. Ward, "New members of the  $[\text{Ru}(\text{diimine})(\text{CN})_4]^{2-}$  family: structural, electrochemical and photophysical properties.," *Dalton transactions (Cambridge, England : 2003)*, no. 1, pp. 39–50, Jan. 2006.
- [207] O. Kahn, Y. Pei, M. Verdaguer, J. P. Renard, and J. Sletten, "Magnetic ordering of manganese(II) copper(II) bimetallic chains; design of a molecular based ferromagnet," *Journal of the American Chemical Society*, vol. 110, no. 3, pp. 782–789, Feb. 1988.
- [208] O. Shekhah, H. Wang, M. Paradinas, C. Ocal, B. Schüpbach, A. Terfort, D. Zacher, R. A. Fischer, and C. Wöll, "Controlling interpenetration in metal-organic frameworks by liquid-phase epitaxy.," *Nature materials*, vol. 8, no. 6, pp. 481–484, Jun. 2009.
- [209] M. Kurmoo, "Magnetic metal-organic frameworks.," *Chemical Society reviews*, vol. 38, no. 5, pp. 1353–1379, May 2009.
- [210] J. Rocha, L. D. Carlos, F. A. A. Paz, and D. Ananias, "Luminescent multifunctional lanthanides-based metal-organic frameworks.," *Chemical Society reviews*, vol. 40, no. 2, pp. 926–940, Feb. 2011.
- [211] M. D. Allendorf, C. A. Bauer, R. K. Bhakta, and R. J. T. Houk, "Luminescent metal-organic frameworks.," *Chemical Society reviews*, vol. 38, no. 5, pp. 1330–1352, May 2009.

- [212] A. Saha, G. Musie, and D. R. Powell, "Sodium tris(acetylacetonato- $\kappa$ 2O, O')manganese(II)," *Acta Crystallographica Section E Structure Reports Online*, vol. 61, no. 6, pp. m1144–m1146, May 2005.
- [213] D. T. Cromer and A. C. Larson, "The structures of the 1:1 complexes of CuCN with pyridazine and with 4-cyanopyridine," *Acta Crystallographica Section B Structural Crystallography and Crystal Chemistry*, vol. 28, no. 4, pp. 1052–1058, Apr. 1972.
- [214] W. Zhang, J. R. Jeitler, M. M. Turnbull, C. P. Landee, M. Wei, and R. D. Willett, "Synthesis, X-ray structures and magnetic properties of linear chain 4-cyanopyridine compounds:  $[\text{Cu}(4\text{-CNpy})_4(\text{H}_2\text{O})](\text{ClO}_4)_2$  and  $\text{M}(4\text{-CNpy})_2\text{Cl}_2$  (M = Mn, Fe, Co, Ni, Cu)," *Inorganica Chimica Acta*, vol. 256, no. 2, pp. 183–198, Mar. 1997.
- [215] B. Weber, C. Carbonera, C. Desplances, and J.-F. Létard, "Stepwise Spin Transition in a Mononuclear Iron(II) Complex with Unusually Wide Plateau," *European Journal of Inorganic Chemistry*, vol. 2008, no. 10, pp. 1589–1598, Apr. 2008.
- [216] S. Yoon and S. J. Lippard, "Water affects the stereochemistry and dioxygen reactivity of carboxylate-rich diiron(II) models for the diiron centers in dioxygen-dependent non-heme enzymes.," *Journal of the American Chemical Society*, vol. 127, no. 23, pp. 8386–8397, Jun. 2005.
- [217] S. Dalai, P. Sarathi Mukherjee, E. Zangrando, and N. Ray Chaudhuri, "Synthesis, crystal structure and magnetic properties of two new dicyanamide bridged 2D and 1D complexes of Mn(II)," *New Journal of Chemistry*, vol. 26, no. 9, pp. 1185–1189, Aug. 2002.

## **Chapter 5:**

# **An Investigation into the Coordination Chemistry of 2,2'-biphenol with Co(II/III); a Structural and Magnetic Study**

## 5.1 Introduction

### 5.1.1 Cobalt

The element cobalt derived its name from the word Kobald, a type of mischievous sprite commonly encountered in German mythology. In medieval Germany, many superstitious miners believed that these creatures dwelled in mines and blamed them for accidents, cave-ins and rock-slides. Cobalt ores such as cobaltite and smaltite would sometimes be mistaken for useful copper or iron, but when smelted they released toxic arsenide fumes. Substituting copper or iron deposits with cobalt ores was considered to be a trick played on the miners by the kobalds, and this is how the ore acquired its name [218]. In 1735, a Swedish chemist called George Brandt discovered that such ores could be reducible to a previously unknown metal [219].

Today, the element is used in a variety of applications – with almost half of the cobalt mined being used in the production of superalloys which are used in jet engines and turbines for energy generation. Cobalt is also an ideal component of magnetic alloys, due to its high magnetic anisotropy and its high Curie temperature of 1120 °C (in its elemental form). This is the highest Curie temperature among the three ferromagnets of the first row transition metals (the other two being iron and nickel) [220].

### 5.1.2 Co(II) in SMMs

The use of Co(II) in the construction of high spin clusters, Single-Molecule Magnets (SMMs – see section 1.8.1) and Single Chain Magnets (SCMs – section 1.8.2) has become increasingly popular in recent years [221], due to the large single ion anisotropy exhibited by this ion in octahedral ligand fields. This large anisotropy is due to the zero-field splitting of the degenerate spin microstates ( $M_s$  levels) of Co(II), giving rise to large  $D$  values, and anisotropic ground states (see section 1.6). Figure 65 shows the crystal field splitting diagram of the Co(II) ion in an octahedral environment. This electronic configuration ( ${}^4T_{1g}$ ) is orbitally degenerate, and although a Jahn-Teller distortion will remove this degeneracy somewhat, the excited states are very low lying and the two ‘spin-down’ electrons (Figure 65), are capable of moving between all three orbitals of the  $t_{2g}$  set. This electron motion gives rise to large values of orbital angular momentum, which the electrons’ spin angular momentum can couple to. Because zero-field splitting arises through the coupling of the ground state with excited electronic states via spin-orbit coupling, Co(II) ions in octahedral

environments possess large single ion anisotropies and thus large  $D$  parameters. The high-spin octahedral Co(II) ion usually exhibits large and positive  $D$  values, meaning that the  $M_S = \pm \frac{1}{2}$  Kramers doublet is the lowest energy sub-level (see section 1.6). For this reason Co(II) ions in polynuclear clusters are usually treated with an effective spin of  $S_{\text{eff}} = \frac{1}{2}$  [222].

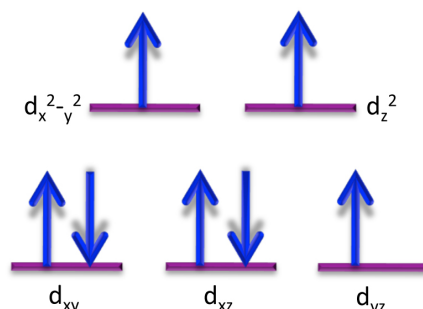


**Figure 65.** Crystal field splitting diagram of octahedral Co(II) in the high spin configuration.

As discussed in section 1.6, possessing a large and negative zero-field splitting parameter is an essential property in order for a high spin cluster to exhibit SMM behaviour, as the energy barrier to the reversal of the magnetization is directly proportional to the  $D$  parameter of the complex. However, as a result of the large first order orbital contribution, magnetic susceptibility measurements performed on Co(II) clusters in their ground spin state often deviate largely from their corresponding spin-only values, leading to magnetic data that is often quite difficult to interpret. In addition, the isotropic exchange Hamiltonian (section 1.5.1) cannot adequately describe the exchange coupling in clusters containing highly anisotropic ions [223]. The magnetic complexity of these compounds not only adds to their beauty, but also pushes researchers in the field to discover more complexes of Co(II), in an effort to implicitly understand their magnetic behaviour.

The first cobalt complex exhibiting SMM behaviour was reported by Yang et al. in 2002 [224]. This cubane complex of formula  $[\text{Co(II)}_4(\text{hmp})_4(\text{MeOH})_4\text{Cl}_4]$  (hmp = hydroxymethylpyridine) possesses a ground spin state of  $S = 6$  with considerable negative magnetoanisotropy – the molecule possessing a  $D$  value of  $\sim -4$  K ( $-2.78 \text{ cm}^{-1}$ ). Out-of-phase ac susceptibility ( $\chi''$ ) measurements showed an increase in the susceptibility as the temperature is decreased towards 1.8 K. This is indicative of slow magnetic relaxation. Unfortunately it was impossible to measure the size of the energy barrier as no peaks are observed in the ac magnetic susceptibility data. The

following year Murrie et al [225] reported two hexanuclear Co(II) cluster also exhibiting slow relaxation of their magnetization. On this occasion, peaks were observed above 1.8 K in the out-of-phase susceptibility data, and thus an energy barrier to the reversal of their magnetization ( $\Delta E$ ) could be extrapolated. Complex **2** in this article ( $2 \cdot 6\text{H}_2\text{O}$ ) possessed an energy barrier  $\Delta E/k_B = 32 \text{ K}$  ( $22 \text{ cm}^{-1}$ ) and  $\tau_0 = 2.1 \times 10^{-9} \text{ s}$ , which was the highest energy barrier recorded for a non-manganese based SMM at the time. Then in 2005 Winpenny et al. reported an octanuclear Co(II) cage complex for which an energy barrier of  $\Delta E/k_B = 84(\pm 2) \text{ K}$  ( $\sim 58.38 \text{ cm}^{-1}$ ) and  $\tau_0 = 1.8(\pm 3) \times 10^{-12} \text{ s}$  was extrapolated from the out-of-phase susceptibility data. Repeating the experiment on a second crystalline sample gave  $\Delta E/k_B = 80 \text{ K}$  ( $55.6 \text{ cm}^{-1}$ ) and  $\tau_0 = 2.1 \times 10^{-11}$  [226].

In this chapter we report the synthesis, structural and magnetic characterization of a family of Co(II) complexes built using 2,2'-biphenol ( $\text{LH}_2$ ). These include a pair of antiferromagnetic Co(II) dimers and a ferromagnetic octanuclear  $[\text{Co(II)}_8]$  cluster. Co(II) dimers are useful as they help us to understand how the exchange mechanisms between individual magnetic ions might be influenced by structural properties in larger complexes. In addition to their importance in the field of molecular magnetism, Co(II) dimers have also been investigated as mimics for metalloenzyme active sites [227].

To our knowledge, just two  $[\text{Co(II)}_8]$  clusters exhibiting ferromagnetic coupling between their constituent Co(II) ions have been reported to date [226], [228] (the phosphonate containing cluster [226] has been previously mentioned above). Both of these complexes also exhibit SMM behaviour, with  $[\text{Et}_3\text{NH}][\text{Co}_8(\text{chp})_{10}(\text{O}_3\text{PPh})_2(\text{NO}_3)_3(\text{Hchp})_2]$  possessing the highest energy barrier to the reversal of its magnetization ( $\Delta E/k_B \approx 55 - 58 \text{ cm}^{-1}$ ) for a monometallic cobalt cluster.

### 5.1.3 Coordination polymers comprising Co(II) ions

In addition to the three discrete clusters described in this chapter, we also report the synthesis and structural characterization of a pair of coordination polymers whose nodes are comprised of magnetically dilute Co(II) ions. Coordination polymers are of particular importance at present, due to their potential applications in fields such as magnetism, gas storage, luminescence, conductivity and catalysis as discussed in chapter 4 [184]. Many Co(II) containing coordination polymers have been published

exhibiting 1– [229], 2– [230] and 3–D [231] topologies. In fact, the first Single Chain Magnet (SCM – see section 1.8.2) ever reported was a 1–D coordination polymer consisting of Co(II) ions linked via the NITPhOMe radical (4,4'-methoxy-phenyl-4,4,5,5-tetramethylimidazoline-1-oxyl-3-oxide) [232]. Other interesting properties that Co(II) coordination polymers have been shown to possess include DNA binding and anti-cancer activity [233], antimicrobial activity [234] and simultaneous semiconducting and spin crossover properties [229]. In the construction of Co(II) based coordination polymers, popular ligand choices have been dipyridyl based [235], and for this reason we have used the co-ligands 4,4'-trimethylenedipyridine [236] and 1,2-di(4-pyridyl)ethylene [237] in conjunction with  $LH_2$  in our synthetic procedures. This has led to two beautiful topologies (*vide infra*).

## 5.2 Results and Discussion

### 5.2.1 Discrete complexes of Co(II)

Akin to the complexes of chapter 4, this chapter reveals 2,2'-biphenol ( $LH_2$ ) in all three accessible levels of deprotonation upon producing polymetallic architectures of Co(II):  $L^{2-}$  (doubly deprotonated),  $LH^-$  (singly deprotonated) and  $LH_2$  (neutral), while again exhibiting a wide range of different coordination modes (Figure 66). More specifically, this ligand will be shown to consistently bridge multiple Co(II) ions, as well as on occasion remaining neutrally charged and acting as a H-bonding book-end ligand.

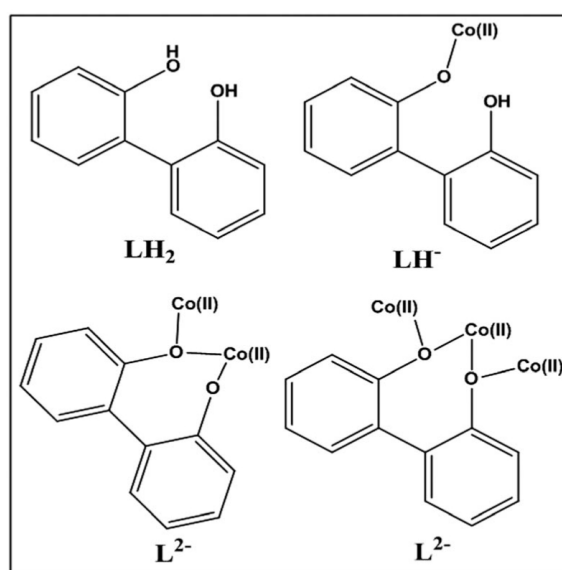


**Figure 66.** Structure of the ligand 2,2'-biphenol ( $LH_2$ ; top left) and the bonding modes it exhibits in this chapter under the various levels of deprotonation.

We present here a set of related complexes representing the first Co(II) species to be built using 2,2'-biphenol (LH<sub>2</sub>). All crystal data described in this work is documented in Table 13. We first highlight the synthesis of the analogous dimeric complexes [Co(II)<sub>2</sub>(L)<sub>2</sub>(py)<sub>4</sub>]·2EtOH (**18**) and [Co(II)<sub>2</sub>(L)<sub>2</sub>(4-pic)<sub>4</sub>]·2(LH<sub>2</sub>) (**19**) (where py = pyridine and 4-pic = 4-picoline). Both are produced by reaction of Co(NO<sub>3</sub>)<sub>2</sub>·6H<sub>2</sub>O and LH<sub>2</sub> in an EtOH/pyridyl ligand solvent mixture (pyridine in **18** and 4-picoline in **19**), along with a suitable base. Both **18** and **19** crystallize in the triclinic P-1 space group (Figure 72), with each possessing one {Co(II)<sub>2</sub>} unit in the asymmetric unit alongside one EtOH solvent of crystallization and one neutral LH<sub>2</sub> ligand, respectively. The dimeric structure in complexes **18** and **19**, is very similar to that of the Cu(II) dimer [Cu<sub>2</sub>(LH)<sub>2</sub>(3-pic)<sub>4</sub>](ClO<sub>4</sub>)<sub>2</sub>·2EtOH (**8**) described in chapter 3, the only difference being the level of deprotonation of LH<sub>2</sub> (LH<sup>-</sup> in **8** and L<sup>2-</sup> in both **18** and **19**).

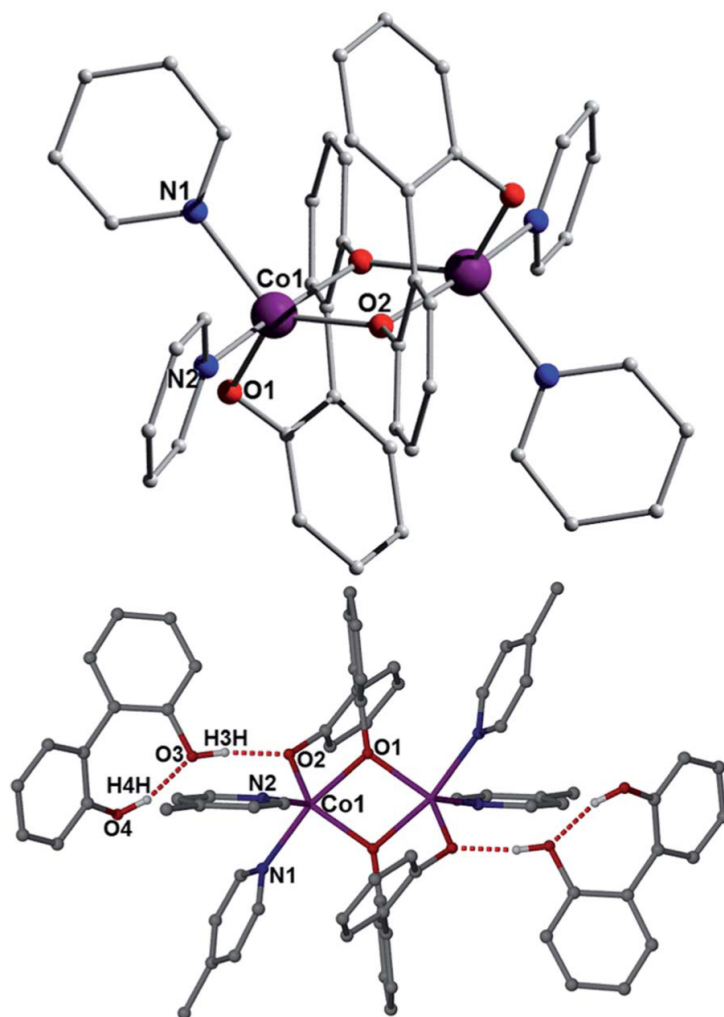


**Figure 67.** Crystal structures of **18** (top) and **19** (bottom) respectively. Colour code: Co (purple), O (red), N (blue), C (grey). Hydrogen atoms have been omitted for clarity. Dashed lines represent H-bonding interactions.

The cores in **18** and **19** comprise two distorted trigonal bipyramidal Co(II) centres ( $\tau = 0.67$  in both **18** and **19**) linked via two  $\eta^1:\eta^2,\mu$ -bridging doubly deprotonated  $L^{2-}$  ligands which produce Co...Co distances of 3.164 and 3.167 Å, respectively (Figure 68). The +2 cobalt oxidation state assessment was carried out via BVS calculations in conjunction with bond length and charge balancing considerations. The coordination spheres at the metal centres are occupied by four terminally bound N-donor ligands ranging in Co–N bond lengths of between 2.073 (Co1–N1 in **18**) and 2.157 Å (Co1–N2 in **18**). The Co–O bond lengths in these siblings lie in the 1.949–2.072 Å range.

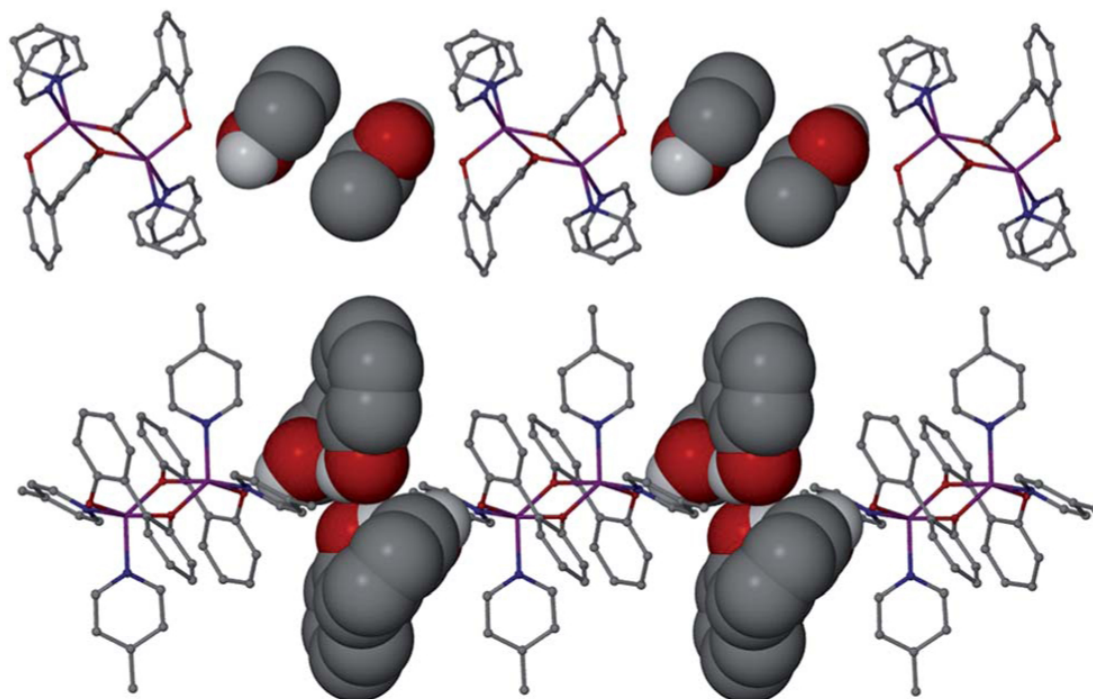


**Figure 68.** Views perpendicular to the superimposable rows with the cells of **18** (top) and **19** (bottom) showing the EtOH solvents (in **18**) and book-end  $LH_2$  ligands (in **19**), both depicted in space-fill mode.

Interestingly the main difference between the two analogues lies in their peripheral connectivity. Two EtOH solvent molecules reside outside the first coordination sphere in **18** (Figure 68). In complex **19** however there are two neutral, crystallographically related  $LH_2$  ligands which act as molecular book-ends which are held via intermolecular H-bonding interactions (Figure 68). More specifically the phenolic protons of each  $LH_2$  (H3H and symmetry equivalent (s.e)) strongly interact with the phenolic O-atoms (O2 and s.e) of the bridging  $L^{2-}$  ligands ( $O3(H3H)\cdots O2 = 1.694$  Å) (Figure 67). An intramolecular H-bond within the  $LH_2$  ligands is also seen at a

distance of  $O4(H4H)\cdots O3 = 1.858 \text{ \AA}$  (Figure 67). These neutral book-ends further interact with one another via symmetry equivalent H bonds through their  $O_{\text{phen}}$  and H-atoms ( $O4\cdots H4H' = 2.504 \text{ \AA}$ ). Moreover these nearby  $LH_2$  units also act as book-end ligands for the neighbouring  $\{Co(II)_2\}$  moieties in **19**, resulting in superimposable  $\{Co(II)_2\}-LH_2-LH_2-\{Co(II)_2\}$ - rows (Figure 68). These chains then assemble in the common space efficient brickwork arrangement within the unit cell and are superimposable along the  $a$  axis. The packing in **18** comprises the superimposable stacking of the individual  $\{Co(II)_2\}$  units along the  $b$  axis of the cell. These columns then also arrange in a brickwork fashion and are linked via off-set inter-chain  $\pi-\pi$  stacking interactions between juxtaposed pyridine ligands ( $C13-C17\cdots C13'-C17' = 3.985 \text{ \AA}$ ) (Figure 69). The result of these spacer EtOH and  $LH_2$  moieties in **18** and **19** are intra-chain Co $\cdots$ Co distances of  $15.14 \text{ \AA}$  and  $10.96 \text{ \AA}$ , respectively (Figure 68), while their corresponding inter-chain distances lie at  $8.38 \text{ \AA}$  in **18** and  $9.36 \text{ \AA}$  in **19**.

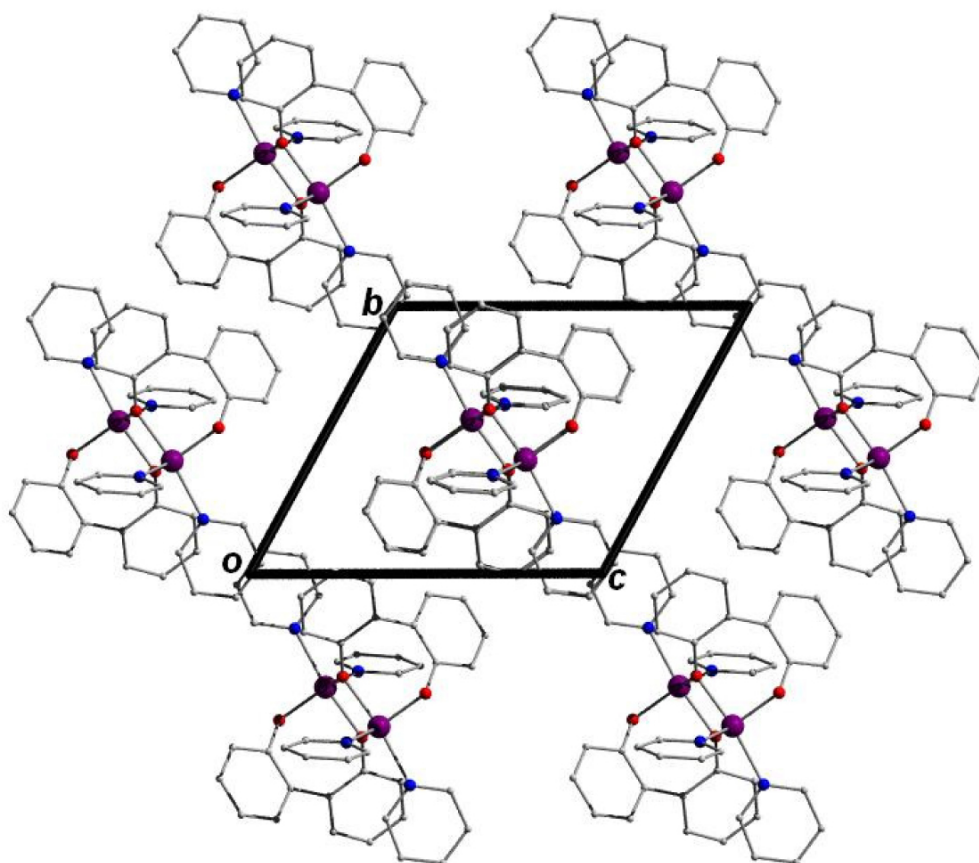


**Figure 69.** Packing of **18** as viewed along the  $a$  axis of the unit cell. Colour code as in Figure 67.

In order to encourage the formation of higher nuclearity clusters, a sensible approach was the introduction of a secondary ligand with metal bridging capabilities in the form of 2-hydroxypyridine (2-hpH). Much to our delight the immediate result was the production of the octametallc complex  $[\text{Co(II)}_8(\text{OMe})_2(\text{L})_4(\text{LH})_2(2\text{-hp})_4(\text{MeCN})_4]\cdot\text{MeCN}$  (**20**) (Figure 70), whose existence represents the second largest cluster ever reported using 2,2'-biphenol, behind the decametallc  $[\text{NMe}_4]_4[\text{Mn}_{10}\text{O}_4(\text{L})_4\text{X}_{12}]$  (where X = Cl, Br) clusters reported by Lippard and co-workers [53], [54].

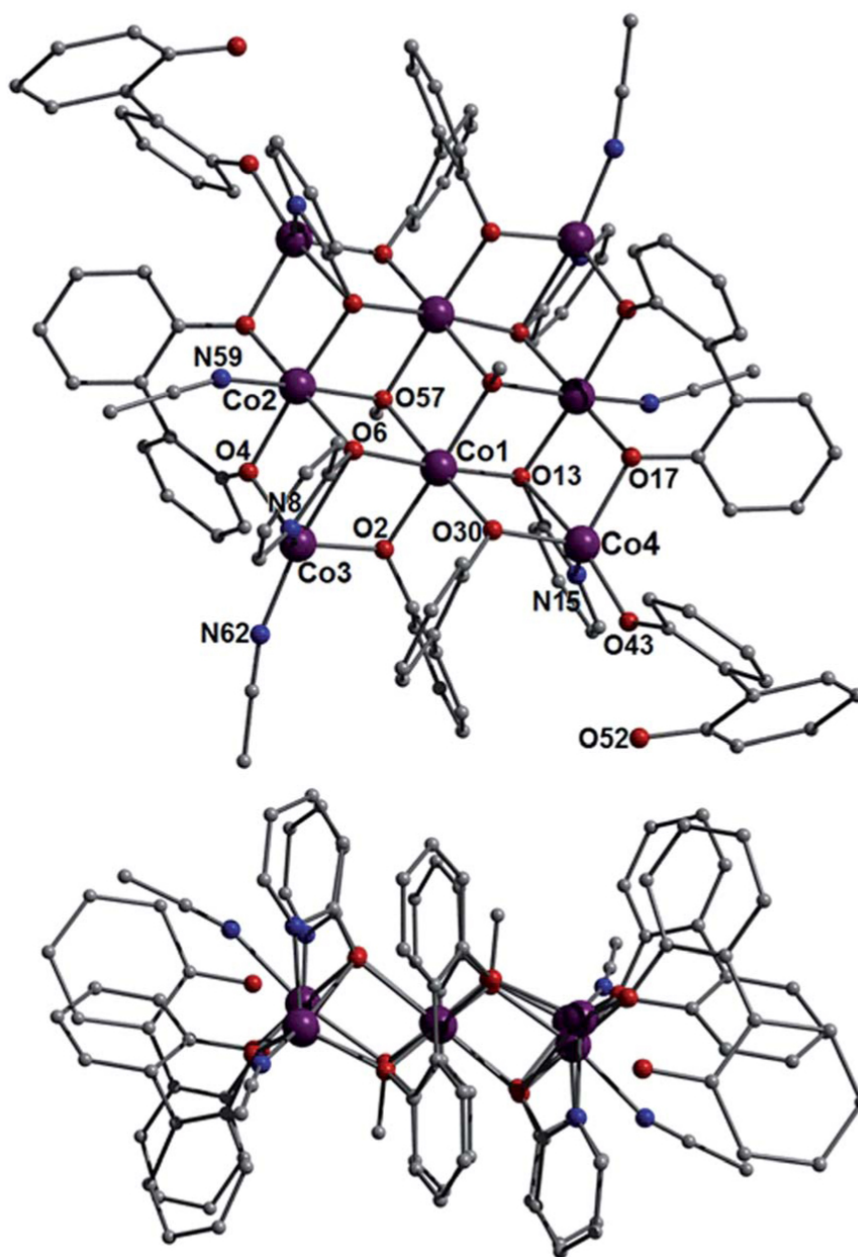


**Figure 70.** Crystal structure of **20** as viewed perpendicular (top) and parallel (bottom) to the  $\{\text{Co(II)}_8\}$  plane. Hydrogen atoms have been omitted for clarity.

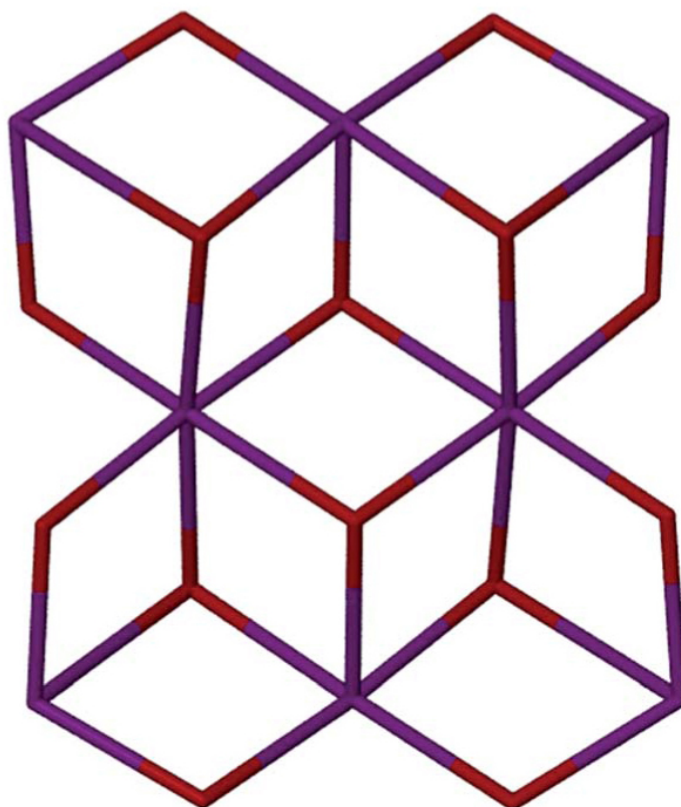


**Figure 71.** Inorganic core in **20** highlighting the six face-sharing  $\{\text{Co(II)}_3\text{O}\}$  triangular units that make up the structure. This arrangement can also be described as comprising six vertex-sharing partial  $[\text{Co(II)}_3\text{O}_4]$  cubes.

The core in **20** comprises a near planar array of Co(II) centres and its inorganic core may be described as comprising six edge-sharing  $[\text{Co(II)}_3]$  triangles, or alternatively as comprising six vertex-sharing partial  $[\text{Co(II)}_3\text{O}_4]$  cubes (Figure 71). The cobalt oxidation states were again assigned using BVS calculations, charge balance and bond length assessments. Co3 and Co4 exhibit distorted trigonal bipyramidal ( $\tau = 0.70$ ) and tetrahedral geometries respectively (although a fifth close contact exists between Co4 and O13:  $\text{Co4}\cdots\text{O13} = 2.595 \text{ \AA}$ ), while Co1 and Co2 possess distorted octahedral geometries. The Co(II) centres in **20** are connected via a combination of  $\mu_3$ -bridging  $\text{OMe}^-$  ions (O57 and s.e), two crystallographically unique  $\eta^1:\eta^2,\mu_3$ -2- $\text{hp}^-$  ions (N15 and O13 and N8 and O6, respectively) and  $\eta^2:\eta^2,\mu_3$ -bridging  $\text{L}^{2-}$  ligands (via the  $\text{O}_{\text{phen}}$  atoms O2, O30, O4 and O17). More specifically the  $\text{OMe}^-$  ions sit above and below the  $\{\text{Co(II)}_8\}$  plane respectively, connecting the central Co1 and Co2 ions with their symmetry equivalents. Likewise the bridging 2- $\text{hp}^-$  ligands sit above and below the planar octametallc core, terminally bonding to the tetrahedral Co3 and Co4 ions (via N8 and N15 respectively), while linking the more central Co1 and Co2 (and s.e) centres. Unlike all the other bridging ligands in **20** the  $\text{L}^{2-}$  ligands

sit approximately parallel to the  $\{\text{Co}_8\}$  plane, lying along the edges of the complex as they bridge three Co(II) centres (Figure 70). The coordination spheres at the metal centres are completed by terminal MeCN ligands at Co2 and Co3 (Co2–N59 = 2.144 Å, Co3–N62 = 2.016 Å), while terminally bonded singly deprotonated  $\text{LH}^-$  ligands (O43) occupy the 4th coordination sites at Co4 (and s.e). Note that these ligands ( $\text{LH}^-$ ) are disordered over two sites and modelled accordingly (see experimental section 5.4.2 for details).

**Table 13.** Crystallographic data table for complexes **18** to **22**

	<b>18</b>	<b>19</b>	<b>20</b>	<b>21</b>	<b>22</b>
Formula <sup>a</sup>	$\text{C}_{48}\text{H}_{48}\text{N}_4\text{O}_6\text{Co}_2$	$\text{C}_{72}\text{H}_{64}\text{N}_4\text{O}_8\text{Co}_2$	$\text{C}_{104}\text{H}_{87}\text{N}_9\text{O}_{18}\text{Co}_8$	$\text{C}_{50}\text{H}_{47}\text{N}_5\text{O}_7\text{Co}_1$	$\text{C}_{60}\text{H}_{42}\text{N}_8\text{O}_{10}\text{Co}_2$
$M_w$	894.76	1231.13	2222.35	888.86	1152.88
Crystal System	Triclinic	Triclinic	Monoclinic	Monoclinic	Monoclinic
Space Group	P-1	P-1	$\text{P}2_1/n$	Pc	$\text{P}2_1/c$
$a/\text{Å}$	10.416(2)	11.119(2)	12.7876(5)	10.572(2)	10.1508(6)
$b/\text{Å}$	11.022(2)	12.486(3)	19.4297(7)	13.755(3)	14.8829(7)
$c/\text{Å}$	11.536(2)	13.342(3)	20.1892(8)	15.127(3)	18.3001(9)
$\alpha$ (°)	114.31(3)	111.49(3)	90	90	90
$\beta$ (°)	92.94(3)	113.74(3)	103.649(4)	94.03(3)	101.469(5)
$\gamma$ (°)	115.71(3)	113.74(3)	90	90	90
$V/\text{Å}^3$	1043.9(4)	1512.3(5)	4874.5(3)	2194.2(8)	2709.5(2)
$Z$	1	1	2	2	2
$T/\text{K}$	150(2)	150(2)	150(2)	150(2)	150(2)
$\lambda^b/\text{Å}$	0.7107	0.7107	0.7107	0.7107	0.7107
$D_c/\text{g cm}^{-3}$	1.423	1.352	1.514	2.345	1.413
$\mu(\text{Mo-K}\alpha)/\text{mm}^{-1}$	0.850	0.610	1.399	0.450	0.680
Meas./indep.( $R_{\text{int}}$ )	3814/3510	5527/4451	11257/6831	5134/3308	4954/3145
refl.	(0.0154)	(0.0239)	(0.0472)	(0.0860)	(0.0429)
Restraints, Parameters	0, 248	0, 389	475, 557	2, 571	0, 362
$wR_2$ (all data)	0.0875	0.0811	0.0232	0.1542	0.2023
$R_1^{\text{d,e}}$	0.0347	0.0337	0.0698	0.0736	0.0695
Goodness of fit on $F^2$	1.042	1.018	1.116	1.027	1.061

<sup>a</sup> Includes guest molecules. <sup>b</sup> Mo-K $\alpha$  radiation, graphite monochromator. <sup>c</sup>  $wR_2 = [\sum w(|F_o| - |F_c|)^2] / \sum w|F_o|^2$ . <sup>d</sup> For observed data. <sup>e</sup>  $R_1 = \sum ||F_o| - |F_c|| / \sum |F_o|$ .



**Figure 72.** Crystal images of complexes **18** to **22** (left to right).

## 5.2.2 Magnetic susceptibility measurements

Magnetic measurements were carried out on polycrystalline samples of **18**–**20** in the 300–5 K temperature range and an external field of 0.1 T (Figures 73 and 74). The room temperature  $\chi_M T$  products for **18** and **19** are both consistent with that expected for two non-interacting  $s = 3/2$  ions with anisotropic  $g$ -values (Figure 73). On decreasing temperature their magnetic susceptibilities decrease slowly down to  $\sim 100$  K, after which a more significant drop in their  $\chi_M T$  products is observed, to minimum values of 0.4 and 1.05  $\text{cm}^3 \text{K mol}^{-1}$ , respectively. This behaviour is consistent with antiferromagnetic exchange and diamagnetic ground states in both. Indeed the rather obtuse Co–OR–Co angles of  $103.5^\circ$  in **18** and  $103.33^\circ$  in **19** would be expected to mediate AF exchange [238], [239]. The behaviour of **20** is however quite different. The  $\chi_M T$  value at 300 K ( $20.76 \text{ cm}^3 \text{K mol}^{-1}$ ) is consistent with that expected for eight non interacting Co(II) centres ( $19.80 \text{ cm}^3 \text{K mol}^{-1}$ ), assuming  $s = 3/2$  and  $g \sim 2.3$  (Figure 74).

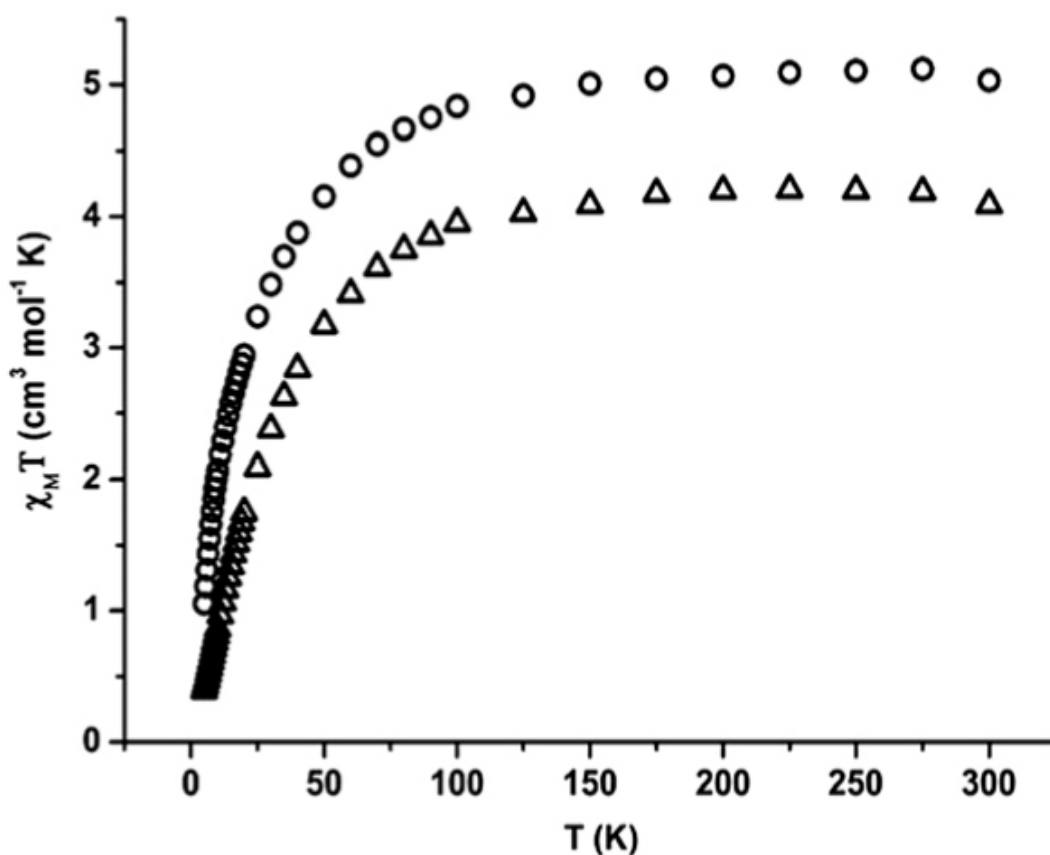


**Figure 73.** Plots of  $\chi_M T$  vs.  $T$  obtained from polycrystalline samples of **18** (○) and **19** (△) in the 300 - 5 K Temperature range in the applied field of 0.1 T.

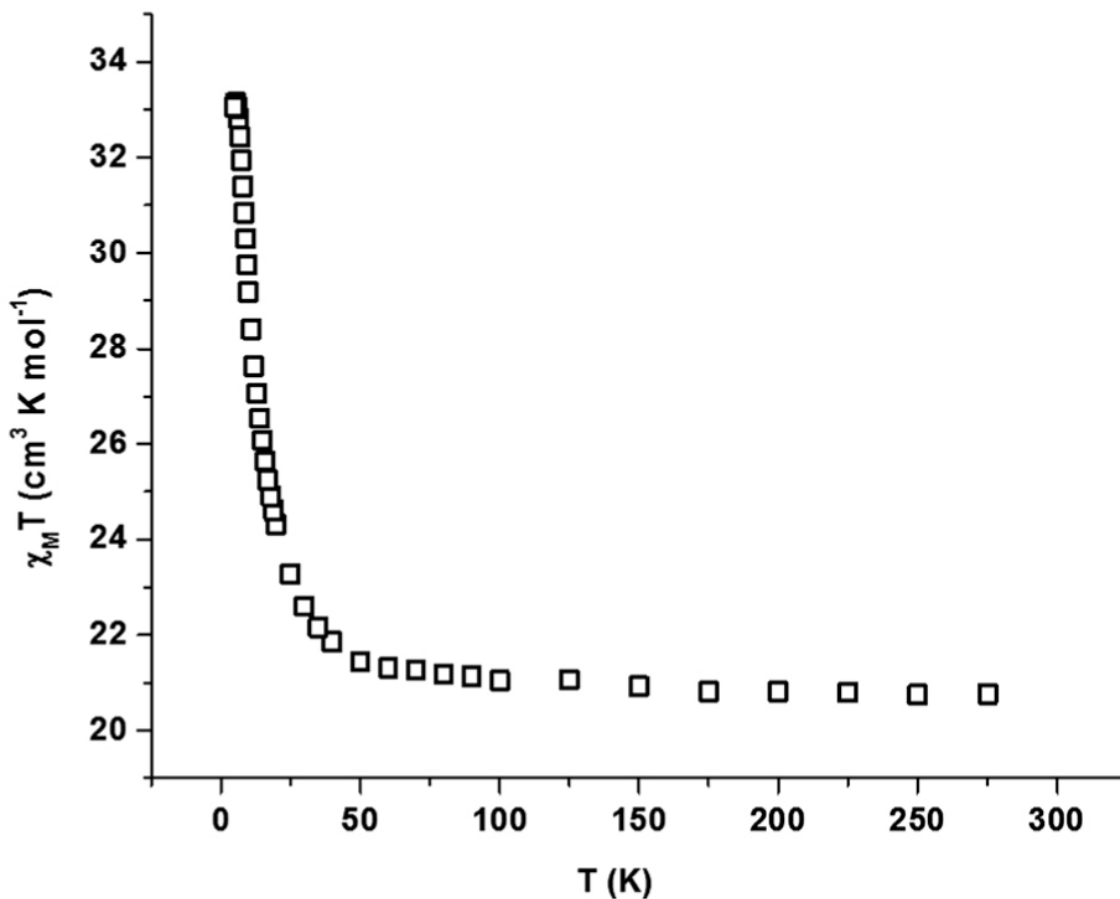


**Figure 74.** Plots of  $\chi_M T$  vs.  $T$  obtained from polycrystalline samples of **20** in the 300 - 5 K Temperature range in the applied field of 0.1 T.

As shown in Figure 10,  $\chi_M T$  rises gradually down to a temperature of approximately 50 K before sharply increasing to a maximum of  $\sim 33 \text{ cm}^3 \text{ K mol}^{-1}$  at 5 K. This is clearly indicative of ferromagnetic exchange, and is corroborated by a Curie–Weiss analysis of the  $1/\chi$  vs.  $T$  data which affords  $\theta = +2.75 \text{ K}$  (Figure 75). Magnetisation measurements in the 2–7 K temperature range in external fields ranging from 0.5–7 T were then obtained (Figure 76). The saturation value of  $M/N\mu_B$  of  $\sim 17.05$  is consistent with an effective  $S' = 4$  ground spin state originating from the weak ferromagnetic coupling of eight Co(II) ions each possessing an effective  $s' = 1/2$  and assuming  $g \sim 4.3$ . Such magnetic exchange is perhaps to be expected for **20** when one considers the metal-oxygen core to be constructed from  $[\text{M}_3\text{O}_4]$  partial cubanes (M(II) cubes are invariably ferromagnetic) [224].

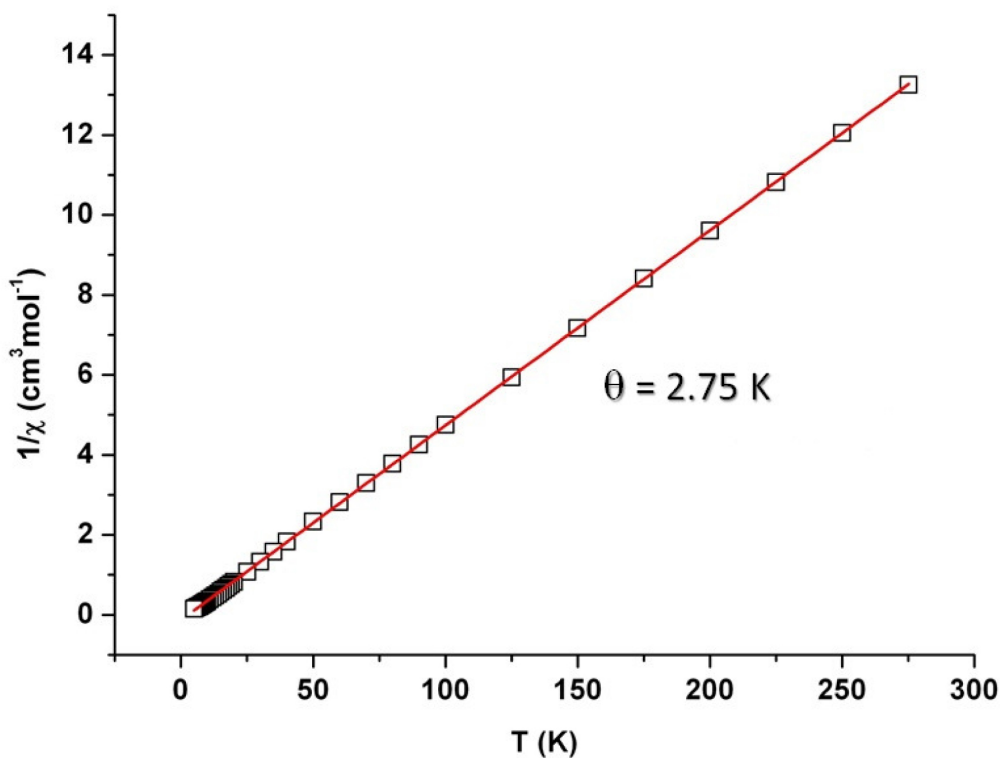


**Figure 75.** Plot of  $1/\chi$  vs.  $T$  obtained from a polycrystalline sample of **20** measured in an external field of 0.1T in the 300-5 K temperature range.

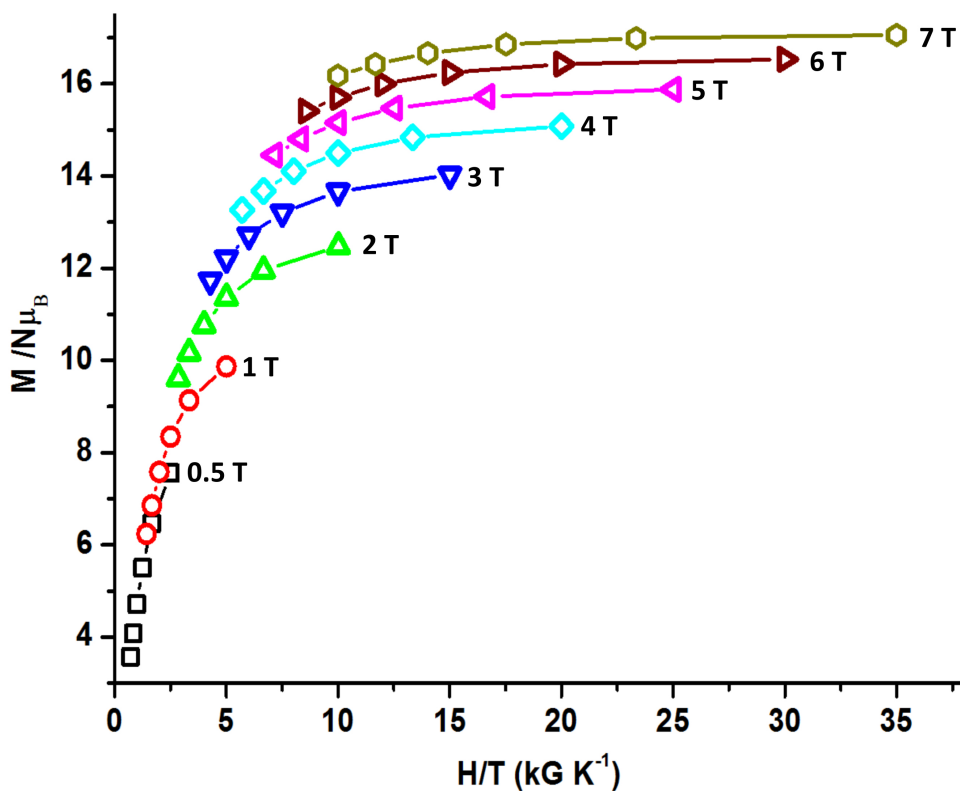


**Figure 76.** Plot of  $M N^{-1}\mu_B$  vs.  $H/T$  ( $\text{kG K}^{-1}$ ) obtained on a polycrystalline sample of **20** in external magnetic fields of 0.5, 1, 2, 3, 4, 5, 6 and 7 T in the 7-2 K temperature range.

### 5.2.3 Coordination Polymers comprising Co(II) nodes

In order to deliberately engineer an extended architecture and expand the coordination chemistry of the  $\text{LH}_2$  ligand, the ditopic dipyridyl ligand 4,4'-trimethylenedipyridine (4,4'-tmdp) was introduced into the  $\text{Co(II)/LH}_2/\text{base}$  synthon used previously in the production of **18–20**. The result was the formation of  $\{[\text{Co(II)(LH)}(4,4'\text{-tmdp})_2(\text{NO}_3)](\text{LH}_2)\}_n$  (**21**): a 1-D coordination polymer comprising both bridging and book-end  $\text{LH}_2$  moieties. **21** crystallizes in the monoclinic  $Pc$  space group with an asymmetric unit (Figure 77) comprising a distorted octahedral  $\text{Co(II)}$  centre connected to two independent 4,4'-tmdp ligands (via N1 and N2 respectively with distances  $\text{Co1-N1} = 2.141 \text{ \AA}$ ,  $\text{Co1-N2} = 2.113 \text{ \AA}$ ); one singly deprotonated terminally bound  $\text{LH}^-$  ligand (O1) and one chelating  $\text{NO}_3^-$  anion (O3 and O4).

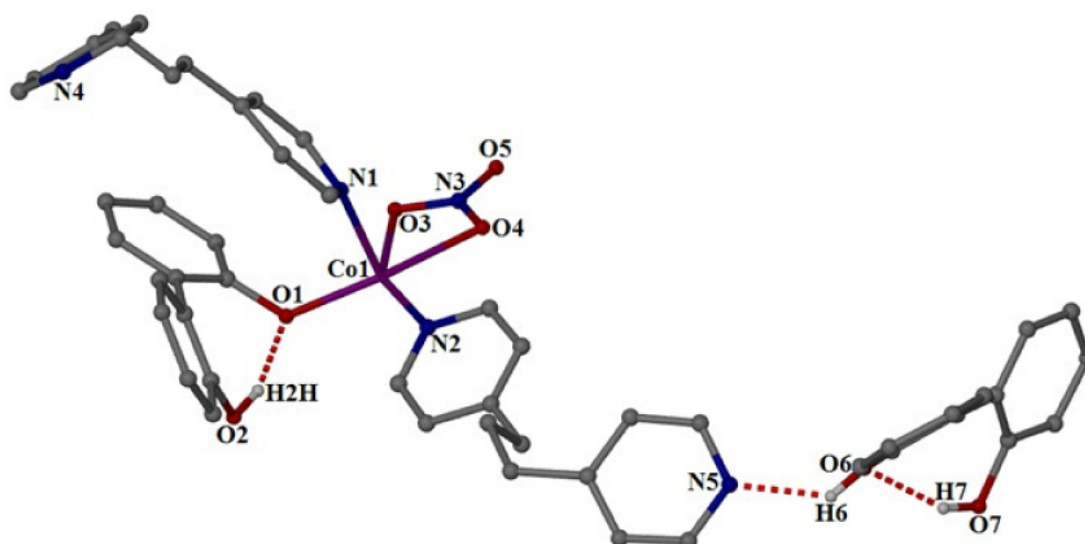


**Figure 77.** The asymmetric unit of complex **21**. Colour code as in Figure 67.

The last coordination spot (not part of the a.s.u) is occupied by another linear connector 4,4'-tmdp ligand (N4') (Figure 78). The singly deprotonated  $\text{LH}^-$  ligand possesses an intra-molecular H-bond between its  $\text{O}_{\text{phen}}$  donor and acceptor atoms ( $\text{O2(H2H)}\cdots\text{O1} = 1.692 \text{ \AA}$ ). The neutral  $\text{LH}_2$  ligand lies at the pendant end of one of the 4,4'-tmdp ligands and is held in this position via H-bonds between its  $\text{O}_{\text{phen}}$  proton (H6) and the juxtaposed N-donor atom N5 to give a distance of  $\text{O6(H6)}\cdots\text{N5} = 1.958 \text{ \AA}$ . Moreover this same  $\text{LH}_2$  unit (as observed previously in **19**) exhibits an intra-molecular H-bond to nearby  $\text{O}_{\text{phen}}$  donor and acceptor atoms ( $\text{O7(H7)}\cdots\text{O6} = 1.826 \text{ \AA}$ ) (Figure 77).

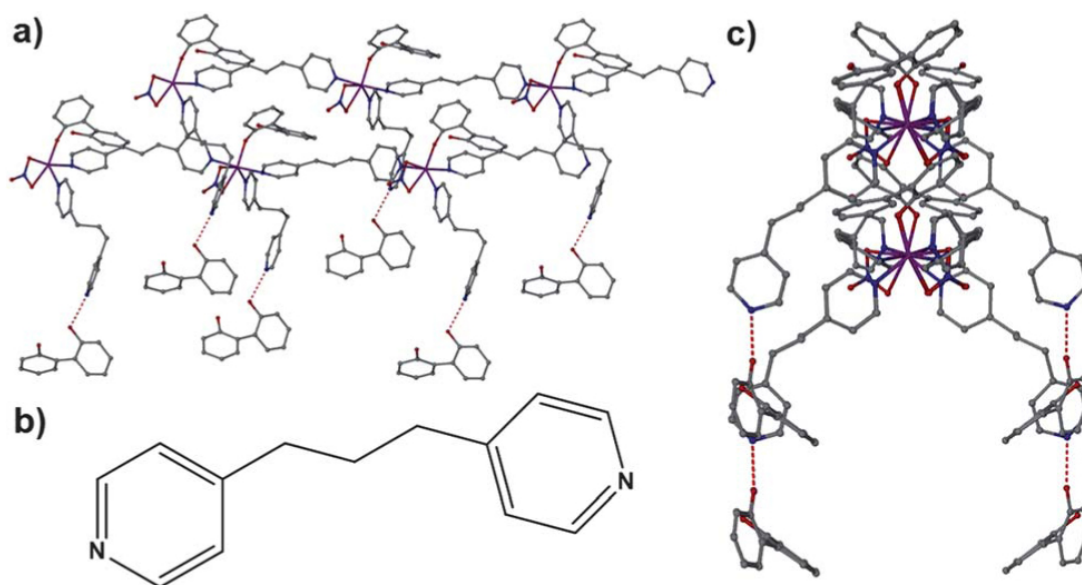


**Figure 78.** Packing in **21** showing the arrangement of two independent  $[-\text{Co(II)}-(4,4'\text{-tmdp})-]_n$  chains as viewed perpendicular (a) and parallel (c) to their linear structures. Dashed red lines represent H-bonding as described in the text. (b) Chem draw representation of the 4,4'-trimethylenedipyridine (4,4'-tmdp) ligand.

The extended structure in **21** is best described as centering on a backbone of Co(II) chains which are propagated by covalently bonded 4,4'-tmdp ligands. These ligands alternate in their relative orientation to give a wave-like shape along the chains (Figure 79a). The singly deprotonated  $\text{LH}^-$  ligands in **21** also alternate their relative orientation with respect to one another along the 1-D  $[\text{Co(II)}-(4,4'\text{-tmdp})-\text{Co(II)}-]_n$  rows, which is best observed in Figure 79c. As briefly mentioned earlier the second type of 4,4'-tmdp ligand in the a.s.u. bonds to Co1 (and s.e) at just one N-donor site (N2) which leaves the second N centre (N5) to interact with the aforementioned pendant  $\text{LH}_2$  unit. Interestingly these pendant arms possess an arc shape and alternate in their direction as they propagate away from the Co(II) centres to form a hemi-ribcage type structure (where the covalent Co(II) chain is the backbone and the pendant arms are the ribs; Figures 78 and 79). These rows of ribcage like structures then stack in an off-set parallel manner on top of one another as highlighted in Figures 78c and 79; interacting via  $\text{C-H}\cdots\pi$  interactions between the 4,4'-tmdp aromatic protons (H10) and nearby  $\text{LH}^-$  aromatic rings (C33–C38) at a distance of  $\text{C10(H10)}\cdots\pi = 2.762 \text{ \AA}$ .

Each hemi-ribcage unit shows alternating phases with respect to their wave-like Co(II) backbone and pendant arm ribs. These stacked 1-D chains arrange in parallel rows along the *b* cell direction in **21** and are linked via H-bonds between individual

LH<sub>2</sub> units of adjacent ribcage units (i.e. C46(H46)···O2 = 2.332 Å) (Figure 79c) to complete 3-D connectivity.

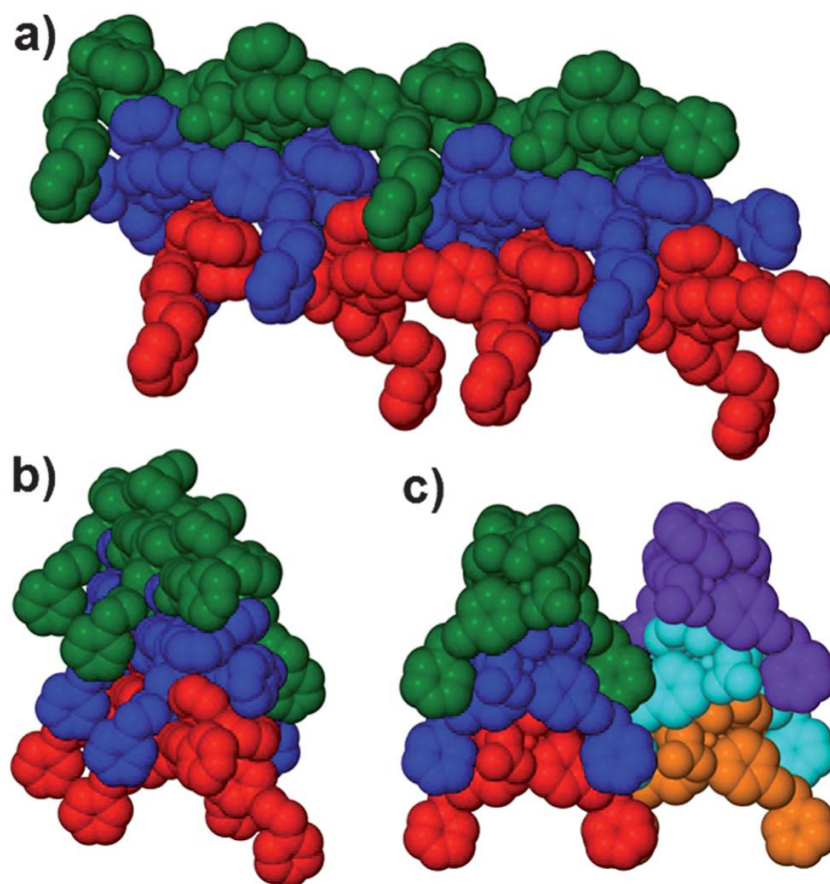


**Figure 79.** Space-fill representations of the separate 1-D Chains in **21** (distinguished via different colours) as viewed perpendicular (a) and along the chain directions (b and c). The pendant LH<sub>2</sub> ligands have been omitted for clarity.

Further investigations into the introduction of other dipyrrolyl ligands led to the use of trans-1,2-bis(4-dipyridyl)ethylene (trans-bpe). Various bench top reactions performed under ambient conditions, involving numerous combinations of Co(II)/LH<sub>2</sub>/trans-bpe/base mixtures gave no isolable/discernable products. It was therefore decided to employ forcing conditions by performing the reaction in a microwave reactor (see experimental section 5.4.3), which gave almost immediate success. Co(NO<sub>3</sub>)<sub>2</sub>·6H<sub>2</sub>O, LH<sub>2</sub> and trans-bpe (1:1:1 ratio) were dissolved in a MeOH/MeCN solvent mixture (50/50) and stirred for 2 minutes before being placed in the microwave reactor for 5 minutes (at 200 W power) at a temperature and pressure of 160 °C and 300 psi, respectively. The resultant pink solution was filtered and crystals of [Co(II)(LH)(trans-bpe)1.5(NO<sub>3</sub>)<sub>n</sub>] (22) (Figure 80) were soon obtained after slow evaporation.

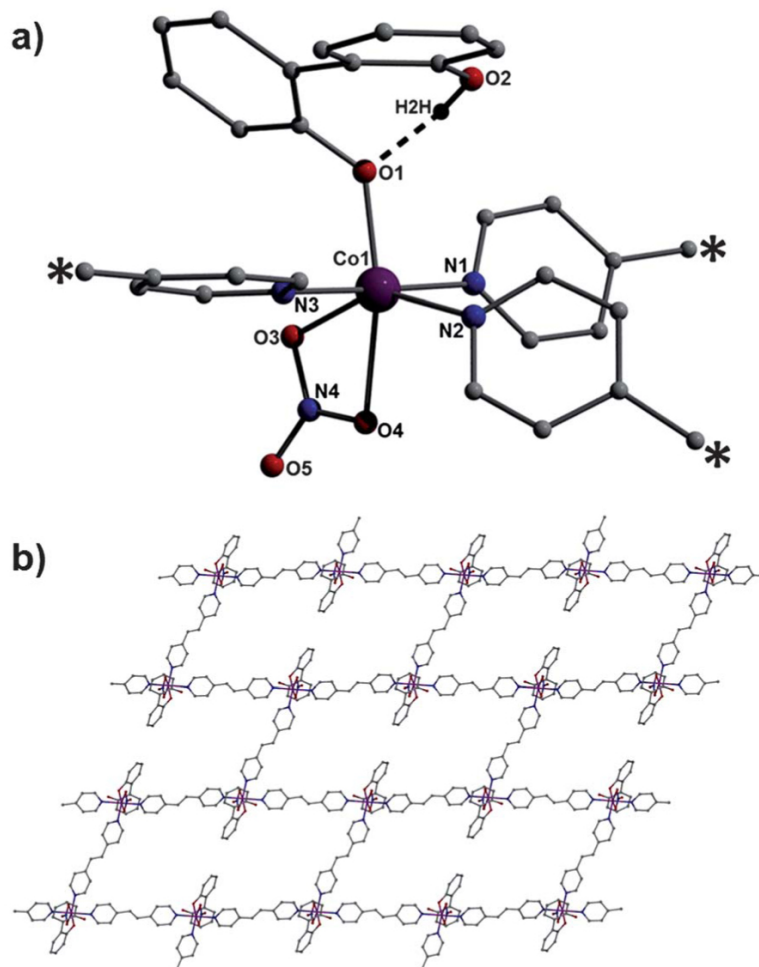


**Figure 80.** (a) Asymmetric unit in **22**. The \* symbols represent the three propagation points at the nodes in **22**. The dashed lines represent the intramolecular hydrogen bond:  $O2(H2H)\cdots O1 = 1.657 \text{ \AA}$ . (b) A 2D sheet of **22** showing a brickwork motif.

The asymmetric unit in **22** comprises a solitary Co(II) centre (Co1) bound to one singly deprotonated  $LH^-$  ligand (O1:  $Co1-O1 = 1.982 \text{ \AA}$ ) which exhibits (as in **21**) an intramolecular H-bond at a distance of  $O2(H2)\cdots O1 = 1.656 \text{ \AA}$ . This Co(II) centre is also coordinated by a  $NO_3^-$  anion along with three terminally bonded 1,2-trans(4-bipyridyl)ethylene ligands, although only half of each ligand appears in the asymmetric unit (Figure 80a). These three dipyriddy ligands act as ditopic linkers to the individual  $\{Co(II)(LH)(NO_3)\}$  nodes, which are T-shaped in nature and the result is a 2-D brickwork lattice topology (Figure 80b). These individual sheets dissect the *ac* plane of the unit cell and stack in a parallel but staggered and interdigitated arrangement along the *b* cell direction. Interestingly the 2-D sheets alternate in their relative orientations whereby the T-shaped nodes on adjacent sheets lie at right angles to one another (Fig. 81a cf. 81b).

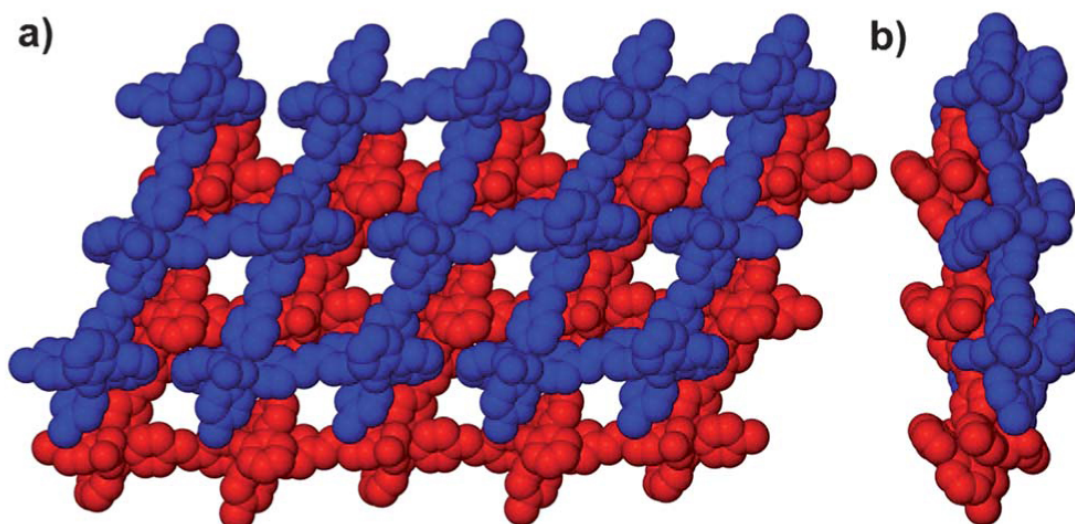


**Figure 81.** Two adjacent colour coded space-fill represented brickwork sheets in **22** as viewed perpendicular (a) and parallel (b) to the 2D plane.

### 5.3 Conclusion

We once again have shown that 2,2'-biphenol ( $\text{LH}_2$ ) is an extremely versatile ligand which, when coupled with the correct co-ligand, will result in the production of magnetically interesting discrete polynuclear Co(II) clusters or magnetically dilute extended network materials comprising Co(II) nodes. These are the first complexes of cobalt built using this ligand. Complex **20** undergoes ferromagnetic ordering at low temperatures and represents the second largest cluster to be produced using  $\text{LH}_2$ , while the production of **21** and **22** represent rare examples of coordination polymers constructed using this ligand (the latter which can only be obtained via microwave synthesis).

In addition we have successfully achieved all three accessible levels of deprotonation of  $\text{LH}_2$  in the complexes of this chapter (as in chapter 4). We have also witnessed this ligand in a variety of coordination modes, including the  $\eta^1:\eta^2,\mu$ -bridging motif as observed in complexes **18** and **19**, the  $\eta^2:\eta^2,\mu_3$ -bridging mode in **20**, and unidentate (and singly deprotonated) in complexes **20** – **22**. In complexes **19** and **21** neutral 'book-end'  $\text{LH}_2$  units exist in the crystal structure. The bridging ligand 2-hydroxypyridine (2-hpH) has aided in the production of our high-nuclearity cluster **20**, adopting the  $\eta^1:\eta^2,\mu_3$ -bridging motif. This leads us on to chapter 6, in which we utilize 2-hpH in the construction of a large family of clusters and coordination polymers comprising lanthanoid and Cu(II) ions. Akin to the Co(II) ion, most

lanthanoid ions are highly anisotropic making them ideal candidates in the construction of Single-Molecule Magnets (SMMs).

## 5.4 Experimental section

### 5.4.1 Physical measurements

Infra-red spectra were recorded on a Perkin Elmer FT-IR Spectrum One spectrometer equipped with a Universal ATR Sampling accessory (NUI Galway). Elemental analysis was carried at the School of Chemistry microanalysis service at NUI Galway. Variable-temperature, solid-state direct current (dc) magnetic susceptibility data down to 1.8 K were collected on a Quantum Design MPMS-XL SQUID magnetometer equipped with a 7 T dc magnet. Diamagnetic corrections were applied to the observed paramagnetic susceptibilities using Pascal's constants. The synthesis of **22** was carried out in a CEM Discovery microwave reactor.

### 5.4.2 Crystallography

The structures of **18–22** were collected on an Xcalibur S single crystal diffractometer (Oxford Diffraction) using an enhanced Mo source. Each data reduction was carried out on the CrysAlisPro software package. The structures were solved by direct methods (SHELXS-97)[125] and refined by full matrix least squares using SHELXL-97. SHELX operations were automated using the OSCAIL software package [127]. All hydrogen atoms in **18–22** were assigned to idealised positions. The two crystallographically related 2,2'-biphenolate ( $\text{LH}^-$ ) ligands in **20** exhibited disorder and so were modelled isotropically over two sites in 50 : 50 occupancy. This was carried out using the CRYSTALS program at the University of Edinburgh (AP). Rigid restraints were also imposed on the aromatic rings of these ligands.

### 5.4.3 Syntheses

All reagents and solvents were used as purchased. *Caution:* Although no problems were encountered in this work, care should be taken when manipulating the potentially explosive nitrate salts.

#### Preparation of $[\text{Co}(\text{II})(\text{L})_2(\text{py})_4]\cdot 2\text{EtOH}$ (**18**)

$\text{Co}(\text{NO}_3)_2\cdot 6\text{H}_2\text{O}$  (0.5 g, 1.7 mmol) and 2,2'-biphenol (0.64 g, 3.4 mmol) were dissolved in 40  $\text{cm}^3$  EtOH. 1  $\text{cm}^3$  of a 40% aqueous solution of  $\text{NEt}_4\text{OH}$  was added

slowly, resulting in a colour change from red to purple. The solution was stirred for 5 min, after which time pyridine (1 cm<sup>3</sup>, 12.4 mmol) was added. The solution was left stirring for a further 5 min, filtered and allowed to stand in a fume-cupboard covered by a perforated lid. Purple X-ray quality crystals were obtained upon slow evaporation of the mother liquor in 20% yield. FT-IR (cm<sup>-1</sup>): 3176.6 (w), 3058.1 (w), 2965.3 (w), 695.1 (vs), 2861.1 (w), 1600.1 (w), 1591.0 (w), 1551.8 (w), 1482.1 (m), 1467.7 (m), 1442.6 (m), 1428.7 (m), 1373.8 (w), 1277.3 (m), 1263.4 (m), 1246.1 (m), 1214.1 (w), 1152.3 (w), 1116.9 (w), 1094.3 (m), 1068.7 (w), 1052.8 (m), 1042.1 (m), 1034.8 (m), 1000.2 (w), 947.0 (w), 931.1 (w), 879.9 (w), 858.8 (m), 850.2 (m), 836.0 (m), 751.2 (s), 731.8 (m). Elemental analysis calculated (found) (%) for C<sub>48</sub>H<sub>48</sub>N<sub>4</sub>O<sub>6</sub>Co<sub>2</sub> (**18**): C: 64.43 (64.02), H: 5.41 (5.15), N: 6.26 (6.39).

#### **Preparation of [Co(II)<sub>2</sub>(L)<sub>2</sub>(4-pic)<sub>4</sub>]<sub>2</sub>(LH<sub>2</sub>) (**19**)**

Co(NO<sub>3</sub>)<sub>2</sub>·6H<sub>2</sub>O (0.5 g, 1.7 mmol) and 2,2'-biphenol (0.64 g, 3.4 mmol) were dissolved in 40 cm<sup>3</sup> EtOH. NMe<sub>4</sub>OH·4H<sub>2</sub>O (0.31 g, 1.9 mmol) was added, followed by 4-picoline (2 cm<sup>3</sup>, 20.54 mmol) and the resultant deep purple solution stirred for 5 min. After this time the solution was filtered and allowed to stand in a fume-cupboard covered by a perforated lid. Purple X-ray quality crystals of **19** were obtained upon slow evaporation of the mother liquor in 20% yield. FT-IR (cm<sup>-1</sup>): 3054.8 (w), 1620.7 (m), 1593.9 (w), 1581.7 (w), 1563.3 (w), 1504.9 (w), 1483.4 (m), 1468.6 (m), 1429.2 (s), 1262.4 (m), 1223.3 (s), 1149.5 (w), 1114.6 (w), 1094.1 (w), 1066.2 (w), 1040.6 (w), 1019.0 (w), 1002.4 (w), 965.6 (w), 935.2 (w), 854.7 (m), 835.8 (m), 806.9 (m), 760.2 (vs), 748.8 (vs), 729.4 (s), 703.6 (m). Elemental analysis calculated (found) (%) for C<sub>72</sub>H<sub>64</sub>N<sub>4</sub>O<sub>8</sub>Co<sub>2</sub> (**19**): C: 70.24 (69.93), H: 5.24 (5.24), N: 4.55 (4.47).

#### **Preparation of [Co(II)<sub>8</sub>(OMe)<sub>2</sub>(L)<sub>4</sub>(LH)<sub>2</sub>(2-hp)<sub>4</sub>(MeCN)<sub>4</sub>]<sub>2</sub>·MeCN (**20**)**

Co(NO<sub>3</sub>)<sub>2</sub>·6H<sub>2</sub>O (0.4 g, 1.37 mmol) and 2,2'-biphenol (0.51 g, 2.74 mmol) were dissolved in a 50 : 50 MeOH/MeCN solvent mix (40 cm<sup>3</sup> total volume). NaOH (0.11 g, 2.74 mmol) and 2-hydroxypyridine (0.39 g, 4.1 mmol) were added in quick succession and the resultant deep purple solution was stirred for 40 mins. After this time the solution was filtered and allowed to stand. Purple X-ray quality crystals of **20** were obtained upon slow evaporation of the mother liquor in 25% yield. FT-IR (cm<sup>-1</sup>): 3013.1 (w), 2920.5 (w), 2819.4 (w), 2277.4 (w), 1644.4 (w), 1606.1 (s), 1557.2 (w),

1490.0 (m), 1471.9 (s), 1435.5 (vs), 1321.8 (m), 1276.7 (s), 1257.0 (m), 1234.5 (s), 1150.6 (w), 1118.2 (w), 1097.6 (w), 1019.1 (m), 1004.1 (w), 930.7 (w), 870.0 (m), 855.0 (m), 846.0 (m), 787.1 (m), 754.0 (vs), 729.7 (s), 707.7 (m). Elemental analysis calculated (found) (%) for  $C_{104}H_{87}N_9O_{18}Co_8$  (**20**): C: 56.21 (56.55), H: 3.95 (3.29), N: 5.67 (5.81).

#### **Preparation of $\{[Co(II)(LH)(4,4-tmdp)_2(NO_3)](LH_2)\}_n$ (**21**)**

$Co(II)(NO_3)_2 \cdot 6H_2O$  (0.5 g, 1.7 mmol) and 2,2'-biphenol (0.64 g, 3.4 mmol) were dissolved in 40 cm<sup>3</sup> EtOH. 2 cm<sup>3</sup> of a 40% aqueous solution of  $NEt_4OH$  was added slowly resulting in a colour change from red to purple. This was quickly followed by the addition of 4,4'-trimethylenedipyridine (0.68 g, 3.4 mmol) and the solution was stirred for 15 min. After this time the solution was filtered and allowed to stand. Pink X-ray quality crystals of **21** were obtained upon slow evaporation of the mother liquor in 15% yield. FT-IR (cm<sup>-1</sup>): 3060.0 (w), 2931.0 (w), 1614.6 (m), 1587.7 (w), 1559.5 (w), 1465.0 (s), 1424.7 (s), 1283.0 (s), 1223.9 (s), 1151.1 (w), 1097.3 (w), 1069.2 (m), 1044.0 (w), 1017.5 (m), 939.1 (w), 845.6 (m), 826.9 (m), 811.6 (m), 793.6 (m), 751.1 (vs), 724.7 (s), 701.1 (m). Elemental analysis calculated (found) (%) for  $C_{50}H_{47}N_5O_7Co$  (**21**): C: 67.56 (67.51), H: 5.33 (5.62), N: 7.88 (8.01).

#### **Preparation of $\{[Co(II)(LH)(4,4-trans-bpe)_{1.5}(NO_3)]_n$ (**22**)**

$Co(NO_3)_2 \cdot 6H_2O$  (0.40 g, 1.37 mmol), 2,2'-biphenol (0.26 g, 1.37 mmol), trans-1,2-bis(4-pyridyl)ethylene (0.25 g, 1.37 mmol) and NaOH (0.055 g, 1.37 mmol) were added to 30 cm<sup>3</sup> of a MeOH: MeCN (50 : 50) solvent mixture. The resultant solution was premixed for two minutes and then microwaved for five minutes at 160 °C, at a power of 200 W and a pressure of 300 psi. The resultant pink solution was cooled to 50 °C and the precipitate was filtered off. The solution was allowed to stand for 2 days, after which time pink X-ray quality crystals of **22** were obtained in 10% yield. FT-IR (cm<sup>-1</sup>): 3057.1 (w), 2283.5 (w), 1712.7 (w), 1605.1 (s), 1489.4 (s), 1416.9 (s), 1276.8 (vs), 1231.0 (m), 1217.4(s), 1204.7 (m), 1152.8 (w), 1120.2 (w), 1097.2 (w), 1067.7 (m), 1016.1 (m), 960.9 (m), 826.9 (s), 808.9 (s), 750.7 (vs), 722.6 (s), 700.7 (m). Elemental analysis calculated (found) (%) for  $C_{30}H_{21}N_4O_5Co_1$  (**22**): C: 62.51 (62.42), H: 3.67 (3.89), N: 9.72 (9.39).

## 5.5 Bibliography

- [218] Merriam-Webster, *The Merriam-Webster New Book of Word Histories*. Merriam-Webster, 1991, pp. 110 – 111.
- [219] M. E. Weeks, *Discovery of the Elements*. Kessinger Publishing, 2003, pp. 21–22.
- [220] F. C. Campbell, *Elements of Metallurgy and Engineering Alloys*. ASM International, 2008, pp. 557–558.
- [221] M. Murrie, “Cobalt(II) single-molecule magnets.,” *Chemical Society reviews*, vol. 39, no. 6, pp. 1986–1995, Jun. 2010.
- [222] F. Lloret, M. Julve, J. Cano, R. Ruiz-García, and E. Pardo, “Magnetic properties of six-coordinated high-spin cobalt(II) complexes: Theoretical background and its application,” *Inorganica Chimica Acta*, vol. 361, no. 12–13, pp. 3432–3445, Sep. 2008.
- [223] A. Palić, B. Tsukerblat, S. Klokishner, K. R. Dunbar, J. M. Clemente-Juan, and E. Coronado, “Beyond the spin model: exchange coupling in molecular magnets with unquenched orbital angular momenta.,” *Chemical Society reviews*, vol. 40, no. 6, pp. 3130–3156, Jun. 2011.
- [224] E.-C. Yang, D. N. Hendrickson, W. Wernsdorfer, M. Nakano, L. N. Zakharov, R. D. Sommer, A. L. Rheingold, M. Ledezma-Gairaud, and G. Christou, “Cobalt single-molecule magnet,” *Journal of Applied Physics*, vol. 91, no. 10, p. 7382, 2002.
- [225] M. Murrie, S. J. Teat, H. Stoeckli-Evans, and H. U. Güdel, “Synthesis and characterization of a cobalt(II) single-molecule magnet.,” *Angewandte Chemie (International ed. in English)*, vol. 42, no. 38, pp. 4653–4656, Oct. 2003.
- [226] S. J. Langley, M. Helliwell, R. Sessoli, P. Rosa, W. Wernsdorfer, and R. E. P. Winpenny, “Slow relaxation of magnetisation in an octanuclear cobalt(II) phosphonate cage complex.,” *Chemical communications (Cambridge, England)*, no. 40, pp. 5029–5031, Oct. 2005.
- [227] Z. Tomkowicz, S. Ostrovsky, S. Foro, V. Calvo-Perez, and W. Haase, “Magneto-optical and Structural Investigations of Five Dimeric Cobalt(II) Complexes Mimicking Metalloenzyme Active Sites.,” *Inorganic chemistry*, vol. 51, no. 11, pp. 6046–6055, Jun. 2012.
- [228] B. Moubaraki, K. S. Murray, T. a. Hudson, and R. Robson, “Tetranuclear and Octanuclear Cobalt(II) Citrate Cluster Single Molecule Magnets,” *European Journal of Inorganic Chemistry*, vol. 2008, no. 29, pp. 4525–4529, Oct. 2008.
- [229] W. Xue, B.-Y. Wang, J. Zhu, W.-X. Zhang, Y.-B. Zhang, H.-X. Zhao, and X.-M. Chen, “A one-dimensional coordination polymer exhibiting simultaneous spin-crossover and semiconductor behaviour.,” *Chemical communications (Cambridge, England)*, vol. 47, no. 37, pp. 10233–10235, Oct. 2011.
- [230] D. Min and S. S. Yoon, “Two-dimensional cobalt-bipyridinedicarboxylate coordination polymer :,” *Inorganic Chemistry Communications*, vol. 5, pp. 143–146, 2002.
- [231] Y. Liu, Y. Qi, Y.-H. Su, F.-H. Zhao, Y.-X. Che, and J.-M. Zheng, “Five novel cobalt coordination polymers: effect of metal–ligand ratio and structure characteristics of flexible bis(imidazole) ligands,” *CrystEngComm*, vol. 12, no. 10, p. 3283, 2010.

- [232] A. Caneschi, D. Gatteschi, N. Lalioti, C. Sangregorio, R. Sessoli, G. Venturi, A. Vindigni, A. Rettori, M. G. Pini, and M. A. Novak, "Cobalt (II) -Nitronyl Nitroxide Chains as Molecular Magnetic Nanowires," no. 9, pp. 1999–2002, 2001.
- [233] D. S. Raja, N. S. P. Bhuvanesh, and K. Natarajan, "A novel water soluble ligand bridged cobalt(II) coordination polymer of 2-oxo-1,2-dihydroquinoline-3-carbaldehyde (isonicotinic) hydrazone: evaluation of the DNA binding, protein interaction, radical scavenging and anticancer activity.," *Dalton transactions (Cambridge, England : 2003)*, vol. 41, no. 15, pp. 4365–4377, Apr. 2012.
- [234] Y.-T. Wang, G.-M. Tang, Y.-C. Zhang, W.-Z. Wan, J.-C. Yu, T.-D. Li, and Y.-Z. Cui, "A new 2-D cobalt coordination polymer with the flexible 2-(1H-imidazole-1-yl)acetate: synthesis, structure, and characterization," *Journal of Coordination Chemistry*, vol. 63, no. 9, pp. 1504–1513, May 2010.
- [235] L.-F. Ma, L.-Y. Wang, Y.-Y. Wang, S. R. Batten, and J.-G. Wang, "Self-assembly of a series of cobalt(II) coordination polymers constructed from H<sub>2</sub>tbp and dipyrityl-based ligands.," *Inorganic chemistry*, vol. 48, no. 3, pp. 915–924, Feb. 2009.
- [236] S.-C. Hsu, P.-S. Chiang, H.-K. Liu, S.-H. Lo, and C.-H. Lin, "Multi-Dimensional Cobalt(II) and Nickel(II) Coordination Polymers," *Journal of the Chinese Chemical Society*, vol. 59, no. 1, pp. 18–27, Jan. 2012.
- [237] X.-H. Chang, L.-F. Ma, G. Hui, and L.-Y. Wang, "Four Low-Dimensional Cobalt(II) Coordination Polymers Based on a New Isophthalic Acid Derivative: Syntheses, Crystal Structures, and Properties," *Crystal Growth & Design*, vol. 2, no. 3, pp. 3638–3646, Jun. 2012.
- [238] J. M. Clemente-Juan, E. Coronado, A. Forment-Aliaga, J. R. Galán-Mascarós, C. Giménez-Saiz, and C. J. Gómez-García, "A new heptanuclear cobalt(II) cluster encapsulated in a novel heteropolyoxometalate topology: synthesis, structure, and magnetic properties of [(Co<sub>7</sub>H<sub>2</sub>O)<sub>2</sub>(OH)<sub>2</sub>(P<sub>2</sub>W<sub>25</sub>O<sub>94</sub>)]<sup>16-</sup>," *Inorganic chemistry*, vol. 43, no. 8, pp. 2689–2694, Apr. 2004.
- [239] M. Moragues-Canovas, C. E. Talbot-Eeckelaers, L. Catala, F. Lloret, W. Wernsdorfer, E. K. Brechin, and T. Mallah, "Ferromagnetic cobalt metallocycles.," *Inorganic chemistry*, vol. 45, no. 18, pp. 7038–7040, Sep. 2006.

## **Chapter 6:**

### **The Role of Cu(I)X (X = Cl<sup>-</sup>, Br<sup>-</sup>) in the Synthesis of Discrete {Ln(III)<sub>x</sub>Cu(I/II)<sub>y</sub>} Cage and Infinite Lattice Formations**

## 6.1 Introduction

### 6.1.1 Magnetic Properties of the lanthanoids

The most common oxidation state for the elements of the lanthanoid series is 3+. With the exception of La(III) and Lu(III), all trivalent lanthanoid ions possess unpaired electrons in their 4f orbitals. As there are seven 4f orbitals, magnetic moments for these ions can be huge. In addition, the 4f orbitals are core-like and are thus shielded by the filled 5s and 5p orbitals. This means that coordinated ligands have very little effect on these orbitals and crystal field splittings are weak. As a result, orbital angular momentum is unquenched (unlike many transition metal ions), and spin-orbit coupling can be huge in these ions. This makes clusters containing lanthanoid ions excellent candidates for Single-Molecule Magnets as not only can the ground spin state ( $S$ ) be very large, but the single-ion anisotropy can also be enormous [240]. However, as Gd(III) possesses seven unpaired electrons (one in each orbital), orbital angular momentum is quenched ( $L = 0$ ) and there is no spin-orbit coupling. This means that Gd(III) is magnetically isotropic (there is no preferred direction for its magnetic moment), and since it also possesses a large ground spin state ( $S = 7/2$ ) it is an ideal candidate for molecular coolants, a potential technology based on adiabatic demagnetization (discussed in section 1.8.3).

Unfortunately, due to the core-like nature of their magnetic orbitals, only very weak exchange coupling is observed between pairs of lanthanoid ions within cluster compounds [241]. This has led to a limited quest to construct molecular based magnets using lanthanoid ions exclusively, and the focus has switched to using these ions in conjunction with other paramagnetic species such as organic radicals and first row transition metal ions. Indeed, the dinuclear species  $\{[(\text{Me}_3\text{Si})_2\text{N}]_2(\text{THF})\text{Tb}\}_2(\mu\text{-}\eta^2:\eta^2\text{-N}_2)^-$  where Dy(III) ions are bridged via the  $\text{N}_2^{3-}$  radical [41], is the hardest molecular magnet known to date, possessing a blocking temperature of 13.9 K.

### 6.1.2 Compounds containing both rare earth and transition metal ions

Although Yttrium (Y) and Scandium (Sc) do not belong to the lanthanoid series, they exhibit very similar chemical properties, and occur in the same ores as lanthanoid elements. For this reason, Yttrium, Scandium and all elements belonging to the lanthanoid series have been grouped into the same category known as the rare earth elements. In this chapter we use Yttrium as a diamagnetic substitute for paramagnetic lanthanoid ions.

Compounds containing both rare earth and transition metal ions have been known for over a century; the first preparation being a ‘Rare Earth Cobalticyanide’ reported in 1873 by Cleve and Hoeglund [242]. Over forty years later, Bonardi and James used potassium hexacyanocobaltate to separate yttrium from erbium, which led to the synthesis and characterization of yttrium cobalticyanide [243]. Soon after, James and Willand continued this work by synthesizing a family of rare earth hexacyanocobaltate hydrates of formula  $[(Y,Ln)Co(CN)_6] \cdot nH_2O$  where  $Ln = La, Ce, Nd, Gd$  and  $Yb$  [244].

Studies involving the magnetic exchange interactions between lanthanoid and transition metal ions was initiated by Gatteschi and co-workers who reported a pair of trinuclear  $Cu(II)-Gd(III)-Cu(II)$  clusters in 1985 [245]. The interaction between the  $Gd(III)$  and  $Cu(II)$  ions turned out to be ferromagnetic, which was unexpected as it was assumed that at least one of the seven singly occupied 4f-orbitals would overlap with the singly occupied orbital on  $Cu(II)$  – resulting in an antiferromagnetic interaction between the two ions. However, as we have previously mentioned, the 4f orbitals are core-like and overlap with the magnetic  $d_{x^2-y^2}$  orbital on  $Cu(II)$  is negligible. Gatteschi et al. went on to explain this observed ferromagnetism in an article published in 1990 using a spin polarization mechanism [246]. He described the ferromagnetic exchange as arising from the overlap of the magnetic orbital on  $Cu(II)$  ( $d_{x^2-y^2}$ ) with the empty 6s orbital on the  $Gd(III)$  ion. The fraction of unpaired electron that is transferred to the  $Gd(III)$  ion aligns itself parallel with the seven f-electrons in accordance with Hund’s rule. As a result, an  $S = 4$  ground state and an  $S = 3$  excited state are established and the interaction between the ions is ferromagnetic. Kahn and co-workers, devised a similar hypothesis to this, suggesting a charge transfer mechanism in which the electron in the  $d_{x^2-y^2}$  orbital on  $Cu(II)$  is transferred to a 5d orbital on the  $Gd(III)$  ion, leading to the same ground and excited states [247]. To back up this hypothesis, a density functional study on the exchange coupling between  $Cu(II)$  and  $Gd(III)$  published in 2009 by Rajaraman et al. strongly suggests the involvement of the partially occupied 5d orbital in the interaction [248]. Aside from the odd exception where the  $Cu(II)$  and  $Gd(III)$  ions are linked via a single bridge [46], [249], [250], ferromagnetism appears to be an intrinsic property of  $Cu(II)-Gd(III)$  coupling [245–248], [251–255]. Because of this inherent ferromagnetism and

the magnetically isotropic nature of the Gd(III) ion, systems containing both Cu(II) and Gd(III) ions are model contenders as molecular coolant materials [44], [45].

Unfortunately, determination of the nature of the exchange mechanism between Cu(II) and other magnetic lanthanoid ions has proven challenging, due to the first order orbital contribution to their magnetic moments. This renders the spin Hamiltonian for isotropic exchange invalid. Kahn and Guillou came up with a generalized scheme for the interaction (ferro- or antiferromagnetic) between Cu(II) and the magnetic Ln(III) ions which was published in 'Research Frontiers in Magnetochemistry' in 1993 [256]. This scheme was based on the fact that the spin momentum and angular momentum of Ln(III) ions prefer to align antiparallel to one another if the number of f-electrons is less than seven ( $f^1 - f^6$ ), and align parallel if the ion possesses more than seven f-electrons ( $f^8 - f^{13}$ ). The Gd(III)–Cu(II) coupling mechanism involving the mixing of the Gd(III)–Cu(II) ground configuration with the charge transfer Gd(II)–Cu(III) configuration that gives rise to ferromagnetic coupling was deemed valid for all magnetic Ln(III) ions under this scheme. Since the Ln(III) and Cu(II) spin momenta align parallel, when  $f < 7$  the resultant spin momentum aligns antiparallel to the angular momentum of the Ln(III) and antiferromagnetic coupling is observed. In contrast, ferromagnetic coupling is observed when  $f > 7$ , because the total spin momentum of the Gd(III)–Cu(II) pair is aligned parallel with the angular momentum.

The idea was explored further by Costes et al., by measuring the magnetic behaviour of a series of homologous dinuclear Cu(II)–Ln(III) complexes (where Ln(III) represents all lanthanoids except La, Pm and Lu) [257]. These dimers were compared to their low spin Ni(II) equivalents ( $\text{Ni(II)}_{\text{LS}}\text{–Ln(III)}$ ) so that the magnetic behaviour of the Ln(III) ions could be isolated, as  $\text{Ni(II)}_{\text{LS}}$  is diamagnetic. For all magnetic Ln(III) ions (except Sm(III) and Eu(III)) the  $^{2S+1}L_J$  ground state is well separated from the first excited state. In the presence of a ligand field, Ln(III) ions exhibit a phenomenon known as the Stark Effect, which splits the degenerate energy levels of this ground state (Stark splitting occurs in the presence of an electric field and is similar to Zeeman splitting in the presence of a magnetic field). As the temperature is lowered, progressive depopulation of these Stark components occurs, leading to a temperature dependence of  $\chi_{\text{M}}T$  for a single Ln(III) ion. In the  $\text{Ni(II)}_{\text{LS}}\text{–Ln(III)}$  dimers, there is no magnetic coupling between the ions, and deviations of  $\chi_{\text{M}}T$  with respect to

T arises purely as a result of the depopulation of these levels. The difference in the  $\chi_M T$  vs T curves between the Ni(II)<sub>LS</sub>-Ln(III) dimers and the Cu(II)-Ln(III) give us some insight into the nature of the exchange. According to this article, the Cu(II)-Ln(III) interaction is antiferromagnetic when Ln = Ce, Nd, Sm, Tm, Yb, and ferromagnetic when Ln = Gd, Tb, Dy, Ho, Er. The Cu(II)-Pr(III) and the Cu(II)-Eu(III) pairs exhibited no significant interaction in accordance with the non-magnetic nature of the ground state for these lanthanide ions. With the exceptions of Tm(III) and Yb(III), these results were in line with Kahn's hypothesis.

In a similar study reported a year later in 1999 [258], Kahn and co-workers used Zn(II) as the diamagnetic replacement for Cu(II) ions in a homologous series of {Ln(III)<sub>2</sub>M(II)<sub>3</sub>} ladder compounds where Ln = Tb, Dy, Ho and Tm. While the Cu(II)-Tb(III) and Cu(II)-Dy(III) compounds exhibited ferromagnetic coupling, the Cu(II)-Ho(III) and the Cu(II)-Tm(III) interactions were assigned as antiferromagnetic and ambiguous respectively. These two studies proved, that the interaction between Cu(II) and the magnetic Ln(III) ions (except for Gd(III)), was not as simple as Kahn had first believed. Although the magnetic properties of compounds containing Tb(III) or Dy(III) coupled with Cu(II) ions may be difficult to interpret, the possibility for large cluster anisotropies and the high probability of ferromagnetic exchange make these combinations attractive candidates for complexes exhibiting Single-Molecule magnet behaviour. Indeed, there are numerous examples in the literature of Tb(III)/Dy(III)-Cu(II) clusters exhibiting SMM behaviour [259-262].

### 6.1.3 2-hydroxypyridine as a bridging ligand in Cu(II)-Ln(III) clusters

The ligand 2-hydroxypyridine (termed 2-pyridonate when deprotonated) and its 6-substituted derivatives have been used extensively by the Winpenny group in the synthesis of Cu(II)-Ln(III) clusters. The first complexes of this type were a pair of hexanuclear [Cu(II)<sub>4</sub>Ln(III)<sub>2</sub>] clusters (where Ln = Gd, Dy) published in 1989 [263], in which the deprotonated oxygen atom of 2-pyridonate bridges a Ln(III) ion to a Cu(II) ion while the nitrogen atom coordinates to one Cu(II) ion. In 1991 an octanuclear [Cu(II)<sub>4</sub>La(III)<sub>4</sub>] cluster emerged in which the ligand again adopts a trinucleating mode ( $\eta^2:\eta^1,\mu_3$ ): this time two La(III) ions are bridged via the oxygen atom, while the nitrogen coordinates to one Cu(II) ion [264]. Attempts to replace the diamagnetic La(III) ions with Gd(III) failed, and instead led to the synthesis of a

hexanuclear  $[\text{Cu(II)}_4\text{Gd(III)}_2]$  cluster. Since then, Winpenny and coworkers have reported numerous Cu(II)-Ln(III) structures whereby the metal ions are bridged via 6-methyl-2-pyridonate [265–267], 6-chloro-2-pyridonate [267–270], 6-bromo-2-pyridonate [267] and 6-fluoro-2-pyridonate [267]. In the same year that Winpenny's  $[\text{Cu(II)}_4\text{La(III)}_4]$  cluster appeared, Wang and co-workers reported a  $[\text{Y(III)}_2\text{Cu(II)}_8]$  compound in which 2-hydroxypyridine was also utilized as a bridging ligand [271]. Soon after a second structure emerged, in which Nd(III) ions took the place of Y(III) [272]. It was not until very recently that a family of these clusters of formula  $[\text{Ln(III)}_2\text{Cu(II)}_8]$  (where Ln = Y, Gd, Dy and Tb) were synthesized and magnetically characterized [273]. The ability of 2-hydroxypyridine and its derivatives to bridge Ln(III) and Cu(II) ions toward high nuclearity clusters encouraged us to use this ligand as a co-ligand in conjunction with 2,2'-biphenol ( $\text{LH}_2$ ).

## 6.2 Results and Discussion

### 6.2.1 A family of discrete $[\text{Ln(III)}_4\text{Cu(II)}_4]$ clusters

Attempts to crystallize complexes containing both rare earth and copper ions using the ligand  $\text{LH}_2$  have unfortunately failed thus far. Many different solvent systems, synthetic techniques (such as solvothermal and microwave synthesis), and co-ligands have been employed to no avail. However, utilization of 2-hydroxypyridine (2-hpH) in a reaction mixture containing  $\text{LH}_2$  and a solvent system comprising methanol, dichloromethane and acetonitrile led to the formation of the discrete cluster  $[\text{Gd(III)}_4\text{Cu(II)}_4(\text{OH})_4(\text{OMe})_2(2\text{-hp})_8(2\text{-hpH})_4(\text{Br})_2(\text{NO}_3)_4] \cdot 2\text{H}_2\text{O} \cdot 2\text{MeOH}$  (**23**, Figure 82). As  $\text{LH}_2$  is not present in the structure, its removal from the reaction yields the same result. The synthesis of **23** involves the reaction of the salts  $\text{Gd(III)(NO}_3)_3 \cdot x\text{H}_2\text{O}$  and  $\text{Cu(I)Br}$  (in a 1.5:1 ratio) along with 2-hpH and NaOH. Replacement of  $\text{Gd(III)(NO}_3)_3 \cdot x\text{H}_2\text{O}$  with  $\text{Dy(III)(NO}_3)_3 \cdot x\text{H}_2\text{O}$  and  $\text{Tb(III)(NO}_3)_3 \cdot x\text{H}_2\text{O}$  in the reaction yields the isostructural clusters  $[\text{Dy(III)}_4\text{Cu(II)}_4]$  (**24**) and  $[\text{Tb(III)}_4\text{Cu(II)}_4]$  (**25**) respectively, although the former is obtained in very low yield (~1 %) and the latter is only obtained if microwave synthesis is employed. These three structures share the general formula  $[\text{Ln(III)}_4(\text{Cu(II)}_4(\text{OH})_4(\text{OMe})_2(2\text{-hp})_8(2\text{-hpH})_4(\text{Br})_2(\text{NO}_3)_4)] \cdot x\text{H}_2\text{O} \cdot y\text{MeOH}$  (where Ln = Gd,  $x = 2$ ,  $y = 2$  (**23**); Dy,  $x = 0$ ,  $y = 4$  (**24**); Tb,  $x = 0$ ,  $y = 4$  (**25**), and represent the first analogues to Winpenny's  $[\text{Ln(III)}_4\text{Cu(II)}_4]$ , comprising paramagnetic lanthanoid ions.

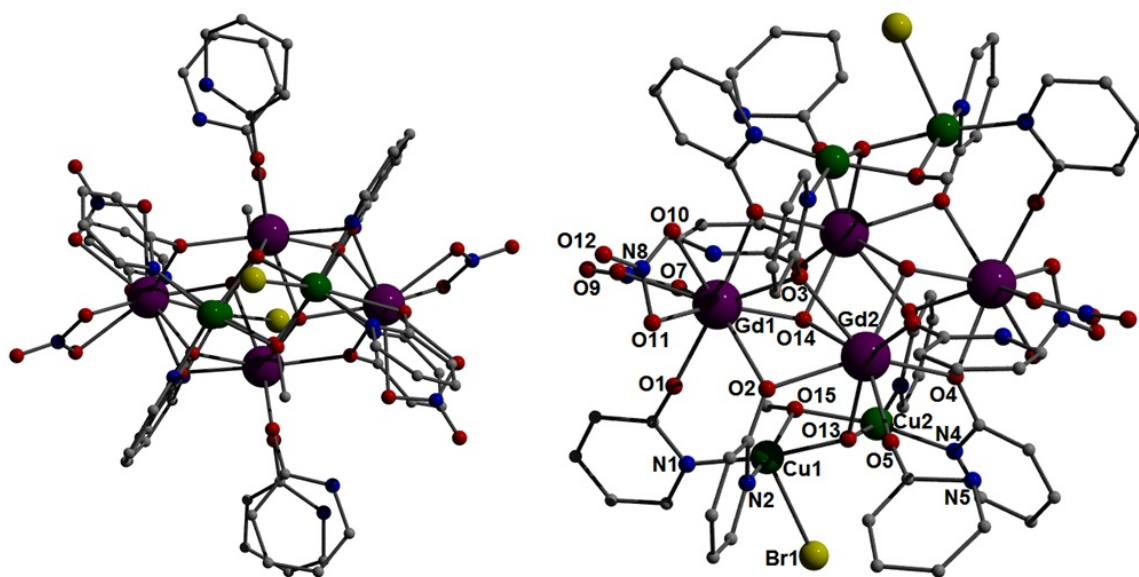


**Figure 82.** Crystal structures of **23** as viewed perpendicular (left) and approximately parallel (right) to the planar  $\{\text{Gd(III)}_4\}$  butterfly motif located at the centre of the molecule. All Hydrogen atoms have been omitted for clarity. Colour code: Purple (Gd), Green (Cu), Red (O), Blue (N), Grey (C) and Yellow (Br).

### 6.2.1.1 Structural descriptions

Complexes **23-25** crystallize in the triclinic P-1 space group and due to their isostructural nature we will describe only complex **23** in detail here (crystallographic data for all three complexes can be found in Table 14). The centre of the molecule in **23** is dominated by a planar array of Gd(III) ions (Gd1, Gd2 and s.e.) arranged in the ‘butterfly’ motif whereby Gd1 and Gd2 (and s.e) occupy the ‘wing-tip’ and ‘body’ positions respectively (Figure 82). A centre of inversion lies at the midpoint between the two ‘body’ Gd(III) ions (Gd2...Gd2'). These Gd(III) centres are connected via the  $\text{O}_{\text{phen}}$  donor atoms from two distinct 2-hp<sup>-</sup> ligands (O2 and O3) and the O donor atoms belonging to two  $\mu_3$ -bridging  $\text{OH}^-$  ions (O14 and s.e). A MeOH solvent molecule of crystallization hydrogen bonds to the hydrogen atom of each bridging  $\text{OH}^-$  ion ( $\text{O16}\cdots\text{H13H} = 1.895 \text{ \AA}$ ). Two pairs of Cu(II) ions (Cu1, Cu2 and s.e) lie above and below this  $\{\text{Gd(III)}_4\}$  core respectively and are connected to one another through bridging  $\text{OMe}^-$  ions (O15 and s.e). These Cu(II) pairs are linked to the central  $\{\text{Gd(III)}_4\}$  belt via two  $\mu_3$ -bridging  $\text{OH}^-$  ions (O13 and s.e) and eight deprotonated 2-hp<sup>-</sup> ligands via the  $\text{N}_{\text{pyridyl}}$  atoms N1-N4 and their symmetry equivalents (Cu1-N1 = 1.975 Å, Cu1-N2 = 1.980 Å, Cu2-N3 = 1.969 Å, Cu2-N4 =

1.973 Å). The result of this extensive connectivity is a  $\{\text{Gd(III)}_4\text{Cu(II)}_4\}$  core best described as a severely distorted face sharing of two trigonal prisms (Figure 83).

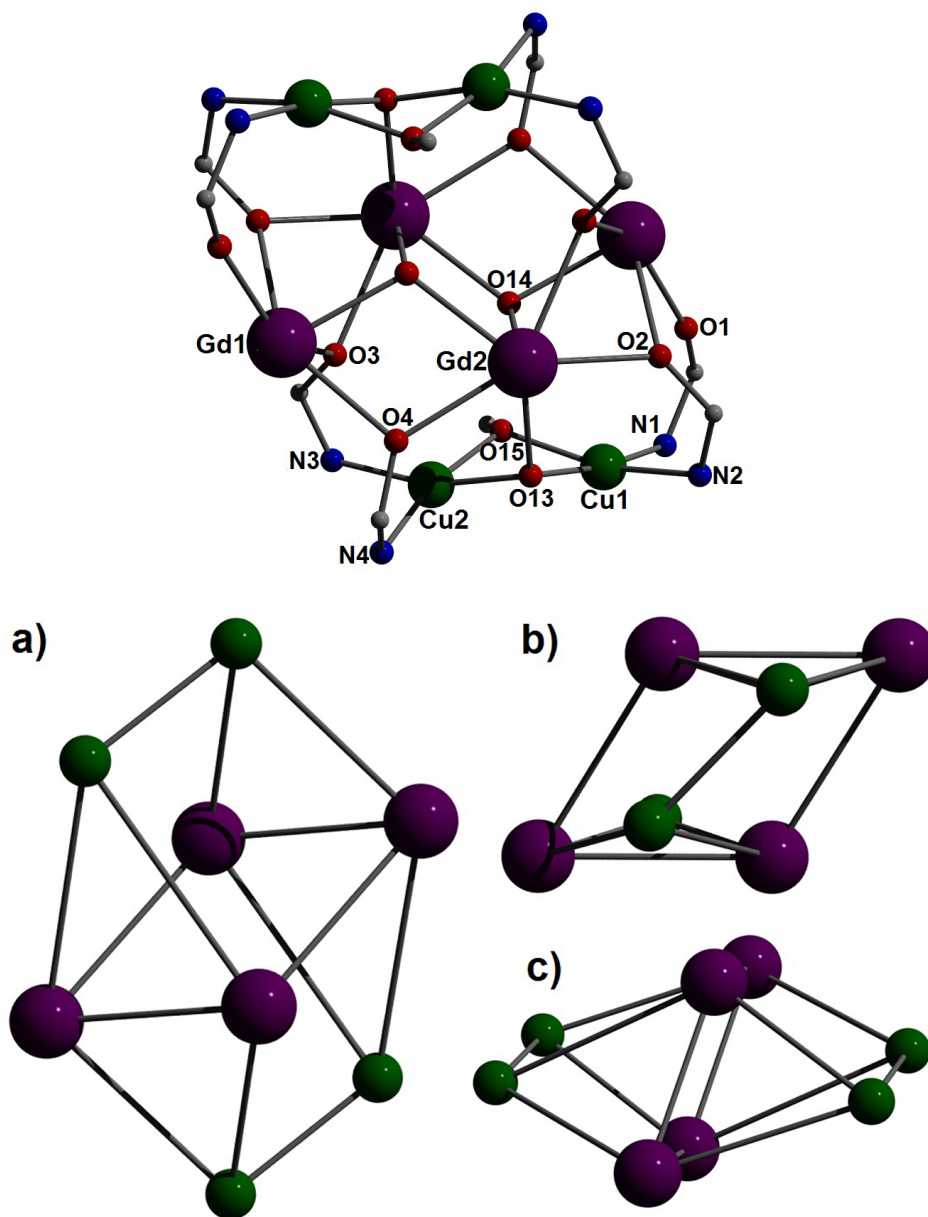


**Figure 83.** (top) The magnetic core of **23** highlighting all bridging pathways. (bottom) Polyhedral representations of the magnetic core in the  $\{\text{Ln(III)}_4\text{Cu(II)}_4\}$  (Ln = Gd (**23**), Dy (**24**) and Tb (**25**)) cages described in this work. Note: These diagrams were produced from the crystal structure data of **23**.

The coordination spheres at Gd1 (and s.e) are completed by two chelating  $\text{NO}_3^-$  ions while two neutral 2-hpH ligands terminally bind to Gd2 and its symmetry equivalents via the  $\text{O}_{\text{phen}}$  donor atoms O5 and O6. These ligands are protonated at their pyridyl N atoms (N5 and N6) and thus remain neutrally charged. Interestingly the pyridyl H6A proton takes part in intra-molecular H-bonding with a nearby  $\text{NO}_3^-$  oxygen acceptor

atom at a close distance of 1.944 Å (N6-H6A...O5). The coordination numbers of Gd1 and Gd2 are nine and eight coordinate and exhibit distorted mono-capped square-antiprismatic and distorted square-antiprismatic geometries respectively. The coordination sphere at the distorted octahedral Cu1 (and s.e) centre is completed by a terminal Br<sup>-</sup> ion at a distance of 2.789 Å. The five coordinate Cu2 centre has a distorted square based pyramidal geometry ( $\tau = 0.06$ ).

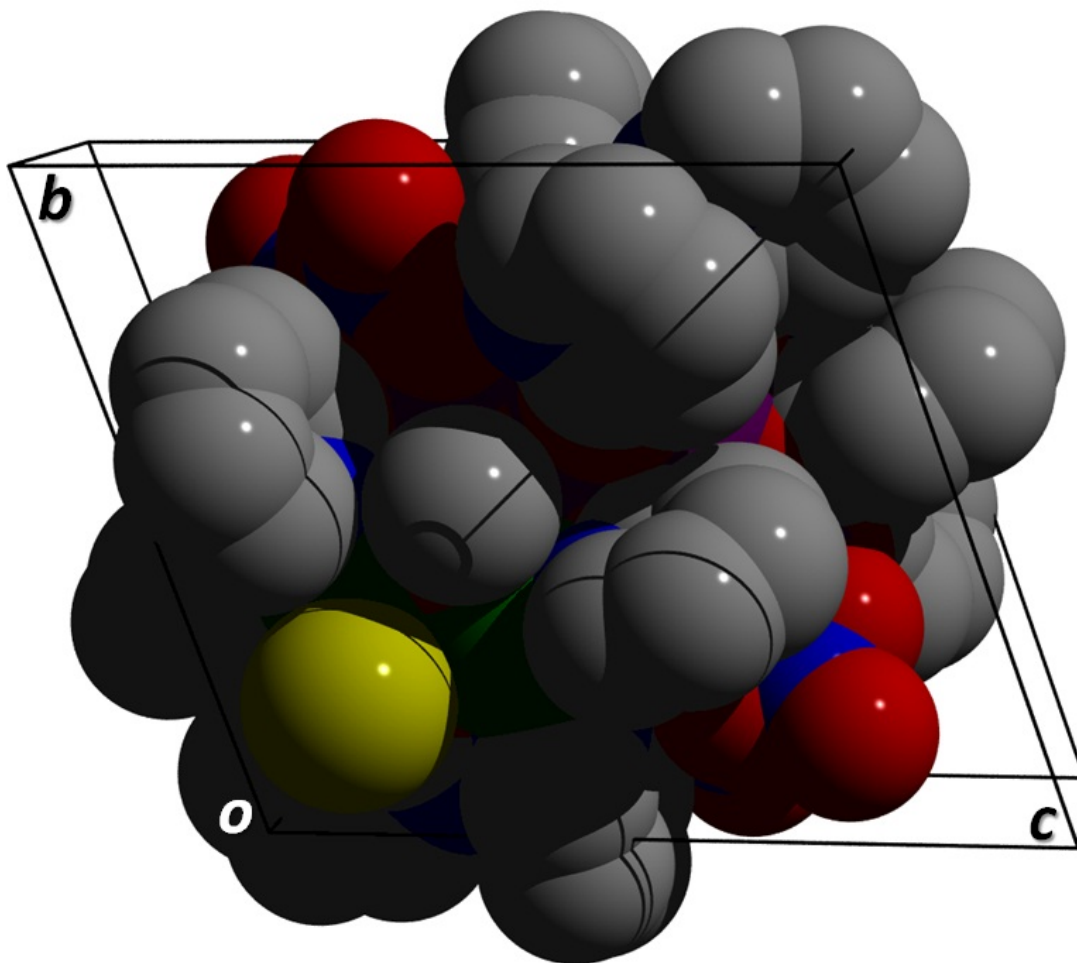


**Figure 84.** Unit cell in **23** as viewed along the *a* axis accommodating one [Gd(III)<sub>4</sub>Cu(II)<sub>4</sub>] cluster represented as space-fill. Hydrogen atoms and solvent molecules (MeOH and H<sub>2</sub>O) are omitted for clarity.

The unit cell of **23** accommodates one [Gd(III)<sub>4</sub>Cu(II)<sub>4</sub>] cluster as shown in Figure 84. These cluster units are linked together via hydrogen bonding interactions and propagate in superimposable rows along all three unit cell axes. Four hydrogen bonding interactions connect neighbouring clusters along the *b* axis; a NO<sub>3</sub><sup>-</sup> oxygen atom interacts with two nearby hydrogen atoms; one aromatic hydrogen atom of a 2-

hpH ring ( $O9\cdots H19 = 2.299 \text{ \AA}$ ), and the other which protonates the nitrogen atom (N5) of the same 2-hpH ligand ( $O9\cdots H5 = 2.631$ ). The remaining two hydrogen bonds are the symmetry equivalents of the aforementioned interactions. Packing along the  $c$  axis is facilitated by a hydrogen bonding interaction between a  $NO_3^-$  oxygen atom and an aromatic hydrogen ( $O11\cdots H8 = 2.456 \text{ \AA}$ ), while the same is observed along the  $a$  axis between a bromide ligand and an aromatic hydrogen atom of a neighbouring cluster ( $Br1\cdots H30 = 2.852 \text{ \AA}$ ). Akin to complex **23**, the cluster units in complexes **24** and **25** stack into superimposable rows occurs along the  $a$ ,  $b$  and  $c$  axes via hydrogen bonding. These hydrogen bonding interactions in each of the three directions are almost identical to those observed in the crystal structure of **23**.

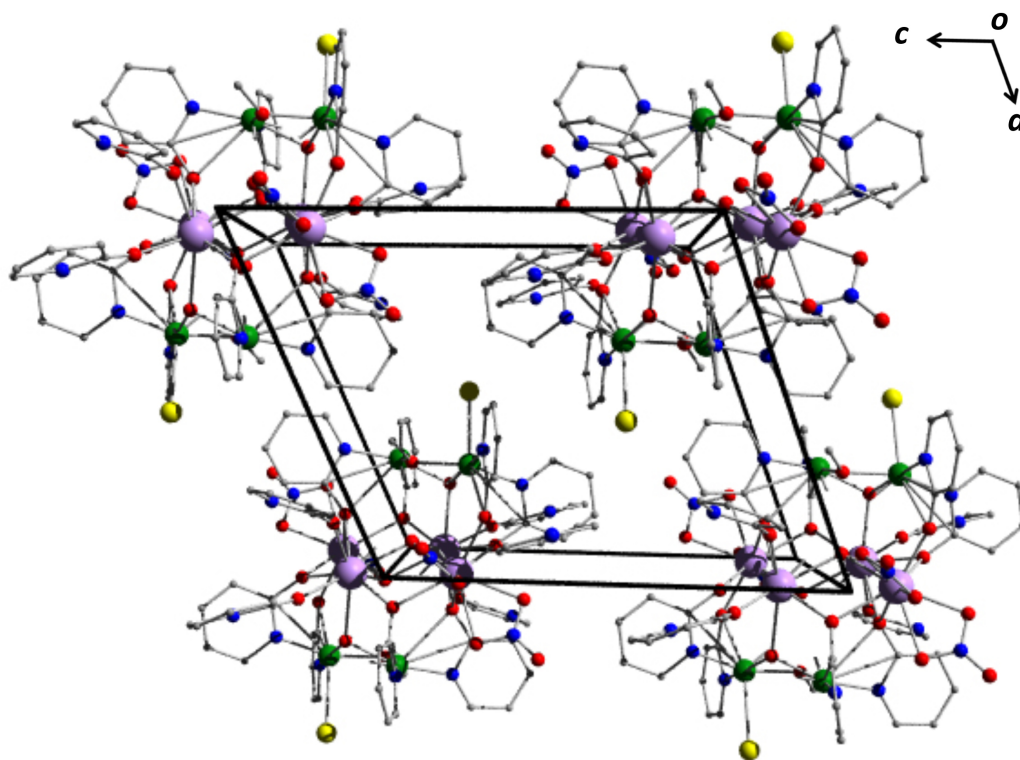


**Figure 85.** The unit cell of complex **24** comprising four quarter  $[Dy(III)_4Cu(II)_4]$  cluster units as viewed along the  $b$  axis. Hydrogen atoms and MeOH solvent molecules of crystallization have been omitted for clarity.

Despite their isostructural molecular structures and intermolecular packing arrangements, the positions of complexes **23**, **24** and **25** with respect to the unit cell are quite different to one another. One quarter of a cluster unit occupies each of the four  $b$  edges of the unit cell of **24** (one quarter from each of four  $[Dy(III)_4Cu(II)_4]$  clusters; Figure 85), while the unit cell of **25** contains two half cluster units; each of the two clusters being dissected by the  $ac$  face of the unit cell (Figure 86).

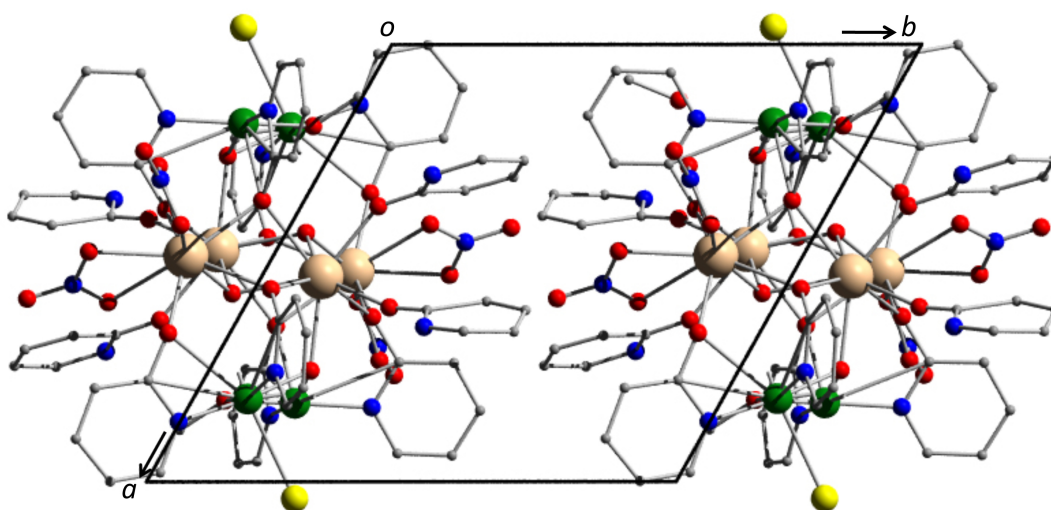


**Figure 86.** The unit cell of complex **25** comprising two half  $\{\text{Tb(III)}_4\text{Cu(II)}_4\}$  cluster units, viewed along the  $c$  axis. Hydrogen atoms and MeOH solvent molecules of crystallization have been omitted for clarity.

**Table 14.** Crystal data obtained from X-ray diffraction studies on **23-25**.

Parameters	<b>23</b>	<b>24</b>	<b>25</b>
Formula <sup>a</sup>	$\text{C}_{64}\text{H}_{70}\text{N}_{16}\text{O}_{34}\text{Br}_2\text{Cu}_4\text{Gd}_4$	$\text{C}_{66}\text{H}_{78}\text{N}_{16}\text{O}_{34}\text{Br}_2\text{Cu}_4\text{Dy}_4$	$\text{C}_{66}\text{H}_{78}\text{N}_{16}\text{O}_{34}\text{Br}_2\text{Cu}_4\text{Tb}_4$
$M_w$	2650.34	2703.42	2689.10
Crystal System	Triclinic	Triclinic	Triclinic
Space group	P-1	P-1	P-1
$a/\text{\AA}$	13.2619(4)	13.1650(4)	13.2115(3)
$b/\text{\AA}$	13.5227(4)	13.5209(4)	13.5184(4)
$c/\text{\AA}$	14.5294(4)	14.5237(5)	14.5178(5)
$\alpha/^\circ$	98.063(2)	97.933(3)	97.923(3)
$\beta/^\circ$	106.543(3)	106.537(3)	106.608(3)
$\gamma/^\circ$	115.055(3)	115.230(3)	115.221(3)
$V/\text{\AA}^3$	2158.27(11)	2139.29(12)	2144.65(11)
$Z$	1	1	1
$T/\text{K}$	150(2)	150(2)	150(2)
$\lambda/\text{\AA}$	0.7107	0.7107	0.7107
$D_c/\text{g cm}^{-3}$	2.039	2.098	2.9046
$\mu(\text{Mo-K}\alpha)/\text{mm}^{-1}$	5.009	5.448	5.248
Meas./indep. ( $R_{\text{int}}$ ) refl.	7901/6613 (0.0257)	7827/6011(0.0368)	7843/5911 (0.0347)
wR2 (all data)	0.1159	0.1246	0.1221
$R1^{d,e}$	0.0409	0.0478	0.0425
Goodness of fit on $F^2$	1.051	1.057	1.063

### 6.2.1.2 Magnetic susceptibility measurements on complex **23**

Magnetic susceptibility measurements on a polycrystalline sample of **23** were carried out in an applied field of 0.1 T over the 2–300 K temperature range (Figure 87). The room temperature  $\chi_M T$  value of  $34.6 \text{ cm}^3 \text{ mol}^{-1} \text{ K}$  is consistent with that expected for an uncoupled  $[\text{Cu(II)}_4\text{Gd(III)}_4]$  unit ( $33.0 \text{ cm}^3 \text{ mol}^{-1} \text{ K}$  assuming  $g = 2.00$ ). The  $\chi_M T$  product in **23** remains nearly constant with decreasing temperature down to  $\sim 25 \text{ K}$ , below which it begins to descend more rapidly before reaching a resting value of  $24.8 \text{ cm}^3 \text{ mol}^{-1} \text{ K}$  at  $5 \text{ K}$ . The magnetization measurements on **23** (Figure 88) show a saturation value of  $29.52 N\mu_B$  at  $2 \text{ K}$  ( $7 \text{ T}$ ) and is suggestive of field induced parallel alignment of the four Gd(III) ions in **23**. This can be rationalised assuming the peripheral Cu(II) pairs are antiferromagnetically coupled ( $\text{Cu1-O13-Cu2} = 96.10^\circ$ ,  $\text{Cu1-O15-Cu2} = 97.20^\circ$ ). Indeed this hypothesis is corroborated by the strong antiferromagnetic exchange observed within similar Cu(II) pairs in the  $[\text{Cu(II)}_4\text{La(III)}_4]$  analogue of Winpenny and co-workers [264].

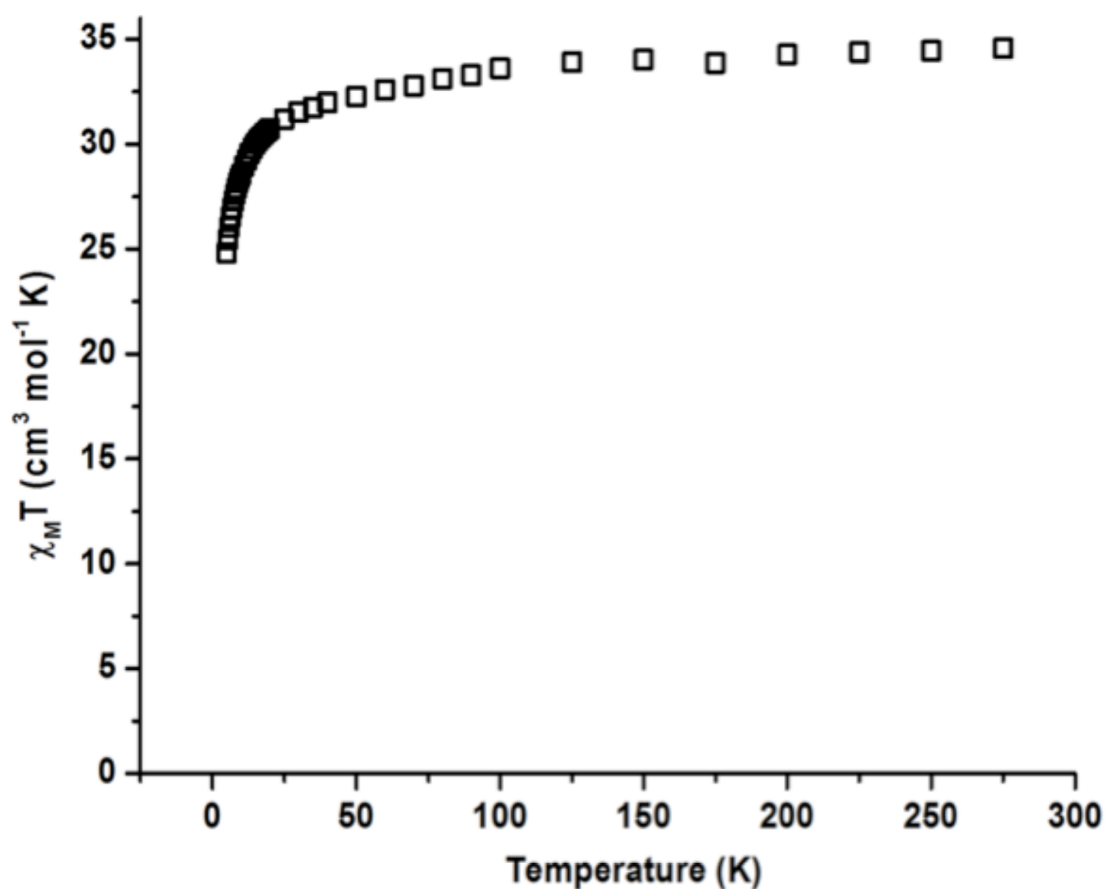


**Figure 87.** Temperature dependence of  $\chi_M T$  for **22** collected in an applied field of 0.1 T.

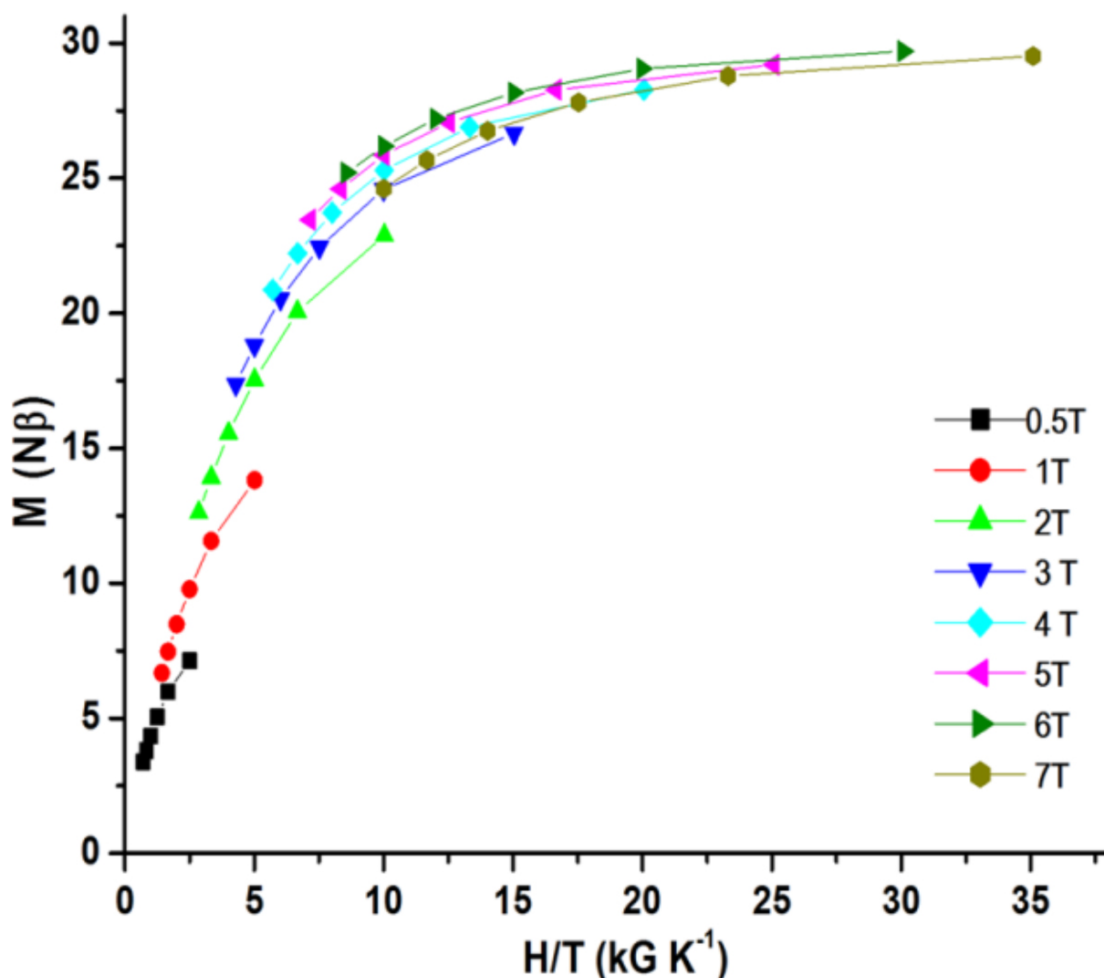


**Figure 88.** Plot of reduced magnetization ( $N\mu_B$ ) vs  $H/T$  ( $\text{kG K}^{-1}$ ) obtained from **22** in the 2-7 K temperature range in the magnetic fields shown. The solid lines are for visual purposes only.

### 6.2.2 Coordination polymers comprising $\{\text{Ln(III)}_2\text{Cu(III)}_8\}$ cluster nodes

Upon production of **23-25** it became apparent that employing a 1.5:1 Ln(III) / Cu(I) ratio yields 1:1 discrete clusters (i.e.  $\{\text{Ln(III)}_4\text{Cu(II)}_4\}$ ). We promptly began repeating the procedures used in synthesising **23-25**, this time employing an excess of our copper source  $[\text{Cu(I)X}]$  where  $X = \text{Cl}, \text{Br}$  with respect to our Ln(III)/Cu(II) precursor mixtures in order to influence the final product. The first success was rapid and came in the crystallization of the Cu(II)/Cu(I) rich  $[\text{Gd(III)}_2\text{Cu(II)}_8\text{Cu(I)}_1(\text{O})_2(2\text{-hp})_{12}(\mu\text{-Cl})_2(\text{Cl})_3(\text{NO}_3)_2]_n$ . (**26**) species (Figure 89). Complex **26** is a 1-D coordination polymer comprising of  $\{\text{Gd(III)}_2\text{Cu(II)}_8\}$  nodes linked into chains via trigonal planar  $\{\text{Cu(I)Cl}_3\}^{2-}$  connector units – a common bonding mode in copper(I) halocuprates (Figure 90) [274], [275]. Indeed the inorganic nature of these  $\{\text{Cu(I)Cl}_3\}^{2-}$  linker moieties means that this coordination polymer may also be described as an infinite linear lattice comprising  $\{\text{Gd(III)}_2\text{Cu(II)}_8\text{Cu(I)}_1\}$  repeating units (Figure 90).

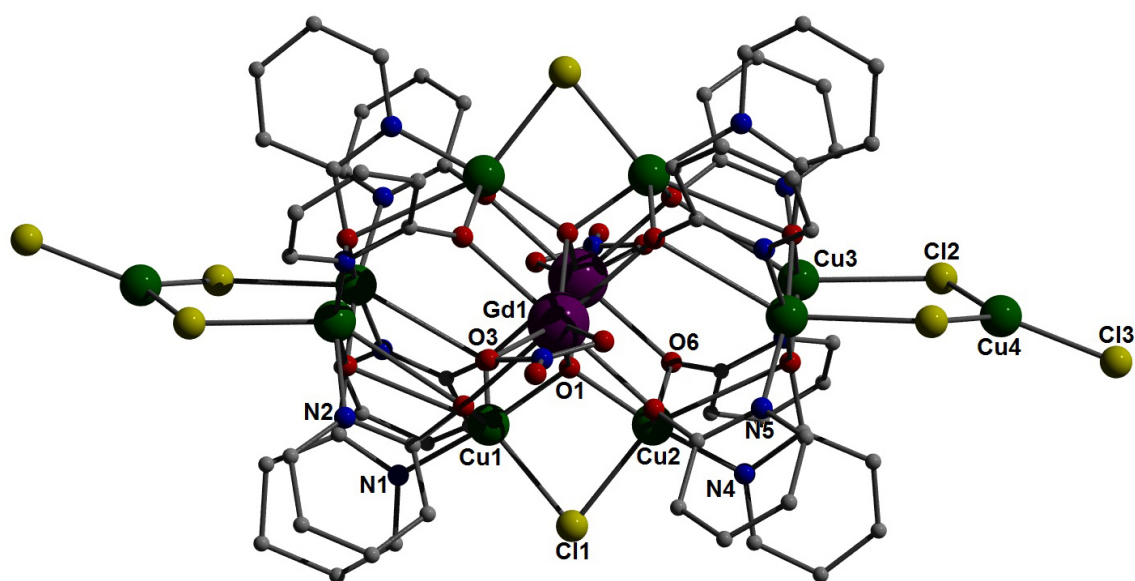


**Figure 89.** Molecular structure of the 1-D polymer of **26** showing one  $\{\text{Gd(III)}_2\text{Cu(II)}_8\}$  node and two crystallographically related  $\{\text{Cu(I)Cl}_3\}^{2-}$  connector units.

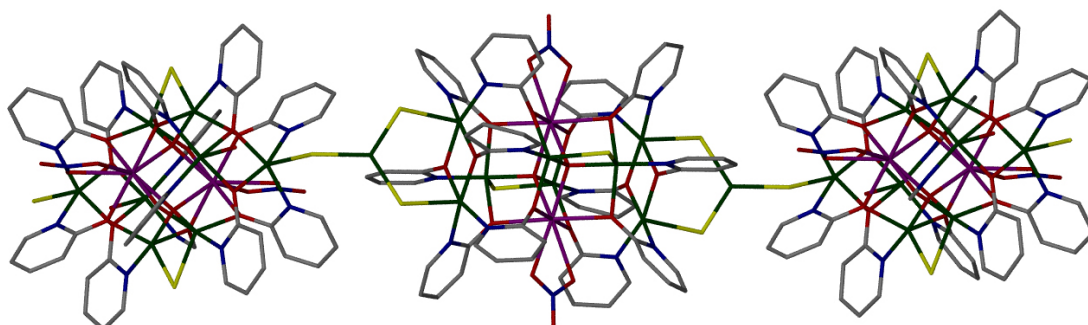


**Figure 90.** The infinite linear structure of **26** showing the  $\{\text{Cu(I)Cl}_3\}^{2-}$  linker moieties.

### 6.2.2.1 Structural descriptions

The polynuclear  $\{\text{Gd(III)}_2\text{Cu(II)}_8\}$  units in **26** comprise a central octahedral core where two equivalent Gd(III) ions (Gd1) lie in the axial positions while the equatorial locales are occupied by Cu(II) centres. Two pairs of Cu(II) centres (Cu3 and s.e) sandwich this central octahedral  $\{\text{Gd(III)}_2\text{Cu(II)}_4\}$  core, their vectors lying perpendicular to its equatorial plane. The result is a  $\{\text{Gd(III)}_2\text{Cu(II)}_8\}$  motif which provides our nodes in **26**. The central octahedral  $\{\text{Gd(III)}_2\text{Cu(II)}_4\}$  core is held together by two symmetry equivalent  $\mu_4\text{-O}^{2-}$  ions (O1 and O12) lying within the cavity while two equivalent  $\mu$ -bridging  $\text{Cl}^-$  ions (Cl1 and Cl4) span two of the  $\text{Cu}\cdots\text{Cu}$  equatorial edges. Each of the Gd(III) ions are eight coordinate and exhibit

distorted dodecahedron geometries. The Cu(II) ions within the  $\{\text{Gd(II)}_2\text{Cu(II)}_8\}$  cluster nodes (Cu1-3 and Cu5-7) are each five coordinate. Cu1, Cu2 and Cu6 each exhibit distorted trigonal bipyramidal geometries ( $\tau$  values range from 0.62 - 0.7) while Cu3, Cu5 and Cu7 are distorted square based pyramidal in nature ( $\tau$  values < 0.05). Eight of the twelve deprotonated 2-hydroxypyridine (2-hp<sup>-</sup>) ligands in **26** bridge the Gd(III) and Cu(II) ions within the  $\{\text{Gd(III)}_2\text{Cu(II)}_8\}$  nodes using a  $\eta^1:\eta^2$ ,  $\mu_3$ -bridging motif. The four remaining ligands use the same bonding mode to bridge the central Cu(II) ions (Cu2 and Cu6) to the peripheral Cu(II) centres (Cu3, Cu5 and Cu7). It should be noted here that the polynuclear  $\{\text{Gd(III)}_2\text{Cu(II)}_8\}$  units in **26** is known in the literature in the guise of a family of discrete  $\{\text{Ln(III)}_2\text{Cu(II)}_8\}$  (Ln = Y, Gd, Tb and Dy) clusters although differing in their specific connectivity [271], [273]. The polynuclear nodes in **26** are connected into 1-D arrays through the aforementioned  $\{\text{Cu(I)Cl}_3\}^{2-}$  ionic linkers. The Cu(I) oxidation state assignment was deduced from charge balancing considerations and is consistent with the use of cuprous chloride as the copper source. The three Cl<sup>-</sup> ions within the  $\{\text{Cu(I)Cl}_3\}^{2-}$  moieties form the long axial bonds of the distorted square based pyramidal Cu(II) ions (Cu3 and Cu5) lying at the edges of the  $\{\text{Gd(III)}_2\text{Cu(II)}_8\}$  nodes (Cu3–Cl2 = 2.780 Å, Cu5–Cl3 = 2.722 Å) (Figure 89). The individual chains in **26** are of wave-like appearance (Figure 91) and propagate along the *ac* intersect of the unit cell. Each  $\{\text{Gd(III)}_2\text{Cu(II)}_8\}$  nodes are oriented at 90° angles to their nearest neighbours resulting in an alternating repeating pattern (Figure 91). In terms of 3-D packing the chains in **26** arrange themselves in the space efficient brickwork pattern (Figure 92).

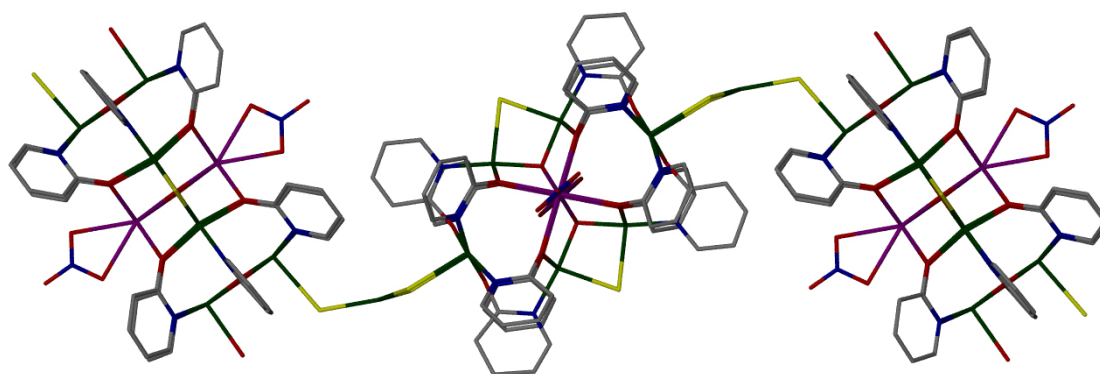


**Figure 91.** Chain structure of **26** highlighting the alternating orientation of the  $\{\text{Gd(III)}_2\text{Cu(II)}_8\}$  nodes as viewed parallel to the plane of the  $\{\text{Cu(I)Cl}_3\}^{2-}$  connector units.

We decided to expand on this interesting discovery and tested the robustness of the synthetic methodology used in the production of **26**. Although slight modifications

were required we are indeed able to systematically produce direct analogues to **26** in the form of the series  $[\text{Ln}(\text{III})_2\text{Cu}(\text{II})_8\text{Cu}(\text{I})_1(\text{O})_2(2\text{-hp})_{12}(\mu\text{-Cl})_2(\text{Cl})_3(\text{NO}_3)_2]_n$  (where  $\text{Ln} = \text{Dy}$  (**28**),  $\text{Ln} = \text{Tb}$  (**30**) and  $\text{Ln} = \text{Y}$  (**32**)). Furthermore by replacing the  $\text{Cu}(\text{I})\text{Cl}$  salt with the  $\text{Br}^-$  analogue we may produce the bromo- analogues to **26**, **28**, **30** and **32** in the form the series  $[\text{Ln}(\text{III})_2\text{Cu}(\text{II})_8\text{Cu}(\text{I})_1(\text{O})_2(2\text{-hp})_{12}(\mu\text{-Br})_2(\text{Br})_3(\text{NO}_3)_2]_n$  (where  $\text{Ln} = \text{Gd}$  (**27**),  $\text{Ln} = \text{Dy}$  (**29**),  $\text{Ln} = \text{Tb}$  (**31**) and  $\text{Ln} = \text{Y}$  (**33**)). Complexes **26**, **29**, **31** and **33** crystallize in the monoclinic  $C_2/m$  space group while complexes **27**, **28**, **30** and **32** instead crystallize in the monoclinic  $C_2$  space group.

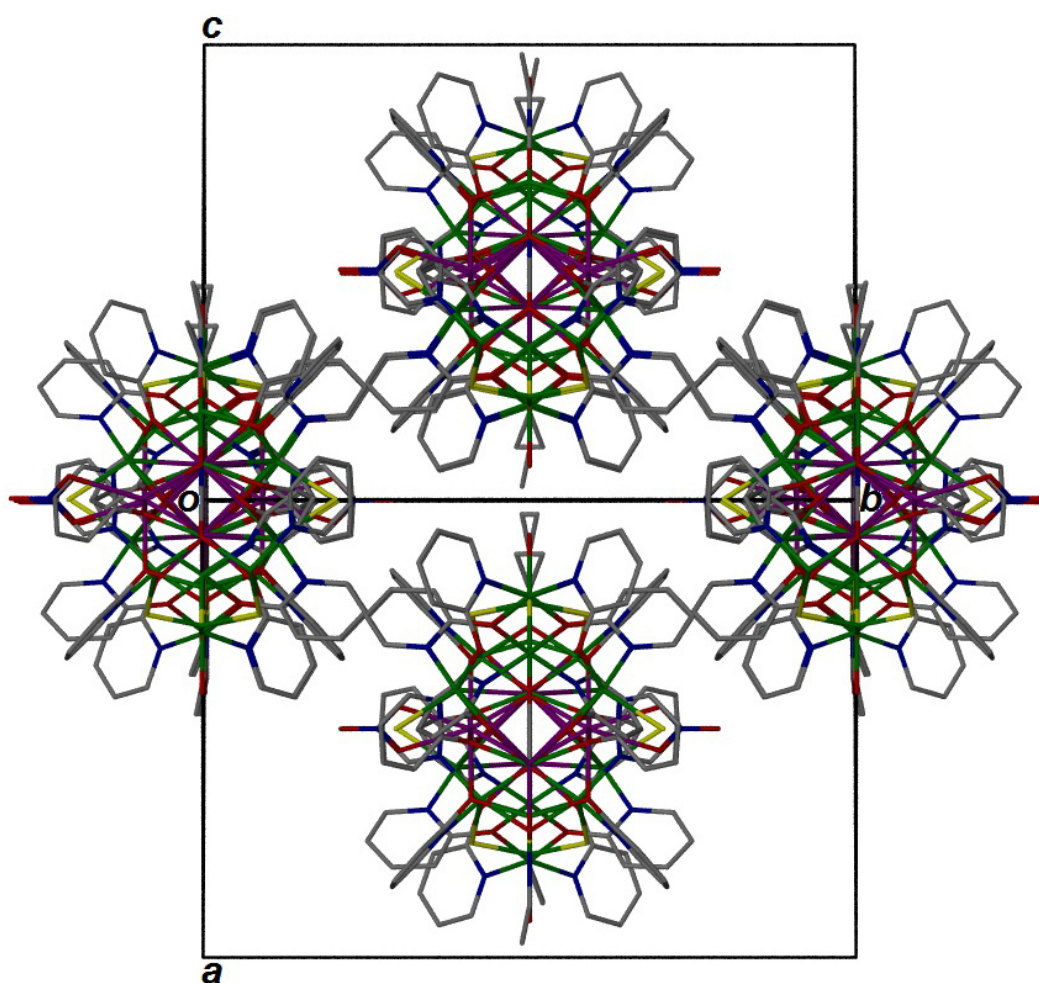


**Figure 92.** Packing diagram of complex **26** as viewed down the 1-D chains.

### 6.3 Conclusion

Although we were unsuccessful in producing complexes comprising both  $\text{Ln}(\text{III})$  and  $\text{Cu}(\text{III})$  ions using the 2,2'-biphenol ligand, our investigations with 2-hydroxyridine (2-hpH) have led to the production of eleven novel  $[\text{Cu}(\text{II})_x\text{Ln}(\text{III})_y]$  cage and

extended lattice formations. In this thesis we have previously utilized 2-hpH as a co-ligand in the formation of  $[\text{Mn(III)}_2(\mu\text{-OEt})_2(\text{L})_2(\text{EtOH})_2(2\text{-hpH})_2]$  (**5**), and  $[\text{Co(II)}_8(\text{OMe})_2(\text{L})_4(\text{LH})_2(2\text{-hpH})_4(\text{MeCN})_4]\cdot\text{MeCN}$  (**20**). Interestingly, crystallization of complexes **23-33** are only possible when a Cu(I) salt is utilized and when all three solvents (MeOH, MeCN and DCM) are present in a 2:1:1 ratio respectively. In addition, the ratio of Cu(I) to Ln(III) salts in the reaction determines whether a  $[\text{Cu(II)}_4\text{Ln(III)}_4]$  cage complex or a  $\{\text{Ln(III)}_2\text{Cu(II)}_8\text{Cu(I)}_1\}$  infinite lattice will be crystallized. Magnetic susceptibility measurements performed on complex **23** indicate antiferromagnetic coupling between the Cu(II) ions. Unfortunately it is impossible to determine whether the four Gd(III) ions are engaging in ferromagnetic coupling or are simply responding to the external magnetic field in a paramagnetic manner. The production of a  $[\text{Zn(II)}_4\text{Gd(III)}_4]$  analogue to complexes **23-25** would help us to extract a value for  $J_{\text{Gd-Gd}}$ . The findings detailed in this chapter significantly build on the work of Winpenny [264], Wang [271], [272] and Wernsdorfer [273].

## 6.4 Experimental Section

### 6.4.1 Physical measurements

Infra-red spectra were recorded on a Perkin Elmer FT-IR *Spectrum One* spectrometer equipped with a Universal ATR Sampling accessory (NUI Galway). UV-visible studies were carried out on a Cary *100 Scan* (Varian) spectrophotometer. Elemental analysis was carried by Marion Vignoles and Gerard Fahy at the School of Chemistry microanalysis service NUI Galway. Variable-temperature, solid-state direct current (dc) magnetic susceptibility data down to 1.8 K were collected on a Quantum Design MPMS-XL SQUID magnetometer equipped with a 7 T dc magnet (University of Edinburgh). Diamagnetic corrections were applied to the observed paramagnetic susceptibilities using Pascal's constants.

### 6.4.2 X-ray crystallography

The structures of **23-33** were collected on an Xcalibur S single crystal diffractometer (Oxford Diffraction) using an enhanced Mo source. Each data reduction was carried out on the CrysAlisPro software package.

### 6.4.3 Syntheses

All reactions were performed under aerobic conditions and all reagents and solvents were used as purchased. The synthesis of **25** was carried out in a CEM Discovery microwave reactor.

#### **Preparation of [Gd(III)<sub>4</sub>Cu(II)<sub>4</sub>(OH)<sub>4</sub>(OMe)<sub>2</sub>(2-hp)<sub>8</sub>(2-hpH)<sub>4</sub>(Br)<sub>2</sub>(NO<sub>3</sub>)<sub>4</sub>].2H<sub>2</sub>O .2MeOH (**23**)**

Anhydrous Cu(I)Br (0.12 g, 0.84 mmol) and Gd(III)(NO<sub>3</sub>)<sub>3</sub>.6H<sub>2</sub>O (0.57 g, 1.26 mmol) were added to 30 cm<sup>3</sup> of a 2:1:1 solvent mixture containing MeOH, MeCN and CH<sub>2</sub>Cl<sub>2</sub>. The ligand 2-hydroxypyridine (2-hpH) (0.24 g, 2.52 mmol) was added, followed by NaOH (0.05 g, 1.25 mmol) and the resultant blue solution was left to stir for 2 hours. After this time the solution was filtered and left to stand. Blue X-ray quality crystals of **23** were obtained after 2 days upon slow evaporation of the mother liquor. Yield: 52 mg, 9.3%. FT-IR (cm<sup>-1</sup>): 3125.1 (w), 2809.1 (w), 1651.0 (m), 1552.6 (w), 1473.4 (s), 1435.3 (s), 1360.1 (m), 1322.9 (m), 1219.6 (w), 1149.7 (m), 1111.0 (w), 1060.9 (w), 1024.6 (m), 997.5 (w), 861.4 (m), 781.6 (vs), 741.8 (m), 719.0 (m). Elemental analysis calculated (found) (%) for C<sub>64</sub>H<sub>74</sub>N<sub>16</sub>O<sub>34</sub>Br<sub>2</sub>Gd<sub>4</sub>Cu<sub>4</sub> (**23**): C: 29.00 (28.64), H: 2.66 (2.48), N: 8.46 (8.94).

#### **Preparation of [Dy(III)<sub>4</sub>(Cu(II)<sub>4</sub>(OH)<sub>4</sub>(OMe)<sub>2</sub>(2-hp)<sub>8</sub>(2-hpH)<sub>4</sub>(Br)<sub>2</sub>(NO<sub>3</sub>)<sub>4</sub>].4MeOH (**24**)**

Anhydrous Cu(I)Br (0.12 g, 0.84 mmol) and Dy(III)(NO<sub>3</sub>)<sub>3</sub>.6H<sub>2</sub>O (0.57 g, 1.26 mmol) were added to 30 cm<sup>3</sup> of a 2:1:1 solvent mixture containing MeOH, MeCN and CH<sub>2</sub>Cl<sub>2</sub>. The ligand 2-hydroxypyridine (2-hpH) (0.24 g, 2.52 mmol) was added, followed by NaOH (0.07 g, 1.75 mmol), and the resultant blue solution was left to stir for 30 minutes. After this time the solution was filtered and left to stand. The resultant blue solution was then filtered from which blue X-ray quality crystals of **24** formed after 2 days upon slow evaporation of the mother liquor. Yield 3 mg, ~0.5 %. FT-IR (cm<sup>-1</sup>): 3260.3 (w), 1645.8 (m), 1603.9 (s), 1544.9 (m) 1473.0 (vs), 1437.4 (s), 1319.7 (s), 1279.7 (s), 1217.8 (m), 1151.6 (m), 1112.2 (w), 1041.0 (w), 1025.5 (m), 997.0 (w), 961.9 (w), 860.5 (m), 778.0 (s), 742.2 (m). Elemental analysis calculated (found) (%) for C<sub>66</sub>H<sub>78</sub>N<sub>16</sub>O<sub>34</sub>Br<sub>2</sub>Dy<sub>4</sub>Cu<sub>4</sub> (**24**): C: 29.32 (29.45), H 2.91 (3.21), N 8.29 (8.63).

**Preparation of [Tb(III)<sub>4</sub>(Cu(II)<sub>4</sub>(OH)<sub>4</sub>(OMe)<sub>2</sub>(2-hp)<sub>8</sub>(2-hpH)<sub>4</sub>(Br)<sub>2</sub>(NO<sub>3</sub>)<sub>4</sub>].4MeOH (25)**

Anhydrous Cu(I)Br (0.12 g, 0.84 mmol) and Tb(III)(NO<sub>3</sub>)<sub>3</sub>.5H<sub>2</sub>O (0.55 g, 1.26 mmol) were added to 20 cm<sup>3</sup> of a 2:1:1 solvent mixture containing MeOH, MeCN and CH<sub>2</sub>Cl<sub>2</sub>. The ligand 2-hydroxypyridine (2-hpH) (0.24 g, 2.52 mmol) was added, followed by NaOH (0.05 g, 1.25 mmol), and the resultant blue solution was stirred for 5 minutes. After this time the solution was then microwaved for five minutes at 150 °C, 200W and 300psi. The solution was then cooled to 30 °C, filtered and allowed to stand. Blue X-ray quality crystals of **25** formed after 2 days upon slow evaporation of the mother liquor. Yield: 39 mg, 6.9%. FT-IR (cm<sup>-1</sup>): 3134.1 (w), 2814.7 (w), 1645.4 (s), 1603.6 (vs), 1552.5 (m), 1472.5 (vs), 1436.6 (vs), 1353.9 (m), 1319.8 (vs), 1279.0 (s), 1217.4 (m), 1151.0 (m), 1111.9 (w), 1095.7 (w), 1055.5 (w), 1041.0 (w), 1025.0 (m), 996.9 (m), 962.2 (w), 859.9 (s), 777.5 (vs), 741.2 (m), 729.6 (m). Elemental analysis calculated (found) (%) for C<sub>66</sub>H<sub>78</sub>N<sub>16</sub>O<sub>34</sub>Br<sub>2</sub>Tb<sub>4</sub>Cu<sub>4</sub> (**25**): C: 29.48 (29.42), H: 2.92 (2.58), N 8.33 (8.03).

**Preparation of [Gd(III)<sub>2</sub>Cu(II)<sub>8</sub>Cu(I)<sub>1</sub>(O)<sub>2</sub>(2-hp)<sub>12</sub>(μ-Cl)<sub>2</sub>(Cl)<sub>3</sub>(NO<sub>3</sub>)<sub>2</sub>]<sub>n</sub> (26)**

Anhydrous Cu(I)Cl (0.22 g, 2.22 mmol) and Gd(III)(NO<sub>3</sub>)<sub>3</sub>.6H<sub>2</sub>O (0.25 g, 0.55 mmol) were added to 30 cm<sup>3</sup> of a 2:1:1 solvent mixture containing MeOH, MeCN and CH<sub>2</sub>Cl<sub>2</sub>. An excess of 2-hydroxypyridine (2-hpH) (0.42 g, 4.42 mmol) was added, followed by NEt<sub>4</sub>(OH).5H<sub>2</sub>O (0.3 g, 1.65 mmol) and the resultant green solution was left to stir for 1.5 hrs. After this time the solution was filtered and left to stand. Green X-ray quality crystals of **26** were obtained after 2 days upon slow evaporation of the mother liquor. Yield (dried): 73 mg, 12.6 %. FT-IR (cm<sup>-1</sup>): 3339.4 (w), 1647.2 (w), 1605.7 (s), 1556.2 (m), 1467.3 (vs), 1435.5 (vs) 1328.7 (m), 1297.8 (s), 1254.4 (m), 1151.3 (m), 1111.4 (w), 1025.0 (m), 950.1 (w), 862.6 (m), 788.2 (s), 743.9 (m). Elemental analysis calculated (found) (%) for C<sub>60</sub>H<sub>48</sub>N<sub>14</sub>O<sub>20</sub>Cl<sub>5</sub>Gd<sub>2</sub>Cu<sub>9</sub> (**26**) (dried on a vacuum line): C: 30.68 (31.12), H: 2.06 (1.83), N: 8.35 (8.59).

**Preparation of [Gd(III)<sub>2</sub>Cu(II)<sub>8</sub>Cu(I)<sub>1</sub>(O)<sub>2</sub>(2-hp)<sub>12</sub>(μ-Br)<sub>2</sub>(Br)<sub>3</sub>(NO<sub>3</sub>)<sub>2</sub>]<sub>n</sub> (27)**

Anhydrous Cu(I)Br (0.32 g, 2.23 mmol) and Gd(III)(NO<sub>3</sub>)<sub>3</sub>.6H<sub>2</sub>O (0.5 g, 1.11 mmol) were added to 30 cm<sup>3</sup> of a 2:1:1 solvent mixture containing MeOH, MeCN and CH<sub>2</sub>Cl<sub>2</sub>. 2-hydroxypyridine (LH) (0.32 g, 3.36 mmol) was then added along with

NaOH (0.045 g, 1.12 mmol) and the resultant green solution was left to stir for 2 hrs. After this time the solution was filtered and left to stand. Dark green X-ray quality crystals of **27** were formed after 2 days upon slow evaporation of the mother liquor. Yield (dried): 70 mg, 11.02 %. FT-IR ( $\text{cm}^{-1}$ ): 3350.7 (w), 1645.7 (w), 1605.4 (s), 1556.3 (m), 1466.9 (vs), 1434.5 (vs), 1328.9 (m), 1295.8 (s), 1252.9 (m), 1151.2 (m), 1111.1 (m), 1043.7 (w), 1024.6 (m), 861.3 (m), 786.4 (s), 743.3 (m). Elemental analysis calculated (found) (%) for  $\text{C}_{60}\text{H}_{48}\text{N}_{14}\text{O}_{20}\text{Br}_5\text{Gd}_2\text{Cu}_9$  (**27**) (dried on a vacuum line): C: 28.03 (27.59), H: 1.88 (2.04), N: 7.63 (7.60).

#### **Preparation of of $[\text{Dy(III)}_2\text{Cu(II)}_8\text{Cu(I)}_1(\text{O})_2(2\text{-hp})_{12}(\mu\text{-Cl})_2(\text{Cl})_3(\text{NO}_3)_2]_n$ (**28**)**

Anhydrous Cu(I)Cl (0.22 g, 2.22 mmol) and Dy(III)(NO<sub>3</sub>)<sub>3</sub>.6H<sub>2</sub>O (0.5 g, 1.1 mmol) were added to 30 cm<sup>3</sup> of a 2:1:1 solvent mixture containing MeOH, MeCN and CH<sub>2</sub>Cl<sub>2</sub>. 2-hydroxypyridine (2-hpH) (0.21 g, 2.22 mmol) was then added and was followed by NaOH (0.045 g, 1.12 mmol). The resultant green solution was left to stir for 2 hours before it was filtered and left to stand. Green X-ray quality crystals of **28** were obtained after 2 days upon slow evaporation of the mother liquor. Yield (dried): 64 mg, 10.99 %. FT-IR ( $\text{cm}^{-1}$ ): 3339.0 (w), 1643.6 (w), 1606.0 (s), 1556.5 (m), 1467.1 (vs), 1435.5 (vs), 1330.8 (m), 1297.4 (s), 1253.7 (m), 1216.6 (w), 1151.7 (m), 1111.3 (w), 1025.3 (m), 871.8 (m), 789.1 (m), 744.7 (m). Elemental analysis calculated (found) (%) for  $\text{C}_{60}\text{H}_{48}\text{N}_{14}\text{O}_{20}\text{Cl}_5\text{Dy}_2\text{Cu}_9$  (**28**) (dried on a vacuum line): C: 30.54 (30.66), H: 1.88 (1.98), N 8.31 (7.88).

#### **Preparation of $[\text{Dy(III)}_2\text{Cu(II)}_8\text{Cu(I)}_1(\text{O})_2(2\text{-hp})_{12}(\mu\text{-Br})_2(\text{Br})_3(\text{NO}_3)_2]_n$ (**29**)**

Anhydrous Cu(I)Br (0.32 g, 2.23 mmol) and Dy(III)(NO<sub>3</sub>)<sub>3</sub>.6H<sub>2</sub>O (0.51 g, 1.12 mmol) were added to 30 cm<sup>3</sup> of a 2:1:1 solvent mixture containing MeOH, MeCN and CH<sub>2</sub>Cl<sub>2</sub>. 2-hydroxypyridine (2-hpH) (0.43 g, 4.5 mmol) was then added along with NEt<sub>4</sub>(OH).5H<sub>2</sub>O (0.2 g, 1.1 mmol) and the resultant green solution was left to stir for 2 hrs. After this time the solution was filtered and left to stand. Dark green X-ray quality crystals of **29** were obtained after 2 days upon slow evaporation of the mother liquor. Yield: 82 mg, 12.86 %. FT-IR ( $\text{cm}^{-1}$ ): 3365.4 (w), 1646.0 (w), 1605.6 (s), 1556.3 (m), 1466.9 (vs), 1434.6 (vs), 1328.6 (m), 1296.5 (s), 1253.0 (m), 1151.2 (m), 1111.2 (m), 1043.2 (w), 1024.9 (m), 949.8 (w), 861.9 (m), 788.8 (s), 744.1 (m).

Elemental analysis calculated (found) (%) for  $C_{60}H_{48}N_{14}O_{20}Br_5Dy_2Cu_9$  (**29**) (dried on a vacuum line): C: 27.91 (28.26), H: 1.87 (1.82), N: 7.60 (7.50).

**Preparation of  $[Tb(III)_2Cu(II)_8Cu(I)_1(O)_2(2-hp)_{12}(\mu-Cl)_2(Cl)_3(NO_3)_2]_n$  (**30**)**

Anhydrous Cu(I)Cl (0.22 g, 2.22 mmol) and Tb(III)(NO<sub>3</sub>)<sub>3</sub>·5H<sub>2</sub>O (0.48 g, 1.1 mmol) were added to 30 cm<sup>3</sup> of a 2:1:1 solvent mixture containing MeOH, MeCN and CH<sub>2</sub>Cl<sub>2</sub>. An excess of 2-hydroxypyridine (2-hpH) (0.42 g, 4.42 mmol) was added, followed by NaOH (0.09 g, 2.25 mmol) and the resultant green solution was left to stir for 2 hrs. After this time the solution was filtered and left to stand. Green X-ray quality crystals of **30** were obtained after 2 days upon slow evaporation of the mother liquor. Yield: 32 mg, 5.5 %. FT-IR (cm<sup>-1</sup>): 3337.7 (w), 1643.1 (w), 1605.7 (s), 1556.0 (m), 1466.8 (vs), 1435.4 (vs), 1330.8 (m), 1296.8 (s), 1253.3 (m), 1217.4 (w), 1151.8 (m), 1111.1 (w), 1025.1 (m), 871.2 (m), 789.3 (s), 744.5 (m). Elemental analysis calculated (found) (%) for  $C_{60}H_{48}N_{14}O_{20}Cl_5Tb_2Cu_9$  (**30**) (dried on a vacuum line): C: 30.64 (31.07), H: 2.06 (2.11), N: 8.34 (8.59).

**Preparation of  $[Tb(III)_2Cu(II)_8Cu(I)_1(O)_2(2-hp)_{12}(\mu-Br)_2(Br)_3(NO_3)_2]_n$  (**31**)**

Anhydrous Cu(I)Br (0.32 g, 2.23 mmol) and Tb(III)(NO<sub>3</sub>)<sub>3</sub>·5H<sub>2</sub>O (0.48 g, 1.1 mmol) were added to 30 cm<sup>3</sup> of a 2:1:1 solvent mixture containing MeOH, MeCN and CH<sub>2</sub>Cl<sub>2</sub>. 2-hydroxypyridine (2-hpH) (0.315 g, 3.31 mmol) was added and was rapidly followed by NaOH (0.045 g, 1.12 mmol). The resultant green solution was left to stir for 3 hours before being filtered and left to stand. A blue precipitate was subsequently formed after 24 hours. This was discarded and the solution was once again allowed to stand. Dark green X-ray quality crystals of **31** were obtained 2 days later upon slow evaporation of the mother liquor. Yield: 45 mg, 7.08 %. FT-IR (cm<sup>-1</sup>): 3363.1 (w), 1645.4 (w), 1605.5 (s), 1556.2 (m), 1467.1 (vs), 1434.8 (vs), 1328.5 (m), 1296.4 (s), 1252.6 (m), 1150.8 (m), 1111.0 (m), 1043.4 (w), 1024.4 (m), 861.5 (m), 786.8 (s), 743.3 (m). Elemental analysis calculated (found) (%) for  $C_{60}H_{48}N_{14}O_{20}Br_5Tb_2Cu_9$  (**31**) (dried on a vacuum line): C: 27.99 (27.65), H: 1.88 (2.07), N: 7.62 (7.77).

**Preparation of  $[Y(III)_2Cu(II)_8Cu(I)_1(O)_2(2-hp)_{12}(\mu-Cl)_2(Cl)_3(NO_3)_2]_n$  (**32**)**

Anhydrous Cu(I)Cl (0.22 g, 2.22 mmol) and Y(III)(NO<sub>3</sub>)<sub>3</sub>·6H<sub>2</sub>O (0.425 g, 1.11 mmol) were added to 30 cm<sup>3</sup> of a 2:1:1 solvent mixture containing MeOH, MeCN and

CH<sub>2</sub>Cl<sub>2</sub>. 2-hydroxypyridine (2-hpH) (0.32 g, 3.36 mmol) was then added and was rapidly followed by NaOH (0.09 g, 2.25 mmol). The resultant green solution was left to stir for 1.5 hours and subsequently filtered and left to stand. Green X-ray quality crystals of **32** were obtained after 2 days upon slow evaporation of the mother liquor. Yield: 57 mg, 10.44 %. FT-IR (cm<sup>-1</sup>): 3336.4 (w), 1644.2 (m), 1606.0 (s), 1556.3 (m), 1466.6 (vs), 1435.3 (vs), 1332.0 (m), 1297.2 (s), 1253.4 (m), 1215.7 (m), 1151.5 (m), 1111.0 (m), 1043.3 (w), 1025.1 (m), 871.7 (m), 788.4 (s), 744.4 (m). Elemental analysis calculated (found) (%) for C<sub>60</sub>H<sub>48</sub>N<sub>14</sub>O<sub>20</sub>Cl<sub>5</sub>Y<sub>2</sub>Cu<sub>9</sub> (**32**) (dried on a vacuum line): C: 32.58 (32.46), H: 2.19 (2.36), N: 8.86 (9.20).

#### **Preparation of [Y(III)<sub>2</sub>Cu(II)<sub>8</sub>Cu(I)<sub>1</sub>(O)<sub>2</sub>(2-hp)<sub>12</sub>(μ-Br)<sub>2</sub>(Br)<sub>3</sub>(NO<sub>3</sub>)<sub>2</sub>]<sub>n</sub> (**33**)**

Anhydrous Cu(I)Br (0.32 g, 2.23 mmol) and Y(III)(NO<sub>3</sub>)<sub>3</sub>·6H<sub>2</sub>O (0.43 g, 1.12 mmol) were added to 30 cm<sup>3</sup> of a 2:1:1 solvent mixture containing MeOH, MeCN and CH<sub>2</sub>Cl<sub>2</sub>. 2-hydroxypyridine (2-hpH) (0.43 g, 4.5 mmol) was then added along with NaOH (0.045 g, 1.12 mmol) and the resultant green solution was left to stir for 2.5 hours. Dark green X-ray quality crystals of **33** were obtained upon filtration and slow evaporation of the mother liquor after 2 days. Yield: 68 mg, 11.31 %. FT-IR (cm<sup>-1</sup>): 3346.9, 1644.2 (m), 1605.6 (s), 1556.5 (m), 1467.1 (vs), 1434.8 (vs), 1330.3 (m), 1296.9 (s), 1252.6 (m), 1216.1 (m), 1151.4 (m), 1110.8 (m), 1043.1 (w), 1024.9 (m), 871.7 (m), 788.1 (s), 744.3 (m). Elemental analysis calculated (found) (%) for C<sub>60</sub>H<sub>48</sub>N<sub>14</sub>O<sub>20</sub>Br<sub>5</sub>Y<sub>2</sub>Cu<sub>9</sub> (**33**) (dried on a vacuum line): C: 29.60 (29.42), H: 1.99 (2.29), N: 8.05 (7.87).

## 6.5 Bibliography

- [240] P.-H. Lin, T. J. Burchell, L. Ungur, L. F. Chibotaru, W. Wernsdorfer, and M. Murugesu, "A polynuclear lanthanide single-molecule magnet with a record anisotropic barrier.," *Angewandte Chemie (International ed. in English)*, vol. 48, no. 50, pp. 9489–9492, Jan. 2009.
- [241] S. Liu, L. Gelmini, S. J. Rettig, R. C. Thompson, and C. Orvig, "Synthesis and characterization of lanthanide  $[\text{Ln}(\text{L})_2]$  complexes of  $\text{N}_4\text{O}_3$  amine phenol ligands with phenolate oxygen bridges: evidence for very weak magnetic exchange between lanthanide ions," *Journal of the American Chemical Society*, vol. 114, no. 15, pp. 6081–6087, Jul. 1992.
- [242] A. Cleve, P. T., Hoeglund, "No Title," *Bull. Soc. Chim.*, vol. 18, p. 193, 1873.
- [243] C. Bonardi, J. P. James, "The separation of yttrium from the yttrium earths. Part 1.," *J. Am. Chem. Soc.*, vol. 37, pp. 2642–2645, 1915.
- [244] P. S. James, C. Willand, "The rare earth Cobalticyanide," *J. Am. Chem. Soc.*, vol. 38, p. 1497, 1916.
- [245] A. Bencini, C. Benelli, A. Caneschi, R. L. Carlin, A. Dei, and D. Gatteschi, "Crystal and molecular structure of and magnetic coupling in two complexes containing gadolinium(III) and copper(II) ions," *Journal of the American Chemical Society*, vol. 107, no. 26, pp. 8128–8136, Dec. 1985.
- [246] C. Benelli, A. Caneschi, D. Gatteschi, O. Guillou, and L. Pardi, "Synthesis, crystal structure, and magnetic properties of tetranuclear complexes containing exchange-coupled dilanthanide-dicopper(lanthanide = gadolinium, dysprosium) species," *Inorganic Chemistry*, vol. 29, no. 9, pp. 1750–1755, May 1990.
- [247] M. Andruh, I. Ramade, E. Codjovi, O. Guillou, O. Kahn, and J. C. Trombe, "Crystal structure and magnetic properties of  $[\text{Ln}_2\text{Cu}_4]$  hexanuclear clusters (where Ln = trivalent lanthanide). Mechanism of the gadolinium(III)-copper(II) magnetic interaction," *Journal of the American Chemical Society*, vol. 115, no. 5, pp. 1822–1829, 1993.
- [248] G. Rajaraman, F. Totti, A. Bencini, A. Caneschi, R. Sessoli, and D. Gatteschi, "Density functional studies on the exchange interaction of a dinuclear Gd(III)-Cu(II) complex: method assessment, magnetic coupling mechanism and magneto-structural correlations.," *Dalton transactions (Cambridge, England : 2003)*, no. 17, pp. 3153–3161, May 2009.
- [249] H.-Z. Kou, Y.-B. Jiang, and A.-L. Cui, "Two-Dimensional Coordination Polymers Exhibiting Antiferromagnetic Gd(III)–Cu(II) Coupling," *Crystal Growth & Design*, vol. 5, no. 1, pp. 77–79, Jan. 2005.
- [250] J.-P. Costes and L. Vendier, "CuLn complexes with a single  $\mu$ -oximate bridge," *Comptes Rendus Chimie*, vol. 13, no. 6–7, pp. 661–667, Jun. 2010.
- [251] J. L. Sanz, R. Ruiz, A. Gleizes, F. Lloret, J. Faus, M. Julve, J. J. Borrás-Almenar, and Y. Journaux, "Crystal Structures and Magnetic Properties of Novel  $[\text{Ln}(\text{III})\text{Cu}(\text{II})_4]$  (Ln = Gd, Dy, Ho) Pentanuclear Complexes. Topology and Ferromagnetic Interaction in the Ln(III)-Cu(II) Pair.," *Inorganic chemistry*, vol. 35, no. 25, pp. 7384–7393, Dec. 1996.
- [252] I. Ramade, O. Kahn, Y. Jeannin, and F. Robert, "Design and Magnetic Properties of a Magnetically Isolated  $\text{Gd}^{\text{III}}\text{Cu}^{\text{II}}$  Pair. Crystal Structures of  $[\text{Gd}(\text{hfa})_3\text{Cu}(\text{salen})]$ ,  $[\text{Y}(\text{hfa})_3\text{Cu}(\text{salen})]$ ,  $[\text{Gd}(\text{hfa})_3\text{Cu}(\text{salen})(\text{Meim})]$ , and

- [La(hfa)<sub>3</sub>(H<sub>2</sub>O)Cu(salen)] [hfa = Hexafluoroacetylacetonato, salen = N, N',]" *Inorganic Chemistry*, vol. 36, no. 5, pp. 930–936, Feb. 1997.
- [253] C. Benelli and D. Gatteschi, "Magnetism of lanthanides in molecular materials with transition-metal ions and organic radicals.," *Chemical Reviews*, vol. 102, no. 6, pp. 2369–2388, 2002.
- [254] I. Rudra and C. Raghun, "Exchange interaction in binuclear complexes with rare-earth and copper ions: A many-body model study," *Physical Review B*, 2002.
- [255] B. Cristóvão, J. Kłak, B. Mirosław, and L. Mazur, "Synthesis, crystal structures and magnetic characterization of heterodinuclear Cu<sup>II</sup>Gd<sup>III</sup> and Cu<sup>II</sup>Tb<sup>III</sup> Schiff base complexes," *Inorganica Chimica Acta*, vol. 378, no. 1, pp. 288–296, Nov. 2011.
- [256] O. Kahn, Olivier Guillou, *Research Frontiers in Magnetochemistry*. 1993, pp. 194 – 197.
- [257] J.-P. Costes, F. Dahan, A. Dupuis, and J.-P. Laurent, "Nature of the Magnetic Interaction in the (Cu<sup>2+</sup>, Ln<sup>3+</sup>) Pairs: An Empirical Approach Based on the Comparison Between Homologous (Cu<sup>2+</sup>, Ln<sup>3+</sup>) and (NiLS<sup>2+</sup>, Ln<sup>3+</sup>) Complexes," *Chemistry - A European Journal*, vol. 4, no. 9, pp. 1616–1620, Sep. 1998.
- [258] M. L. Kahn, C. Mathonière, and O. Kahn, "Nature of the Interaction between Ln(III) and Cu(II) Ions in the Ladder-Type Compounds Ln<sub>2</sub>[Cu(opba)]<sub>3</sub>.S (Ln = Lanthanide Element; opba = ortho-Phenylenebis(oxamato), S = Solvent Molecules).," *Inorganic Chemistry*, vol. 38, no. 16, pp. 3692–3697, 1999.
- [259] S. Osa, T. Kido, N. Matsumoto, N. Re, A. Pochaba, and J. Mrozinski, "A tetranuclear 3d-4f single molecule magnet: [Cu<sup>II</sup>LTb<sup>III</sup>(hfac)<sub>2</sub>]<sub>2</sub>," *Journal of the American Chemical Society*, vol. 126, no. 2, pp. 420–421, Jan. 2004.
- [260] V. Baskar, K. Gopal, M. Helliwell, F. Tuna, W. Wernsdorfer, and R. E. P. Winpenny, "3d-4f clusters with large spin ground states and SMM behaviour.," *Dalton transactions (Cambridge, England : 2003)*, vol. 39, no. 20, pp. 4747–4750, May 2010.
- [261] H. L. C. Feltham, R. Clérac, A. K. Powell, and S. Brooker, "A tetranuclear, macrocyclic 3d-4f complex showing single-molecule magnet behavior.," *Inorganic chemistry*, vol. 50, no. 10, pp. 4232–4234, May 2011.
- [262] S. K. Langle, L. Ungur, N. F. Chilton, B. Moubaraki, L. F. Chibotaru, and K. S. Murray, "Structure, magnetism and theory of a family of nonanuclear Cu(II)<sub>5</sub>Ln(III)<sub>4</sub>-triethanolamine clusters displaying single-molecule magnet behaviour.," *Chemistry (Weinheim an der Bergstrasse, Germany)*, vol. 17, no. 33, pp. 9209–9218, Aug. 2011.
- [263] D. M. L. Goodgame, D. J. Williams, and R. E. P. Winpenny, "Bimetallic hexanuclear compounds containing unusual copper-lanthanide arrays: the crystal structures of Cu<sub>4</sub>Ln<sub>2</sub>L<sub>8</sub>(LH)<sub>4</sub>(OH)<sub>2</sub>(NO<sub>3</sub>)<sub>4</sub>(H<sub>2</sub>O)<sub>2</sub> (Ln = Dy or Gd; LH = 2-(1H)-Pyridone, C<sub>5</sub>H<sub>5</sub>NO)," *Polyhedron*, vol. 8, no. 12, pp. 1531–1536, Jan. 1989.
- [264] A. J. Blake, P. E. Y. Milne, R. E. P. Winpenny, and P. Thornton, "Heterometallic Compounds Involving d- and f-Block Elements: Synthesis, Structure, and Magnetic Properties of Two New Ln<sub>x</sub>Cu<sub>4</sub> Complexes," *Angewandte Chemie International Edition in English*, vol. 30, no. 9, pp. 1139–1141, Sep. 1991.

- [265] A. J. Blake, R. O. Gould, P. E. Y. Milne, and R. E. P. Winpenny, "New routes to copper-lanthanoid complexes I: via a metallomacrocycle," *Journal of the Chemical Society, Chemical Communications*, no. 20, p. 1453, 1991.
- [266] A. J. Blake, V. A. Cherepanov, A. A. Dunlop, C. M. Grant, P. E. Y. Milne, J. M. Rawson, and R. E. P. Winpenny, "Synthesis, crystal structures and thermal decomposition studies of a series of copper/lanthanoid complexes of 6-methyl-2-pyridone," *Journal of the Chemical Society, Dalton Transactions*, no. 18, p. 2719, 1994.
- [267] A. J. Blake, R. O. Gould, C. M. Grant, P. E. Y. Milne, S. Parsons, and R. E. P. Winpenny, "Reactions of copper pyridonate complexes with hydrated lanthanoid nitrates," *Journal of the Chemical Society, Dalton Transactions*, no. 4, p. 485, 1997.
- [268] A. J. Blake, R. O. Gould, P. E. Y. Milne, and R. E. P. Winpenny, "New routes to copper-lanthanoid complexes - via a metal dimer," *Journal of the Chemical Society, Chemical Communications*, no. 6, p. 522, 1992.
- [269] A. J. Blake, P. E. Y. Milne, and R. E. P. Winpenny, "Solvent control of structural type: three different structures from the reaction of a dimeric copper complex with lanthanum nitrate in three different solvents," *Journal of the Chemical Society, Dalton Transactions*, no. 24, p. 3727, 1993.
- [270] C. Benelli, A. J. Blake, P. E. Y. Milne, J. M. Rawson, and R. E. P. Winpenny, "Magnetic and Structural Studies of Copper-Lanthanoid Complexes; the Synthesis and Structures of New  $\text{Cu}_3\text{Ln}$  Complexes of 6-chloro-2-Pyridone (Ln = Gd, Dy and Er) and Magnetic Studies on  $\text{Cu}_2\text{Gd}_2$ ,  $\text{Cu}_4\text{Gd}_2$  and  $\text{Cu}_3\text{Gd}$  Complexes," *Chemistry - A European Journal*, vol. 1, no. 9, pp. 614-618, Dec. 1995.
- [271] S. Wang, "Heterometallic yttrium-copper complexes. Synthesis and crystal structure of  $\text{Y}_2\text{Cu}_8(\mu\text{-PyO})_{12}(\mu\text{-Cl})_2(\mu_4\text{-O})_2(\text{NO}_3)_4(\text{H}_2\text{O})_2 \cdot 2\text{H}_2\text{O}$  (PyO<sup>-</sup> = deprotonated 2-hydroxypyridine)," *Inorganic Chemistry*, vol. 30, no. 10, pp. 2252-2253, May 1991.
- [272] S. Wang, Z. Pang, and M. J. Wagner, "Comparative study of crystal structures and thermal magnetic properties of a yttrium-copper  $\text{Y}_2\text{Cu}_8$  and a neodymium-copper  $\text{Nd}_2\text{Cu}_8$  complex," *Inorganic Chemistry*, vol. 31, no. 26, pp. 5381-5388, Dec. 1992.
- [273] A. Borta, E. Jeanneau, Y. Chumakov, D. Luneau, L. Ungur, L. F. Chibotaru, and W. Wernsdorfer, "Synthesis, structure, magnetism and theoretical study of a series of complexes with a decanuclear core  $[\text{Ln}(\text{III})_2\text{Cu}(\text{II})_8]$  (Ln = Y, Gd, Tb, Dy)," *New Journal of Chemistry*, vol. 35, no. 6, p. 1270, 2011.
- [274] H. Place, B. Scott, and R. D. Willett, "A new one-dimensional copper(I) halide lattice:  $\text{Cu}_4\text{Cl}_6$ ," *Inorganica Chimica Acta*, vol. 319, no. 1-2, pp. 43-48, Jul. 2001.
- [275] L. Subramanian and R. Hoffmann, "Bonding in halocuprates," *Inorganic Chemistry*, vol. 31, no. 6, pp. 1021-1029, Mar. 1992.

# **Chapter 7:**

# **Conclusion**

In summary, a small contribution to the fields of molecular magnetism and coordination polymers has been achieved. The thesis comprises a collection of thirty-two novel molecular assemblies which have been used in the magnetic and structural studies of chapters 2–6.

In chapter 2 we have reported the synthesis and magnetic characterization of 5 novel alkoxide bridged Mn(III) dimers or general formula  $[\text{Mn}_2(\mu\text{-OR})_2(\text{L})_2(\text{ROH})_y(\text{X})_z]$  (where R = Me, Et;  $\text{LH}_2 = 2,2'$ -biphenol and X = terminally bonded MeOH or N-donor ligand). We have used these five complexes in a unique magneto-structural correlation study in which we investigate the structural factors influencing the magnetic exchange interaction in all reported Mn(III) dimeric structures possessing two alkoxide-bridges. We have concluded that the most significant factor influencing the sign and magnitude of the exchange interaction ( $J$ ) is the relative orientation of the Mn(III) ions' Jahn-Teller axes, and we have used DFT analysis to probe the nature of these interactions. This study represents a valuable contribution to the field of molecular magnetism, as it will aid in the understanding of the exchange interactions in large clusters comprising  $[\text{Mn}(\mu\text{-OR})_2]$  units. Our findings conclude that a moderately strong ferromagnetic interaction will only be present in alkoxide bridged  $[\text{Mn}(\text{III})_2]$  dinuclear species if the Jahn-Teller axes are perpendicular to one another. Our study therefore suggests that large anisotropy and a strong ferromagnetic interaction are unlikely to coexist in Mn(III) clusters containing only  $[\text{Mn}(\mu\text{-OR})_2]$  building blocks.

Following on the theme of magnetic exchange interactions in dimers, chapter 3 reports three novel complexes, two of which are rare examples of dimeric Mn(III)-Cu(II) moieties, and are the first to possess a Jahn-Teller compressed Mn(III) ion. The antiferromagnetic exchange interaction in  $[\text{MnCu}(\text{L})_2(\text{py})_4](\text{ClO}_4)\cdot\text{EtOH}$  (**6**) has been probed using DFT analysis, and has been compared to the ferromagnetic interaction in a previously reported analogous Mn(III)-Cu(II) dimer, which possesses an elongated Mn(III) ion [151]. The moderately strong antiferromagnetic interaction in **6** was found to be mainly due to the superexchange interaction involving overlap between the half-filled  $d_{x^2-y^2}$  orbital of the Cu(II) ion with the half-filled  $d_{x^2-y^2}$  orbital of the compressed Mn(III) ion. The interaction between the same orbitals is ferromagnetic in the analogous Mn(III)-Cu(II) dimer, due to the absence of electron density in the  $d_{x^2-y^2}$  orbital of its Mn(III) ion. This study rather elegantly shows how the nature of the

Jahn-Teller distortion dramatically influences the sign and magnitude of  $J$ . In addition, high-field, high frequency EPR studies on both powdered and single-crystal samples of **6** have given us values of the zero-field splitting parameters  $D(\text{Mn(III)}) = +4.78 \text{ cm}^{-1}$  and  $E(\text{Mn(III)}) = +0.405 \text{ cm}^{-1}$  for complex **6**.

Continuing on the theme of heterometallic coordination chemistry, in chapter 4 we have reported the first 1-D architectures constructed using the 2,2'-biphenol ligand (complexes **10-15** and **17**). We have shown how the type of N-donor pyridyl co-ligand used determines whether a covalently linked or H-bonded chain will be formed. On close inspection of all members we can first conclude that regardless of whether the pyridyl ligand used is functionalised at the 3- or 4-position, both H-bonded and covalent chains can be produced. In addition, the type of functional group on the pyridyl co-ligand seems to have no effect on the resultant complex formed, as utilizing 3-cyanopyridine leads to the production of a covalent chain (**14**), while using 4-cyanopyridine produces a H-bonded chain (**13**). In the covalent chains, the intrachain  $\text{M}\cdots\text{M}$  distance ranges render the Mn(III) and Fe(III) ions in this series as magnetically isolated or *dilute* due to the presence of the  $\{\text{Na(I)}\}$  spacer units.

Following this introduction to the field of coordination polymers, chapter 5 reports the production of two structurally interesting coordination polymers comprising magnetically dilute Co(II) nodes (**21** and **22**), built using 2,2'-biphenol. In addition to these 1- and 2-D extended structures, we also report three magnetically interesting discrete polynuclear Co(II) clusters (**18-20**). These five structures are the first complexes of Co(II/III) built using the ligand 2,2'-biphenol. The octanuclear complex  $[\text{Co(II)}_8(\text{OMe})_2(\text{L})_4(\text{LH})_2(2\text{-hp})_4(\text{MeCN})_4]\cdot\text{MeCN}$  (**20**) undergoes ferromagnetic ordering at low temperatures and represents the second largest cluster to be produced using 2,2'-biphenol, whose formation is facilitated by the introduction of a co-ligand with metal ion bridging abilities – 2-hydroxypyridine (2-hpH).

In chapter 6, the ligand 2-hydroxypyridine is exploited further, in the production of a large family of discrete clusters (**23-25**) and coordination polymers (**26-33**) comprising both Cu(II) and Ln(III) ions ( $\text{Ln} = \text{Gd, Tb, Dy, Y}$ ). We show how the metal ion ratio in the reactant solution drastically influences the product formed. Magnetic susceptibility measurements performed on  $[\text{Gd(III)}_4\text{Cu(II)}_4(\text{OH})_4(\text{OMe})_2(2\text{-hp})_8(2\text{-hpH})_4(\text{Br})_2(\text{NO}_3)_4]\cdot 2\text{H}_2\text{O}\cdot 2\text{MeOH}$  (complex **22**) indicate antiferromagnetic coupling between the Cu(II) ions, and suggest field induced parallel alignment of the

four Gd(III) ions. These findings significantly build on the work of Winpenny [264], Wang [271], [272] and Wernsdorfer [273].

Overall, we have shown that 2,2'-biphenol is an extremely versatile ligand, capable of adopting a variety of different coordination modes and exhibiting all three accessible levels of deprotonation in the many complexes described in this thesis. Initially, we witnessed the doubly deprotonated form of 2,2'-biphenol ( $L^{2-}$ ) adopting a chelating mode in the  $[Mn(III)_2]$  complexes of chapter 2 (**1–5**), while in the heterometallic Mn(III)-Cu(II) dimers of chapter 3 (**6** and **7**) it adopts the  $\eta^1:\eta^2,\mu$ -bridging mode. The  $[Cu(II)_2]$  dimer (**8**) of the same chapter, exhibits this ligand in the same bridging mode, although this time in its singly deprotonated form ( $LH^-$ ). Chapter 4 reveals this ligand in a huge variety of coordination modes, from  $L^{2-}$  adopting the  $\eta^2:\eta^2,\mu_3$ -triply bridging mode in the covalent chains of **10**, **14**, **15** and **17**, to singly deprotonated and unidentate in the monomeric complex **16**, to chelating both Mn(III) and Na(I) ions in both its  $L^{2-}$  and  $LH_2$  forms respectively in the ionic chains of **11–13**. The versatility of 2,2'-biphenol is further highlighted in the Co(II) complexes of chapter 5, in which several modes are again observed. These include the  $\eta^1:\eta^2,\mu$ -bridging motif observed in the dimeric complexes **18** and **19**, the  $\eta^2:\eta^2,\mu_3$ -bridging mode witnessed in the octometallic cluster (**20**), and unidentate (and singly deprotonated) in complexes **20–22**. In addition, neutral 'book-end'  $LH_2$  units also exist in the crystal structures of complexes **19** and **21**, where no metal binding is exhibited at all.

Although only a small number of coordination compounds comprising 2,2'-biphenol have been reported prior to our research, we have proven this ligand to be extremely useful and versatile in the construction of discrete and extended molecular aggregates. The large family of magnetically and structurally interesting complexes described in this thesis has increased the number of reported coordination compounds containing 2,2'-biphenol by a factor of 5.

## Appendix A: Chapter 2

**Table A1.** DFT computed energies of high spin (HS) and broken symmetry (BS) state,  $\langle S^2 \rangle$  values for complexes 1-IV (b).

	HS	BS	$\langle S^2 \rangle$	
<b>Complex 1</b>	-4220.56586	-4220.566817	20.1087	12.5431
<b>Complex 4</b>	-4411.734994	-4411.736128	20.0014	12.4842
<b>Complex 5</b>	-4793.743906	-4793.744969	20.0014	12.4746
<b>Complex II - 1</b>	-4829.965823	-4829.965756	20.0011	12.4305
<b>Complex II - 2</b>	-1458.104561	-1458.104618	20.0034	12.7151
<b>Complex III - 1</b>	-4446.440333	-4446.439469	20.0015	12.5086
<b>Complex III - 2</b>	-8304.395881	-8304.394984	20.0009	12.3593
<b>Complex IV - 1</b>	-4220.558864	-4220.559623	20.0017	12.5696
<b>Complex IV - 2</b>	-8304.293759	-8304.291795	20.0011	12.3533

**Table A2.** Overlap integral values are given for Complex 1, II-2, III-2

Complex 1			Complex II-2			Complex III-2		
Alpha	Beta	overlap integrals	Alpha	Beta	overlap integral	Alpha	Beta	overlap intergral
163( $d_z^2$ )	163( $d_z^2$ )	-0.07159	249( $d_z^2$ )	249( $d_z^2$ )	-0.0735	302 ( $d_z^2$ )	299( $d_z^2$ )	-0.0491
	175( $d_x^2-y^2$ )	-0.01001		255( $d_x^2-y^2$ )	0.0464		305( $d_x^2-y^2$ )	0.04
	141( $d_{xy}$ )	0.02019		219( $d_{xy}$ )	-0.00832		259( $d_{xy}$ )	0.0103
	145( $d_{xz}$ )	-0.02582		225( $d_{xz}$ )	-0.0164		253( $d_{xz}$ )	-0.0394
	157( $d_{yz}$ )	-0.19149		224 ( $d_{yz}$ )	-0.00708		268( $d_{yz}$ )	-0.00241
175( $d_x^2-y^2$ )	163( $d_z^2$ )	-0.01001	255( $d_x^2-y^2$ )	249( $d_z^2$ )	0.0464	306( $d_x^2-y^2$ )	299( $d_z^2$ )	0.143
	175( $d_x^2-y^2$ )	-0.25742		255( $d_x^2-y^2$ )	-0.0341		305( $d_x^2-y^2$ )	0.0231
	141( $d_{xy}$ )	0.01727		219( $d_{xy}$ )	-0.0474		259( $d_{xy}$ )	0.16
	145( $d_{xz}$ )	-0.057		225( $d_{xz}$ )	-0.0275		253( $d_{xz}$ )	-0.00534
	157( $d_{yz}$ )	-0.01361		224 ( $d_{yz}$ )	-0.0000751		268( $d_{yz}$ )	0.0441
141( $d_{xy}$ )	163( $d_z^2$ )	0.02019	219( $d_{xy}$ )	249( $d_z^2$ )	-0.00832	264 ( $d_{xy}$ )	299( $d_z^2$ )	-0.0466
	175( $d_x^2-y^2$ )	0.01727		255( $d_x^2-y^2$ )	-0.0474		305( $d_x^2-y^2$ )	0.055
	141( $d_{xy}$ )	0.06893		219( $d_{xy}$ )	0.1511		259( $d_{xy}$ )	-0.0815
	145( $d_{xz}$ )	0.01452		225( $d_{xz}$ )	-0.10787		253( $d_{xz}$ )	-0.106
	157( $d_{yz}$ )	-0.09312		224 ( $d_{yz}$ )	0.0705		268( $d_{yz}$ )	-0.0185
145( $d_{xz}$ )	163( $d_z^2$ )	-0.02582	225( $d_{xz}$ )	249( $d_z^2$ )	0.0164	263( $d_{xz}$ )	299( $d_z^2$ )	-0.06874
	175( $d_x^2-y^2$ )	-0.057		255( $d_x^2-y^2$ )	-0.0275		305( $d_x^2-y^2$ )	-0.03489
	141( $d_{xy}$ )	0.01452		219( $d_{xy}$ )	0.10787		259( $d_{xy}$ )	-0.1011
	145( $d_{xz}$ )	-0.08056		225( $d_{xz}$ )	0.27067		253( $d_{xz}$ )	0.10534
	157( $d_{yz}$ )	0.06876		224 ( $d_{yz}$ )	-0.2494		268( $d_{yz}$ )	0.00834
157( $d_{yz}$ )	163( $d_z^2$ )	-0.19149	224 ( $d_{yz}$ )	249( $d_z^2$ )	-0.0708	290( $d_{yz}$ )	299( $d_z^2$ )	0.00453
	175( $d_x^2-y^2$ )	-0.01361		255( $d_x^2-y^2$ )	-0.000751		305( $d_x^2-y^2$ )	0.0292
	141( $d_{xy}$ )	-0.09312		219( $d_{xy}$ )	0.0705		259( $d_{xy}$ )	0.0366
	145( $d_{xz}$ )	0.06876		225( $d_{xz}$ )	-0.2494		253( $d_{xz}$ )	-0.0167
	157( $d_{yz}$ )	-0.59823		224 ( $d_{yz}$ )	-0.2143		268( $d_{yz}$ )	0.0201

**Table A3.** Overlap integral analysis for bond angle correlation for complex **1**

Mn-O-Mn: 115.3° J=-13.82 cm <sup>-1</sup>			Mn-O-Mn: 103.7° J=-10.50 cm <sup>-1</sup>			Mn-O-Mn: 90.2° J=-31.99 cm <sup>-1</sup>			Mn-O-Mn: 80.1° J=-113.27 cm <sup>-1</sup>		
Alpha	Beta	overlap integrals	Alpha	Beta	overlap integral	Alpha	Beta	overlap intergral	Alpha	Beta	overlap integrals
166(d <sub>z</sub> <sup>2</sup> )	166(d <sub>z</sub> <sup>2</sup> )	0.58967	163(d <sub>z</sub> <sup>2</sup> )	163(d <sub>z</sub> <sup>2</sup> )	-0.07159	165(d <sub>z</sub> <sup>2</sup> )	165(d <sub>z</sub> <sup>2</sup> )	0.17232	165(d <sub>z</sub> <sup>2</sup> )	165(d <sub>z</sub> <sup>2</sup> )	-0.00592
	175(d <sub>x<sup>2</sup>-y<sup>2</sup>)</sub>	-0.004232		175(d <sub>x<sup>2</sup>-y<sup>2</sup>)</sub>	-0.01001		175(d <sub>x<sup>2</sup>-y<sup>2</sup>)</sub>	0.01476		175(d <sub>x<sup>2</sup>-y<sup>2</sup>)</sub>	-0.01361
	141(d <sub>xy</sub> )	-0.04486		168(d <sub>xy</sub> )	-0.09176		141(d <sub>xy</sub> )	0.02536		166(d <sub>xy</sub> )	0.42178
	146(d <sub>xz</sub> )	-0.01985		145(d <sub>xz</sub> )	-0.02582		142(d <sub>xz</sub> )	-0.02006		161(d <sub>xz</sub> )	-0.23256
	148(d <sub>yz</sub> )	-0.03343		157(d <sub>yz</sub> )	-0.19149		143(d <sub>yz</sub> )	-0.02045		143(d <sub>yz</sub> )	0.03188
175(d <sub>x<sup>2</sup>-y<sup>2</sup>)</sub>	166(d <sub>z</sub> <sup>2</sup> )	-0.004232	175(d <sub>x<sup>2</sup>-y<sup>2</sup>)</sub>	163(d <sub>z</sub> <sup>2</sup> )	-0.01001	175(d <sub>x<sup>2</sup>-y<sup>2</sup>)</sub>	165(d <sub>z</sub> <sup>2</sup> )	0.01476	175(d <sub>x<sup>2</sup>-y<sup>2</sup>)</sub>	165(d <sub>z</sub> <sup>2</sup> )	-0.01361
	175(d <sub>x<sup>2</sup>-y<sup>2</sup>)</sub>	-0.38365		175(d <sub>x<sup>2</sup>-y<sup>2</sup>)</sub>	-0.25742		175(d <sub>x<sup>2</sup>-y<sup>2</sup>)</sub>	-0.06556		175(d <sub>x<sup>2</sup>-y<sup>2</sup>)</sub>	0.00039
	141(d <sub>xy</sub> )	-0.05688		168(d <sub>xy</sub> )	-0.0049		141(d <sub>xy</sub> )	-0.00779		166(d <sub>xy</sub> )	-0.01418
	146(d <sub>xz</sub> )	0.02526		145(d <sub>xz</sub> )	-0.057		142(d <sub>xz</sub> )	-0.00788		161(d <sub>xz</sub> )	0.00391
	148(d <sub>yz</sub> )	0.00358		157(d <sub>yz</sub> )	-0.01361		143(d <sub>yz</sub> )	-0.01567		143(d <sub>yz</sub> )	0.02226
141(d <sub>xy</sub> )	166(d <sub>z</sub> <sup>2</sup> )	-0.04486	168(d <sub>xy</sub> )	163(d <sub>z</sub> <sup>2</sup> )	-0.09176	141(d <sub>xy</sub> )	165(d <sub>z</sub> <sup>2</sup> )	0.02536	166(d <sub>xy</sub> )	165(d <sub>z</sub> <sup>2</sup> )	0.42178
	175(d <sub>x<sup>2</sup>-y<sup>2</sup>)</sub>	-0.05688		175(d <sub>x<sup>2</sup>-y<sup>2</sup>)</sub>	-0.0049		175(d <sub>x<sup>2</sup>-y<sup>2</sup>)</sub>	-0.00779		175(d <sub>x<sup>2</sup>-y<sup>2</sup>)</sub>	-0.01418
	141(d <sub>xy</sub> )	0.01858		168(d <sub>xy</sub> )	-0.06213		141(d <sub>xy</sub> )	0.14752		166(d <sub>xy</sub> )	0.16845
	146(d <sub>xz</sub> )	-0.06026		145(d <sub>xz</sub> )	0.00135		142(d <sub>xz</sub> )	-0.06884		161(d <sub>xz</sub> )	0.23985
	148(d <sub>yz</sub> )	-0.08571		157(d <sub>yz</sub> )	-0.04356		143(d <sub>yz</sub> )	-0.13118		143(d <sub>yz</sub> )	0.00997
146(d <sub>xz</sub> )	166(d <sub>z</sub> <sup>2</sup> )	-0.01985	145(d <sub>xz</sub> )	163(d <sub>z</sub> <sup>2</sup> )	-0.02582	142(d <sub>xz</sub> )	165(d <sub>z</sub> <sup>2</sup> )	-0.02006	161(d <sub>xz</sub> )	165(d <sub>z</sub> <sup>2</sup> )	-0.23256
	175(d <sub>x<sup>2</sup>-y<sup>2</sup>)</sub>	0.02526		175(d <sub>x<sup>2</sup>-y<sup>2</sup>)</sub>	-0.057		175(d <sub>x<sup>2</sup>-y<sup>2</sup>)</sub>	-0.00788		175(d <sub>x<sup>2</sup>-y<sup>2</sup>)</sub>	0.00391
	141(d <sub>xy</sub> )	-0.06026		168(d <sub>xy</sub> )	0.00135		141(d <sub>xy</sub> )	-0.06884		166(d <sub>xy</sub> )	0.23985
	146(d <sub>xz</sub> )	-0.28566		145(d <sub>xz</sub> )	-0.08056		142(d <sub>xz</sub> )	0.12476		161(d <sub>xz</sub> )	-0.10037
	148(d <sub>yz</sub> )	0.33108		157(d <sub>yz</sub> )	0.06876		143(d <sub>yz</sub> )	0.59949		143(d <sub>yz</sub> )	-0.13621
148(d <sub>yz</sub> )	166(d <sub>z</sub> <sup>2</sup> )	-0.03343	157(d <sub>yz</sub> )	163(d <sub>z</sub> <sup>2</sup> )	-0.19149	143(d <sub>yz</sub> )	165(d <sub>z</sub> <sup>2</sup> )	-0.02045	160(d <sub>yz</sub> )	165(d <sub>z</sub> <sup>2</sup> )	-0.21866
	175(d <sub>x<sup>2</sup>-y<sup>2</sup>)</sub>	0.00358		175(d <sub>x<sup>2</sup>-y<sup>2</sup>)</sub>	-0.01361		175(d <sub>x<sup>2</sup>-y<sup>2</sup>)</sub>	-0.01567		175(d <sub>x<sup>2</sup>-y<sup>2</sup>)</sub>	-0.03115
	141(d <sub>xy</sub> )	-0.08571		168(d <sub>xy</sub> )	-0.04356		141(d <sub>xy</sub> )	-0.13118		166(d <sub>xy</sub> )	0.09628
	146(d <sub>xz</sub> )	0.33108		145(d <sub>xz</sub> )	0.06876		142(d <sub>xz</sub> )	0.59949		161(d <sub>xz</sub> )	0.16737
	148(d <sub>yz</sub> )	-0.10911		157(d <sub>yz</sub> )	-0.59823		143(d <sub>yz</sub> )	-0.06111		143(d <sub>yz</sub> )	-0.18946

**Table A4.** Overlap integral analysis for bond distance correlation for complex 1

Mn...O: 2.306 Å J = 2.771 cm <sup>-1</sup>			Mn...O: 2.156 Å J = 0.122 cm <sup>-1</sup>			Mn...O: 2.056 Å J = -3.22 cm <sup>-1</sup>			Mn...O: 1.956 Å J = -10.50 cm <sup>-1</sup>		
Alpha	Beta	Overlap integral									
160(d <sub>z</sub> <sup>2</sup> )	160(d <sub>z</sub> <sup>2</sup> )	0.10695	159(d <sub>z</sub> <sup>2</sup> )	159(d <sub>z</sub> <sup>2</sup> )	-0.43233	163(d <sub>z</sub> <sup>2</sup> )	163(d <sub>z</sub> <sup>2</sup> )	-0.35681	163(d <sub>z</sub> <sup>2</sup> )	163(d <sub>z</sub> <sup>2</sup> )	-0.07159
	175 (d <sub>x</sub> <sup>2</sup> -y <sup>2</sup> )	-0.02648		175 (d <sub>x</sub> <sup>2</sup> -y <sup>2</sup> )	-0.04833		175 (d <sub>x</sub> <sup>2</sup> -y <sup>2</sup> )	0.00784		175 (d <sub>x</sub> <sup>2</sup> -y <sup>2</sup> )	-0.01001
	163(d <sub>xy</sub> )	-0.26621		149(d <sub>xy</sub> )	0.02865		168(d <sub>xy</sub> )	-0.05438		168(d <sub>xy</sub> )	-0.09176
	156(d <sub>yz</sub> )	-0.06909		156(d <sub>yz</sub> )	0.10015		148(d <sub>yz</sub> )	0.03063		145(d <sub>xz</sub> )	-0.02582
	147(d <sub>zx</sub> )	-0.05997		146(d <sub>zx</sub> )	-0.00765		146(d <sub>zx</sub> )	0.04565		157(d <sub>yz</sub> )	-0.19149
175 (d <sub>x</sub> <sup>2</sup> -y <sup>2</sup> )	160(d <sub>z</sub> <sup>2</sup> )	-0.08122	175 (d <sub>x</sub> <sup>2</sup> -y <sup>2</sup> )	159(d <sub>z</sub> <sup>2</sup> )	-0.05326	175 (d <sub>x</sub> <sup>2</sup> -y <sup>2</sup> )	163(d <sub>z</sub> <sup>2</sup> )	0.01231	175 (d <sub>x</sub> <sup>2</sup> -y <sup>2</sup> )	163(d <sub>z</sub> <sup>2</sup> )	-0.01001
	175 (d <sub>x</sub> <sup>2</sup> -y <sup>2</sup> )	-0.12698		175 (d <sub>x</sub> <sup>2</sup> -y <sup>2</sup> )	-0.17328		175 (d <sub>x</sub> <sup>2</sup> -y <sup>2</sup> )	-0.20895		175 (d <sub>x</sub> <sup>2</sup> -y <sup>2</sup> )	-0.25742
	163(d <sub>xy</sub> )	0.01731		149(d <sub>xy</sub> )	-0.07413		168(d <sub>xy</sub> )	-0.02809		168(d <sub>xy</sub> )	-0.0049
	156(d <sub>yz</sub> )	0.01544		156(d <sub>yz</sub> )	0.02373		148(d <sub>yz</sub> )	0.00197		145(d <sub>xz</sub> )	-0.057
	147(d <sub>zx</sub> )	0.03537		146(d <sub>zx</sub> )	0.04234		146(d <sub>zx</sub> )	0.03508		157(d <sub>yz</sub> )	-0.01361
162(d <sub>xy</sub> )	160(d <sub>z</sub> <sup>2</sup> )	0.45277	149(d <sub>xy</sub> )	159(d <sub>z</sub> <sup>2</sup> )	0.12516	168(d <sub>xy</sub> )	163(d <sub>z</sub> <sup>2</sup> )	-0.10659	168(d <sub>xy</sub> )	163(d <sub>z</sub> <sup>2</sup> )	-0.09176
	175 (d <sub>x</sub> <sup>2</sup> -y <sup>2</sup> )	0.00648		175 (d <sub>x</sub> <sup>2</sup> -y <sup>2</sup> )	-0.06524		175 (d <sub>x</sub> <sup>2</sup> -y <sup>2</sup> )	-0.02827		175 (d <sub>x</sub> <sup>2</sup> -y <sup>2</sup> )	-0.0049
	163(d <sub>xy</sub> )	0.12024		149(d <sub>xy</sub> )	0.00718		168(d <sub>xy</sub> )	0.08754		168(d <sub>xy</sub> )	-0.06213
	156(d <sub>yz</sub> )	-0.00269		156(d <sub>yz</sub> )	0.04319		148(d <sub>yz</sub> )	-0.054		145(d <sub>xz</sub> )	0.00135
	147(d <sub>zx</sub> )	-0.00775		146(d <sub>zx</sub> )	-0.13845		146(d <sub>zx</sub> )	-0.03023		157(d <sub>yz</sub> )	-0.04356
152(d <sub>yz</sub> )	160(d <sub>z</sub> <sup>2</sup> )	-0.10016	156(d <sub>yz</sub> )	159(d <sub>z</sub> <sup>2</sup> )	-0.10692	148(d <sub>yz</sub> )	163(d <sub>z</sub> <sup>2</sup> )	0.03764	145(d <sub>xz</sub> )	163(d <sub>z</sub> <sup>2</sup> )	-0.02582
	175 (d <sub>x</sub> <sup>2</sup> -y <sup>2</sup> )	-0.01334		175 (d <sub>x</sub> <sup>2</sup> -y <sup>2</sup> )	0.00126		175 (d <sub>x</sub> <sup>2</sup> -y <sup>2</sup> )	0.00002		175 (d <sub>x</sub> <sup>2</sup> -y <sup>2</sup> )	-0.057
	163(d <sub>xy</sub> )	0.00605		149(d <sub>xy</sub> )	-0.05432		168(d <sub>xy</sub> )	-0.05173		168(d <sub>xy</sub> )	0.00135
	156(d <sub>yz</sub> )	0.00128		156(d <sub>yz</sub> )	-0.08646		148(d <sub>yz</sub> )	-0.1131		145(d <sub>xz</sub> )	-0.08056
	147(d <sub>zx</sub> )	-0.01206		146(d <sub>zx</sub> )	-0.00034		146(d <sub>zx</sub> )	0.2936		157(d <sub>yz</sub> )	0.06876
146(d <sub>zx</sub> )	160(d <sub>z</sub> <sup>2</sup> )	-0.00557	153(d <sub>zx</sub> )	159(d <sub>z</sub> <sup>2</sup> )	-0.1278	146(d <sub>zx</sub> )	163(d <sub>z</sub> <sup>2</sup> )	0.04858	157(d <sub>yz</sub> )	163(d <sub>z</sub> <sup>2</sup> )	-0.19149
	175 (d <sub>x</sub> <sup>2</sup> -y <sup>2</sup> )	0.02333		175 (d <sub>x</sub> <sup>2</sup> -y <sup>2</sup> )	0.0196		175 (d <sub>x</sub> <sup>2</sup> -y <sup>2</sup> )	0.03156		175 (d <sub>x</sub> <sup>2</sup> -y <sup>2</sup> )	-0.01361
	163(d <sub>xy</sub> )	-0.0112		149(d <sub>xy</sub> )	-0.33706		168(d <sub>xy</sub> )	-0.03018		168(d <sub>xy</sub> )	-0.04356
	156(d <sub>yz</sub> )	0.00734		156(d <sub>yz</sub> )	-0.04844		148(d <sub>yz</sub> )	0.28918		145(d <sub>xz</sub> )	0.06876
	147(d <sub>zx</sub> )	-0.00924		146(d <sub>zx</sub> )	-0.04405		146(d <sub>zx</sub> )	-0.02467		157(d <sub>yz</sub> )	-0.59823

**Table A5.** Overlap integral analysis for Dihedral angle correlation for complex **1**

Dihedral: 0° J = -10.50			Dihedral: 21.2° J = -5.40676			Dihedral: 35.4° J = -4.58373		
Alpha	Beta	Overlap integral	Alpha	Beta	Overlap integral	Alpha	Beta	Overlap integral
163(d <sub>z</sub> <sup>2</sup> )	163(d <sub>z</sub> <sup>2</sup> )	-0.07159	167(d <sub>z</sub> <sup>2</sup> )	163(d <sub>z</sub> <sup>2</sup> )	-0.03166	163(d <sub>z</sub> <sup>2</sup> )	162(d <sub>z</sub> <sup>2</sup> )	0.02899
	175(d <sub>x</sub> <sup>2</sup> -y <sup>2</sup> )	-0.01001		175(d <sub>x</sub> <sup>2</sup> -y <sup>2</sup> )	-0.01374		175(d <sub>x</sub> <sup>2</sup> -y <sup>2</sup> )	0.00972
	168(d <sub>xy</sub> )	-0.09176		141(d <sub>xy</sub> )	-0.02497		167(d <sub>xy</sub> )	0.03158
	145(d <sub>xz</sub> )	-0.02582		142(d <sub>yz</sub> )	-0.0336		161(d <sub>yz</sub> )	0.02301
	157(d <sub>yz</sub> )	-0.19149		145(d <sub>xz</sub> )	-0.02127		156(d <sub>xz</sub> )	0.09884
175(d <sub>x</sub> <sup>2</sup> -y <sup>2</sup> )	163(d <sub>z</sub> <sup>2</sup> )	-0.01001	175(d <sub>x</sub> <sup>2</sup> -y <sup>2</sup> )	163(d <sub>z</sub> <sup>2</sup> )	0.04255	175(d <sub>x</sub> <sup>2</sup> -y <sup>2</sup> )	162(d <sub>z</sub> <sup>2</sup> )	0.04131
	175(d <sub>x</sub> <sup>2</sup> -y <sup>2</sup> )	-0.25742		175(d <sub>x</sub> <sup>2</sup> -y <sup>2</sup> )	-0.2027		175(d <sub>x</sub> <sup>2</sup> -y <sup>2</sup> )	-0.1471
	168(d <sub>xy</sub> )	-0.0049		141(d <sub>xy</sub> )	0.05601		167(d <sub>xy</sub> )	0.00576
	145(d <sub>xz</sub> )	-0.057		142(d <sub>yz</sub> )	-0.02619		161(d <sub>yz</sub> )	0.00719
	157(d <sub>yz</sub> )	-0.01361		145(d <sub>xz</sub> )	-0.05508		156(d <sub>xz</sub> )	0.04227
168(d <sub>xy</sub> )	163(d <sub>z</sub> <sup>2</sup> )	-0.09176	141(d <sub>xy</sub> )	163(d <sub>z</sub> <sup>2</sup> )	0.02144	150(d <sub>xy</sub> )	162(d <sub>z</sub> <sup>2</sup> )	0.10648
	175(d <sub>x</sub> <sup>2</sup> -y <sup>2</sup> )	-0.0049		175(d <sub>x</sub> <sup>2</sup> -y <sup>2</sup> )	0.00315		175(d <sub>x</sub> <sup>2</sup> -y <sup>2</sup> )	-0.10246
	168(d <sub>xy</sub> )	-0.06213		141(d <sub>xy</sub> )	0.07841		167(d <sub>xy</sub> )	-0.05104
	145(d <sub>xz</sub> )	0.00135		142(d <sub>yz</sub> )	0.12435		161(d <sub>yz</sub> )	-0.05831
	157(d <sub>yz</sub> )	-0.04356		145(d <sub>xz</sub> )	-0.15893		156(d <sub>xz</sub> )	0.02061
145(d <sub>xz</sub> )	163(d <sub>z</sub> <sup>2</sup> )	-0.02582	142(d <sub>yz</sub> )	163(d <sub>z</sub> <sup>2</sup> )	-0.02339	162(d <sub>yz</sub> )	162(d <sub>z</sub> <sup>2</sup> )	0.02991
	175(d <sub>x</sub> <sup>2</sup> -y <sup>2</sup> )	-0.057		175(d <sub>x</sub> <sup>2</sup> -y <sup>2</sup> )	0.08783		175(d <sub>x</sub> <sup>2</sup> -y <sup>2</sup> )	-0.0404
	168(d <sub>xy</sub> )	0.00135		141(d <sub>xy</sub> )	0.17037		167(d <sub>xy</sub> )	0.26563
	145(d <sub>xz</sub> )	-0.08056		142(d <sub>yz</sub> )	0.15563		161(d <sub>yz</sub> )	-0.24778
	157(d <sub>yz</sub> )	0.06876		145(d <sub>xz</sub> )	-0.01117		156(d <sub>xz</sub> )	-0.12072
157(d <sub>yz</sub> )	163(d <sub>z</sub> <sup>2</sup> )	-0.19149	148(d <sub>xz</sub> )	163(d <sub>z</sub> <sup>2</sup> )	0.04131	159(d <sub>xz</sub> )	162(d <sub>z</sub> <sup>2</sup> )	-0.37277
	175(d <sub>x</sub> <sup>2</sup> -y <sup>2</sup> )	-0.01361		175(d <sub>x</sub> <sup>2</sup> -y <sup>2</sup> )	0.02236		175(d <sub>x</sub> <sup>2</sup> -y <sup>2</sup> )	-0.07806
	168(d <sub>xy</sub> )	-0.04356		141(d <sub>xy</sub> )	-0.3344		167(d <sub>xy</sub> )	-0.07806
	145(d <sub>xz</sub> )	0.06876		142(d <sub>yz</sub> )	-0.01875		161(d <sub>yz</sub> )	0.00438
	157(d <sub>yz</sub> )	-0.59823		145(d <sub>xz</sub> )	0.11934		156(d <sub>xz</sub> )	0.0397

**Table A6.** Overlap integral analysis for out of plane displacement of methyl group correlation for complex **1**

$\tau = 174^\circ$ $J = -10.50$			$\tau = 150^\circ$ $J = -8.2204$			$\tau = 130^\circ$ $J = -7.2196$		
163( $d_z^2$ )	163( $d_z^2$ )	-0.07159	163( $d_z^2$ )	163( $d_z^2$ )	0.02892	163( $d_z^2$ )	163( $d_z^2$ )	0.26714
	175( $d_x^2-y^2$ )	-0.01001		175( $d_x^2-y^2$ )	-0.0017		175( $d_x^2-y^2$ )	-0.00655
	168( $d_{xy}$ )	-0.09176		168( $d_{xy}$ )	-0.10668		168( $d_{xy}$ )	-0.13399
	145( $d_{xz}$ )	-0.02582		161( $d_{xz}$ )	-0.18848		152( $d_{xz}$ )	0.04062
	157( $d_{yz}$ )	-0.19149		157( $d_{yz}$ )	0.099804		157( $d_{yz}$ )	0.03663
175( $d_x^2-y^2$ )	163( $d_z^2$ )	-0.01001	175( $d_x^2-y^2$ )	163( $d_z^2$ )	-0.0017	175( $d_x^2-y^2$ )	163( $d_z^2$ )	-0.00655
	175( $d_x^2-y^2$ )	-0.25742		175( $d_x^2-y^2$ )	-0.23447		175( $d_x^2-y^2$ )	-0.20704
	168( $d_{xy}$ )	-0.0049		168( $d_{xy}$ )	-0.00626		168( $d_{xy}$ )	-0.00057
	145( $d_{xz}$ )	-0.057		161( $d_{xz}$ )	-0.01591		152( $d_{xz}$ )	-0.06558
	157( $d_{yz}$ )	-0.01361		157( $d_{yz}$ )	0.00888		157( $d_{yz}$ )	0.01886
168( $d_{xy}$ )	163( $d_z^2$ )	-0.09176	168( $d_{xy}$ )	163( $d_z^2$ )	-0.10668	168( $d_{xy}$ )	163( $d_z^2$ )	-0.13399
	175( $d_x^2-y^2$ )	-0.0049		175( $d_x^2-y^2$ )	-0.00626		175( $d_x^2-y^2$ )	-0.00057
	168( $d_{xy}$ )	-0.06213		168( $d_{xy}$ )	-0.12599		168( $d_{xy}$ )	-0.16706
	145( $d_{xz}$ )	0.00135		161( $d_{xz}$ )	0.00873		152( $d_{xz}$ )	-0.00511
	157( $d_{yz}$ )	-0.04356		157( $d_{yz}$ )	-0.08533		157( $d_{yz}$ )	-0.0788
145( $d_{xz}$ )	163( $d_z^2$ )	-0.02582	161( $d_{xz}$ )	163( $d_z^2$ )	-0.18848	152( $d_{xz}$ )	163( $d_z^2$ )	0.04062
	175( $d_x^2-y^2$ )	-0.057		175( $d_x^2-y^2$ )	-0.01591		175( $d_x^2-y^2$ )	-0.06558
	168( $d_{xy}$ )	0.00135		168( $d_{xy}$ )	0.00873		168( $d_{xy}$ )	-0.00511
	145( $d_{xz}$ )	-0.08056		161( $d_{xz}$ )	0.3636		152( $d_{xz}$ )	-0.39639
	157( $d_{yz}$ )	0.06876		157( $d_{yz}$ )	-0.1548		157( $d_{yz}$ )	0.17139
157( $d_{yz}$ )	163( $d_z^2$ )	-0.19149	157( $d_{yz}$ )	163( $d_z^2$ )	0.099804	157( $d_{yz}$ )	163( $d_z^2$ )	0.03663
	175( $d_x^2-y^2$ )	-0.01361		175( $d_x^2-y^2$ )	0.00888		175( $d_x^2-y^2$ )	0.01886
	168( $d_{xy}$ )	-0.04356		168( $d_{xy}$ )	-0.08533		168( $d_{xy}$ )	-0.0788
	145( $d_{xz}$ )	0.06876		161( $d_{xz}$ )	-0.1548		152( $d_{xz}$ )	0.17139
	157( $d_{yz}$ )	-0.59823		157( $d_{yz}$ )	-0.15031		157( $d_{yz}$ )	-0.18453

## Appendix B: Chapter 3

**Table B1.** DFT calculated D tensor on complex **6** with varying computational protocols.

Complexes	Method	D (cm <sup>-1</sup> )	E/D	g-tensor
With counter ion(MnCu)	B3LYP/TZVPPP	16.96	0.01	2.03
With counter ion(MnZn)	B3LYP/TZVPPP	1.75	0.3	1.99
Without counter ion(MnCu)	B3LYP/TZVPPP	12.47	0.02	2.03
Without counter ion(MnZn)	B3LYP/TZVPPP	1.78	0.3	1.99
Without counter ion(MnCu)	BP86/TZVPPP	2.35	0.06	1.98
Without counter ion(MnZn)	BP86/TZVPPP	1.94	0.06	1.99
Experimental MnCu	-----	6.27	0.09	----
Experimental Single ion	-----	4.78	0.08	1.98

**Table B2.** DFT calculated  $J$  values for **6** with  $\langle S^{**2} \rangle$  value.

Complex	Spin configuration	Energies	$J$ value	$\langle S^{**2} \rangle$ values
<b>6</b>	HS	-5769.99075	-83.7234265	8.8156
	BS	-5769.992657		4.7834
<b>No counterion</b>	HS	-5009.45679	-71.2361979	8.8134
	BS	-5009.458413		4.7751

**Table B3.** Overlap Integral Analysis on **6**

Mn orbitals	Cu orbital	overlap integral
212(d <sub>xy</sub> )	209(d <sub>x<sup>2</sup>-y<sup>2</sup></sub> )	-0.003
213(d <sub>xz</sub> )		0.009
217(d <sub>yz</sub> )		-0.023
220(d <sub>x<sup>2</sup>-y<sup>2</sup></sub> )		-0.144
227(d <sub>z<sup>2</sup></sub> )		-0.007

## Appendix C: Chapter 4

**Table C1.** BVS calculations on the Mn(III) ions described in this chapter.

Chain		Atom label and BVS result
<b>(10)</b>	<b>Calculated as:</b>	<b>Mn1</b>
	Mn(II)	3.39
	Mn(III)	3.13
	Mn(IV)	3.09
	<b>Calculated as:</b>	<b>Mn3</b>
	Mn(II)	3.38
	Mn(III)	3.11
	Mn(IV)	3.05
<b>(11)</b>	<b>Calculated as:</b>	<b>Mn1</b>
	Mn(II)	3.23
	Mn(III)	2.98
	Mn(IV)	2.92
<b>(13)</b>	<b>Calculated as:</b>	<b>Mn1</b>
	Mn(II)	3.30
	Mn(III)	3.04
	Mn(IV)	2.98
<b>(14)</b>	<b>Calculated as:</b>	<b>Mn1</b>
	Mn(II)	3.24
	Mn(III)	2.99
	Mn(IV)	2.93
	<b>Calculated as:</b>	<b>Mn3</b>
	Mn(II)	3.48
	Mn(III)	3.20
	Mn(IV)	3.14
<b>(16)</b>	<b>Calculated as:</b>	<b>Mn1</b>
	Mn(II)	1.88
	Mn(III)	1.74
	Mn(IV)	1.70

**Table C2.** Intra-chain metal...metal distances in the 1-D chains **10-15** and **17**

<b>(10)</b>		<b>(14)</b>	
Mn2...Na2	3.306	Mn1...Na1	3.182
Mn2...Na1	3.339	Mn3...Na2	3.074
Mn1...Na1	3.153	Mn2...Na2	3.295
Mn3...Na2	3.142	Mn2...Na1	3.231
<b>(11)</b>		<b>(15)</b>	
Mn1...Na1	5.251	Mn1...Na1	3.310
<b>(12)</b>		Mn1...Na2	3.293
Fe1...Na1	5.242	Mn2...Na1	3.273
<b>(13)</b>		Mn2...Na2	3.327
Mn1...Na1	5.256	<b>(17)</b>	
		Fe1...Na1	3.439

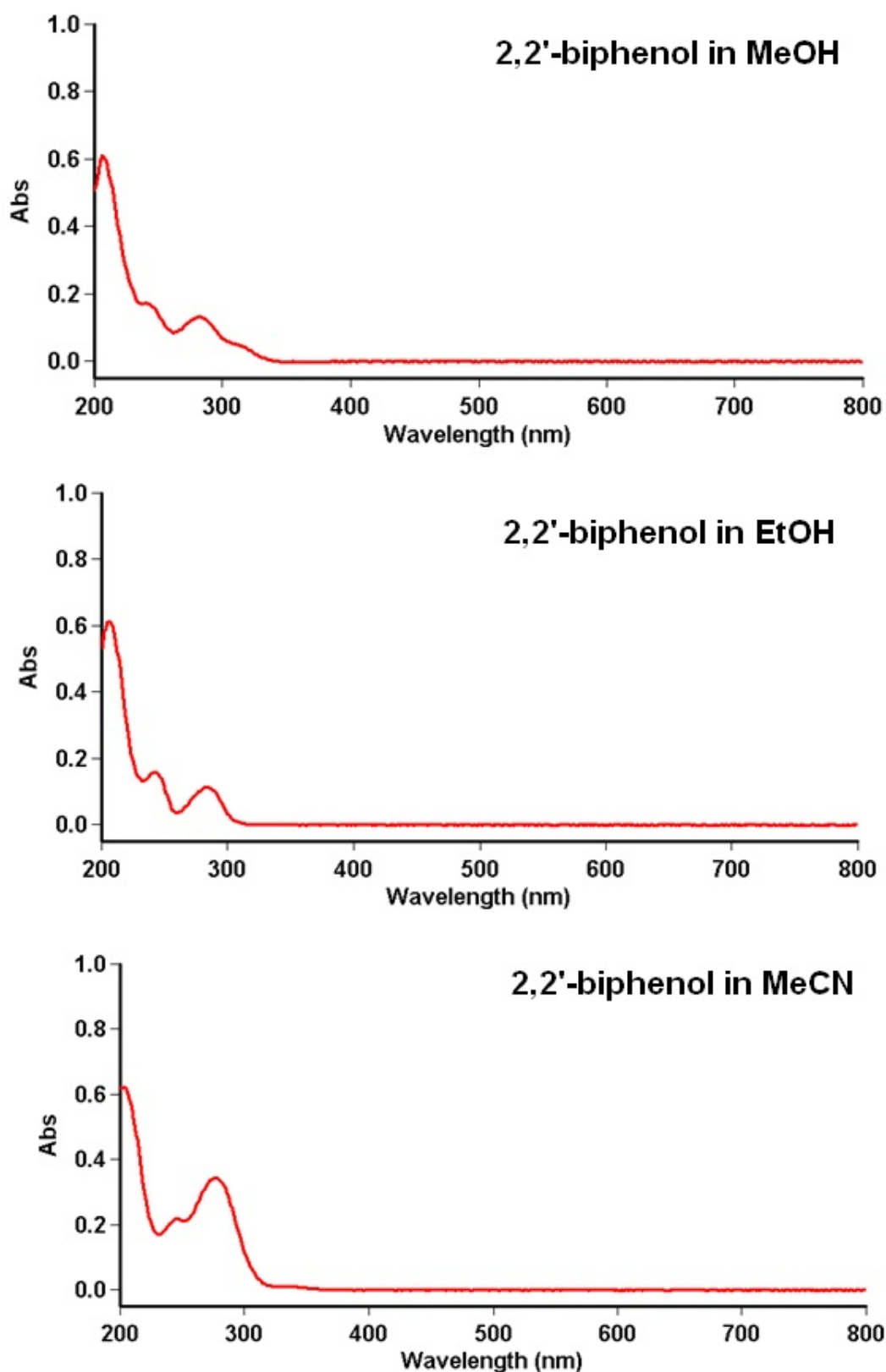


**Figure C1.** UV/vis spectra obtained from MeOH (top), EtOH (middle) and MeCN (bottom) solutions of 2,2'-biphenol. UV/vis (MeOH):  $\lambda_{\text{max}}$  [nm] ( $\epsilon_{\text{max}}$  103 dm<sup>3</sup> mol<sup>-1</sup> cm<sup>-1</sup>): 206 (37.9), 241 (10.8), 292 (8.2), 318(sh). (EtOH): 207 (38.1), 243 (9.8), 284 (8.3). (MeCN): 203 (38.6), 246 (13.6), 277 (21.2), 319 (2.6).

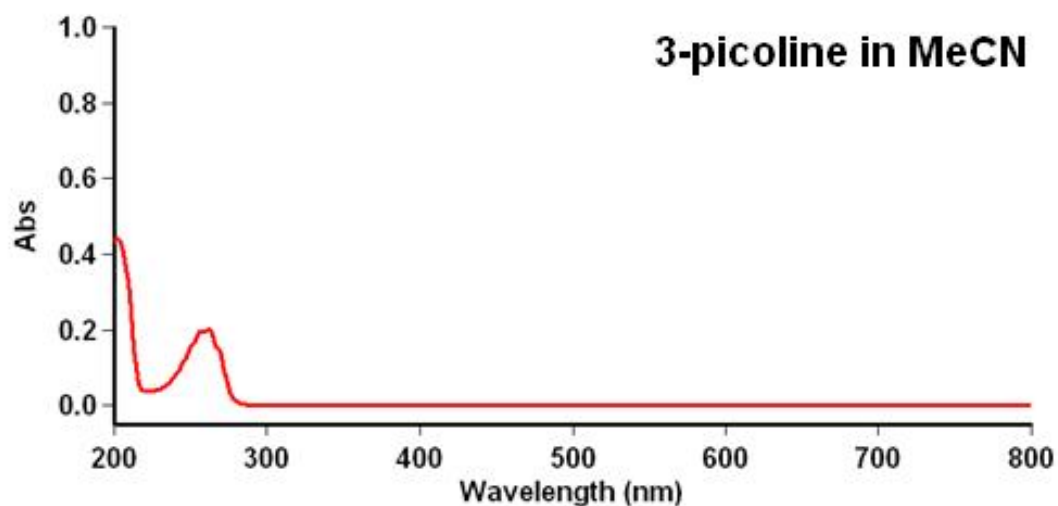
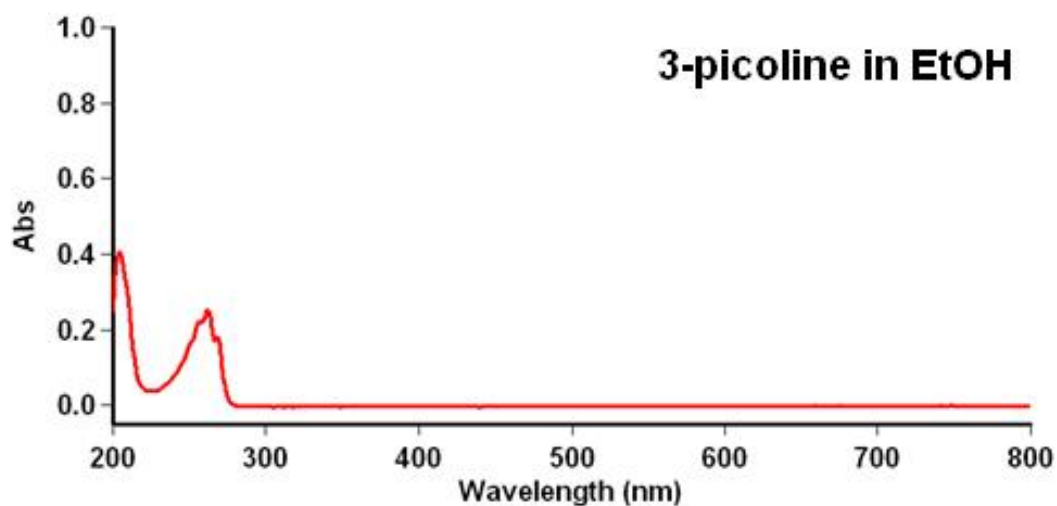
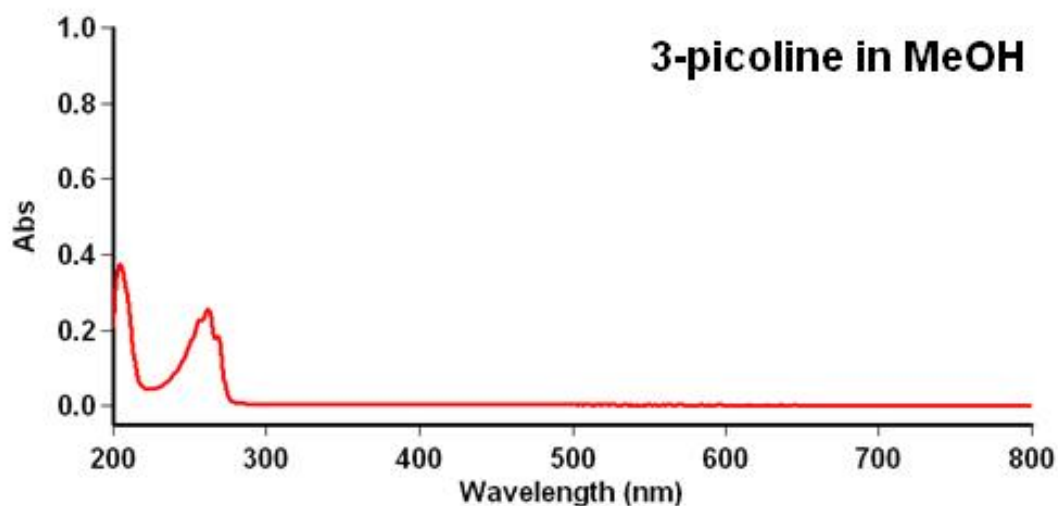


**Figure C2.** UV/vis spectra obtained from MeOH (top), EtOH (middle) and MeCN (bottom) solutions of 3-picoline. UV/vis (MeOH):  $\lambda_{\text{max}}$  [nm] ( $\epsilon_{\text{max}}$  103 dm<sup>3</sup> mol<sup>-1</sup> cm<sup>-1</sup>): 204 (4.5), 256 (2.7), 262 (3.1), 268 (2.25). (EtOH): 204 (4.95), 250 (1.99), 257 (2.75), 262 (3.06), 269 (2.16). (MeCN): 202 (5.0), 257 (2.37), 262 (2.46), 268 (1.87).

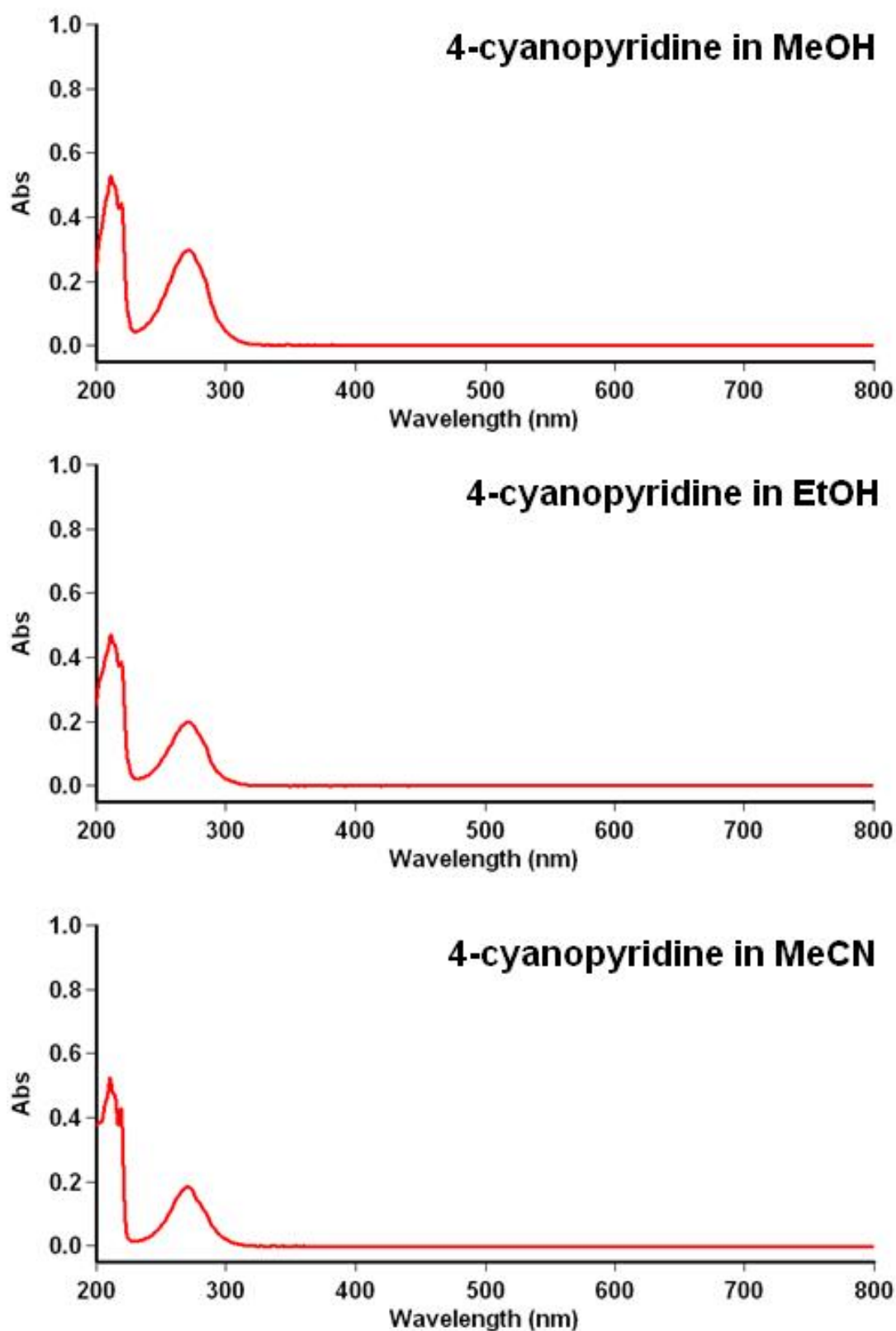


**Figure C3.** UV/vis spectra obtained from MeOH (top), EtOH (middle) and MeCN (bottom) solutions of 4-cyanopyridine. UV/vis (MeOH):  $\lambda_{\text{max}}$  [nm] ( $\epsilon_{\text{max}}$  103 dm<sup>3</sup> mol<sup>-1</sup> cm<sup>-1</sup>): 211 (9.18), 219 (7.69), 271 (5.16). (EtOH): 211 (8.16), 219 (6.7), 271 (3.44). (MeCN): 210 (9.10), 219 (7.43), 270 (3.21).

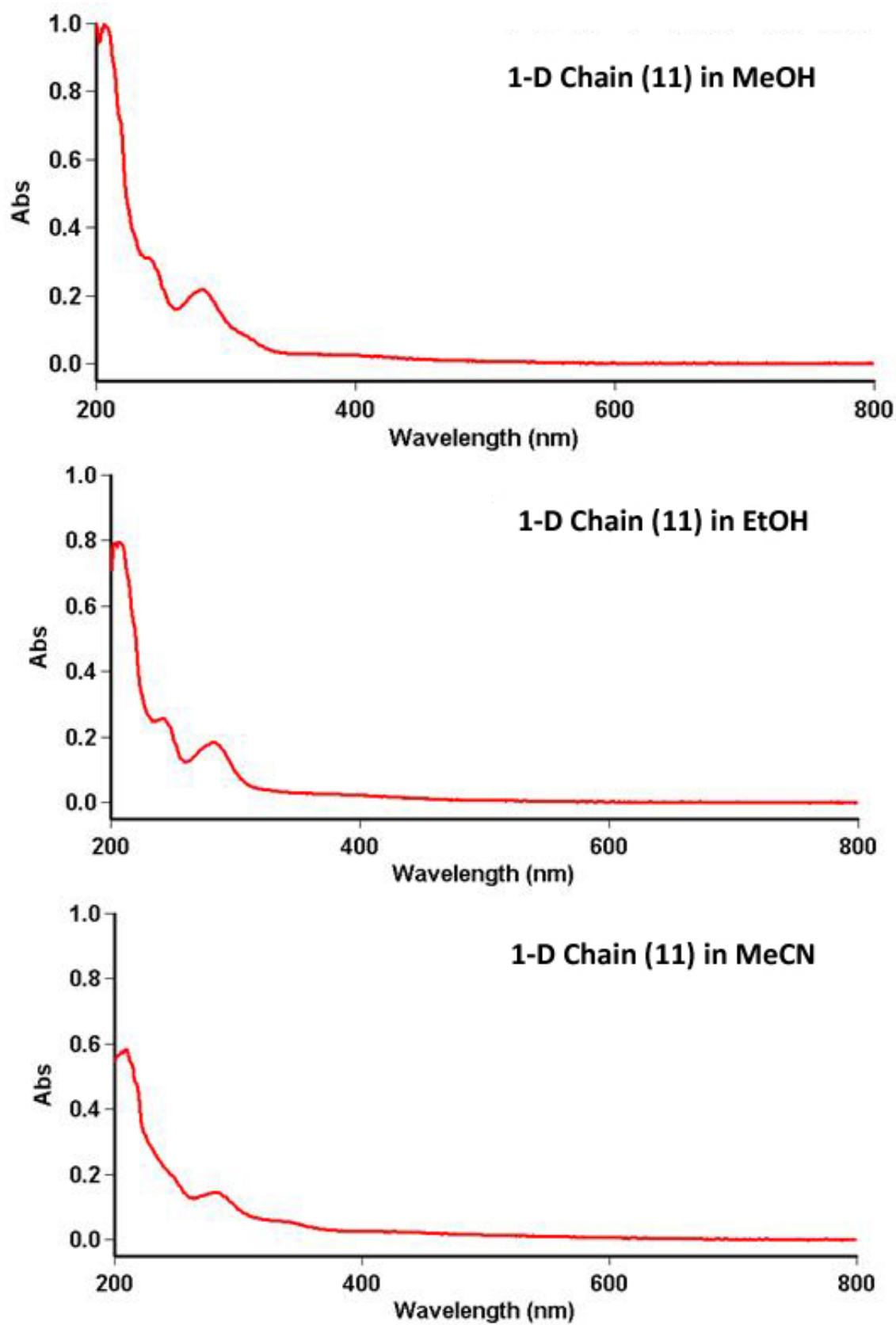


**Figure C4.** UV/vis spectra obtained from MeOH (top), EtOH (middle) and MeCN (bottom) solutions of the 1-D chain in **11**.

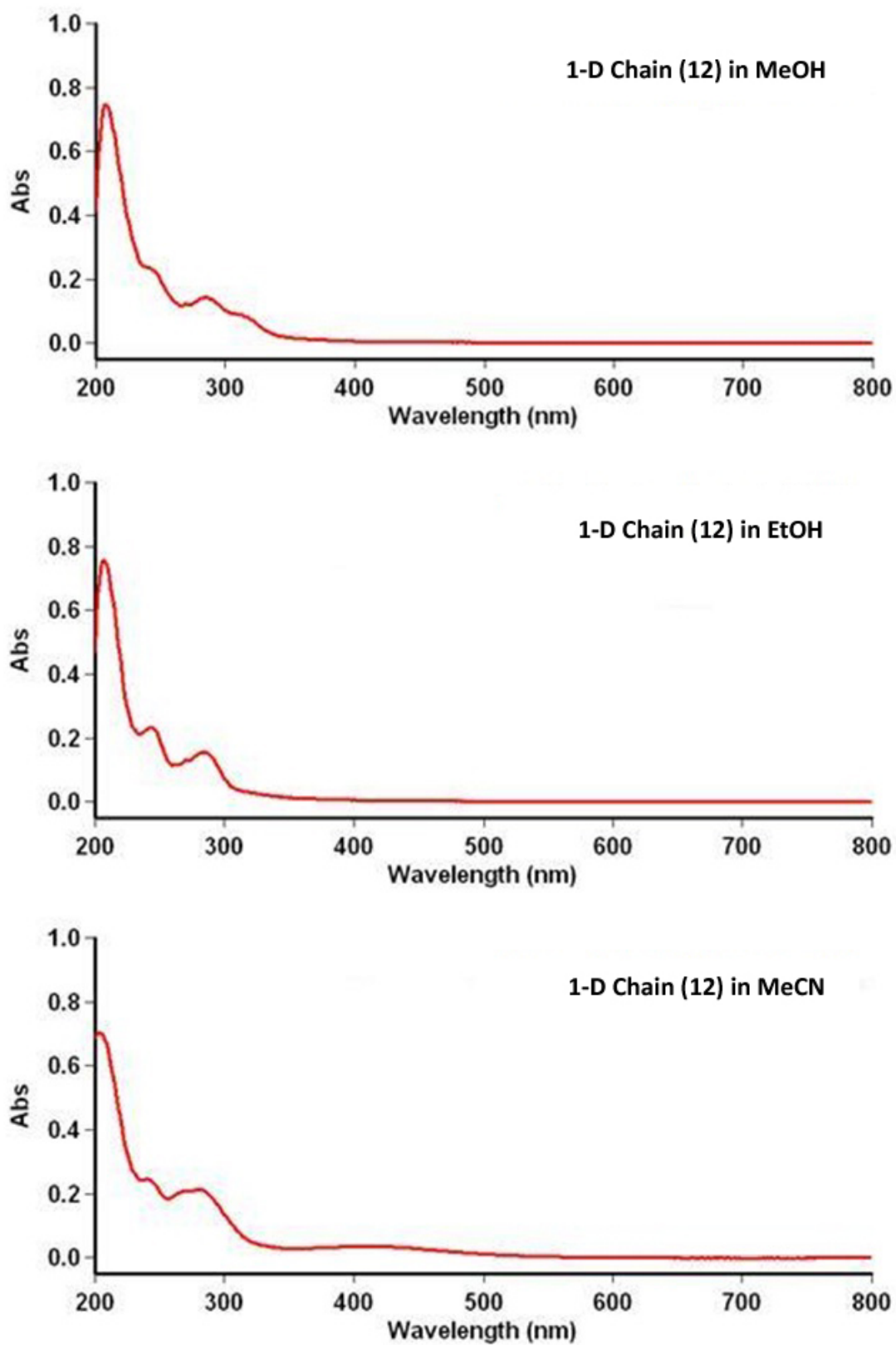


**Figure C5.** UV/vis spectra obtained from MeOH (top), EtOH (middle) and MeCN (bottom) solutions of the chain in **12**.

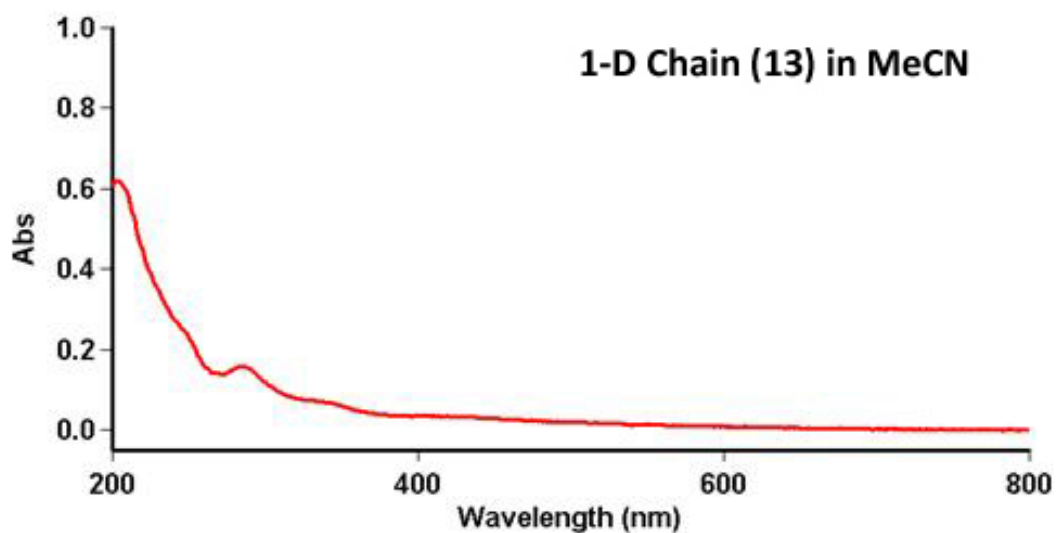
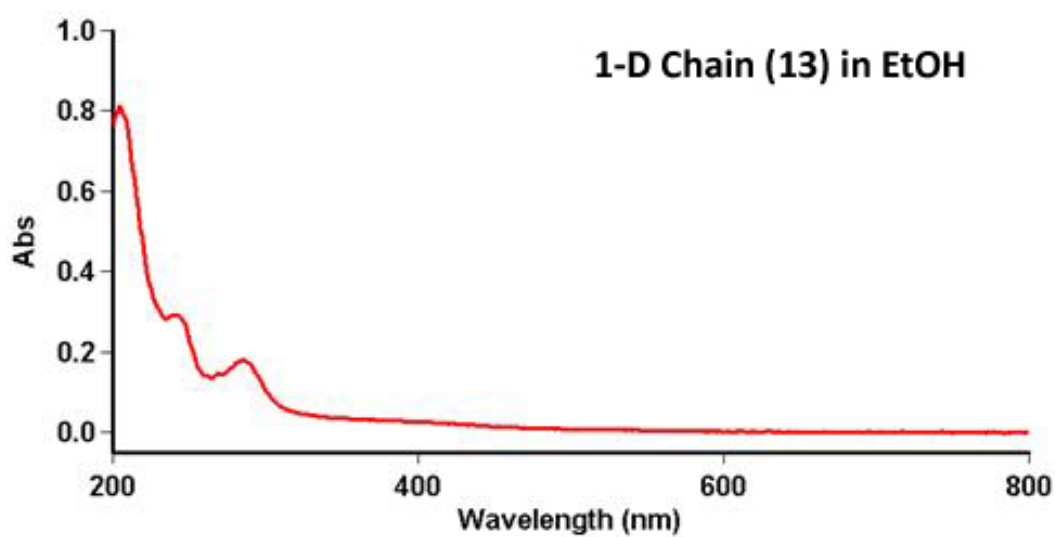
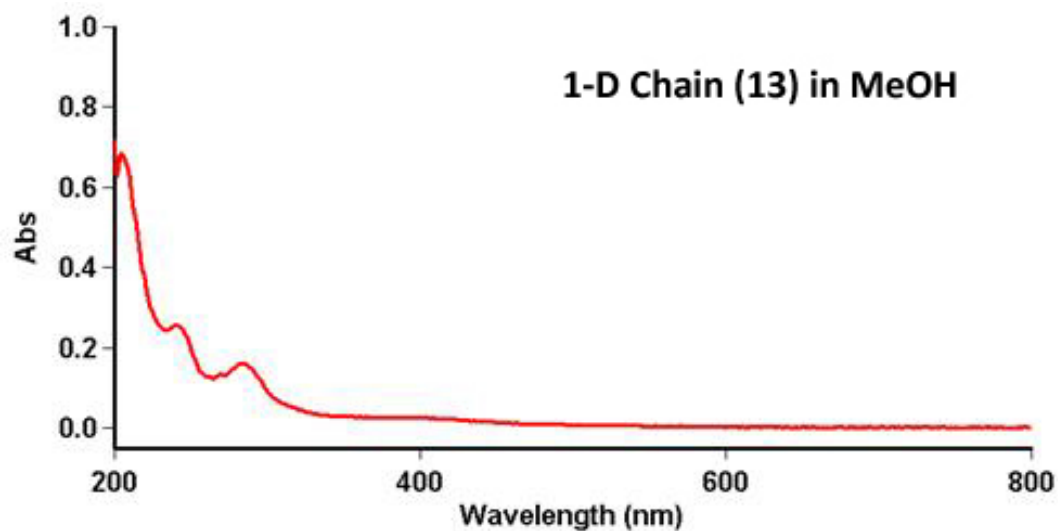


**Figure C6.** UV/vis spectra obtained from MeOH (top), EtOH (middle) and MeCN (bottom) solutions of the Fe / Na chain in **13**.